

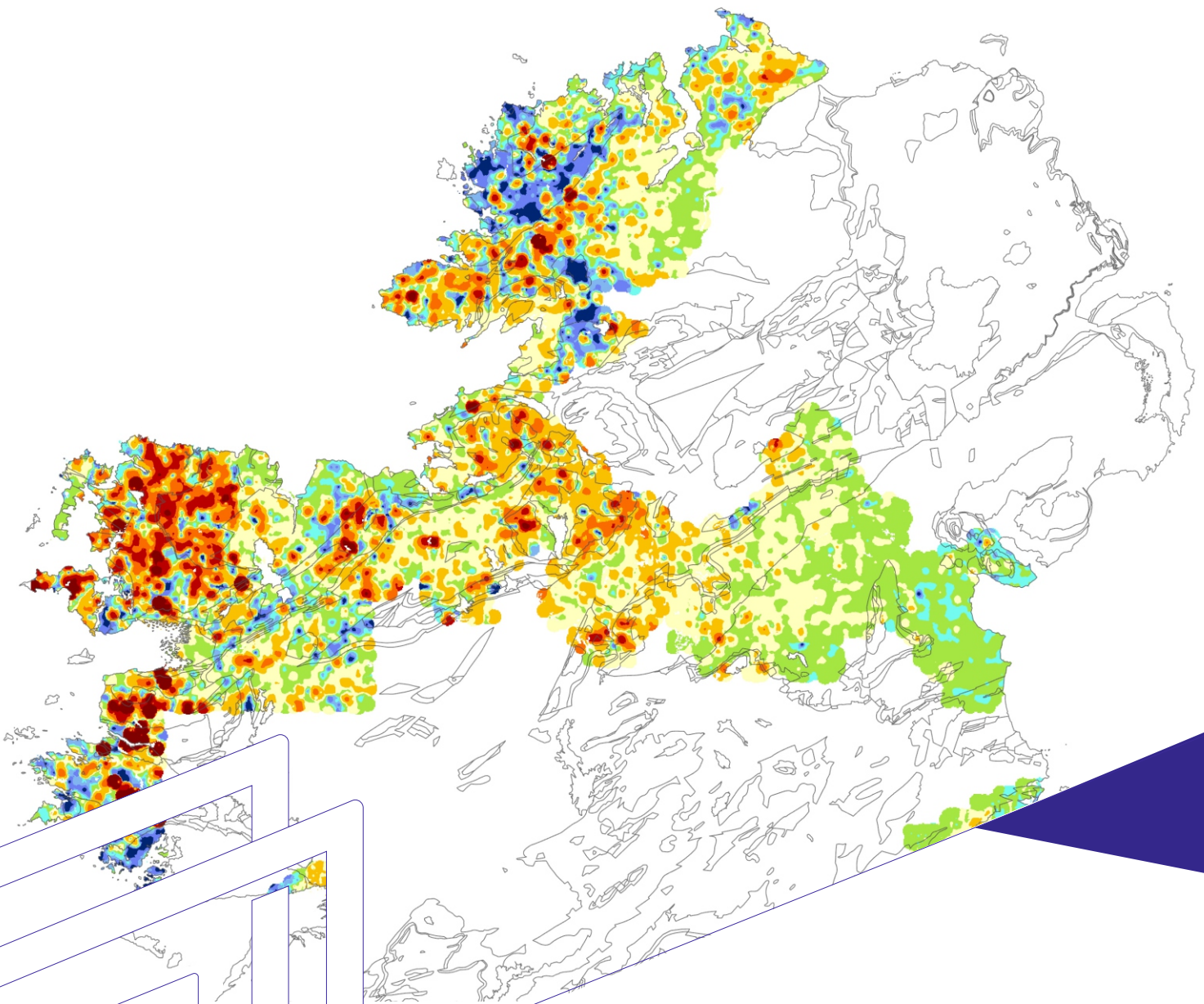


Rialtas na hÉireann
Government of Ireland



Geological Survey
Suirbhéireacht Gheolaíochta
Ireland | Éireann

Investigating the relationship between Tellus topsoil geochemical and airborne radiometric measurements of potassium, uranium and thorium



Geological Survey Ireland Report 2022

Document Information

Project title: Investigating the relationship between Tellus topsoil geochemical and airborne radiometric measurements of potassium, uranium and thorium.
Current Document version: Version 2.0

Prepared By	Date	Comment
S. Lilburn	19/04/2022	

Reviewed by	Date	Comment
J. Hodgson	24/09/2021	Review of Version 0.1.
J. Weatherill (Academic supervisor, UCC)	01/10/2021	Review of Version 0.2.
J. Hodgson	29/04/2022	Review Version 2.0

Approved By	Date	Comment
J. Hodgson	29/04/2022	Geological Survey Ireland

Version History

Ver. No.	Ver. Date	Comment	By
0.1	24/09/2021	Dissertation draft (incomplete)	S. Lilburn
0.2	30/09/2021	First complete draft of dissertation.	S. Lilburn
0.3	14/10/2021	Final draft of dissertation for submission.	S. Lilburn
1.0	13/04/2022	Report v1	S. Lilburn
2.0	19/04/2022	Report v2	S. Lilburn



Acknowledgements

The work presented in this publication was carried out at the Tellus programme, Geological Survey Ireland, and was originally detailed in a dissertation submitted to University College Cork (UCC) in partial fulfilment of the requirements for the degree of Master of Science in Applied Environmental Geoscience. The author gratefully acknowledges the efforts of project supervisors Dr Jim Hodgson (Geological Survey Ireland) and Dr John Weatherill (UCC) and the invaluable support from the Tellus team.

This publication is published with the approval of the Director, Geological Survey Ireland.

Disclaimer

Although every effort has been made to ensure the accuracy of the material contained in this publication, complete accuracy cannot be guaranteed. Neither Geological Survey Ireland nor the authors accept any responsibility whatsoever for loss or damage occasioned, or claimed to have been occasioned, in part or in full as a consequence of any person acting, or refraining from acting, as a result of a matter contained in this publication.

Copyright

Base maps are published subject to OSI copyrights. © Government of Ireland. Ordnance Survey Ireland Licence No. EN 0047222. © Ordnance Survey Ireland/Government of Ireland.



Abstract

The relationship between geochemical and airborne gamma-ray spectrometric measurements of potassium, uranium and thorium concentrations in the shallow subsurface of the northern half of the island of Ireland was investigated using Tellus shallow topsoil and radiometric data. Using a GIS, radiometric data were re-sampled and joined to soil points to enable a pairwise comparison of concentrations across varying geological units, geochemical signatures, soil types and land use classes. Radiometric data showed a strong positive correlation with XRFs soil data, with typical 'soil:air' ratios of 1.32, 2.75 and 1.4 observed for K, U and Th, respectively. Despite the similar radioelement distributions observed in ICP-MS/OES soil and radiometric datasets, variable *Aqua Regia* extraction rates for the elements across the study area significantly affected the correlation, rendering the former dataset unsuitable for this investigation.

The influence of geochemistry and geology on the relationship was minor. Moderate-to-strong correlation was observed between the datasets when classified by 'Geochemical Domain' (i.e., split into zones of similar geochemical signature based on underlying bedrock and subsoil lithologies), however, variation between domains was thought to be related to differences in typical ground conditions associated with each. Greater ' $X_{\text{soil}}/X_{\text{air}}$ ' values were observed over areas of peat due to increased gamma-ray attenuation, although the co-occurrence of upland blanket peat and outcropping rock, as well as possible variations in peat thickness and saturation, resulted in a wide range of values in these areas. Soil texture was also a factor, with clay soils exhibiting high $X_{\text{soil}}/X_{\text{air}}$ values while lows were observed for K and Th in sandy and fine loamy drift. Land use appeared to influence the relationship, with soil and radiometric measurements affected disproportionately by changes in vegetation cover and anthropogenic interference, however these findings were not conclusive due to differing sample sizes and covariance of land use and soil properties.

Finally, linear regression equations were used to create Inverse Distance Weighted maps of predicted soil concentrations based on radiometric data. Predictions were improved by using separate equations for areas with and without peat in each Geochemical Domain, with deviations from 'true' soil concentrations averaging 22.33 %, 16.49 % and 25.61 % for K, U and Th, respectively. The identification of other factors affecting the soil-radiometric relationship throughout this study suggests that the accuracy of such predictions may be improved by incorporating additional parameters.



Table of Contents

Abstract.....	4
List of Abbreviations	8
1. Introduction	9
1.1. Background	9
1.2. Context.....	10
1.2.1. Geochemical and Radioelement Mapping.....	10
1.2.2. Peat Mapping.....	10
1.2.3. Public Health	11
2. Review of Existing Literature	12
2.2. Terrestrial Radioelements K, U, Th and Their Geological Associations	12
2.2.1. Potassium.....	12
2.2.2. Uranium	13
2.2.3. Thorium.....	14
2.3. Radioactivity & Gamma-ray Spectrometry	15
2.4. Radiometric Survey Design, Calibration, Data Collection and Processing.....	19
2.5. Gamma-ray Attenuation	20
2.6. Radon Emanation.....	22
2.7. XRFs vs ICP Methods.....	23
2.8. Comparing and/or Integrating Geochemical and Radiometric Observations	24
3. Research Aims and Objectives	26
4. Study Area.....	27
4.1. Bedrock Geology	27
4.2. Superficial (Quaternary) Geology	29



4.3.	Soils.....	29
4.4.	Land Use.....	34
4.5.	Topography and Rainfall.....	34
5.	Materials and Methods.....	37
5.1.	Data Used.....	37
5.2.	Geochemical Data: Background.....	39
5.2.1.	Sample collection, preparation, analysis and reporting.....	39
5.2.2.	Geochemistry QA/QC.....	40
5.3.	Radiometric Data: Background.....	40
5.3.1.	Survey Specifications.....	40
5.3.2.	Radiometric calibrations, data processing and QC.....	42
5.4.	Research Methods.....	43
5.4.1.	Data manipulation in ArcGIS Pro.....	44
5.4.2.	Classifying data.....	46
5.4.3.	Data manipulation, treatment of outliers and statistics in Excel.....	48
5.4.4.	Mapping.....	50
6.	Results and Discussion.....	52
6.1.	ICP _{ar} Soil and Radiometric Data.....	52
6.1.1.	Comparing radioelement concentrations.....	52
6.1.2.	Geochemical Domains.....	58
6.1.3.	Peat.....	60
6.1.4.	XRFS vs ICP _{ar}	61
6.2.	XRFS Soil and Radiometric Data.....	65
6.2.1.	Joining XRFS geochemical data and radiometric data.....	65
6.2.2.	Comparing radioelement concentrations.....	65



6.2.3.	Ratio maps	70
6.2.4.	Geochemical Domains	73
6.2.5.	Regression analysis	76
6.2.6.	Peat	77
6.2.7.	Soil texture	80
6.2.8.	Land use	83
6.2.9.	Outcrops, subcrops and depth to bedrock	86
6.2.10.	Bedrock geology	88
6.2.11.	Soil parent material	92
6.3.	Predicting Soil Geochemistry from Radiometric Data	93
6.3.1.	Prediction errors	100
6.3.2.	High resolution predicted geochemical maps	102
7.	Conclusions	105
8.	Recommendations For Further Work.....	106
	References.....	107
	Appendix A: Supplementary Figures	113
	Appendix B: Supplementary Tables	138



List of Abbreviations

- AGL** – Above Ground Level
- BGL** – Below Ground Level
- CRS** – Coordinate Reference System
- DEM** – Digital Elevation Model
- EPA** – Environmental Protection Agency (Ireland)
- GIS** – Geographic Information System
- GPS** – Global Positioning System
- GSI** – Geological Survey Ireland
- ICP-MS** – Inductively Coupled Plasma Mass Spectrometry
- ICP-OES** – Inductively Coupled Plasma Optical Emission Spectrometry
- ICP_{ar}** – Analysis by ICP-MS/OES following *Aqua Regia* digestion
- IDW** – Inverse Distance Weighting
- ITM** – Irish Transverse Mercator
- K_{air}** – K [%] determined by airborne gamma-ray spectrometry (⁴⁰K measured)
- K_{soil}** – K [%] measured in soil samples by ICP-MS/OES or XRFs
- LLD** – Lower Limit of Detection
- LOI** – Loss on Ignition
- n** – Sample size
- N.I.** – Northern Ireland
- ppm** – parts per million (note: ppm by weight (w/w) equivalent to mg/kg)
- QA/QC** – Quality Assurance/Quality Control
- R.o.I.** – Republic of Ireland
- SIS Soils** – Irish Soil Information System (Teagasc-EPA)
- soil:air** – ratio of soil concentration to airborne radiometric concentration for a given element
- TC** – Total Count (spectral window incorporating ⁴⁰K, ²¹⁴Bi and ²⁰⁸Tl gamma-ray photopeaks)
- Th_{air}** – eTh [ppm] determined by airborne gamma-ray spectrometry (inferred from measurement of ²⁰⁸Tl)
- Th_{soil}** – Th [mg/kg] measured in soil samples by ICP-MS/OES or XRFs
- U_{air}** – eU [ppm] determined by airborne gamma-ray spectrometry (inferred from measurement of ²¹⁴Bi)
- U_{soil}** – U [mg/kg] measured in soil samples by ICP-MS/OES or XRFs
- X_{air}** – concentration of element 'X' measured by airborne gamma-ray spectrometry, where X = K, U or Th
- X_{soil}** – concentration of element 'X' measured in soil samples, where X = K, U or Th
- XRFs** – X-ray Fluorescence Spectroscopy



1. Introduction

1.1. Background

Tellus is a national programme, managed by Geological Survey Ireland (GSI) and funded by the Department of the Environment, Climate and Communications, aimed at collecting geochemical and geophysical data across Ireland to provide reliable baseline information and support environmental and natural resource management (Ture 2020). The programme has been running in the Republic of Ireland since 2011 and follows-on from the Tellus surveys of the north of Ireland which began in 2004 with funding from the Government of Northern Ireland, Geological Survey of Northern Ireland, British Geological Survey and the INTERREG IVA programme of the European Regional Development Fund (Tellus Border) (Knights *et al.* 2020; Ture and Muller 2020; Young 2016).

The ground geochemical survey involves collecting samples of topsoil ('A' at 5–20 cmBGL; 'S' at 35–50 cmBGL), stream sediment and stream water (Knights *et al.* 2020). Topsoil samples are analysed for pH, LOI and a large suite of elements by inductively coupled plasma mass spectrometry/optical emission spectrometry (ICP-MS/OES) and X-ray fluorescence spectroscopy (XRFS). The airborne geophysical survey collects magnetic, electromagnetic and radiometric data from a typical survey height of 60 mAGL (Ture and Muller 2020).

The radiometric dataset comprises concentrations of potassium (K, %), equivalent uranium (eU, ppm) and equivalent thorium (eTh, ppm) measured by gamma-ray spectrometry, which are among the many elements analysed in soil by ICP-MS/OES and XRFS. The latter can be thought of as a purely geochemical analysis while the former is a geophysical technique used to infer geochemical information. Although both Tellus surveys collect data on K, U and Th concentrations and report these data in identical units (% K and mg/kg i.e., ppm U, Th), with the exception of a preliminary investigation in the Tellus Border region (Hodgson *et al.* 2013) there has been little work done to assess the compatibility of the datasets and investigate the relationship between the concentrations measured by the respective methods to date.



1.2. Context

1.2.1. Geochemical and Radioelement Mapping

Understanding how concentrations of K, U and Th in soil relate to their airborne radiometric signals could benefit a range of applications. If the relationship between the two datasets is consistent or can be reliably predicted across different geological units, soil types, land uses, etc., then airborne radiometric surveys provide an attractive means of gathering high resolution geochemical data across large or inaccessible areas quickly and cost-effectively (Taylor *et al.* 2002). The ability to predict soil concentrations of K, U and Th from gamma-ray data could allow radiometric surveys to be used to improve interpolation of low-density geochemical data, to target sampling sites more effectively, or even replace large-scale soil surveys depending on the application. Maps of K, U and Th may be useful even where these elements themselves are not of interest because of their chemical associations with other elements (e.g., uranium with vanadium) or the conditions that may be responsible for their presence (e.g., redox or pH) (Guagliardi *et al.* 2013; IAEA 2010). It is important to understand, therefore, what a radiometric survey actually measures and whether or not it over- or underestimates concentrations due to its footprint (section 2.3), the presence of large lithics, or the attenuation of gamma-rays in saturated overburden, for example (Rawlins *et al.* 2007; Beamish 2013, 2015).

1.2.2. Peat Mapping

The principle of gamma-ray attenuation (detailed in section 2.4) in dense or saturated materials has made radiometric surveying a useful tool for mapping soil properties such as texture (Moonjun *et al.* 2017) and for delineating areas of dry and/or thin peat within larger deposits (Beamish 2014). The latter could prove particularly useful in assessing peatland condition and the success of re-wetting efforts, compiling greenhouse gas inventories and estimating the potential for removing atmospheric carbon in line with Ireland's Climate Action Plan (Government of Ireland 2019), National Inventory Report (Duffy *et al.* 2020), IPCC guidelines (IPCC 2013) and Regulation (EU) 2018/841 on the inclusion of greenhouse gas emissions and removals from land use, land use change and forestry in the 2030 climate and energy framework. If radiometric data are to be used for such assessments, then it is useful to understand how the gamma-ray signal relates to true soil concentrations so as not to mistake natural radioelement lows for areas of increased attenuation or vice-versa.



1.2.3. Public Health

Globally, gamma-rays from terrestrial radionuclides are responsible for 15 % of the total dose of ionising radiation received by the population (Cinelli *et al.* 2020). Highly mobile radon gas (^{222}Rn), a decay product of ^{238}U , is of particular concern hence minimising exposure to the gas is prioritised in a National Radon Control Strategy as mandated in the Radiological Protection Act 1991 (Ionising Radiation) Regulations 2019 (S.I. No. 30 of 2019). Intrinsic to such a strategy is the production of accurate radon potential maps to delineate areas where radon poses a significant public health risk. Radiometric data have been used to estimate geogenic radon potential using equivalent uranium (eU) to calculate the concentration of radon gas in soil assuming a secular equilibrium in the uranium decay series (Elío *et al.* 2020). This equilibrium is also assumed when determining eU concentrations from ^{214}Bi gamma-ray counts (section 2.2) and is a notable source of error. Further insight into how airborne eU relates to soil U concentrations could improve the accuracy of such determinations, and thus the mapping of radon prone areas. Understanding how radiometric K, U and Th measurements relate to their soil concentrations would also facilitate the use of airborne surveys for accurate radioelement “baseline” mapping to inform environmental and public health related decision making (IAEA 2010) and help to identify areas where leaching of toxic U and Th from soil to public water supplies poses a substantial risk.



2. Review of Existing Literature

2.2. Terrestrial Radioelements K, U, Th and Their Geological Associations

Potassium, uranium and thorium are naturally occurring radioelements that were synthesised during the formation of the Earth (IAEA 2003; Minty 1997). The radioactive isotopes of these elements are extremely long lived and remain abundant in rocks and soils today, representing, along with their decay products, the most significant source of terrestrial radiation (Guagliardi *et al.* 2013; IAEA 2003).

2.2.1. Potassium

Potassium is a major component of many igneous and metamorphic rocks as well as soil, primarily the mineral fraction, where its concentration relates to the bedrock from which it is derived (Cinelli *et al.* 2019). It is a highly incompatible lithophile, preferentially incorporated into felsic melts and concentrated in the late stages of crystallisation (Guagliardi *et al.* 2013; Wang *et al.* in press). Potassium is therefore enriched in felsic igneous rocks such as granites and rhyolites (averaging 2.5–6 % K₂O) as well as some evaporitic sequences and fine-grained sedimentary rocks such as shales, while its concentrations are low in mafic to ultramafic rocks including basalts, dunites and serpentinites (0.5–1.3 %) (Cinelli *et al.* 2019; Moonjun *et al.* 2017). The potassium contents of most metamorphic rocks mirror those of their protoliths (Cinelli *et al.* 2019).

Potassium in soil is derived from silicate minerals including K-feldspars, feldspathoids and micas such as muscovite and biotite, as well as clay minerals derived from the weathering of these, most notably illite (Manning 2010; Wang *et al.* in press; Taylor *et al.* 2002; Rawlins *et al.* 2007). K concentration is correlated with clay content as large K⁺ ions released during silicate weathering are readily adsorbed by clay minerals. The clay mineralogy of fine-grained sedimentary rocks such as shales, mudstones and siltstones is largely responsible for their K content, as is the case for carbonate rocks which in their purest forms contain only traces of K (Cinelli *et al.* 2019; Wang *et al.* in press; Guagliardi *et al.* 2013). Thus, K concentrations are often correlated with smaller particle sizes. Contributing to this is the presence of radionuclide-poor quartz in the larger fractions (Rawlins *et al.* 2007; Taylor *et al.* 2002). The K content of arenaceous sedimentary rocks depends on the



abundance of minerals such as feldspars and micas and is typically low (Cinelli *et al.* 2019; Moonjun *et al.* 2017).

Potassium is also a highly soluble biophile and an essential element for plant nutrition (Wang *et al.* in press; Manning 2010). Organic matter can absorb K^+ from soil solution depending on its cation exchange capacity which increases with increasing soil pH (Helling *et al.* 1964). Soluble potassium salts (“potash”) are commonly added to soil as fertilizer and such additions may be detectable by both geochemical and radiometric methods (Guimaraes *et al.* 2013; IAEA 2003; Dierke and Werban 2013). Since K^+ is a major component of seawater (Wang *et al.* in press) deposition of atmospheric potassium in the form of sea-spray may also contribute to localised high soil concentrations.

2.2.2. Uranium

Uranium also behaves incompatibly during magmatic differentiation and concentrates in the late stages of crystallisation (Cinelli *et al.* 2019). U is therefore enriched (typically 2-10 mg/kg) in felsic igneous rocks such as granites, granodiorites and rhyolites (Guagliardi *et al.* 2013; Moonjun *et al.* 2017). It is not easily substituted for major ions in the early stages of crystallisation due to its high ionic charges and large radii, so U concentrations are largely controlled by the presence of accessory minerals in acid igneous rocks (Taylor *et al.* 2002), and are low in mafic and ultramafic rocks (usually <1 mg/kg in basalts and gabbros, for example) (Guagliardi *et al.* 2013; Cinelli *et al.* 2019). Uranium is a major component of uraninite, brannerite and carnotite (Cinelli *et al.* 2019). U-bearing heavy accessory minerals include zircon, monazite and apatite (Moonjun *et al.* 2017; Guagliardi *et al.* 2013) which are resistant to chemical weathering and are responsible for much of the uranium content of siliciclastic sedimentary rocks, (Cinelli *et al.* 2019). Pure evaporite deposits have low U, as do most carbonates, in which traces of U are thought to substitute calcium in the lattice (Cinelli *et al.* 2019). On the other hand, high U is found in sandstones (Moonjun *et al.* 2017), phosphate rocks (Wetterlind *et al.* 2012; Ahmed *et al.* 2012) and shales, perhaps most notably black shales which commonly contain around 11-13 mg/kg U (Moonjun *et al.* 2017; Zanin *et al.* 2016). Uranium concentrations in sedimentary rocks can be higher than in the igneous parent rocks (Cinelli *et al.* 2019) because of the mobility of its soluble hexavalent (U^{6+}) ion which predominates under oxidising conditions (Fall *et al.* 2020). At low pH hexavalent uranium is present as soluble UO_2^{2+} (uranyl ion) and at higher pH forms soluble uranyl carbonates (Harmsen and de Haan 1980; Ahmed *et al.* 2012). Its mobility, however, is redox sensitive. In a reducing environment uranium, which is readily absorbed (and in some cases bioconcentrated) in organic matter or dissolved in aqueous media in its hexavalent state, is fixed with organic matter as insoluble U^{4+} (Zanin *et al.* 2016; Fall *et al.* 2020;



Ahmed *et al.* 2012), hence significant concentrations may be found in black shales and organic sediments such as coal and lignite (Cinelli *et al.* 2019).

Uranium in soil is associated with more stable weathering products than potassium since it mainly occurs in the resistant accessory mineral fraction which is retained in the soil profile (Moonjun *et al.* 2017; Cinelli *et al.* 2019). In mildly acidic soils it is more soluble than thorium, therefore more easily mobilised, but can be absorbed by Fe- and Al-oxides in clay minerals and soil organic matter (SOM) (Moonjun *et al.* 2017; Ahmed *et al.* 2012). As for potassium, the solubility of uranium in SOM is pH dependent as this influences the SOM's cation exchange capacity (Dierke and Werban 2013; Helling *et al.* 1964). Gravitational separation of heavy minerals means U tends to accumulate in the fine fraction during aeolian and fluvial processes and is concentrated in highly weathered soil profiles (Guagliardi *et al.* 2013; Fall *et al.* 2020).

Most chemical phosphorus fertilizers are derived from sedimentary phosphate rocks into which U can be incorporated through ionic substitution or absorption. Wetterlind *et al.* (2012) found that long-term P-fertilizer application could lead to the accumulation of up to 0.63 mg/kg U in topsoil. Other anthropogenic inputs include fly ash from coal burning power stations and waste residues associated with uranium and coal mining activities (IAEA 2010). Quarries and landfills can also expose the population to higher doses of radiation arising from uranium and its decay products and may appear as anomalies in airborne radiometric surveys (IAEA 2003).

2.2.3. Thorium

Thorium, like uranium, is a lithophilic element enriched in acidic-to-intermediate igneous rocks, with concentrations between 10 and 50 mg/kg common in granites, granodiorites, rhyolites and syenites (Cinelli *et al.* 2019; Moonjun *et al.* 2017), and poor in mafic rocks (0.1-4 mg/kg in basalts and gabbros) and ultramafic rocks (<0.1 mg/kg). Th is a major component of monazite and rare minerals thorite and thorianite and is commonly found in resistant heavy accessory minerals including zircon, apatite, allanite and epidote (Moonjun *et al.* 2017; Cinelli *et al.* 2019; Guagliardi *et al.* 2013).

Th content varies in sedimentary rocks and is typically moderate-to-high in sandstones (1-7 mg/kg) and shales (12 mg/kg) (Moonjun *et al.* 2017; Cinelli *et al.* 2019), the latter being known to contain high concentrations of all three radioelements. Thorium exists predominantly as tetravalent Th^{4+} and its chemical properties largely mirror those of U^{4+} (Guagliardi *et al.* 2013). Its solubility is dependent



on Eh-pH conditions and the presence of dissolved organic carbon (Ahmed *et al.* 2012) and is found to be highest in acidic soils (pH 3.6 – 4.7), with highest soil concentrations of Th observed in the upper 20 cm of the profile, likely due to its correlation with organic matter (Moonjun *et al.* 2017; Ahmed *et al.* 2012). At pH > 7 thorium is almost completely adsorbed to organic matter and clay minerals (Von Gunten *et al.* 1996) hence any Th released by weathering is separated from more mobile elements such as U. In sedimentary basins, unlike U which is initially dissolved and subsequently fixed (reduced) in organic matter, insoluble Th is generally introduced as an element adsorbed on to the surface of clay or Fe-hydroxide particles (Zanin *et al.* 2016). Thorium distribution is influenced by gravitational separation, accumulating in fine-grained sediments with associations to clays such as kaolinite observed (Taylor *et al.* 2002), however Th is also associated with the largest soil fraction (detrital plant matter) because of its affinity to organic material (Bednar *et al.* 2004).

The immobile nature of Th relative to K in most environments allows Th/K ratios to be used to assess the degree of weathering or hydrothermal activity in areas of silicate rock (Fall *et al.* 2020; Moonjun *et al.* 2017). Since K is a mobile element and a major constituent of many felsic rocks it will be selectively leached as the material is weathered, causing a “passive enrichment [of Th] by mass balance” (Fall *et al.* 2020) since their concentrations are measured in % or ppm w/w (“weight per weight,” i.e., mg/kg). In Ireland, where the landscape is dominated by relatively young Quaternary deposits and leaching of soil nutrients is slow, compared to tropical oxisols or laterites for example, concentrations of K, U and Th relate primarily to bedrock mineralogy and geochemistry and are only altered to a minor extent by weathering processes (Manning 2010; Taylor *et al.* 2002; Rawlins *et al.* 2007).

2.3. Radioactivity & Gamma-ray Spectrometry

Radioactive decay is a spontaneous process whereby an unstable nucleus disintegrates to eventually form a more stable product by emitting ionising radiation, often via a chain of radioactive “daughter” nuclei (Minty 1997). Decay events are independent of one another and the probability of a decay taking place is characteristic of a given radioisotope, represented in the decay constant, λ (s^{-1}). This relates to the half-life ($t_{1/2}$) of the isotope, which is the time taken for half of the nuclei in a sample to undergo radioactive decay, calculated as:

$$t_{1/2} = \frac{\ln(2)}{\lambda} \quad (1)$$



Three forms of ionising radiation may be emitted during a radioactive disintegration, namely alpha particles ($[\frac{4}{2}\text{He}]^{2+}$), beta particles (e^-), and gamma-rays (photons of electromagnetic energy). Alpha and beta particles are attenuated in a few centimetres and a metre of air, respectively, whereas gamma-rays can travel hundreds of metres in air and up to 30 cm in rock (IAEA 2003; Minty 1997). Gamma-rays from primordial nuclides present in the shallow subsurface can therefore be detected above the ground and since their energies are quantized and characteristic of the nuclei undergoing radioactive decay they may be used as a diagnostic tool to determine the abundance of terrestrial gamma sources. This is the principle underlying gamma-ray spectrometry (IAEA 2003).

Gamma-ray spectrometry measures both the energy and intensity of the radiation. The latter is proportional to the radioisotope abundance and decreases with increasing distance from the source as the energy is absorbed by the media it passes through (Guagliardi *et al.* 2013; Beamish 2014; Dierke and Werban 2013; Minty 1997). Although there are numerous sources of natural radiation, “only potassium, and the uranium and thorium decay series, have radioisotopes that produce gamma-rays of sufficient energy and intensity to be measured by gamma-ray spectrometry” (IAEA 2003).

Potassium has an average crustal abundance of about 2–2.5 % (Cinelli *et al.* 2019; IAEA 2003). It has three natural isotopes, two of which, ^{39}K and ^{41}K , are stable and represent 93.3 % and 6.7 % of the total K mass, respectively. Radioactive ^{40}K makes up only 0.0117 % by mass of total K and has a half-life of 1.3×10^9 years, decaying either by beta emission to ^{40}Ca or by electron capture and subsequent emission of 1.46 MeV gamma-rays to ^{40}Ar (Guagliardi *et al.* 2013; IAEA 2003). This radiation is sufficiently penetrating to be measured by gamma-ray spectrometry and can be used to estimate the concentration of total K directly since the proportion of ^{40}K nuclei decaying by gamma emission and the natural abundance of ^{40}K relative to total K, are fixed (probabilistic) (IAEA 2003).

Uranium has an average crustal abundance of 2–3 ppm and has three major isotopes found in nature: ^{238}U (99.28 % total U by mass), which is usually in radioactive equilibrium with decay product ^{234}U (0.0054 %), and ^{235}U (0.71 %) which has a separate decay series (Cinelli *et al.* 2017). All three isotopes are alpha emitters (IAEA 2010). ^{238}U has a half-life of 4.47×10^9 years and its decay series terminates at the stable ^{206}Pb isotope, while ^{235}U has a half-life of 7.13×10^8 years and ultimately decays to the stable ^{207}Pb isotope (Minty 1997; IAEA 2003).

Thorium has an average crustal abundance of 8–12 ppm, as quoted in literature, and has 27 radioisotopes, the most abundant and long-lived of which is ^{232}Th , which makes up 99.98 % of all Th



by mass and has a half-life of 1.41×10^{10} years (IAEA 2003; Guagliardi *et al.* 2013). ^{232}Th decays by alpha emission, terminating in the stable isotope ^{208}Pb (IAEA 2010; Minty 1997). Since neither U nor Th are gamma emitters their concentrations are inferred by measuring gamma radiation from daughter nuclei in their decay series. Uranium concentrations are estimated from the intensity of the 1.765 MeV ^{214}Bi (a daughter of ^{238}U) gamma-ray peak and thorium concentrations from the 2.614 MeV ^{208}Tl peak (IAEA 2003). Energies and intensities of gamma-rays emitted by nuclei in the ^{235}U series are “too low to be diagnostic in airborne gamma-ray surveying” (Minty 1997). Uranium and thorium concentrations are reported as “equivalent” eU and eTh, signifying that they are estimated indirectly from daughter products under the assumption that secular radioactive equilibrium is preserved (Elío *et al.* 2020; Grasty 1997; IAEA 2003) which is almost always the case for thorium but can introduce significant error in uranium estimates (Minty 1997; Cinelli *et al.* 2017; Cinelli *et al.* 2018).

The rate at which a radioactive daughter changes is controlled by the rate at which it is produced and that at which it decays, which is related to its own half-life and that of the parent. Daughter nuclei are generally shorter-lived than the parent and reach a state wherein they are decaying at the same rate as they are being produced. If this is the case for all daughters in the decay series then “secular equilibrium” is achieved and the total activity decreases at the same rate as that of the parent (Minty 1997). If one or more daughters are removed from or added to the system, by selective leaching of certain isotopes in the decay series, for example, disequilibrium occurs. Disequilibrium in the ^{238}U series is common as both uranium and its daughter radium (Ra) are soluble and very mobile, as is the gaseous decay product radon (Rn) (Minty 1997). The gamma emitter ^{214}Bi occurs further down the series and so its activity will diminish if Rn escapes to the atmosphere, for example, affecting the accuracy of the inferred uranium concentration.

Scattering of gamma photons in the source, the media through which the radiation travels (e.g., air) and the detector results in a continuous measured spectrum with energies up to the theoretical maxima (unscattered photon energy peaks) for ^{40}K , ^{214}Bi and ^{208}Tl instead of a line spectrum with discrete energies (Minty 1997) (figure 1). Compton scattering is the dominant process for the observed energy range of terrestrial gamma-rays (Beamish 2014) and occurs when photons collide with electrons and are deflected upon imparting some of their energy to the electrons (Billings and Hovgaard 1999).



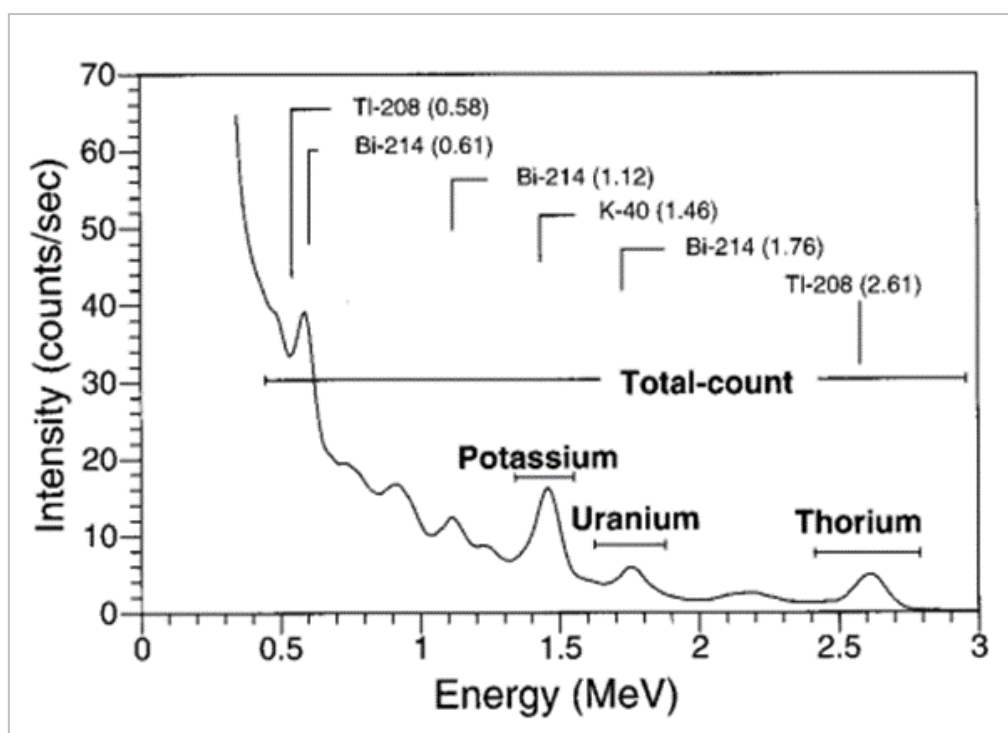


Figure 1: Gamma-ray spectrum measured at 100 mAGL showing major photopeaks and the Total Count, K, U and Th spectral windows. [Source: Minty, 1997].

Gamma-ray spectrometers measure the intensity of the gamma-rays within defined “spectral windows” corresponding to the highest energy photopeaks for each isotope as well as “Total Count (TC)” which gives a measure of total terrestrial radioactivity (IAEA 2003). The energy ranges for each window are given in Table 1 (adapted from IAEA 2003).

Table 1: Energy ranges of TC, K, U and Th spectral windows.

<i>Window</i>	<i>Nuclide</i>	<i>Energy Range (window) [MeV]</i>
Total count	-	0.400 – 2.810
Potassium	^{40}K	1.370 – 1.570
Uranium	^{214}Bi	1.660 – 1.860
Thorium	^{208}Tl	2.410 – 2.810

The highest energy peaks are measured because the photons producing them are more penetrating than those responsible for the lower energy peaks also seen in figure 1. The intensities are therefore high enough to be diagnostic and their measurement is less susceptible to changes in detector height (Minty 1997).



2.4. Radiometric Survey Design, Calibration, Data Collection and Processing

Airborne radiometric surveys employ a gamma-ray spectrometer to measure the number of counts per second attributed to K, U and Th decays (and total count), typically at 1 s intervals equating to one reading every 60 m for a survey velocity of 60 m/s (Beamish 2013; IAEA 2003). Count rates are subsequently converted to specific activities for each nuclide [Bq/kg] which can be used to estimate total element abundances (Dierke and Werban 2013). Airborne spectrometers typically use TI-doped NaI (sodium iodide) crystals, which produce scintillations upon interaction with gamma-rays. Electrons liberated from a photocathode, convert scintillations to an electrical signal whose output voltage is proportional to the incident gamma-ray intensity (Minty 1997). The number of gamma photons entering the crystal, and the proportion detected, are sensitive to the detector specifications including its crystal volume, directional sensitivity, efficiency in detecting photons of different energies, ability to resolve signals from two photons very close in energy, and “dead-time” (time taken to process count for individual photons). These factors and the calibrations and data processing they necessitate are detailed in Minty (1997) and IAEA (2003). The larger the crystal volume, the higher the detected count rate, giving an improved signal-to-noise ratio (Wetterlind *et al.* 2012).

Further calibrations must also be carried out before any airborne radiometric survey to extract meaningful information. These are largely empirical and are only valid for that particular survey’s “source-detector” system (Minty 1997).

- Lines are flown at a range of high altitudes to determine the aircraft and cosmic background radiation.
- Measurements are made over concrete calibration pads of known radioelement concentrations to calculate stripping ratios (to remove counts in a given spectral window not due to that particular isotope).
- Flights are repeated over a calibration range at different heights to determine the sensitivity of the detector to altitude variations and known radioelement concentrations.
- “Upward-looking” crystals in the detector are used to subtract any signal due to atmospheric radon, leaving only radiation from terrestrial sources (IAEA 2003).



Since gamma-rays are attenuated in air, increasing the survey height decreases the measured count rate, increasing the signal-to-noise ratio while also increasing the survey “footprint.” This footprint is the area from which the detector measures emitted radiation for each 1 s reading (Beamish and Farr 2013) (illustrated in figure 2). For a stationary airborne measurement at a given height, Pitkin and Duval (1980) showed how fixed contributions to the total radiometric signal came from within concentric circles, and Kock and Samuelsson (2011) calculated that 90 % of this signal would come from a circle of radius 160-180 m at a survey height of 60 m. For a measurement from a moving aircraft the footprint will be an ellipse, elongated along the axis parallel to the flight line (Billings and Hovgaard 1999; Beamish and Farr 2013). Survey design therefore affects both spatial and spectral resolution, both of which may be maximised by flying as low as possible (Billings and Hovgaard 1999). In order to achieve this flight lines need to be more closely spaced, which is time consuming, so there is usually a trade-off between data quality and efficiency while accommodating concurrent airborne surveys (e.g. magnetics) (Minty 1997).

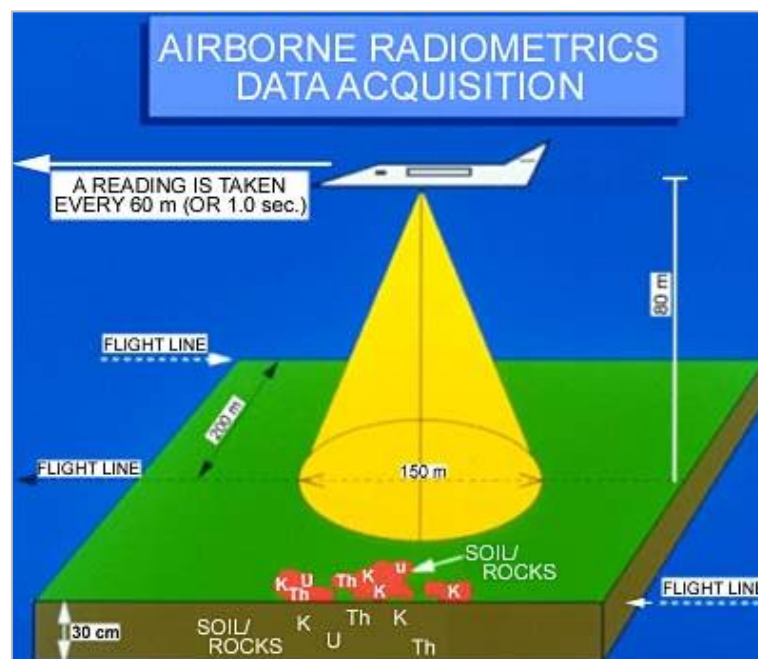


Figure 2: Schematic of typical airborne radiometric data collection, showing the area surveyed by the detector during each 1 s measurement, i.e., the footprint. [Source: <http://vro.agriculture.vic.gov.au>].

2.5. Gamma-ray Attenuation

Using gamma-ray spectrometry for geological mapping relies on the assumption that the radiogenic content of the soil and subsoil is derived from the underlying bedrock (Beamish 2014, 2015; Cinelli *et*



al. 2018). This assumption holds for the young landscapes of the UK and Ireland which are largely covered by Quaternary deposits (Rawlins *et al.* 2007; Rawlins *et al.* 2012). Unlike landscapes exposed to longer periods of weathering (e.g., tropical regions), which has modified the soil profile to significant depths, weathering in the UK and Ireland is generally restricted to depths < 1 m (Rawlins *et al.* 2012). The assumption that soil geochemistry “reflects the composition of the rocks from which [it is] derived” (Glennon *et al.* 2020) allows information about the bedrock to be extracted using gamma-ray spectrometry, since the measured radiation originates from the shallow subsurface, typically only the uppermost 20–60 cm (IAEA 2003; Beamish and Farr 2013; Rawlins *et al.* 2012). This is because gamma-rays lose their energy and are attenuated as they interact with matter.

As previously mentioned, Compton scattering is the dominant interaction. The extent to which this occurs in a given material, and therefore the material’s gamma-ray attenuation behaviour, is related to its electron density. Løvborg (1984) and Duval *et al.* (1971) argue that this attenuation is independent of the material since the elements oxygen and nitrogen dominate most Earth materials per unit volume and the difference between attenuation coefficients for elements with atomic numbers < 30 is negligible (Taylor *et al.* 2002; Beamish 2014). It is noted, however, that water contains approximately 1.11 times as many electrons per unit volume as most of these materials (Grasty 1997). The attenuation behaviour of a material is therefore controlled largely by its moisture content “with density and porosity acting as secondary variables” as these properties relate to the sensitivity of the attenuation to varying degrees of saturation (Beamish 2014).

Beamish (2013) modelled the theoretical attenuation due to limestone bedrock, high/low density mineral soil and wet/dry peat using typical values of density and porosity for each material. The simplest model considers a three-layer system comprising bedrock overlain by subsoil and soil, and assumes the radiogenic component of the upper layers is derived from the bedrock. The attenuation curves (figure 3) show the effect of varying thickness and saturation.

Graph (a) indicates that for a dense mineral soil, even if gamma-rays are emanating from the soil itself, 90 % of the radiation detected will originate in the upper 40 cm. For bedrock most of the signal originates in the upper 20 cm. This signal may be strong where bedrock is exposed but can be attenuated rapidly in non-radioactive overburden. Graph (b) shows how all the materials attenuate more gamma-rays with increasing saturation, but the extent to which the attenuation is affected is controlled by the amount of pore space available to be occupied by water.



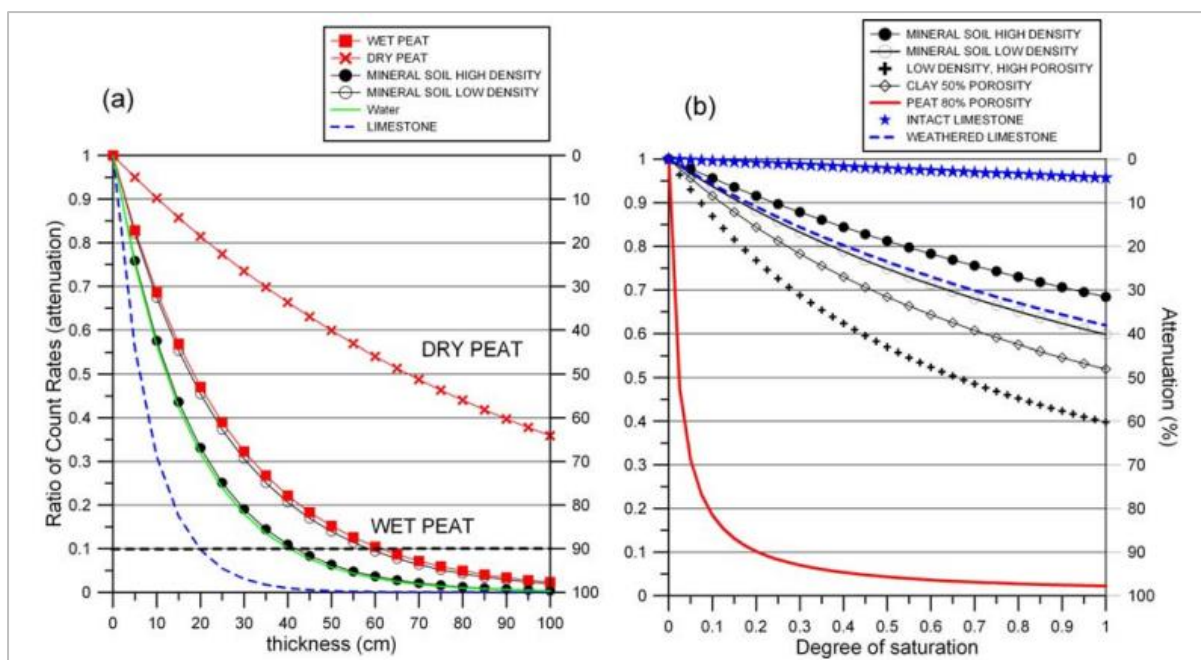


Figure 3: Theoretical attenuation curves for a variety of soil and bedrock types showing attenuation behaviour with varying (a) material thickness and (b) saturation. [Source: Beamish 2013].

Low density, high porosity peat soils exhibit unique attenuation behaviour. When dry, gamma-ray signals can penetrate >1 m of peat, compared to 30–70 cm in most other materials because of its low density. When wet, however, peaty soils can have moisture contents > 90 % and since water is 1.11 times more effective at attenuating gamma-rays than most dry materials the peat attenuation curve shows high sensitivity to degree of saturation, falling steeply between 0–20 % (Beamish 2013). The gamma-ray signal over peat therefore may exhibit significant highs or lows depending on how wet and how thick the peat is, making gamma-ray spectroscopy a useful tool for mapping areas of thin peat cover and investigating intra-peat variations in near-surface saturation (Beamish 2013; Beamish and Farr 2013).

2.6. Radon Emanation

Accurate interpretation of radiometric uranium data requires the effects of radon emanation to be considered. Radon (^{222}Rn) is a radioactive gaseous decay product of ^{226}Ra which forms part of the ^{238}U decay series (Elío *et al.* 2020). When ^{226}Ra nuclei in soil decay a fraction of the ^{222}Rn produced escapes into the pore space and can diffuse through the soil and into the atmosphere. This “emanating fraction” varies for different soil types but can range from 20 % to > 50 % (Grasty 1997). ^{222}Rn has a half-life of 3.8 days and can travel distances of up to 10-20 cm in soil (Grasty 1997), however this is controlled largely by the moisture content, with the radon diffusion coefficient



decreasing rapidly as soil moisture increases. In a dry soil much of the ^{222}Rn escapes from the upper 10-20 cm to the atmosphere resulting in a lower ^{214}Bi (daughter) gamma-ray count and lower reported eU concentration since this is the depth range from which most of the detected gamma-rays originates (Grasty 1997). As soil moisture increases the radon diffusion coefficient decreases and more of the gas is trapped in the upper 10 cm, resulting in an increased near-surface ^{214}Bi concentration and observed count rate (Grasty 1997). This effect competes with the increased gamma-ray attenuation observed for saturated soils and affects the reliability of the airborne uranium measurement. For clay soils radon emanation is found to be more significant whereas sandy soils have low emanation coefficients (Grasty 1997).

2.7. XRFs vs ICP Methods

Tellus topsoil samples are analysed by ICP-MS/OES following *Aqua Regia* digestion as is common practice in many environmental geochemical studies involving waste, sludge and soil matrices (Kisser 2005). *Aqua Regia* is a 3:1 mixture of concentrated hydrochloric acid and nitric acid and is “considered adequate for dissolving most base element sulphates, sulphides, oxides and carbonates” (Gaudino *et al.* 2007) but performs poorly on refractory compounds such as SiO_2 and Al_2O_3 which are common in rock-forming minerals (Kisser 2005). For this reason it is considered a “partial extraction” but is fit for many environmental purposes, removing elements that are weakly bound to organic matter and often giving total concentrations of Cd, Cu, Pb and Zn (Glennon *et al.* 2020; Gaudino *et al.* 2007). Extraction in *Aqua Regia* is affected by a number of factors including particle size, digestion temperature, and time, and variations of up to 20 % can be observed for refractory matrices. Analysis by XRFs or following “total digestion” with mixtures containing HF are therefore recommended where refractory compounds are concerned (Kisser 2005; Gaudino *et al.* 2007; Cinelli *et al.* 2019). XRFs measure the fluorescence that results after a sample is excited upon irradiation with X-Rays. This can be conducted on solid samples, avoiding the need to first extract elements from the soil matrix.

A review of Tellus and GEMAS (European agricultural soils survey) data comparing samples with element concentrations determined by both ICP_{ar} and XRFs found *Aqua Regia* extraction rates between 75-85 % for As, Ni, Pb and Zn and only about 35 % for Cr, which typically occurs as chromite, a spinel particularly resistant to *Aqua Regia* digestion. It was noted, however, that the extraction rate of a given element is not constant but rather varies with the mineralogical composition of the soil (Glennon *et al.* 2020). Feldspars are also difficult to digest so poor extraction



of potassium is expected where its occurrence is predominantly in alkali feldspar (Wang *et al.* in press; Manning 2010).

2.8. Comparing and/or Integrating Geochemical and Radiometric Observations

Although geochemical and airborne radiometric surveying methods are fundamentally different in terms of both what they measure and how, comparisons of the results from such surveys have found they agree to a large extent (Rawlins *et al.* 2007; Cinelli *et al.* 2018) and are often complementary, providing information on soil texture (Taylor *et al.* 2002) or mineralogy (Guagliardi *et al.* 2013) to inform interpretations, aiding interpolation between low density sampling points and across geological boundaries (Paasche and Eberle 2010) and enabling one dataset to be “calibrated” against another (Cinelli *et al.* 2017; Cinelli *et al.* 2018), for example.

A geostatistical comparison of K, U and Th concentrations measured by soil geochemical and airborne radiometric methods in England was carried out by (Rawlins *et al.* 2007), who modelled the coregionalization of the two datasets and found a high degree of correlation for K and Th and a weaker correlation for U which they attributed to greater error in its measurement in both surveys. Soil concentrations were found to be consistently higher, attributed to the fact that only a sieved soil fraction was analysed geochemically, thereby removing a large proportion of radioelement-poor quartz which makes up part of the “whole soil” measured by gamma-ray spectrometry. They also acknowledged that the soil sample depth was fixed at 35-50 cm whereas the radiometric data generally corresponded to only the top 35 cm of material, but claimed this had a minimal effect on the cross-correlation (Rawlins *et al.* 2007).

Cinelli *et al.* (2017) and Cinelli *et al.* (2018) used European geochemical soil data (FOREGS and GEMAS) and radiological data collected in Belgium (measured both in-situ using a handheld spectrometer 1 mAGL, and in a laboratory on soil samples) to create a harmonised database of radioelement concentrations with which to calibrate airborne radiometric data before comparing the respective maps (harmonised “ground” vs airborne). A harmonisation factor of 1.4 was consistently observed in the case of the in-situ spectrometer measurement, and a satisfactory correlation coefficient (0.66) was found between airborne and harmonised ground measurements of K. Much of the variation in radioelement concentrations across the study area was explained using simplified geological units and soil classes, with only minor improvement upon introducing further complexity to the classifications. The interpolated maps generally showed good agreement



irrespective of the mapping method (Cinelli *et al.* 2018) and in the case of uranium (Cinelli *et al.* 2017) differences between the two were thought to be related to the accuracy of the airborne survey's atmospheric radon correction, as errors were not random but had a "geographical structure."

Taylor *et al.* (2002) used gamma-ray spectrometry (airborne and ground-based) to investigate the relationship between the radiometric data and soil properties such as texture, noting a strong linear relationship between TC and the clay content of the uppermost 10 cm. Using X-Ray diffraction, they determined the mineralogy of a subset of soil samples that were representative of the variation in material across the study area, understanding that the geochemistry of the soil's parent material (as well as the weathering history) must be understood in order to make meaningful interpretations about soil properties (Taylor *et al.* 2002). The use of a ground spectrometer, which has a much smaller footprint, was recommended "during field evaluations" to overcome issues that may arise from average measurements across the airborne spectrometer's footprint not being representative of the soil properties at the sample point (Taylor *et al.* 2002). Guagliardi *et al.* (2013) also investigated mineralogy using X-Ray diffraction and scanning electron microscopy to inform geological interpretations based on gamma-ray data, acknowledging that "[the use of] gamma-ray spectrometry as a mapping tool requires an understanding of radioelements distribution and mobility." They found that the distribution of K, U and Th was related not only to the geology of the study area but also influenced by weathering processes.

There are numerous examples in the literature of airborne radiometric data being used in the creation of geochemical, soil texture and parent material, peat, terrestrial gamma dose and radon potential maps, to name a few (Paasche and Eberle 2010; Kirkwood *et al.* 2016; Moonjun *et al.* 2017; Beamish 2014; Rawlins *et al.* 2012; Appleton *et al.* 2008; Elío *et al.* 2020) which commonly exploit the high resolution and spatial coverage of the airborne data to improve the prediction of interpolated values. Radiometric data have been used to predict soil geochemistry even where K, U and Th are not the elements being targeted. Paasche and Eberle (2010) used radiometric K, U and Th data along with satellite imagery to identify 18 clusters across a heterogeneous 3500 km² study area. On the basis of this membership information 46 sample sites (of a total 3012) were chosen and a typical zinc concentration determined for each cluster. These values were interpolated to give a map of Zn concentrations across the entire study area, which were then compared to the true measured concentrations at the remaining sample sites with "good linear correlation between the measured and predicted data" observed (Paasche and Eberle 2010).



3. Research Aims and Objectives

The aim of this study was to investigate the relationship between Tellus topsoil geochemical and airborne radiometric data for potassium, uranium and thorium, and to assess the feasibility of using radiometric data to predict soil concentrations of these elements. To achieve this the following objectives were addressed:

- Determine whether a fixed ratio or linear relationship exists between the radiometric and soil concentrations for each element.
- Examine the influence of factors such as geology, geochemistry, soil texture and land use on radioelement concentrations and on the 'soil:air' ratio for each element.
- Assess the performance of *Aqua Regia* in the extraction of K, U and Th from soil samples.
- Create maps of soil concentrations of K, U and Th based on values predicted from radiometric data using linear regression equations.



4. Study Area

The initial area chosen for this study was the northern half of the Island of Ireland. This area corresponds to the extent of the available Tellus Topsoil 'A' ICP_{ar} data coverage across Ireland and Northern Ireland. Tellus airborne geophysical data also exist for this region. Over the course of the study, N.I. was removed and the study area was further refined when XRFS soil data replaced ICP_{ar} (see section 6.4). The XRFS coverage is limited to the G1 (Border), G3 (West) and G6 (Dublin/Galway periurban) geochemical survey blocks which constitute the final study area.

4.1. Bedrock Geology

Figure 4 shows the diverse bedrock geology of the study area. Neoproterozoic metasedimentary and metavolcanic rocks of the Dalradian Supergroup, along with Siluro-Devonian granites, dominate the northwest in County Donegal and parts of Mayo and Galway. Lower Carboniferous limestone, sandstone, mudstone and evaporite extend across much of Connacht and into Monaghan and Northern Ireland, with Namurian shale, sandstone, siltstone and coal units found in Leitrim. Ordovician slate, sandstone, greywacke and conglomerate, Dalradian schist and gneiss, and Lower-Middle Palaeozoic intrusives (basic and granitic) are all found in the Connemara region of west Galway and southwest Mayo. Carboniferous limestone and shale sequences dominate the 'midlands' region and extend towards Dublin in the southeast of the study area. Much of the east is occupied by the Ordovician-Silurian marine greywackes and mudstones of the Longford-Down inlier which host younger intrusives such as the Palaeogene granites of the Mourne Mountains and the Siluro-Devonian Newry complex. Extensive Palaeogene basalt covers much of the northwest, which also features Oligocene lacustrine sediments, Dalradian metasediments and Triassic sandstone, mudstone and evaporite. Major bedrock faults have a predominant NE-SW orientation.



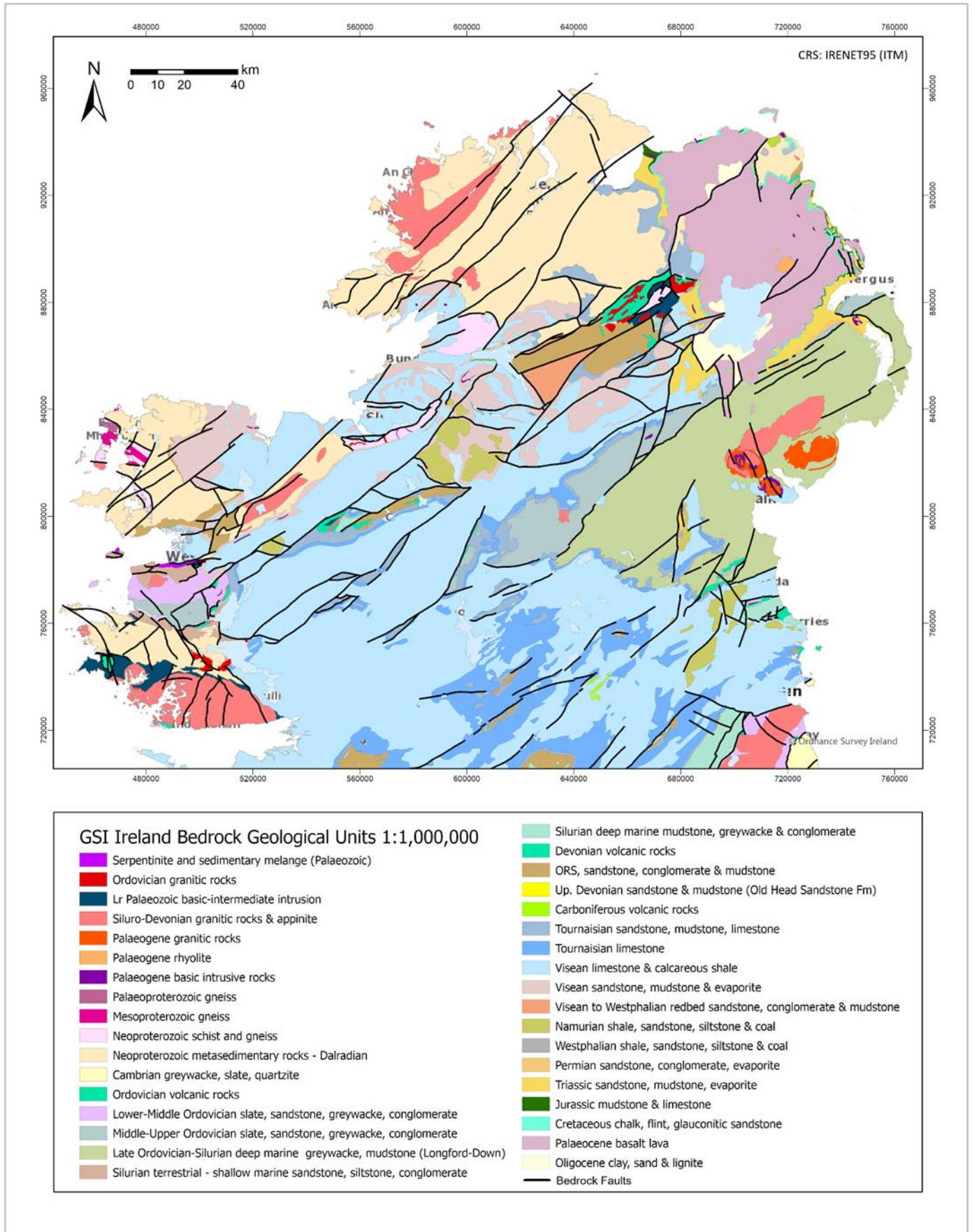


Figure 4: Bedrock geology of Ireland and Northern Ireland (GSI, 1:1 million).



4.2. Superficial (Quaternary) Geology

The Quaternary geology of the study area is shown in figures 5 and 6. Much of the island is covered by glacial till deposits largely derived from the underlying bedrock. Extensive limestone tills occupy the midlands, while tills derived from Lower Palaeozoic clastic sedimentary rocks predominate in the east/northeast and metamorphic and granitic tills cover much of the west and northwest, although these upland areas are largely characterised by blanket peat deposits and outcropping bedrock. Figure 6 shows other significant bedrock outcrops in counties Antrim and Down. Raised peat deposits are common across the midlands of Ireland, as are glaciofluvial sands and gravels which are also found across north/northeast N.I. Alluvial deposits are also prevalent across Ireland and N.I.

4.3. Soils

Figure 7 shows the 1:50,000 Teagasc National Soils map. In upland areas to the west and northwest blanket peat is found neighbouring shallow, rocky soils both peaty and non-peaty in nature. Mineral soils are typically acidic in the Border region overlying clastic sedimentary or metamorphic bedrock. Contrastingly, basic mineral soils are found overlying carbonate bedrock across the midlands, along with areas of cutover peat. The mineral soils are derived from the underlying Quaternary deposits which in turn reflect local bedrock. Made ground is observed across the Greater Dublin Area and to a lesser extent across Galway City. Areas of shallow and exposed bedrock predominate over much of the west and northwest. This can also be seen in figure 8, which maps depth to bedrock and was derived from the GSI Groundwater Vulnerability map (Lee *et al.* 2008).

Figure 9 is based on the Teagasc-EPA Irish Soil Information System map, reclassified to show how soil texture varies across the study area. The drainage properties in this database were also consulted. Peat soils are generally poorly draining, as are the clayey soils and alluvium. Loamy drift soils vary but are predominantly well-to-moderately draining.



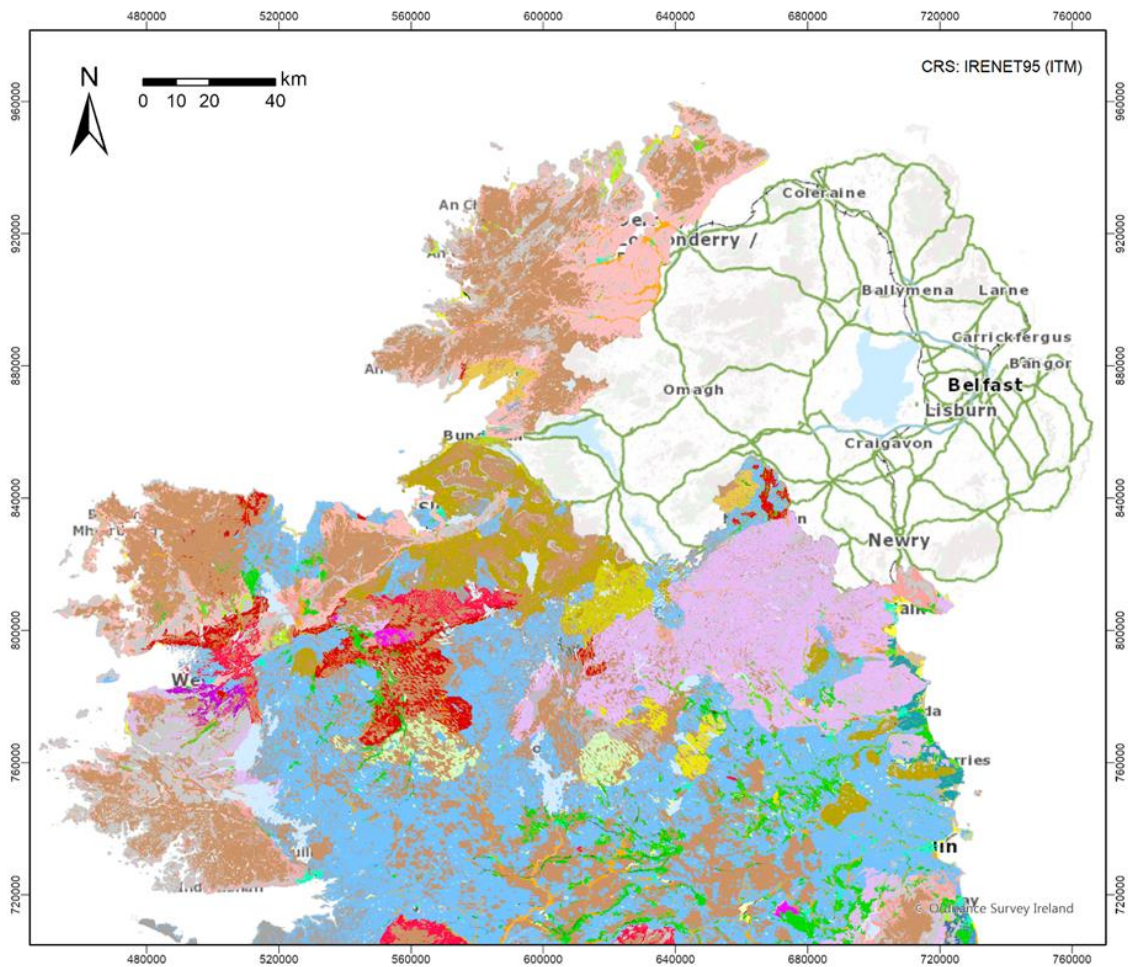


Figure 5:
Quaternary
(superficial)
geology of the
Republic of
Ireland
(GSI, 1:50,000).

Quaternary Sediments

- | | |
|-------------------------------------------------------------------------------------------------------------------|-------------------------------------------------------------------------------------------------------------------------|
| ■ A, Alluvium | ■ L, Lacustrine sediments |
| ■ Ac, Alluvium (clayey) | ■ Landfill |
| ■ AcEsk, Eskers comprised of gravels of acidic reaction | ■ Lc, Lacustrine clays |
| ■ Ag, Alluvium (gravelly) | ■ Lg, Lacustrine gravel |
| ■ Airfield/Airport | ■ Ls, Lacustrine sands |
| ■ As, Alluvium (sandy) | ■ Lsi, Lacustrine silts |
| ■ Asi, Alluvium (silty) | ■ MGs, Marine gravel and sands (often raised) |
| ■ BasEsk, Eskers comprised of gravels of basic reaction | ■ Mbs, Marine beach sands |
| ■ BktPt, Blanket Peat | ■ Mesc, Estuarine silts and clays |
| ■ Causeway, Causeway | ■ Mrl, Lake marl |
| ■ Crannog, Crannog | ■ Pier |
| ■ Cut, Cut over raised peat | ■ Rck, Bedrock outcrop or subcrop |
| ■ Dam | ■ RsPt, Raised Peat (intact) |
| ■ Embankment | ■ Scree, Scree |
| ■ FenPt, Fen Peat | ■ Spoil Heap, Spoil Heap |
| ■ Fill, Made ground | ■ TAV, Till derived from acidic volcanic rocks |
| ■ GBi, Gravels derived from basic igneous rocks | ■ TBI, Till derived from basic igneous rocks |
| ■ GCSs, Gravels derived from Cambrian sandstones and shales | ■ TCSs, Till derived from Carboniferous sandstones |
| ■ GCh, Gravels derived from chert | ■ TCSCh, Till derived from Carboniferous sandstones and cherts |
| ■ GDCSs, Gravels derived from Devonian and Carboniferous sandstones | ■ TCSsS, Till derived from Cambrian sandstones and shales |
| ■ GDSs, Gravels derived from Devonian sandstones | ■ TCh, Till derived from cherts |
| ■ GG, Gravels derived from granite | ■ TDCSs, Till derived from Devonian and Carboniferous sandstones |
| ■ GLCSsS, Gravels derived from Carboniferous sandstones and shales | ■ TDCSsS, Till derived from Devonian and Carboniferous sandstones and shales |
| ■ GLPDS, Gravels derived from Lower Palaeozoic and Devonian sandstones | ■ TDSs, Till derived from Devonian sandstones |
| ■ GLPS, Gravels derived from Lower Palaeozoic shales | ■ TG, Till derived from granites |
| ■ GLPSS, Gravels derived from Lower Palaeozoic sandstones | ■ TLCSsS, Till derived from lower Carboniferous sandstones and shales |
| ■ GLPSSs, Gravels derived from Lower Palaeozoic sandstones and shales | ■ TLPCSsS, Till derived from Lower Palaeozoic and Carboniferous sandstones and shales |
| ■ GLSCh, Gravels derived from silicified limestones and chert | ■ TLPDSs, Till derived from Lower Palaeozoic and Devonian sandstones |
| ■ GLs, Gravels derived from Limestones | ■ TLPS, Till derived from Lower Palaeozoic shales |
| ■ GMp, Gravels derived from Metamorphic rocks | ■ TLPSs, Till derived from Lower Palaeozoic sandstones |
| ■ GNSSs, Gravels derived from Namurian sandstones and shales | ■ TLPSsS, Till derived from Lower Palaeozoic sandstones and shales |
| ■ GQz, Gravels derived from quartzite | ■ TLSCh, Till derived from Silicified Limestone and cherts |
| ■ GIMar, Glaciomarine sediments | ■ Tls, Till derived from limestones |
| ■ Hardstand | ■ Tmp, Till derived from Metamorphic rocks |
| ■ Industrial | ■ TNCSsS, Till derived from Namurian and Carboniferous sandstones and shales |
| ■ IrSTAV, Irish Sea Till derived from acidic volcanic rocks | ■ TNSSs, Till derived from Namurian sandstones and shales |
| ■ IrSTBI, Irish Sea Till derived from basic igneous rocks | ■ TQz, Till derived from quartzites |
| ■ IrSTCcsS, Irish Sea Till derived from Cambrian sandstones and shales | ■ Tailings Pond |
| ■ IrSTDsS, Irish Sea Till derived from Devonian sandstones | ■ TdlMr, Tidal Marsh |
| ■ IrSTLPSsS, Irish Sea Till derived from Lower Palaeozoic sandstones and shales | ■ Urban |
| ■ IrSTLs, Irish Sea Till derived from Limestones | ■ Water |
| ■ KaRck, Kartsified bedrock outcrop or subcrop | ■ Ws, Windblown sands |
| | ■ Wsd, Windblown sands and dunes |



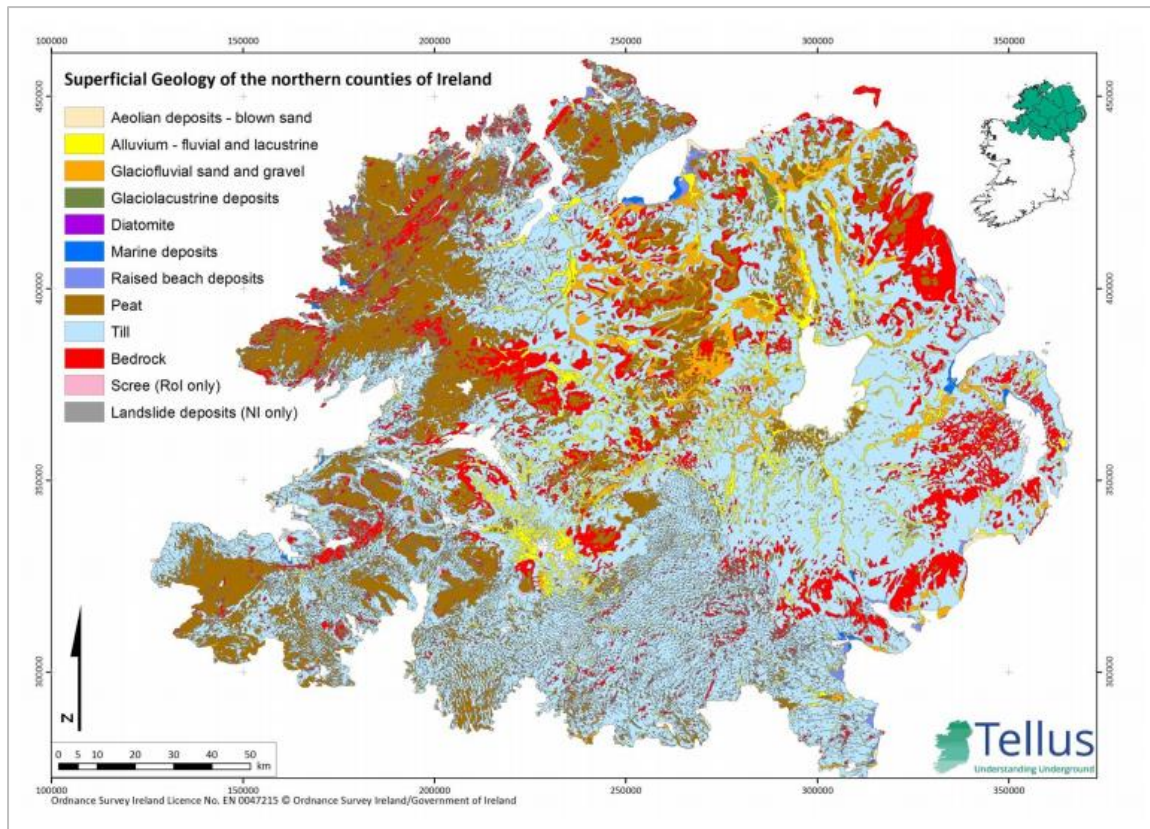


Figure 6: Superficial Geology of Northern Ireland and the border counties of the Republic of Ireland. [source: Gallagher *et al.* 2016].



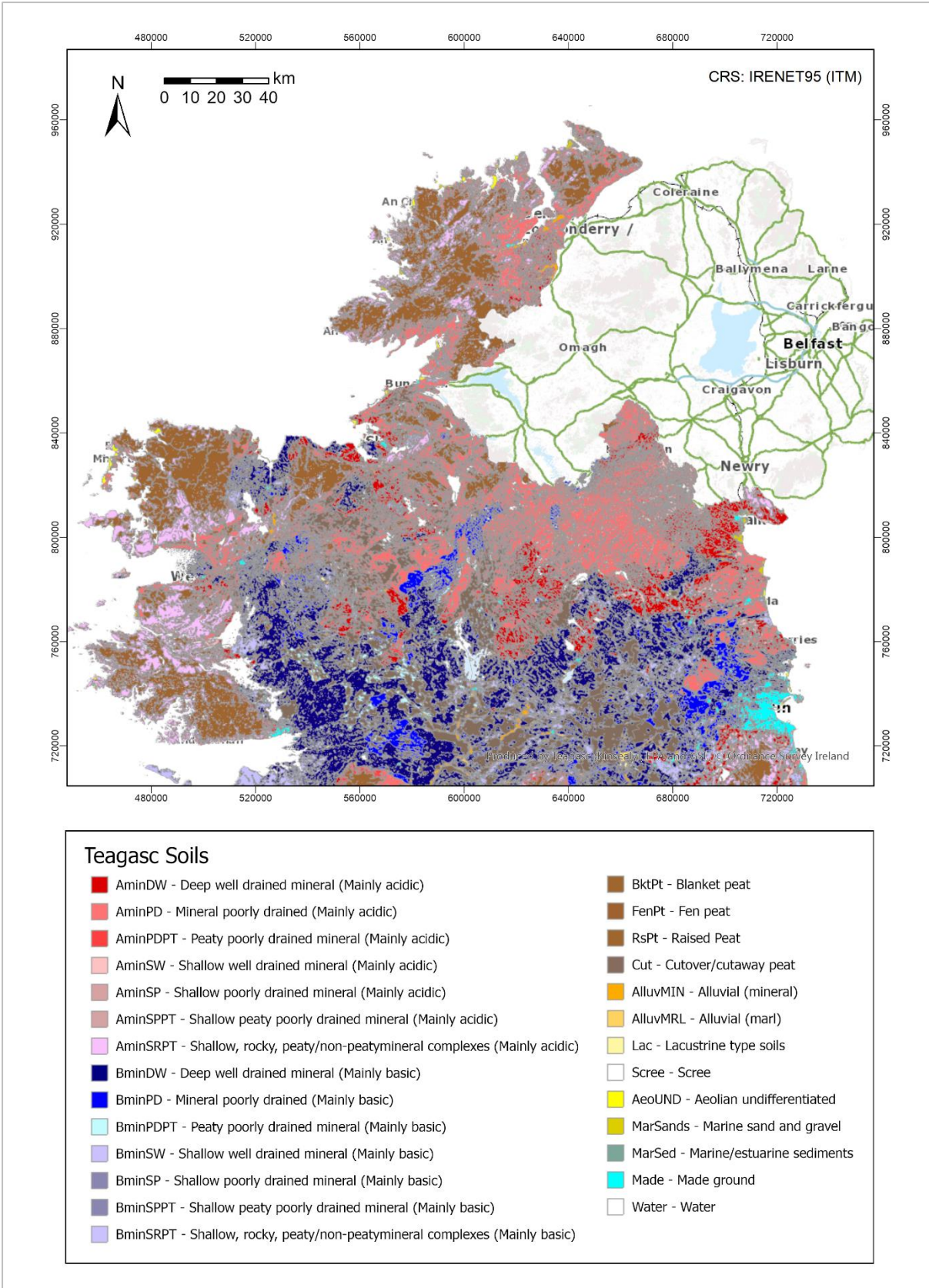


Figure 7: Teagasc National Soils (1:50,000).



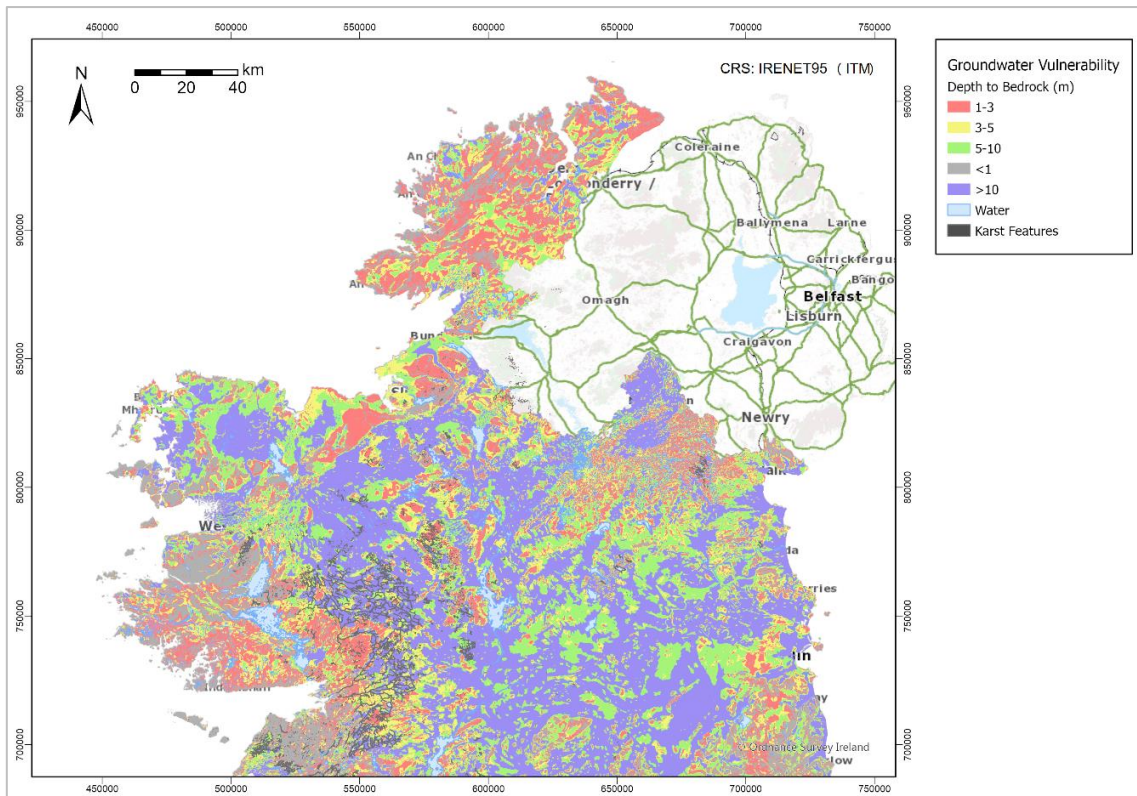


Figure 8: Depth to bedrock, mapped using attribute information from the GSI Groundwater Vulnerability database.

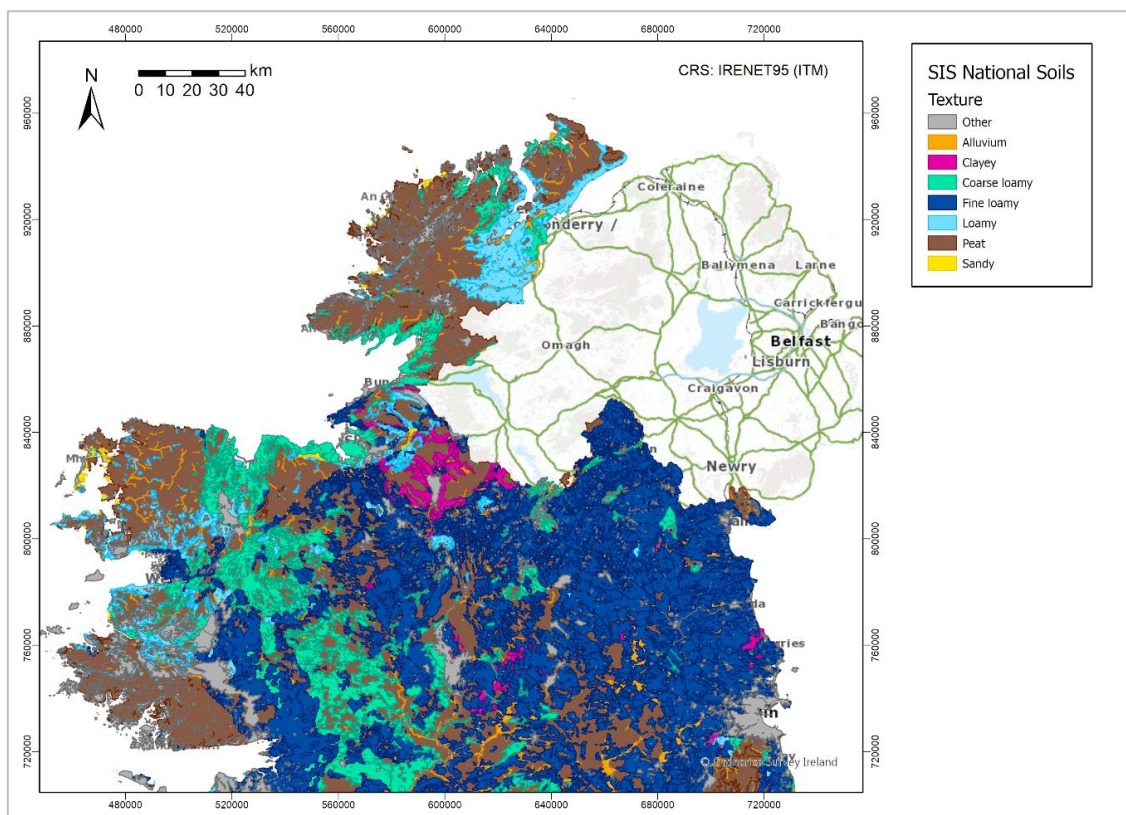


Figure 9: Teagasc-EPA Irish Soil Information System (SIS) map (1:250,000), classified by soil texture.



4.4. Land Use

Land use across Ireland as classified in the CORINE Land Cover dataset (2018) is shown in figure 10. While a variety of land uses exist, the area is largely devoted to agriculture with pastures, non-irrigated arable land and land “principally occupied by agriculture” taking up a significant proportion of the total area. Land classified as peat bog is also extensive while forests and natural grasslands are confined to smaller areas. Dublin City and its suburbs represent by far the largest urban area, with Galway City and other moderately-sized towns dispersed across the study area.

4.5. Topography and Rainfall

Figure 11 shows notable upland areas in west Galway, Mayo, Cavan/Fermanagh (Cuilcagh Mountains), Donegal, Derry/Tyrone (Sperrin Mountains), Down (Mourne Mountains) and south Dublin/Wicklow. Annual average rainfall is typically higher in these upland areas (> 3300 mm/year) as well as exhibiting an overall increase from east to west.



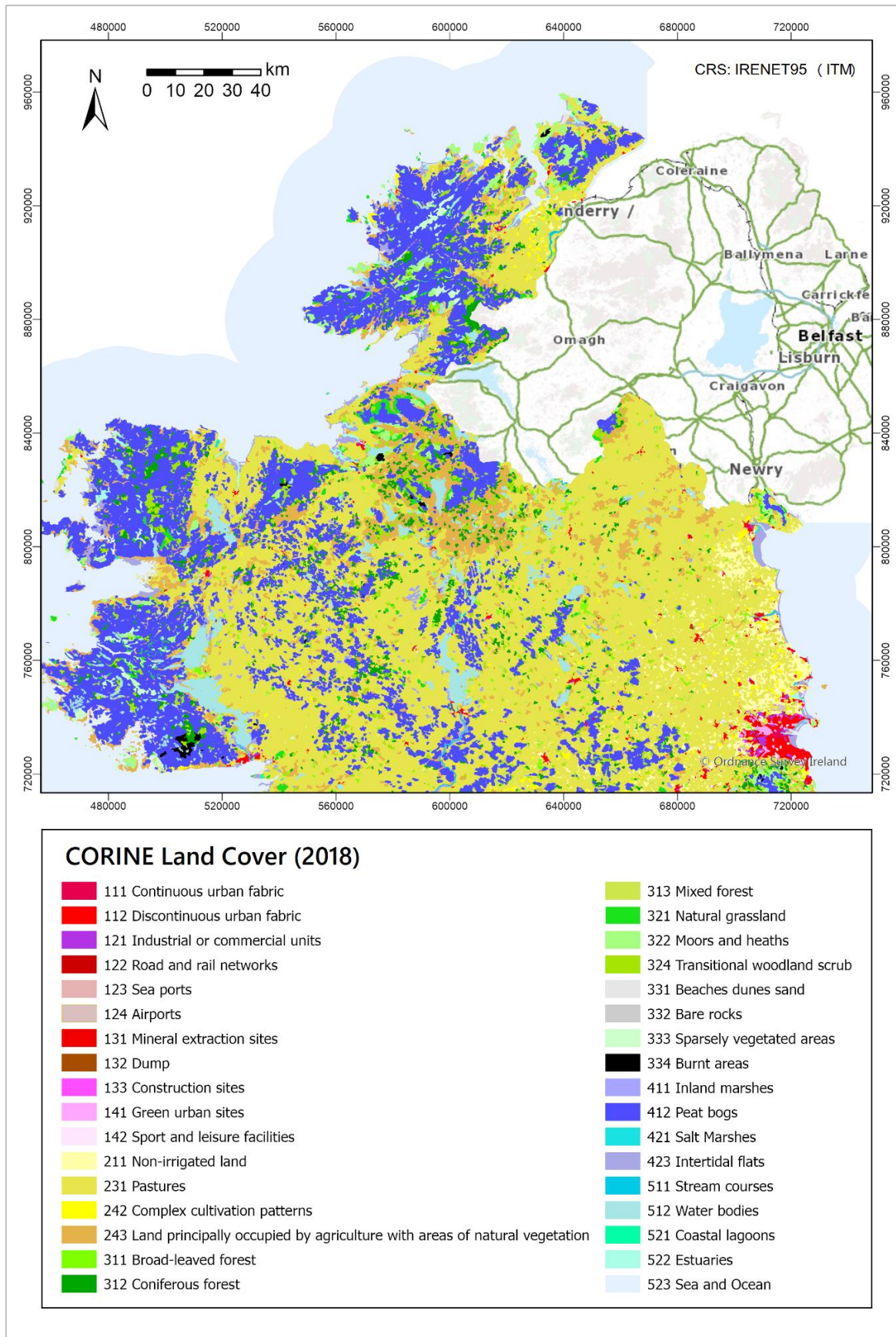


Figure 10: CORINE Land Cover map (2018).



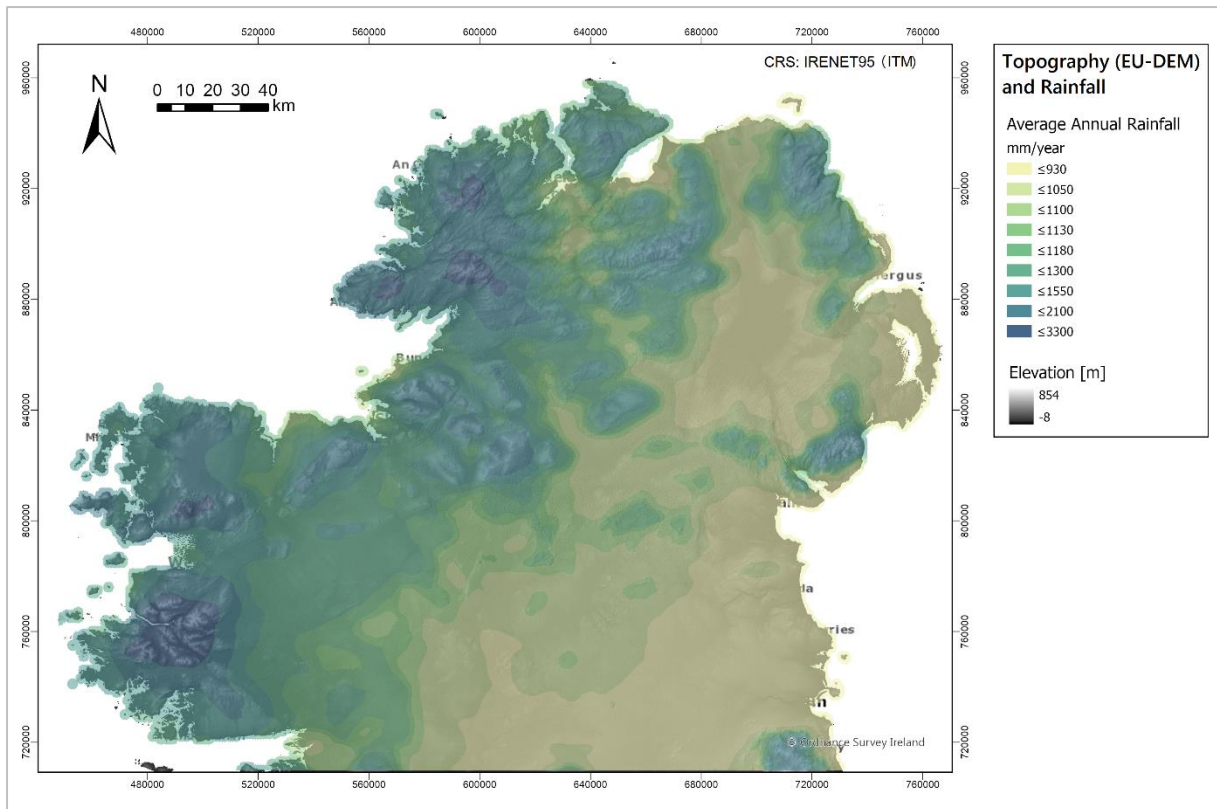


Figure 11: Regional Topography, created from the Digital Elevation Model over Europe (EU-DEM) with shaded relief (5x vertical exaggeration) and superimposed Annual Average Rainfall (Met Éireann 2018).



5. Materials and Methods

5.1. Data Used

Data for the Republic of Ireland were provided by the Geological Survey Ireland's Tellus programme and are freely available online (GSI n.d.-a). Data for Northern Ireland were made available by the Geological Survey of Northern Ireland © Crown copyright, 2022.

The following were used in this research:

- Tellus Shallow Topsoil 'A' – survey areas G1, G3 and G6 (see figure 12); multi-element XRFs.
- Tellus Shallow Topsoil 'A' – survey areas G1, G3, G5, G6, and N.I. (re-sampled from a higher density); multi-element ICP_{ar}.
- Tellus Radiometric K, U, Th and TC (merged) – survey areas NI, TB, TNM, CAV, A1, A2, A3 and A4 (see figure 13); shapefile (point) layer; clipped to coast; negative values (total count after corrections) removed.
- Tellus geophysical survey altitude raster (.tiff).

In addition to Tellus geochemical and geophysical data, the following datasets were used:

- Geochemical Domains (GSI, Glennon *et al.* 2020)
- Irish Soil Information System (SIS National Soils) (1:250k, Teagasc-EPA)
- National Soils Map (1:50k, Teagasc)
- Bedrock Geology (1:1 million, GSI)
- Quaternary Geology (1:50k, GSI)
- Groundwater Vulnerability (1:40k, GSI)
- CORINE Land Cover 2018 (Copernicus)
- EU-DEM, v1.1 (Copernicus)

Basemaps © Ordnance Survey Ireland (Geological Survey Ireland License No. EN 0047222).



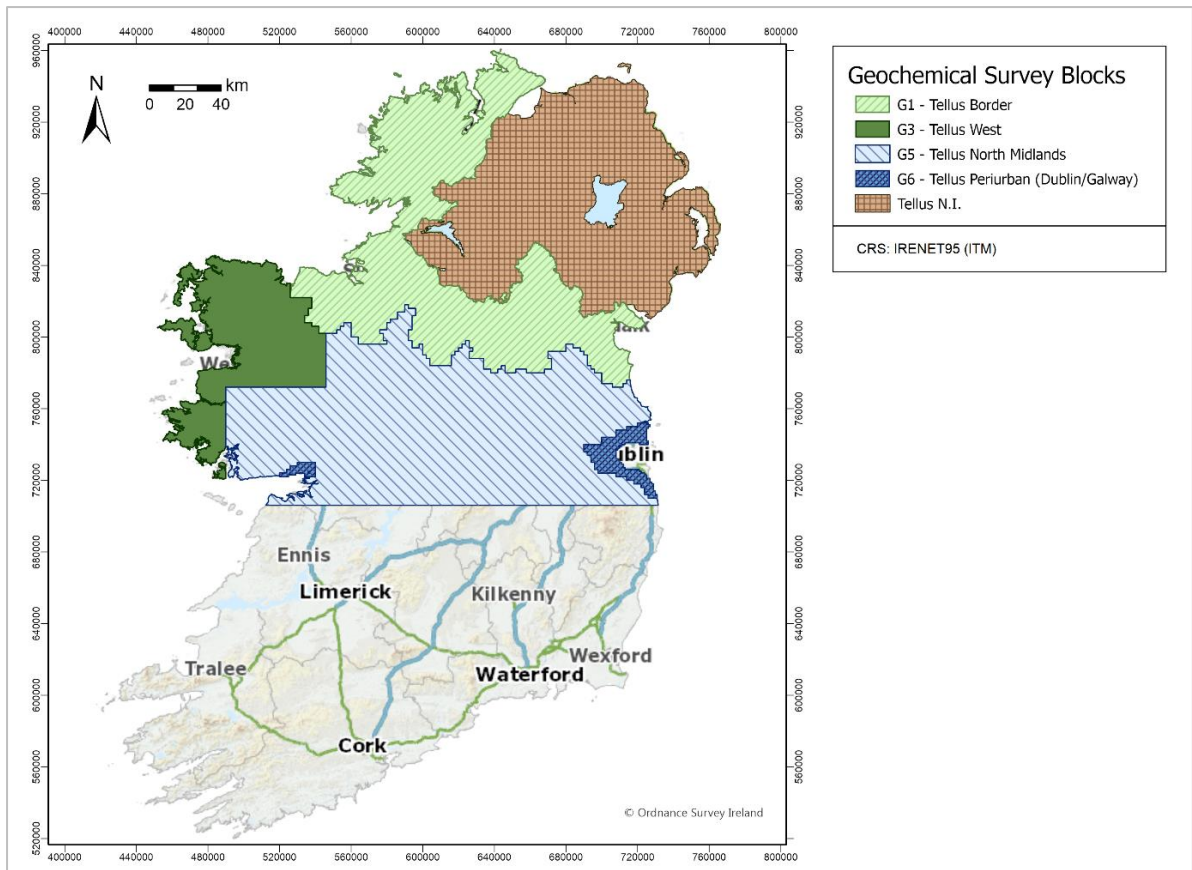


Figure 12: Tellus Northern Ireland (NI), Tellus Border, and Tellus (Ireland) geochemical survey blocks.

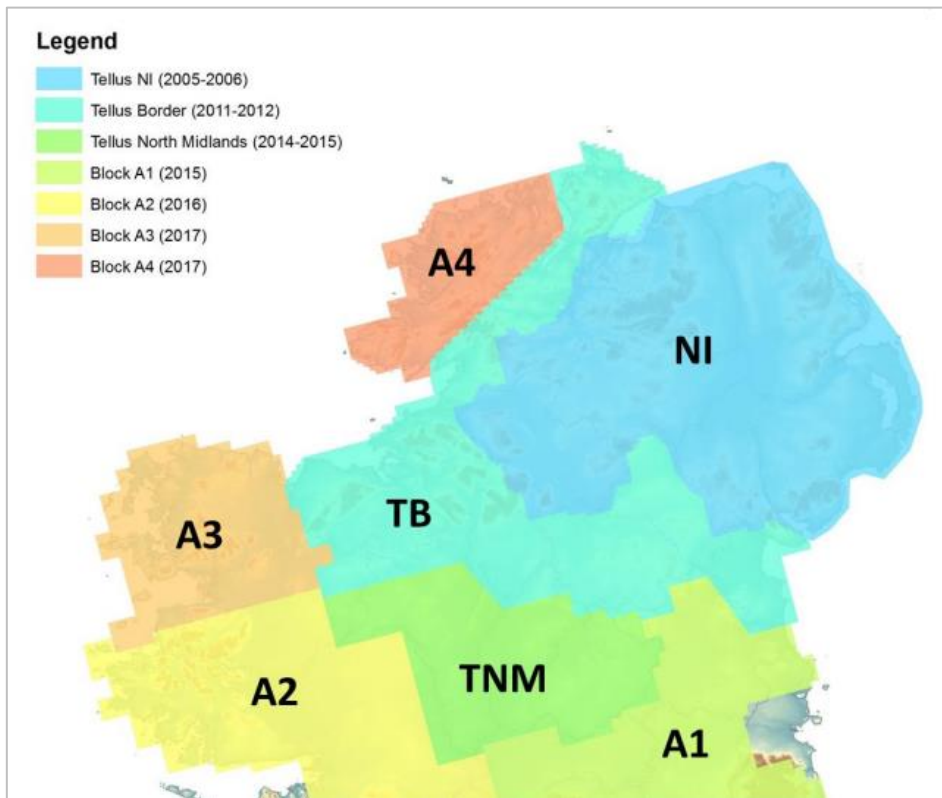


Figure 13: Tellus airborne survey blocks, adapted from (Ture and Muller 2020).



5.2. Geochemical Data: Background

5.2.1. Sample collection, preparation, analysis and reporting

The shallow topsoil 'A' data used in this research describe samples taken between 2004 and 2006 (N.I.) and 2011 to 2019 (R.o.I.), from a depth of 5–20 cmBGL, and at an average density of one sample per 2 km² in N.I., per 1 km² in G6, and per 4 km² in the R.o.I. blocks G1, G3 and G5 (Browne and Gallagher 2020). Sites were selected by sampling teams within predefined 2 km x 2 km grid cells such that they represented the dominant land use in the cell, were on undisturbed/unforested land where possible, > 200 m from major infrastructure and waterbodies, > 100 m from mapped or unmapped infrastructure and small waterbodies, and upslope and as far away as possible from contaminants (Knights *et al.* 2020). A hand-held auger was used to collect a five-point composite sample of 'A' soil to a total mass of approximately 1 kg. Samples were air dried before being sent to the designated preparation laboratory.

Dried samples were disaggregated and a representative subsample (approx. 40 g) was milled using an agate ball mill to achieve a sample of which 99 % is <53 µm and 95 % is <32 µm. LOI at 450 °C and multi-element analyses by XRFs and ICP_{ar} were performed on milled material and the coarse fraction (sieved to < 2 mm) was used for pH analysis.

For quality control purposes, separate laboratories were contracted for sample preparation and geochemical analyses. Table 2 summarises the multi-element analyses carried out in each lab to obtain potassium, uranium and thorium concentrations for the A-soil samples. Full details of the analytical procedures may be found in Knights *et al.* (2020) and Szpak *et al.* (2020).

Table 2: Geochemical analytical method specifications for K, U and Th determinations in contracted laboratories.

<i>Analytical Method</i>	<i>Laboratory</i>	<i>Digestion Method</i>	<i>Instrument</i>	<i>Sample Form</i>	<i>Elements Reported As</i>
XRFS	Malvern Panalytical	N/A	XRFDWD (Wavelength-dispersive).	40 mm diameter pellet (12 g milled soil + 3 g Licowax C).	K ₂ O [weight oxide equivalent, %] U [mg/kg] Th [mg/kg]
ICP _{ar}	SGS	<i>Aqua Regia</i> variant, 2:1 HNO ₃ :HCl	ICP-OES for K, ICP-MS for U, Th.	1 g milled soil, digested and bulked to 50 mL with dH ₂ O.	K [weight, %] U [mg/kg] Th [mg/kg]
ICP _{ar}	ALS	75 % <i>Aqua Regia</i> , 3:1 HNO ₃ :HCl	ICP-MS for K, U, Th.	0.5 g milled soil, digested and bulked to 12.5 mL with dH ₂ O.	K [weight, %] U [mg/kg] Th [mg/kg]



Table 3 details the lower limit of detection (LLD) for each of the multi-element analytical methods. Geochemical data used in this research were partially censored, meaning that data reported as being “< LLD” were replaced with an artificial concentration equal to (0.5 * LLD), however in some cases concentrations below the LLD were reported by the laboratory. Although the analytical method is not accredited below the LLD, these data may provide meaningful information about the distribution of low concentration values and are therefore included (Knights *et al.* 2020).

Table 3: Method LLDs (Lower Limits of Detection) for XRFS and ICP_{ar} geochemical analyses.

	<i>K [%]</i>	<i>U [mg/kg]</i>	<i>Th [mg/kg]</i>
LLD - XRFS	0.01 (K ₂ O equivalent)	0.7	0.5
LLD - ICP _{ar} (G1 block)	0.01	0.1	0.05
LLD - ICP _{ar} (G3 block)	0.0001	0.00005	0.00002

5.2.2. Geochemistry QA/QC

Soil data are subject to rigorous quality control procedures throughout all stages of the survey. 12 samples in every batch of 100 are designated QC samples comprising field duplicates, replicates and both certified and secondary reference materials to assess natural geochemical variance and laboratory precision and accuracy (Ramsey *et al.* 1992). Sample identities were randomised to avoid systematic biases and evenly distribute random and instrumental errors across the survey area (Knights *et al.* 2020).

5.3. Radiometric Data: Background

5.3.1. Survey Specifications

Radiometric data were collected between 2005 and 2017 as part of the Tellus airborne geophysical surveys of Northern Ireland and the Republic of Ireland (Ture 2020). Table 4 details the survey block names and the year(s) each survey took place.



Table 4: Geophysical survey block names and years flown.

<i>Survey</i>	<i>Area covered</i>	<i>Year(s) flown</i>
NI	Northern Ireland	2005 - 2006
CAV	Parts of Cavan and Monaghan	2006
TB	Tellus Border	2011 - 2012
TNM	Tellus North Midlands	2014 - 2015
A1	East	2015
A2	Galway	2016
A3	Mayo	2017
A4	Donegal	2017

Data were collected using an aircraft equipped with two magnetometers, an EM transmitter and receiver and a gamma-ray spectrometer with a sodium iodide (NaI) crystal detector (specifications shown in table B.1 (Appendix B)), pressure and temperature sensors. The aircraft was also fitted with differential GPS (DGPS) and an altimeter (Ture 2020).

The sampling frequency was 1 Hz and the aircraft was flown at a nominal speed of 60 m/s (70 m/s for NI and CAV surveys) along pre-planned survey lines (traverse lines) and perpendicular tie-lines as specified in table 5, equating to approximately one measurement every 60 m (or 70 m for NI/CAV). Figure 14 illustrates the relative sampling densities of both surveys.

Table 5: Airborne geophysical survey specifications, adapted from Ture (2020).

<i>Traverse line spacing [m]</i>	200
<i>Tie-line spacing [m]</i>	2000
<i>Traverse line heading [°]</i>	165/345
<i>Tie-line heading [°]</i>	75/255
<i>Fly height [mAGL]</i>	60 (rural)* / 240 (urban/planned high-fly zones)
<i>Projection</i>	Irish Transverse Mercator
<i>Vertical Datum</i>	Malin Head

* The nominal fly height for the TNM survey was 90 m.



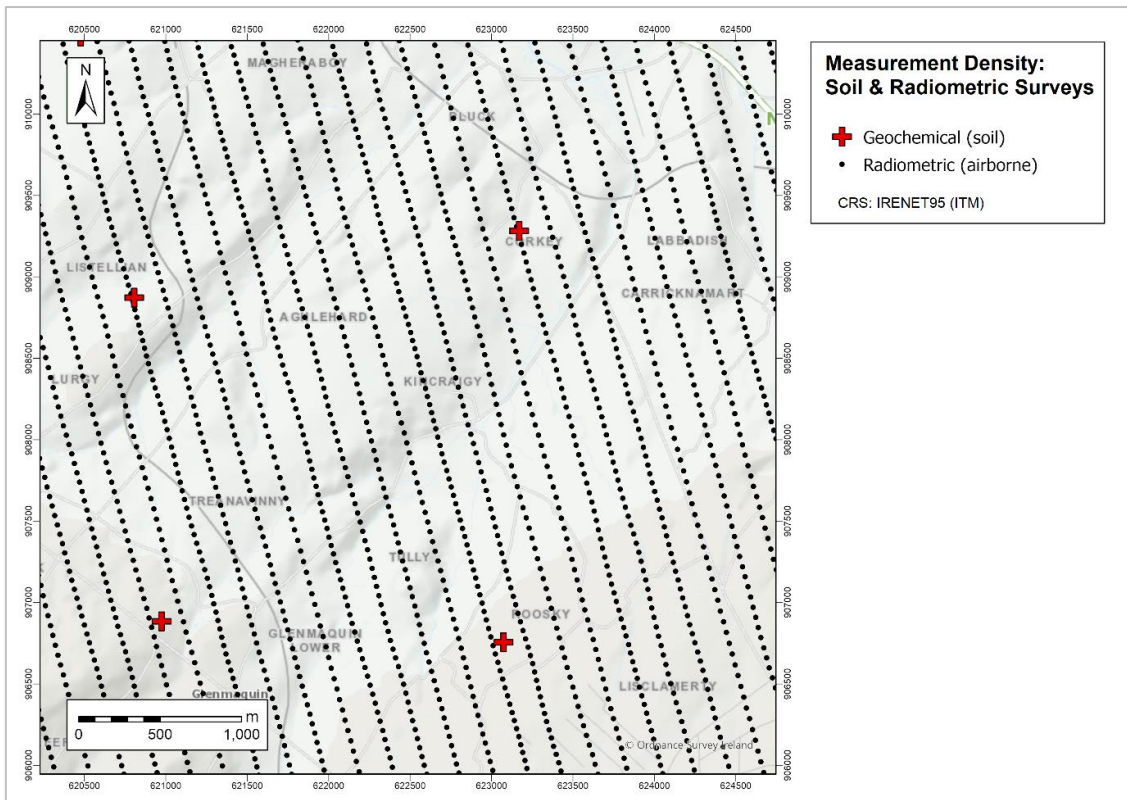


Figure 14: Density of data points recorded by the geochemical and radiometric surveys.

High-fly zones were established over urban areas with populations > 2500, as well as areas requested by landowners with sensitive livestock. Otherwise, the aircraft was required to not exceed +/- 20 m of the nominal survey height for more than five continuous kilometres (or +/- 40 m at any time), except where topography rendered this unavoidable.

Further details of survey operations and equipment specifications may be found in Ture (2020).

5.3.2. Radiometric calibrations, data processing and QC

Airborne geophysical equipment was tested and calibrated by the contractor in Canada before mobilisation and further calibrations were carried out in Ireland. Calibrations were carried out in accordance with the guidelines documented in IAEA (2003) and Grasty and Minty (1995).

To assess the repeatability of measurements between surveys and facilitate merging of the data collected over the various blocks during different years and survey conditions, a 6 km “repeat test calibration line” near Bundoran, Co. Donegal was flown during each survey season at six different elevations, crossing from land to sea. TC readings varied by approximately +/- 5 % between surveys



(Ture 2020). The range of elevations tested allows the sensitivity of the spectrometer to survey altitude to be assessed and the land-water boundary is used for data scaling/shifting corrections.

Data were processed by the contractor and quality checked by Tellus geophysicists in relation to terrain clearance and flight line deviation criteria. Standard processing, as detailed in Sander Geophysics (2016) includes correcting for effective height above ground level, cosmic and aircraft background radiation, radon background concentrations, element stripping ratios and altitude attenuation (Sander Geophysics 2016; Grasty and Minty 1995). Where negative count readings arose after the various corrections were applied (e.g., over waterbodies where most of the radiometric signal was attenuated) the points were removed from the shapefile.

Element concentrations were calculated from corrected count rates and experimentally determined sensitivities for each spectral window, and total element concentrations were reported for K [%] (measured directly from ^{40}K), eU [ppm] (inferred from ^{214}Bi), and eTh [ppm] (inferred from ^{208}Tl) (IAEA 2003). Data from individual surveys were levelled and merged block-by-block by applying correction factors calculated from average readings in overlap zones between survey blocks (Ture 2020).

5.4. Research Methods

All analysis was carried out using ArcGIS™ Pro, version 2.6.1. (with Spatial Analyst extension) and Microsoft® Excel®, version 2107 for Microsoft 365.

Figure 15 shows the project workflow and outlines the main steps taken to analyse and interpret the data.



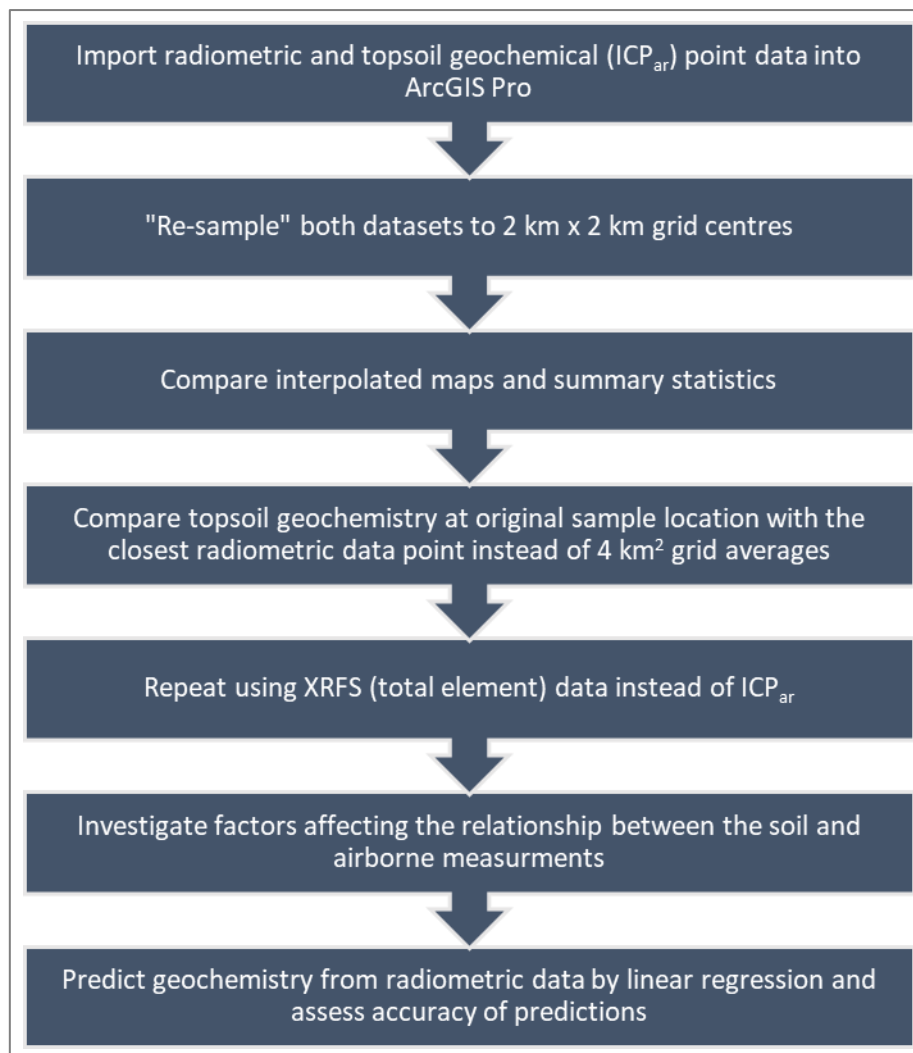


Figure 15: Overview of project workflow.

5.4.1. Data manipulation in ArcGIS Pro

- i. Shallow topsoil 'A' (hereinafter referred to as 'soil') geochemical data for K, U and Th, analysed by ICP_{ar}, were imported into ArcGIS as XY point data.
- ii. The *Create Fishnet* tool was used to generate a regular grid of 2 km x 2 km square polygons based on the extent of the soil point data, which was then clipped (*Clip* tool) to the coastline and subsequently clipped to exclude islands and lakes.
- iii. Mean (arithmetic) K, U and Th concentrations were calculated for each grid using the *Summarize Within* tool and these values were assigned to a point created at the centroid of each grid to give a regular array of soil points.



- iv. Radiometric point data for K, eU, and eTh were imported into ArcGIS as a shapefile and step 3 was repeated to calculate the mean airborne element concentrations in each 4 km² grid square and assign this value to the centre point. This reduced the radiometric dataset to a workable total of 12,961 points (from 4,082,659) to enable pointwise comparison of airborne and soil measurements both statistically in Excel and spatially in ArcGIS by creating interpolated maps with the same resolution.
- v. The *Spatial Join* tool was used to join the soil and radiometric data at each point (*join operation = one-to-one; match option = intersect*). points without both geochemical and radiometric data were deleted. A table of XY co-ordinates and the associated mean soil and radiometric K, U and Th (or eU and eTh) concentrations for each grid square was exported using the *Table to Excel* tool.
- vi. Pointwise comparison of soil and radiometric data was repeated, this time joining each soil point at its original sampling location with the closest radiometric point (*Spatial Join; one-to-one; closest geodesic*). This tool also calculated the distance between the soil and radiometric points. Considering the soil sample density, this method is more likely to give a set of airborne measurements that are representative of the geology and ground conditions at the soil sampling site. N.I. and G6 were excluded from this analysis because these soil data were previously re-sampled to a density of 1 per 4 km² and the original sampling locations were unknown.
- vii. Concentrations of K (converted from K₂O, see equation 2), U and Th in topsoil, determined by XRFs, were imported as XY point data and joined with the closest radiometric point as before to analyse the relationship statistically and investigate factors influencing it. These XRFs measurements were carried out on sub-samples of the same soil analysed by ICP_{ar} therefore both sets of soil data are directly comparable and have identical XY co-ordinates. The XRFs and ICP_{ar} data were also joined (*one-to-one; intersect*) and exported to Excel to compare the analytical methods.
- viii. Concentrations at each soil point (now using XRFs data) in its original location and the closest radiometric point were compared and the relationship between the datasets was investigated statistically, classifying pairs of data according to geology, soil type, land use etc.



- ix. Sets of linear regression equations were generated and used to predict the soil concentrations of K, U and Th at each point based on the airborne K [%], eU [ppm] and eTh [ppm] values. Predicted soil concentrations were calculated in Excel, first using one linear regression equation ($a = b(x) + c$, where $a = X_{\text{soil, predicted}}$ and $b = X_{\text{air}}$) for all of the data, then using separate equations for areas of 'peat' and 'no peat,' and finally using separate equations for areas of 'peat' and 'no peat' within each Geochemical Domain (see section 5.4.2). The deviation [%] of each predicted concentration from the true soil value was calculated in Excel and mapped in ArcGIS to assess prediction accuracy spatially.
- x. The final set of equations in step ix were used again, this time for every radiometric point in the original dataset, to generate high resolution maps of predicted soil concentrations for the northern half of the country.

5.4.2. Classifying data

The auxiliary datasets listed in section 5.1, were used to group data into various classes to investigate factors influencing the relationship between topsoil geochemistry and airborne radiometrics:

Soil/radiometric point data were classified by:

- i. Joining the auxiliary dataset in question to the point data (*Spatial Join*; one-to-many (polygon to points); intersect), or
- ii. Clipping the point data with feature classes created based on chosen attributes (e.g., Teagasc Soils: all polygons with 'PAR_MAT=peat').

Tables of classified data were exported and analysed statistically in Excel.

The "Geochemical Domains" dataset was originally created as part of an applied geochemistry project by the GSI (Glennon *et al.* 2020). GSI 1:500,000 scale bedrock geology and 1:40,000 scale Teagasc-EPA subsoil maps were simplified by amalgamating units with broadly similar rock types/ages and parent material, respectively, to give two "lithological domain" maps which were then merged to create one generalised map (figure 16) which divides the Republic of Ireland into seven domains "based on similar geochemical signature" (Glennon *et al.* 2020). Zones are classified according to the subsoil domain, where assigned, and according to the bedrock domain in areas of peat, made ground and bedrock (Glennon *et al.* 2020). This simplified classification avoids



unnecessary complexity while still accounting for the variations in subsoil and bedrock geochemistry observed across Ireland which are likely to be reflected in the topsoils (< 1 mBGL) derived from such materials.

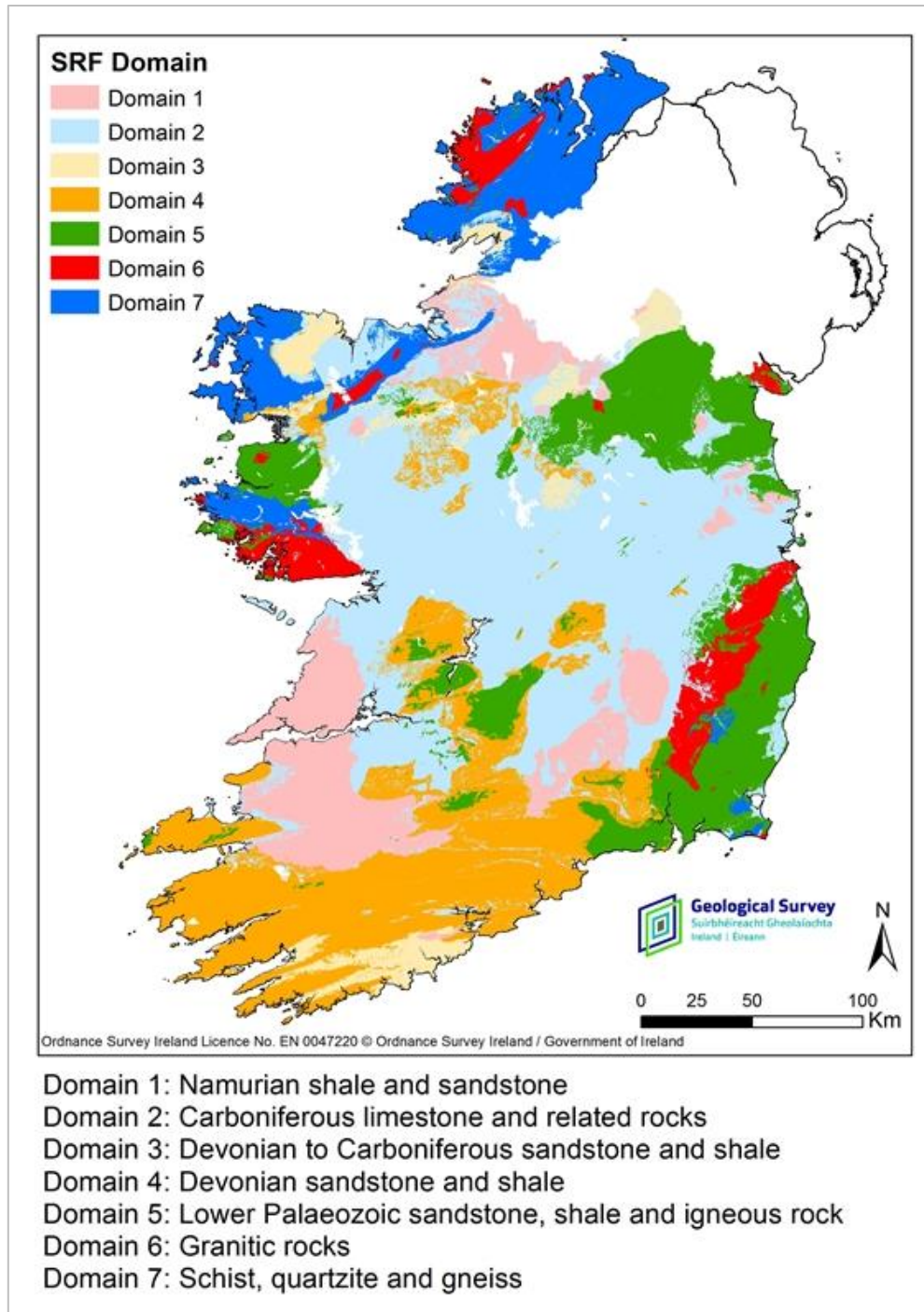


Figure 16: Geochemical Domains [source: Glennon *et al.* 2020].



5.4.3. Data manipulation, treatment of outliers and statistics in Excel

Considering the robust QA/QC programmes in place for both geochemical and geophysical data collection, it was decided that minimal additional data treatment would be carried out. As noted by Rock (1988) “geochemistry is an unusual discipline in that true (...) outliers can be of prime interest” and indeed in this research anomalous concentrations, or ratios of concentrations, revealed patterns that helped to understand the nature of geochemical and airborne survey methods and their relationship.

Geochemical data was left partially censored and the radiometric data was used as provided (i.e. clipped to coast and with negative values removed, but with no additional filtering or editing). Potassium concentrations measured by XRFs, reported as K_2O [%] (weight oxide equivalent) were converted to K [%] using equation 2.

$$K \text{ [%]} = \frac{(2) \left(39.0983 \frac{g}{mol} \right)}{\left(94.196 \frac{g}{mol} \right)} \times K_2O \text{ [%]} = 0.830 \times K_2O \text{ [%]} \quad (2)$$

Non-parametric summary statistics (median, interquartile range) were used to describe the data and distributions of values were visualised using histograms and Tukey boxplots. The latter comprise a box that spans the interquartile range, with a line crossing the box at the median and whiskers representing an “extraquartile range” (defined by equations 3 and 4) (see figure 17). Values outside this range are considered outliers (Banks *et al.* 2001). These measures of location and spread were favoured over the arithmetic mean and standard deviation considering much of the data used in this research, like many geochemical datasets, is non-normally distributed and includes numerous outliers and values < LLD (e.g., figure A.1 (Appendix A)). According to Rock (1988), “the mean is the worst average” for such datasets and is commonly an overestimate, especially for trace elements which are usually positively skewed with large outliers.

When using linear regression equations to predict soil concentrations, outliers, as defined in the boxplots, were first removed to improve the coefficient of determination (R^2). A point was considered an outlier if the ratio (X_{soil}/X_{air}) was greater than the upper whisker “maximum” or less than the lower whisker “minimum”, where:



Upper whisker "maximum" = $Q3 + 1.5 \times (IQR)$ (3), and

Lower whisker "minimum" = $Q1 - 1.5 \times (IQR)$ (4).

$Q1$ and $Q3$ are the first and third quartiles, respectively, and IQR is the interquartile range, equal to $Q3 - Q1$.

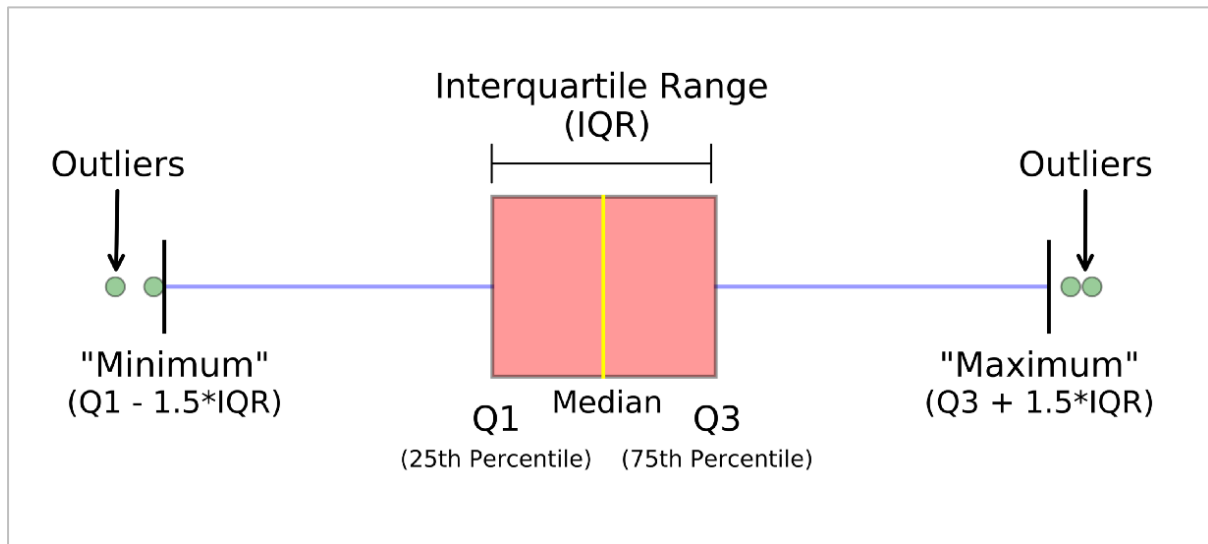


Figure 17: Summary statistics using a Tukey Boxplot. Note whiskers are shown in blue. Black lines at the end of the whiskers represent actual values in the data, i.e. the highest and lowest values that lie between $Q1 - 1.5 \times IQR$ and $Q3 + 1.5 \times IQR$. [Source: https://miro.medium.com/max/1400/1*2c21SkzJMf3frPXPg_gZA.png].

Outliers were removed within each Geochemical Domain separately so as not to discard values that may lie within a normal range for their geological context but appear anomalous relative to the entire dataset (Cinelli *et al.* 2017). Where boxplots were used to simply observe trends across different classes of data, outliers were hidden for clarity but not removed.

Although both the radiometric and geochemical methods report concentrations in the same units (% K and ppm U, Th) the methods of determining these concentrations differ significantly. It was therefore considered informative to look at the 'soil:air' concentration ratios rather than the 'soil - air' residual at each point. Therefore, at points where the airborne concentration equals zero it was necessary to substitute a low, non-zero concentration. The lowest reported airborne value of 0.01 (% or ppm) was chosen as a suitable replacement as this value does not imply a lower detection limit or greater accuracy than can be achieved and should not significantly alter the median or range of outlying values, whereas deleting these values would.



5.4.4. Mapping

Interpolated maps were created in ArcGIS using Inverse Distance Weighting (*IDW* tool, Spatial Analyst toolbox).

The mapping parameters are given in Table 6. The sensitivity of the interpolation to a change in parameters was tested using various cell sizes between 100 and 250 m and search radii between 500 and 2500 m. Differences between outputs were negligible for both datasets.

Table 6: Parameters used to create interpolated radioelement maps in ArcGIS Pro.

<i>Interpolation Method</i>	<i>Output Cell Size [m]</i>	<i>Distance Exponent (Power)</i>	<i>Fixed/Variable Search Radius</i>	<i>Search Radius [m]</i>
IDW	250	2	Fixed	2000

Interpolated maps were classified to match those of published Tellus geochemical outputs. The upper limit of each percentile class and the colour scheme are shown in figure 18. This classification was used for maps of geochemical, geophysical and predicted geochemical concentrations of K, U and Th.

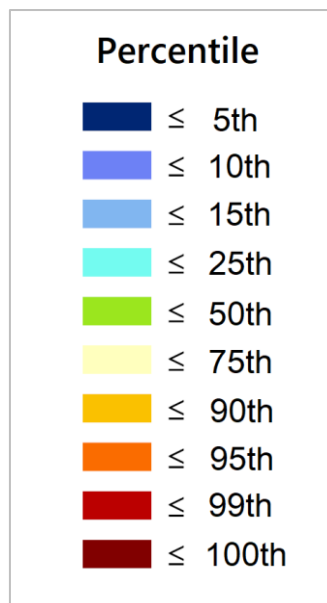


Figure 18: Tellus percentile classification colour scheme for interpolated maps.

Maps showing the deviation (%) of predicted soil concentrations from true values were also interpolated using the parameters in table 6 but were classified differently, with points grouped into nine classes ranging from “> +100 %” (over-predicted by 100% or more) to “< -100 %” (under-predicted by 100 % or more) (see figures 67-69).



Hillshade maps (figures 11, 71) were created from the EU-DEM for Ireland (Copernicus). [*Azimuth* = 315°, *Altitude* = 45°, *Z-factor* (vertical exaggeration) = 5].

IDW is a deterministic interpolation technique which generates a raster based on measured data points, using a linear combination of the neighbouring points, each weighted as a function of distance from the output cell location such that the data points closest to the output cell influence its value the most and those further away carry less weight (Childs 2004). The IDW formulae are given in equations 5 and 6, where \hat{R}_p is unknown data, R_i are the values at known locations, N is the number of points (locations of known values) being used to determine each unknown data point, w_i is the weighting applied to each known point in the determination as calculated in equation 6. Here d_i is the distance from each known point to the one being interpolated and α is the power (most often two) (Chen and Liu 2012):

$$\hat{R}_p = \sum_{i=1}^N w_i R_i \quad (5)$$

$$w_i = \frac{d_i^{-\alpha}}{\sum_{i=1}^N d_i^{-\alpha}} \quad (6)$$

IDW, unlike geostatistical methods such as Kriging, does not make assumptions about the “vector of relationships between data points” (Knights *et al.* 2020) hence it will not predict values that lie outside the range of values found in the data, potentially missing highs or lows between sample points. While alternative techniques could potentially produce more useful maps for smaller-scale investigations, considering this research is conducted at a regional scale, with soil sampled at a density of one site per 4 km², it may be misleading to assume directional trends and spatial correlation over short distances (Cinelli *et al.* 2018). Additionally, geostatistical interpolation may be unreliable where data distributions are strongly skewed, which is very common for geochemical datasets, as the calculated variogram may be strongly biased (Rawlins *et al.* 2012).

IDW was also favourable as this method was used to generate the geochemical maps that are found in various Tellus outputs including the online data viewer, factsheets and reports (Browne and Gallagher 2020). Similar parameters (output cell size, power, search radius) and classification scheme (percentiles, colour ramp) were chosen so that outputs of this research are compatible with other Tellus products and may be compared to geochemical maps of other elements to facilitate potential identification of trends that go beyond the scope of this research.



6. Results and Discussion

6.1. ICP_{ar} Soil and Radiometric Data

6.1.1. Comparing radioelement concentrations

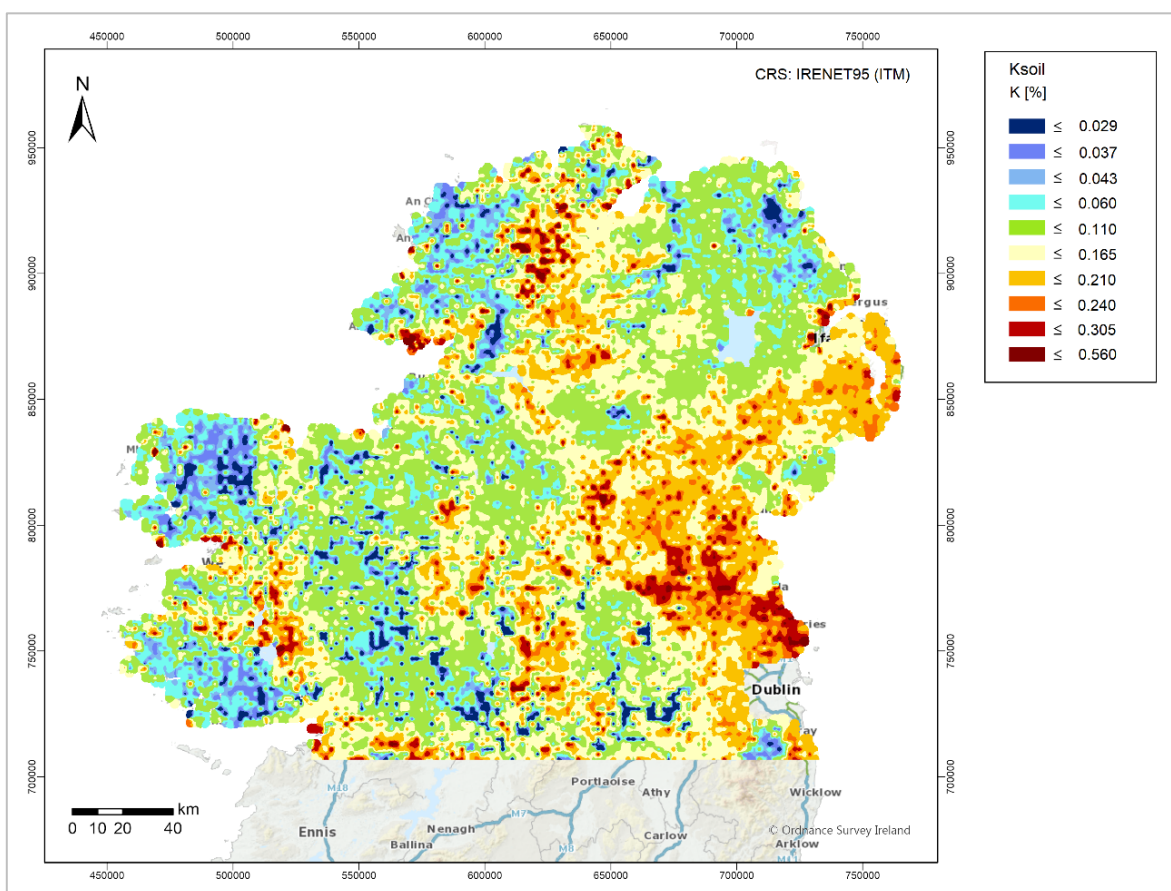


Figure 19: Map of K_{soil} based on regular array of 2 x 2 km grid squares with mean concentration (determined by ICP_{ar}) assigned to centre point.



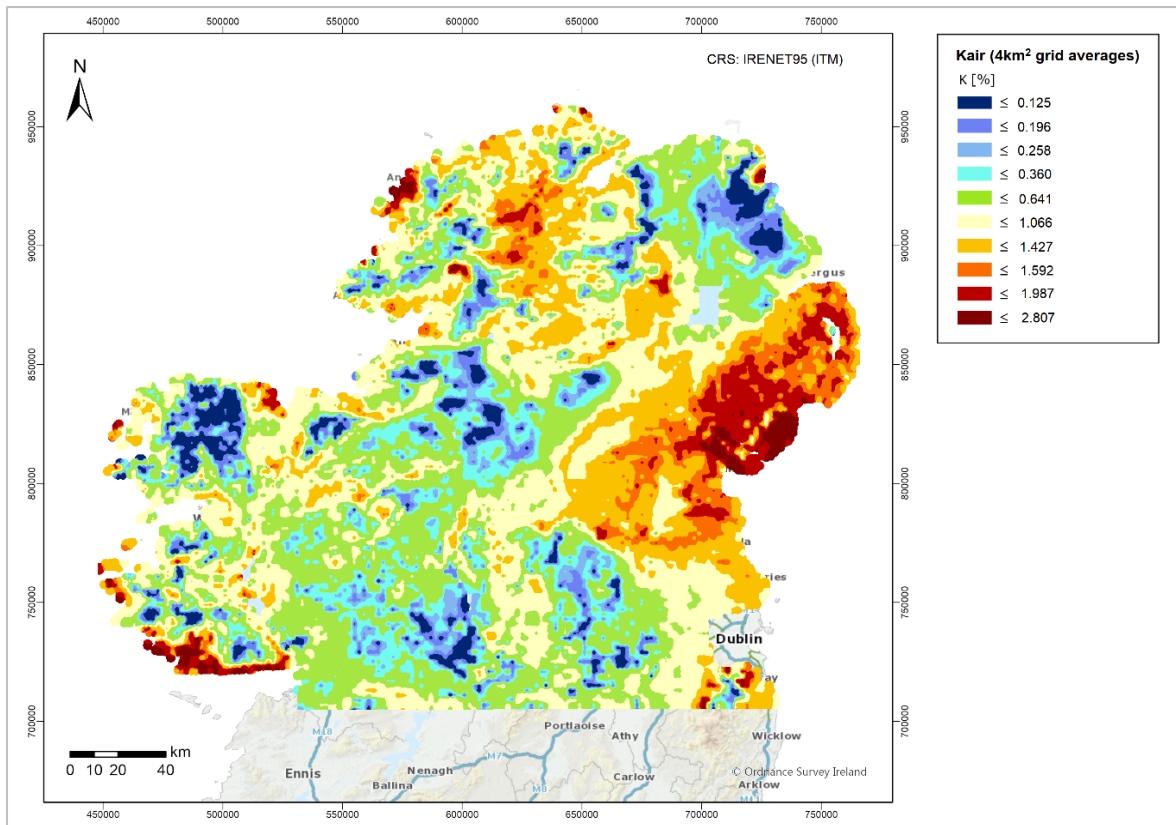


Figure 20: Map of K_{air} (radiometric) based on re-sampled 2 x 2 km array with mean concentration in each grid square assigned to centre point.

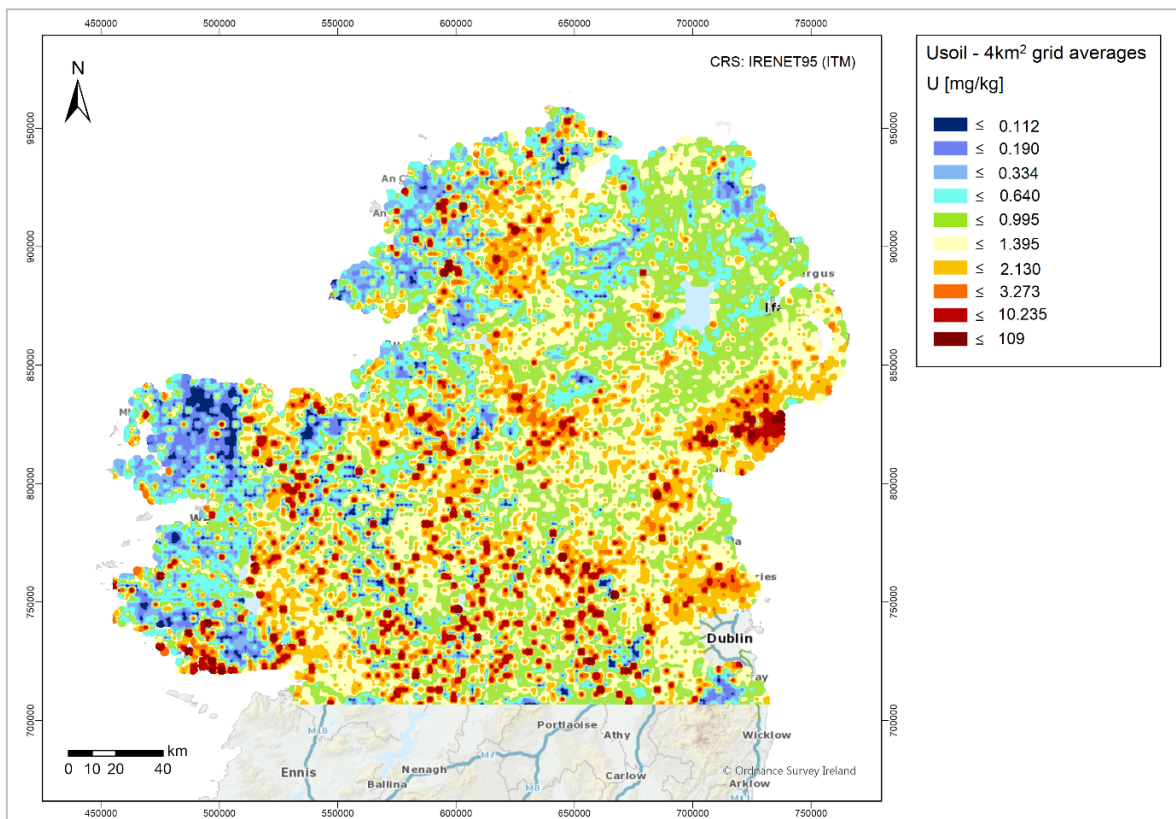


Figure 21: Map of U_{soil} based on regular array of 2 x 2 km grid squares with mean concentration (determined by ICP_{ar}) assigned to centre point.



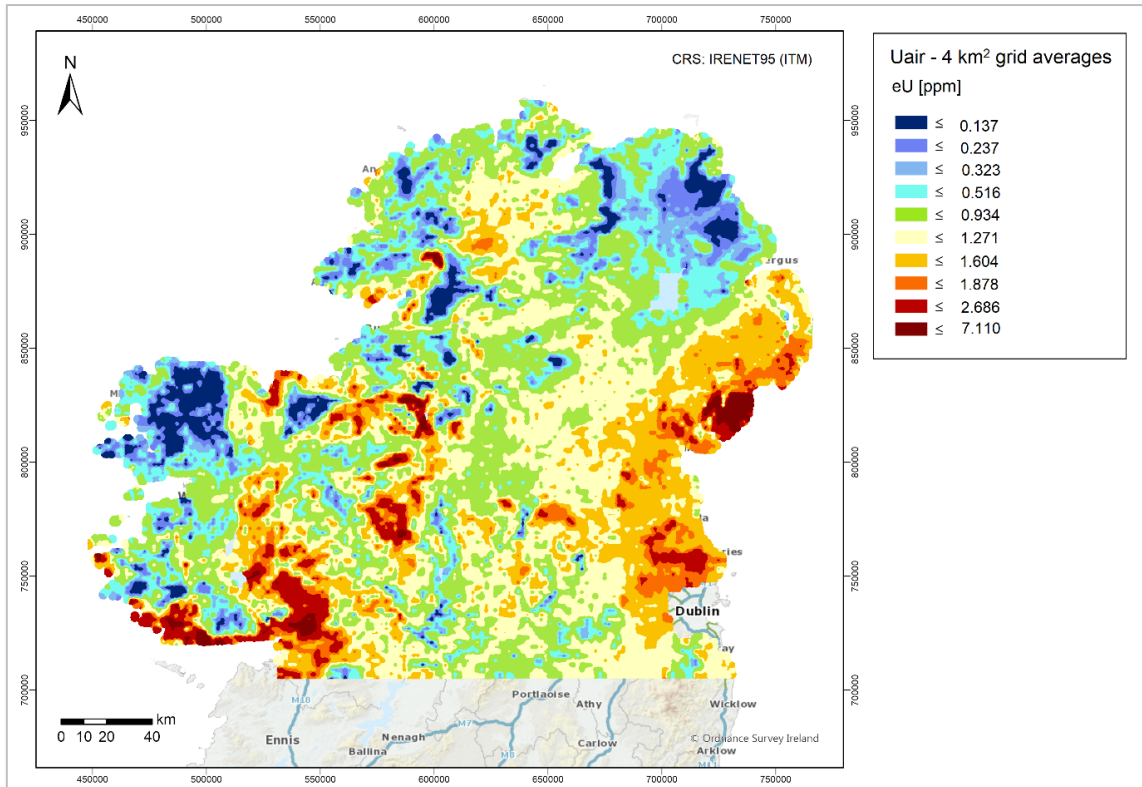


Figure 22: Map of U_{air} (radiometric) based on re-sampled 2×2 km array with mean concentration in each grid square assigned to centre point.

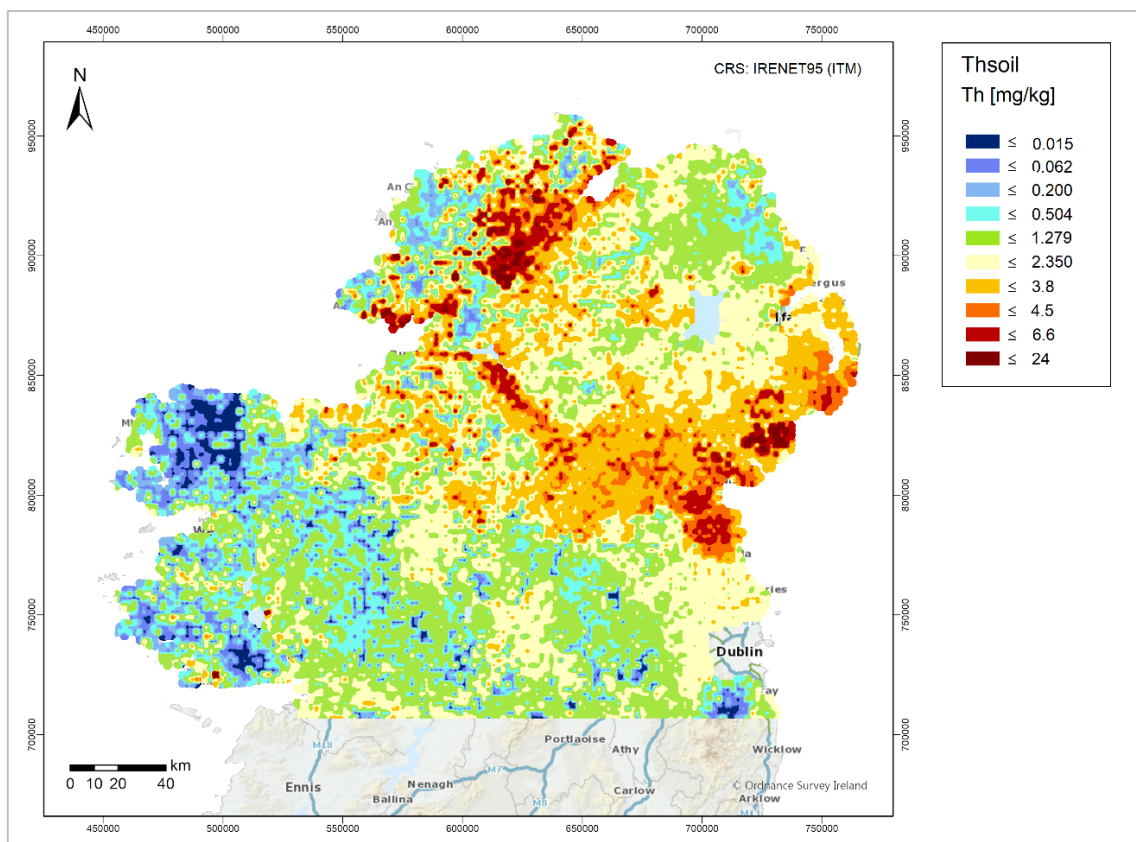


Figure 23: Map of Th_{soil} based on regular array of 2×2 km grid squares with mean concentration (determined by ICP_{ar}) assigned to centre point.



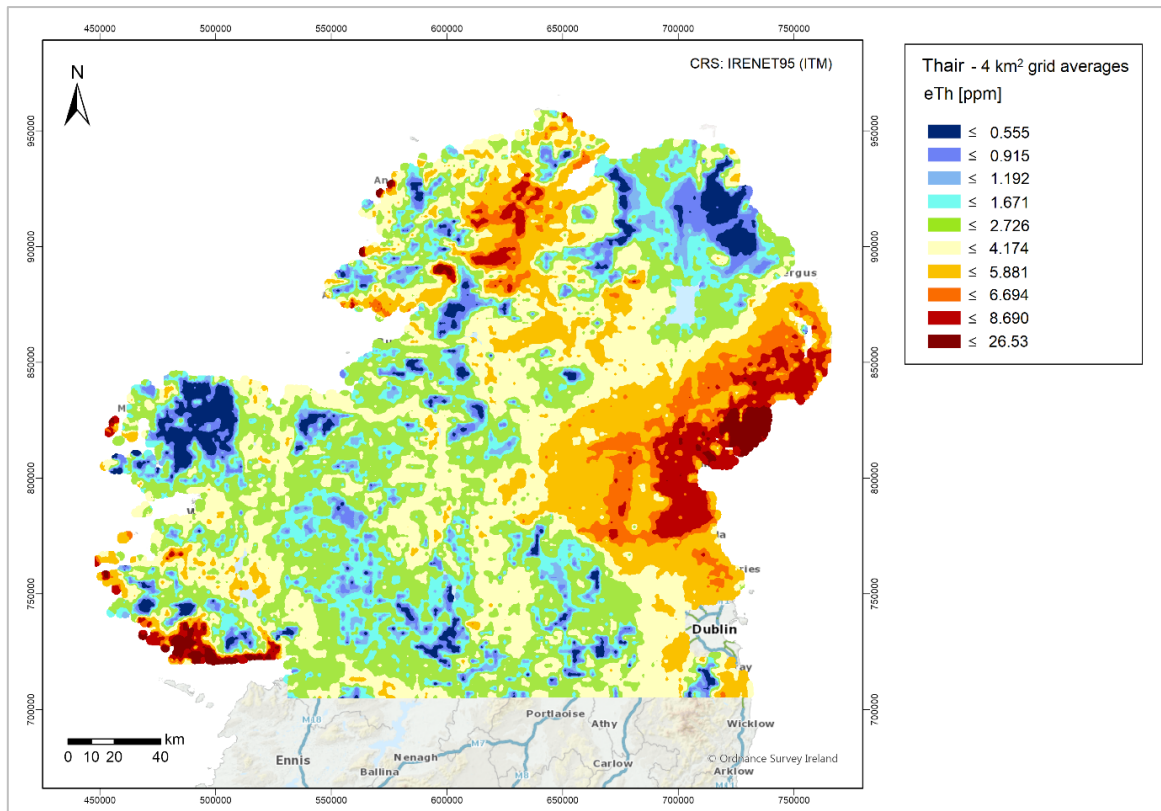


Figure 24: Map of Th_{air} (radiometric) based on re-sampled 2 x 2 km array with mean concentration in each grid square assigned to centre point.

Comparing interpolated maps of soil and radiometric K, U and Th concentrations (figures 19-24), several areas appear characteristically high in all three radioelements while others are typically low in all three. Despite both surveys measuring only the top 20-60 cm of soil both sets of maps clearly show the influence of the underlying bedrock on the radioelement signatures. The Antrim basalts are generally low in all three radioelements, with notable lows coinciding with peat deposits. Extensive peat deposits in northwest Mayo and southwest Galway are characterised by lows in all six maps, while areas of granitic bedrock show distinct highs in all maps except K_{soil} (figure 19), which may be due to poor *Aqua Regia* extraction of K from highly resistant silicates (Kisser 2005). Other lows common to all six maps are observed in areas of blanket peat in Donegal, Wicklow, and the Slieve Beagh Ramsar-designated blanket bog in the central Border region (Beamish 2014). High radioelement concentrations are also found in areas underlain by Ordovician-Silurian deep marine clastic sedimentary rocks of the Longford-Down inlier and Neoproterozoic metamorphic rocks of the Dalradian Supergroup.

Elevated concentrations of uranium found in east Galway and Roscommon where potassium and thorium are not noticeably high may be due to the presence of karstified limestone, which is not typically high in radioelements but contains dissolution features which can act as effective conduits



for radon gas originating from more radioactive Siluro-Devonian granite, Neoproterozoic schist and gneiss, and Namurian shale units (O'Connor *et al.* 1993; GSI n.d.-b). Since eU is inferred from ^{214}Bi , a decay product of radon, this would explain why the effect is more pronounced in the radiometric map (figure 22).

The radioelement highs observed across southwest Galway in all three maps created from airborne data are likely due to the presence of outcropping granite, particularly along the coast, in which high K, U and Th concentrations but poor *Aqua Regia* extraction rates may be expected, hence the lack of accompanying highs in ICP_{ar} soil maps.

A northwest-southeast trending area of high K/U/Th can be observed on the border between counties Fermanagh and Cavan/Leitrim in all three soil maps but none of the airborne maps with no obvious bedrock or soil unit responsible for such a feature. This high is particularly distinct in the Th_{soil} map (23), in which another feature with no geological or pedological explanation can be discerned near the Louth-Meath border. These are interpreted as artefacts arising from the merging of datasets from different survey blocks, noting that the ICP_{ar} analyses for the Tellus Border (G1) block were conducted at a different laboratory to the other blocks and have higher associated LLDs (Knights *et al.* 2020).

While similar radioelement patterns are found in both sets of maps and the underlying shapes of the distributions (non-normal and often bi-/multimodal) are similar for both datasets (figure A.1), the boxplots in figure 25 illustrate how the actual K, U and Th concentrations measured by the geochemical and radiometric methods are different (summarised in table 7). Typical *soil:air* ratios (table 8) were calculated as the median soil concentration divided by the median air concentration rather than the median of all $X_{\text{soil}}/X_{\text{air}}$ values, which is represented in the ratio boxplots. These values were almost identical in most cases but the latter was found to be more sensitive to extreme outliers.



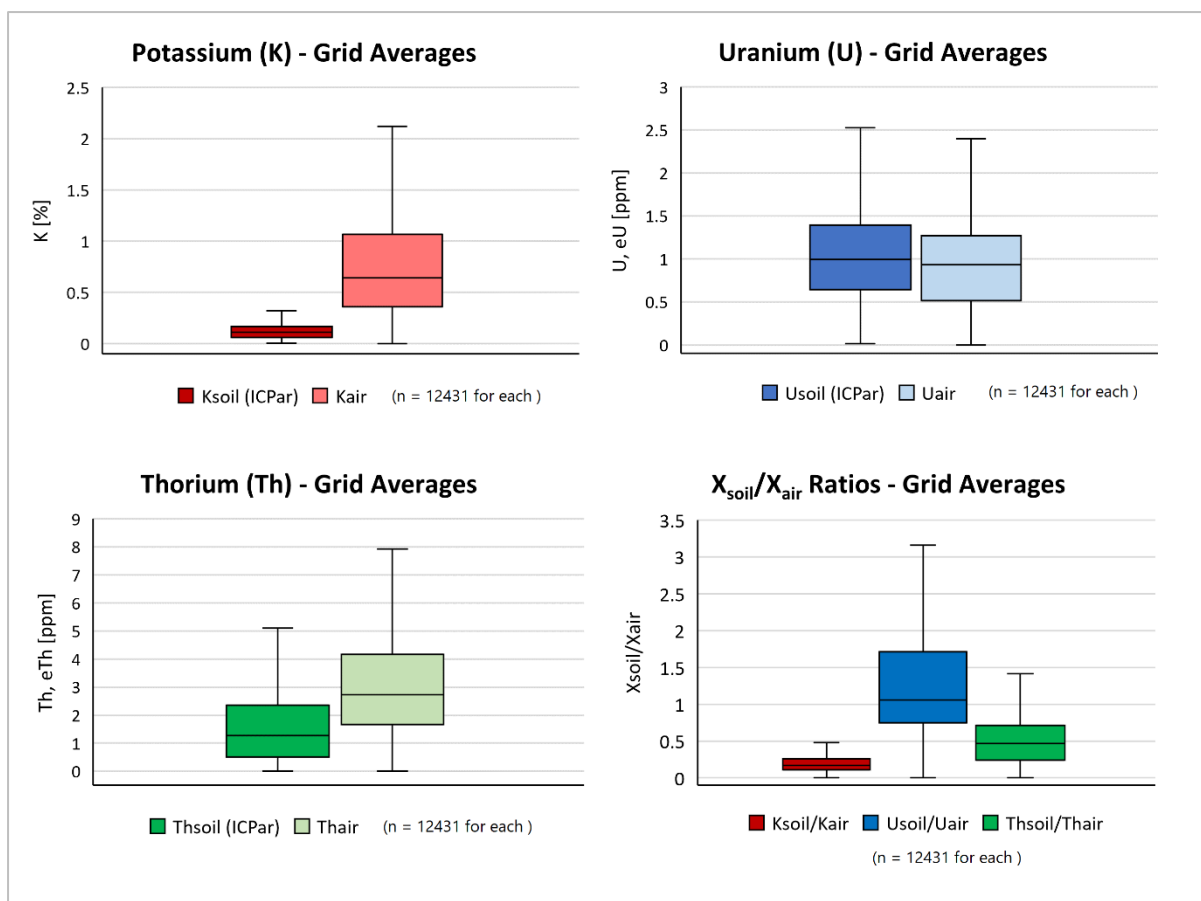


Figure 25: Boxplots of soil (ICPar) and radiometric concentrations of K, U and Th and ratios of soil:air concentrations (X_{soil}/X_{air}).

Table 7: Summary statistics for soil (ICPar) and radiometric K, U and Th concentrations based on 4km² grid averages across initial study area; no outliers removed.

	K_{soil} [%]	U_{soil} [mg/kg]	Th_{soil} [mg/kg]	K_{air} [%]	U_{air} [ppm]	Th_{air} [ppm]
Sample size	12431	12431	12431	12431	12431	12431
Median	0.110	0.995	1.279	0.641	0.934	2.726
Q1	0.060	0.640	0.504	0.360	0.516	1.671
Q3	0.165	1.395	2.350	1.066	1.271	4.174
IQR	0.105	0.755	1.846	0.706	0.755	2.503
Maximum	0.560	109.000	24.000	2.807	7.110	26.530
Minimum	0.005	0.013	0.000	0.000	0.000	0.000

Table 8: Median soil:air ratios for all 4km² grid averages (initial study area).

K_{soil}/K_{air}	U_{soil}/U_{air}	Th_{soil}/Th_{air}
0.172	1.065	0.469

Pointwise comparison of the two datasets (averaged to 4 km² grids) reveals a relationship between soil and airborne concentrations that varies from element to element. The median soil:air ratio is approximately 1:1 for uranium, however the wide interquartile range suggests that this ratio varies



quite considerably across the study area and is likely affected by soil point anomalies (figure 21) causing the positive skew and range of high outlying values in figure A.1 (U_{soil}). K_{soil} concentrations are consistently lower than K_{air} by a factor of almost six, while Th_{soil} is on average half of Th_{air} .

6.1.2. Geochemical Domains

To investigate whether the geochemistry of the underlying bedrock and subsoil influences the relationship between soil and airborne radioelement concentrations the data were classified by Geochemical Domain (Glennon *et al.* 2020) (see figure 16). As this information is only available for the R.o.I., the data for N.I. were excluded from this analysis. The remaining data ($n = 8955$) are summarised in table 9.

Table 9: Median soil and airborne concentrations and *soil:air* ratios for K, U and Th in each Geochemical Domain.

	<i>All</i>	<i>Domain 1</i>	<i>Domain 2</i>	<i>Domain 3</i>	<i>Domain 4</i>	<i>Domain 5</i>	<i>Domain 6</i>	<i>Domain 7</i>
Sample size	8955	497	4000	403	363	1395	604	1693
K_{soil} [%]	0.11	0.09	0.11	0.09	0.10	0.17	0.05	0.07
U_{soil} [mg/kg]	1.01	1.19	1.12	0.88	0.95	1.02	0.55	0.56
Th_{soil} [mg/kg]	1.06	1.70	1.00	1.11	0.82	2.50	0.30	0.70
K_{air} [%]	0.597	0.384	0.481	0.635	0.584	1.168	0.792	0.657
U_{air} [ppm]	0.992	1.076	1.120	0.829	0.879	1.200	0.683	0.503
Th_{air} [ppm]	2.604	2.503	2.306	2.557	2.372	5.120	2.661	2.413
$K_{\text{soil}}/K_{\text{air}}$	0.184	0.23	0.23	0.14	0.17	0.15	0.06	0.12
$U_{\text{soil}}/U_{\text{air}}$	1.018	1.11	1.00	1.07	1.08	0.93	0.80	1.11
$Th_{\text{soil}}/Th_{\text{air}}$	0.407	0.68	0.43	0.43	0.34	0.49	0.11	0.29

As expected, individual radioelement concentrations vary with the predominant geochemical signature of the parent material (boxplots shown in figures A.2-A.7), however one must consider differences in sample size, land use, topography, soil type and the variation in *Aqua Regia* extraction rates expected between domains when interpreting these results. The boxplots below (figures 26-28) illustrate how the relationship between soil and radiometric concentrations also varies between domains. Many factors could be influencing this, including the extent of highly attenuating, non-radioactive overburden, the occurrence of bedrock outcrops, measurement errors associated with low concentrations, and the phases in which the radioelements occur which influences their recovery rate in *Aqua Regia*.



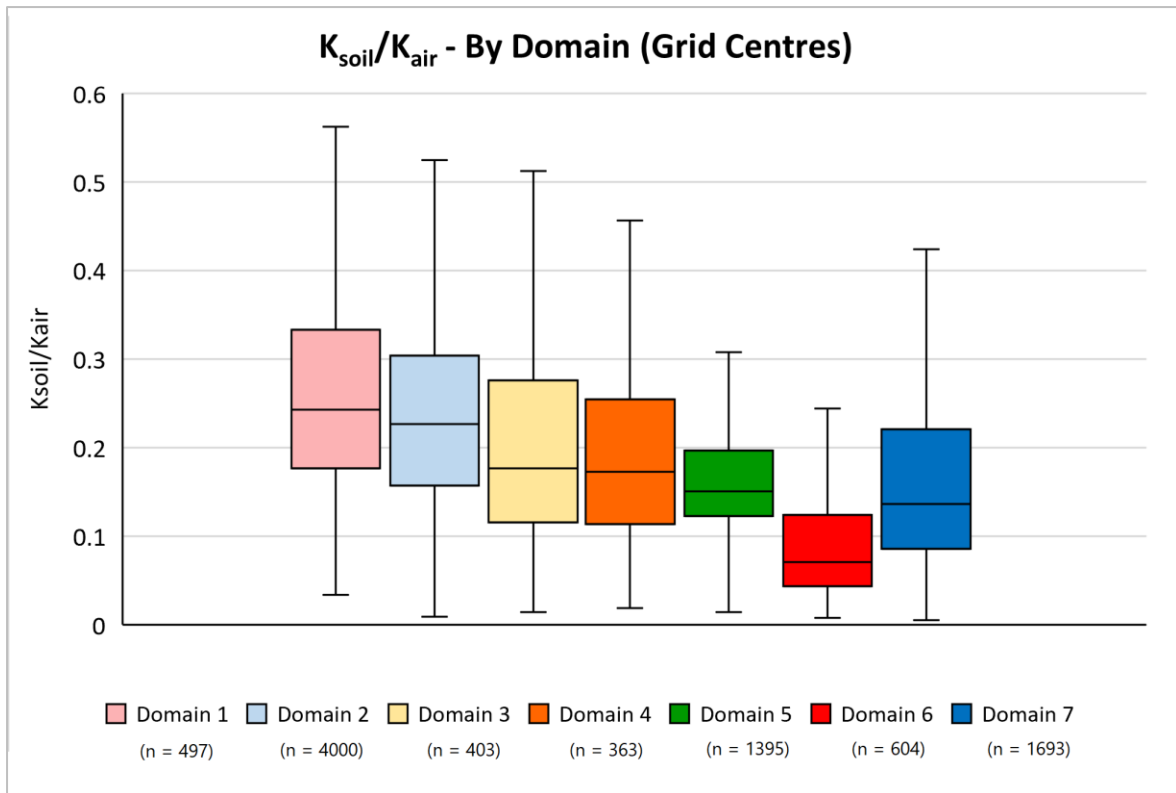


Figure 26: Boxplots of K_{soil}/K_{air} by Geochemical Domain (4 km^2 grid averages) with outliers hidden for clarity.

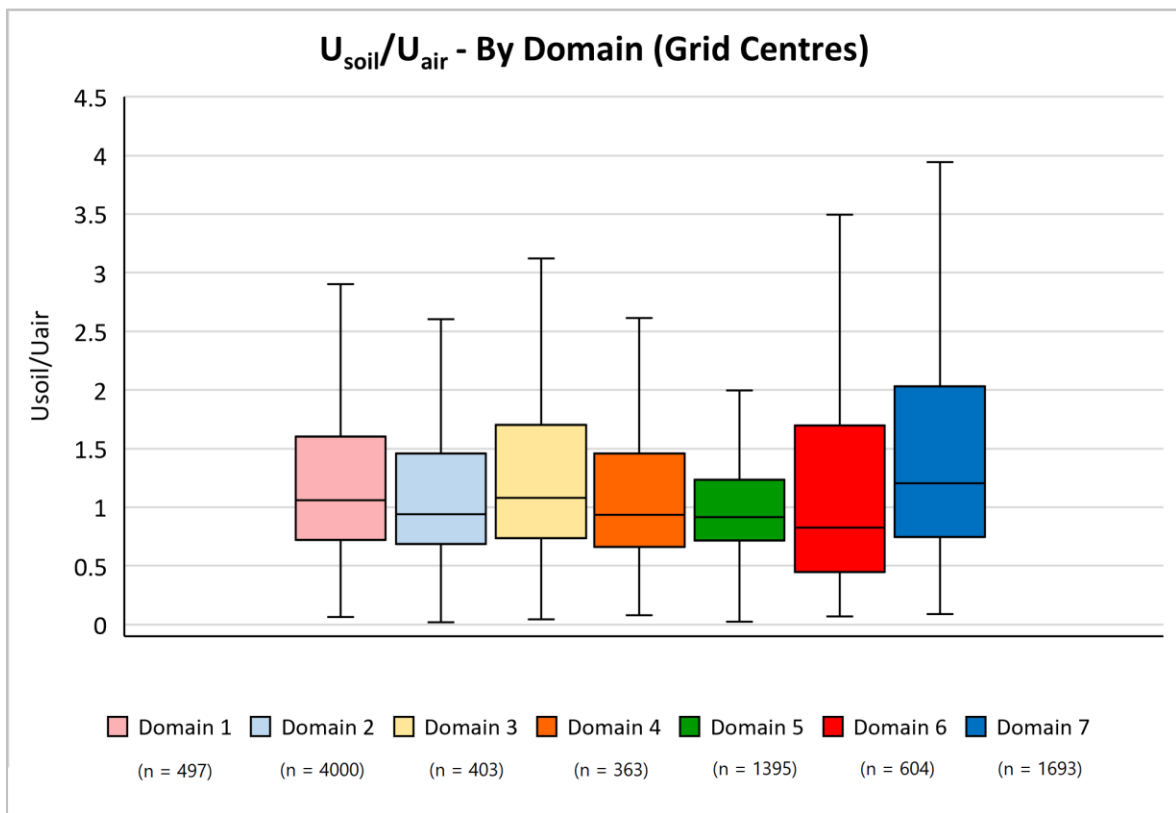


Figure 27: Boxplots of U_{soil}/U_{air} by Geochemical Domain (4 km^2 grid averages) with outliers hidden for clarity.



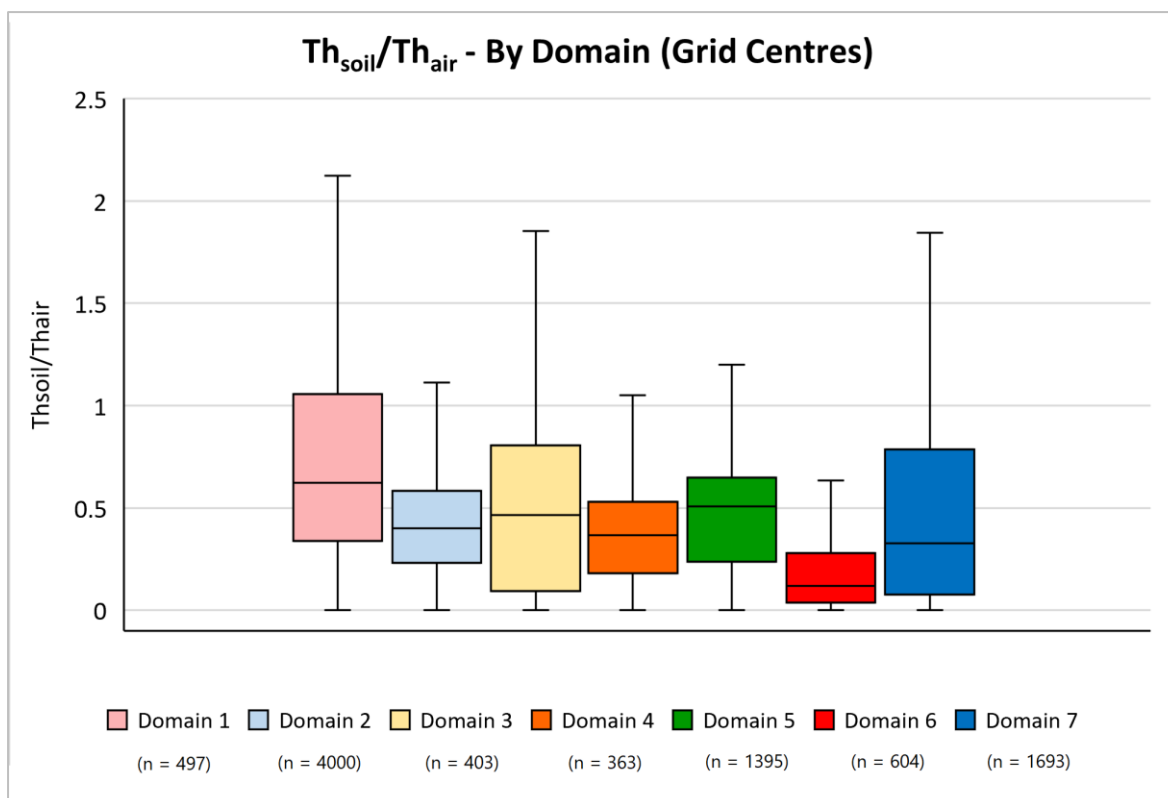


Figure 28: Boxplots of Th_{soil}/Th_{air} by Geochemical Domain (4 km² grid averages) with outliers hidden for clarity.

6.1.3. Peat

Multiple studies have noted the increased attenuation of gamma-rays in wet peat (Beamish 2014, 2013, 2015; Beamish and Farr 2013) so a subset of the data intersecting areas of mapped peat (Teagasc Soils database) was investigated. Figure 8 shows how mapped peat extents are patchy in places, so to ensure that radioelement data classified as “peat” were actually collected from peat, the average soil and radiometric values in each 4 km² grid were replaced with soil concentrations measured at actual sample sites joined with the closest radiometric point. The average values did not change substantially (table 10) but these data pairs are likely to be more representative when grouping the data spatially, and better correlated where point anomalies exist. The median join distance was 53.15 m, with several large outliers where radiometric data were removed due to negative count rates.

Table 10: Effect of comparing closest soil and radiometric pairs instead of grid averages on median ratios.

	K_{soil}/K_{air}	U_{soil}/U_{air}	Th_{soil}/Th_{air}
4km ² grid centres	0.184	1.018	0.407
Closest pair	0.181	1	0.393



N.I. was excluded from subsequent analyses because the original soil sample locations were missing and many of the databases used to classify the data do not cover N.I. (see maps in section 4).

Table 11 shows the effect of peat on radioelement concentrations and the soil-airborne relationship for the G1, G3 and G5 blocks. For all three elements the median airborne values decrease greatly over peat. Median soil concentrations are also reduced significantly, so the relative change in each governs how the *soil:air* ratio is affected. In the case of K and U, the overall ratio between soil and radiometric concentrations is higher in areas of peat, whereas for Th this ratio is lower as Th_{soil} appears to decrease to a greater extent.

It is noted that the low mineral content of peat soils and the low analyte masses (remaining after LOI analysis) lead to significant errors associated with the determination of radioelement concentrations in such materials.

Table 11: Median soil and radiometric K, U and Th concentrations and ratios for areas with and without peat (Teagasc) (closest soil/radiometric pairs; excluding Northern Ireland).

	K_{soil} [%]	K_{air} [%]	K_{soil}/K_{air}	U_{soil} [mg/kg]	U_{air} [ppm]	U_{soil}/U_{air}	Th_{soil} [mg/kg]	Th_{air} [ppm]	Th_{soil}/Th_{air}
Without peat (n = 6816)	0.13	0.76	0.17	1.10	1.20	0.92	1.36	3.34	0.41
Peat only (n = 2588)	0.04	0.16	0.25	0.313	0.22	1.42	0.130	0.75	0.17

6.1.4. XRFS vs ICP_{ar}

Geochemical data for the G1, G3 and G6 blocks include multi-element analysis by XRFS. Concentrations measured by XRFS are considered ‘total,’ as the method uses solid samples and does not depend on extraction of elements from soil matrices. Figures 29-31 show how total soil concentrations of K, U and Th compare to those measured by ICP_{ar} for the same sample. The XRFS values are consistently higher than the corresponding ICP_{ar} values for each element and interestingly the areas in which the ICP_{ar} concentration is closest to the ‘true’ concentration appear to coincide with areas of peat in the case of potassium (figure 32), whereas the opposite effect is observed for U and to some extent Th. Kissler (2005) notes that *Aqua Regia* dissolves organic matrices to a large extent but does not effectively extract metals from refractory minerals such as silicates. Regions in which potassium occurs predominantly in K-feldspars and refractory clay minerals therefore exhibit much higher K_{soil} concentrations when analysed by XRFS, as can be seen in figure 29 where notable XRFS/ ICP_{ar} highs coincide with granitic and certain metamorphic and clastic sedimentary units.



A similar distribution might be expected for U and Th as these elements are typically found in resistant accessory minerals such as zircon, monazite and apatite (Cinelli *et al.* 2019). Since very low U and Th concentrations are found in peat to begin with, the XRFs/ICP_{ar} highs observed are likely due to the lower LLDs of the ICP_{ar} analyses compared to XRFs as outlined in table 3.

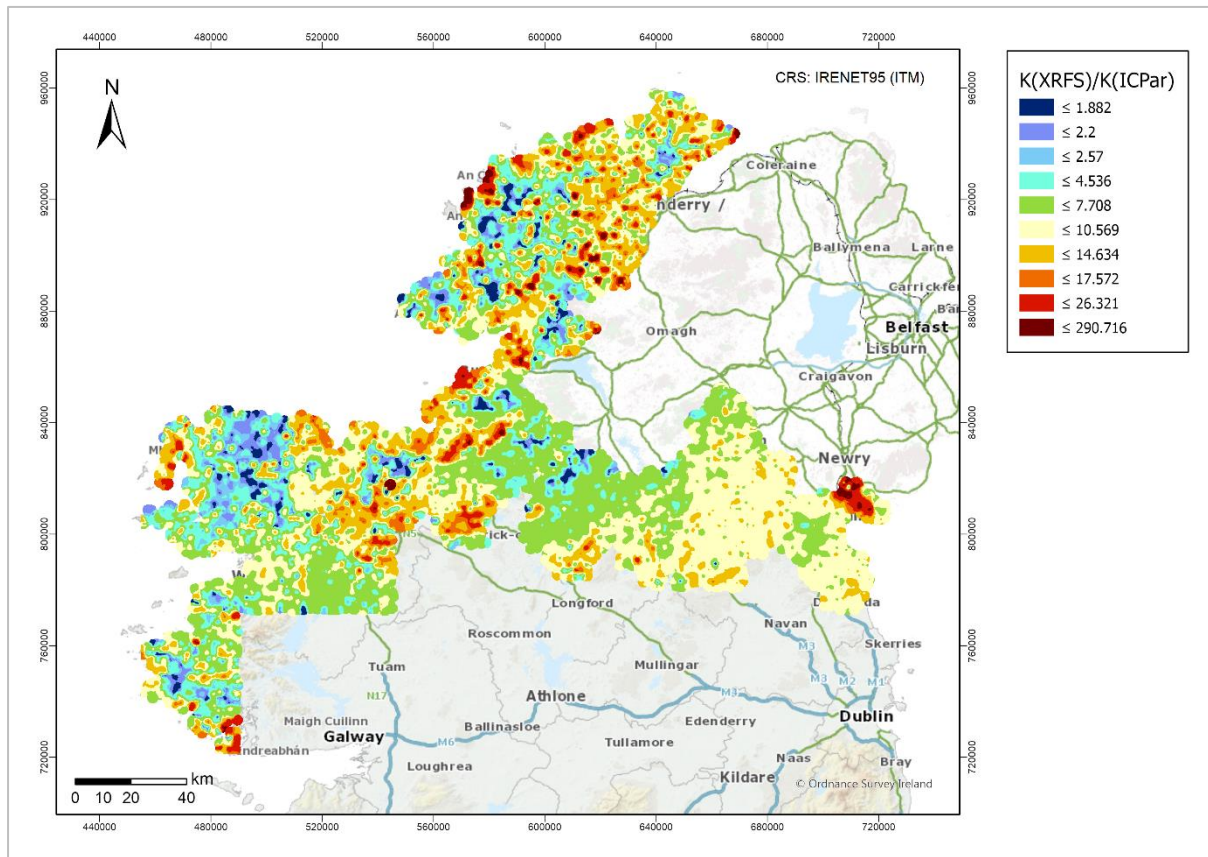


Figure 29: Ratio of XRFs to ICP_{ar} soil concentrations for potassium (G1 and G3 blocks).



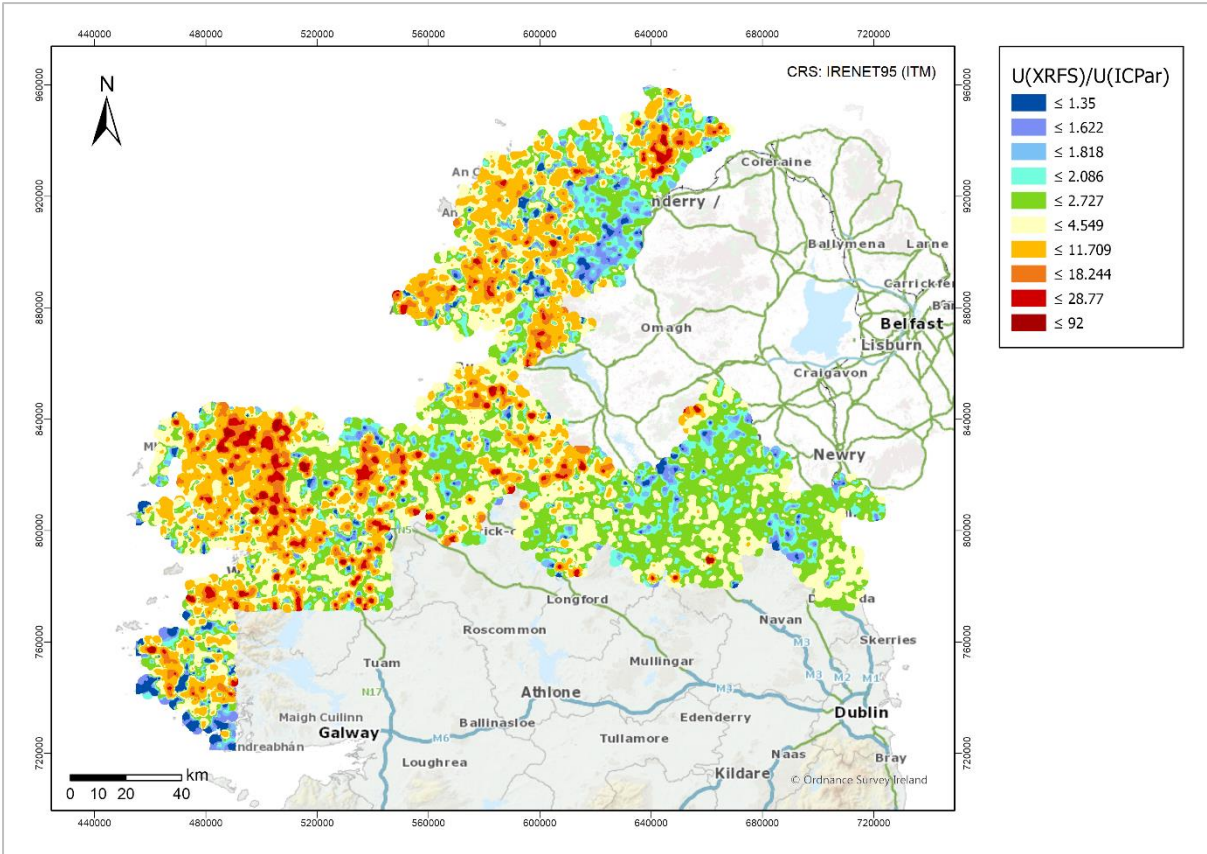


Figure 30: Ratio of XRFs to ICP_{ar} soil concentrations for uranium (G1 and G3 blocks).

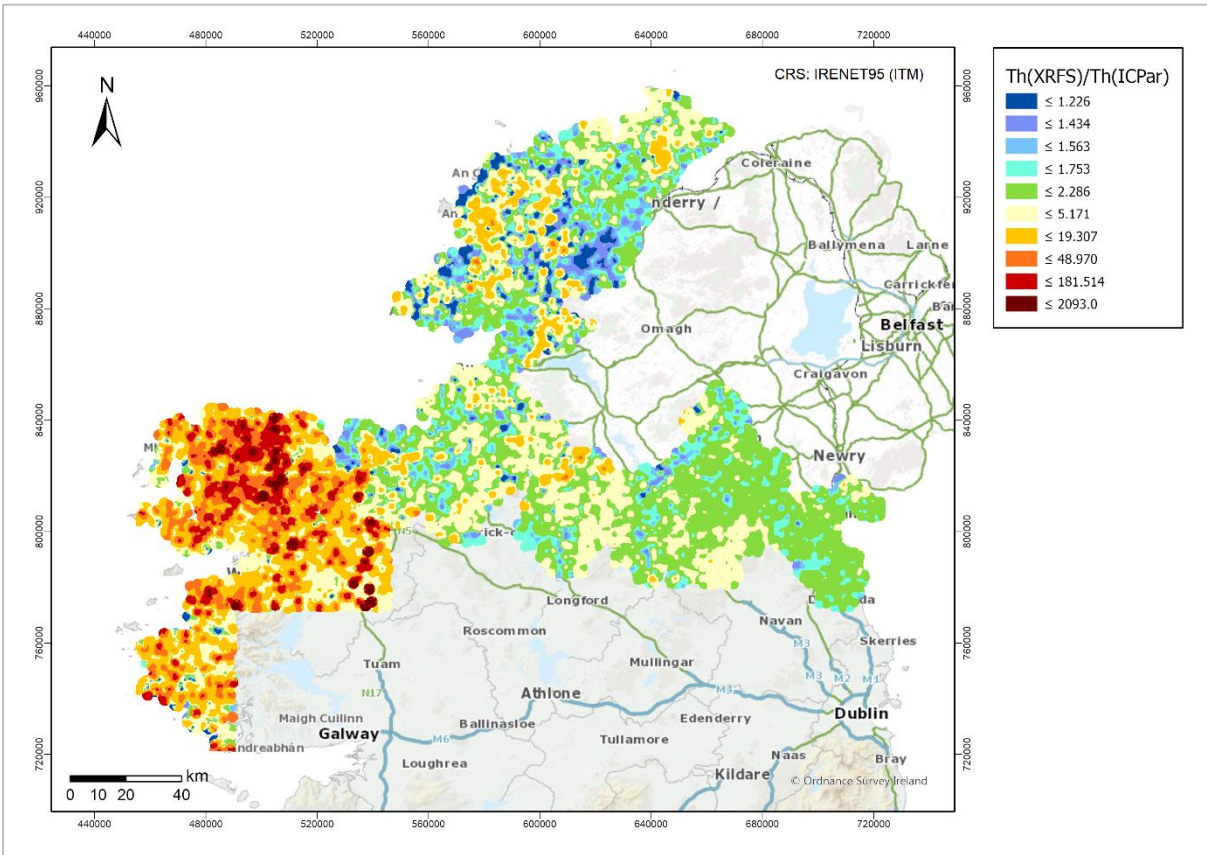


Figure 31: Ratio of XRFs to ICP_{ar} soil concentrations for thorium (G1 and G3 blocks).



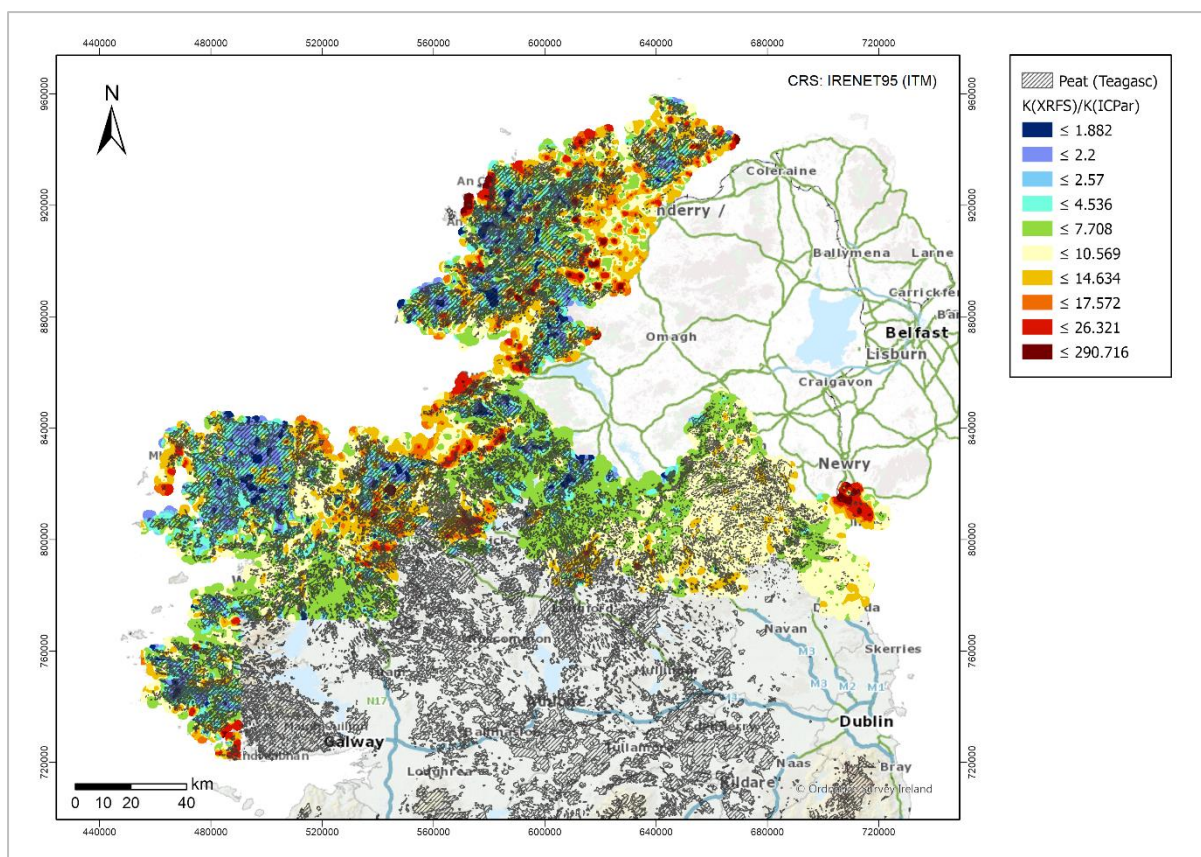


Figure 32: Ratio of XRFS to ICP_{ar} soil concentrations for potassium with superimposed areas of mapped peat (Teagasc soils).

Histograms of XRFS/ICP_{ar} ratios (figures A.8-A.10) help to further understand the performance of *Aqua Regia*. The long high-value tails in the positively skewed distributions of XRFS/ICP_{ar} for U and Th are likely due to differences in method LLDs, but in both cases the spread of XRFS/ICP_{ar} values from < 1 to 6 shows how the extractability of the element depends on the phase in which it is present. This is in part related to how weathered the soil is, as U and Th ions released by weathering from accessory mineral phases are readily absorbed by clay minerals and organic matter (Cinelli *et al.* 2019) which may be less resistant to *Aqua Regia* digestion (Kisser 2005). This continuum of XRFS/ICP_{ar} ratios is also observed in the second peak of the bimodal distribution for potassium (figure A.8). Here, the lower values represent 'easily extractable' K, present in organic complexes for example, while the higher values relate to K present in refractory mineral matrices.

The *Aqua Regia* extraction rate is calculated according to equation 7:

$$\% \text{ Extraction by aqua regia} = \left(\frac{X_{ICPar} [\% \text{ or ppm}]}{X_{XRFS} [\% \text{ or ppm}]} \right) \times 100, \quad (7)$$

where X = K, U or Th.



Table 12: Average (mean) Aqua Regia extraction rates by domain [calculated as $100*(X_{ICP}/X_{XRFS})$].

<i>Domain</i>	1	2	3	4	5	6	7
Sample size	462	812	396	135	1026	371	1710
K	22.3%	20.8%	22.6%	14.3%	15.1%	26.8%	23.9%
U	34.2%	36.5%	33.5%	33.8%	41.2%	40.9%	36.9%
Th	46.2%	37.3%	35.4%	33.1%	44.1%	47.4%	43.7%

Table 12 shows the average extraction rates for each geochemical domain. Based on lack of consistent or easily predicted rates across the study area, the ICP_{ar} concentrations are considered an unsuitable database with which to accurately compare the radiometric data.

6.2. XRFS Soil and Radiometric Data

6.2.1. Joining XRFS geochemical data and radiometric data

Table 13 shows the median join distance (soil-radiometric) for the new (n = 5609) study area extent, which is higher than that of the original study area because of the inclusion of the Galway and Dublin periurban soil data, the latter covering a small area that is not included in the radiometric dataset. The join distances here are significantly higher so it is possible that the concentrations for a given pair (soil, airborne) could reflect different geological or pedological settings.

Table 13: Average soil – radiometric point join distances for new (G1, G3, G6) study area.

<i>Survey block</i>	<i>Median join distance (m)</i>
G1, G3, G6	76.33
G6 Dublin only (n = 408)	2677.53

6.2.2. Comparing radioelement concentrations

Data are summarised in tables 14 and 15 and illustrated in figure 33.

Table 14: Soil (XRFS) and radiometric concentration summaries for new (G1, G3, G6) study area.

	<i>Ksoil [%]</i>	<i>Usoil [mg/kg]</i>	<i>Thsoil [mg/kg]</i>	<i>Kair [%]</i>	<i>Uair [ppm]</i>	<i>Thair [ppm]</i>
Sample size	5609	5609	5609	5609	5609	5609
Median	0.96	2.50	4.20	0.73	0.91	3.01
Q1	0.35	1.90	1.40	0.31	0.33	1.42
Q3	1.50	3.10	6.40	1.17	1.32	4.73
IQR	1.15	1.20	5.00	0.86	0.99	3.31
Minimum	0.004	0.1	0.1	0	0	0
Maximum	3.57	100.10	22.00	3.56	6.24	17.76



Table 15: Median soil/air ratios using XRFs data in new study area (n=5609).

K_{soil}/K_{air}	U_{soil}/U_{air}	Th_{soil}/Th_{air}
1.32	2.75	1.40

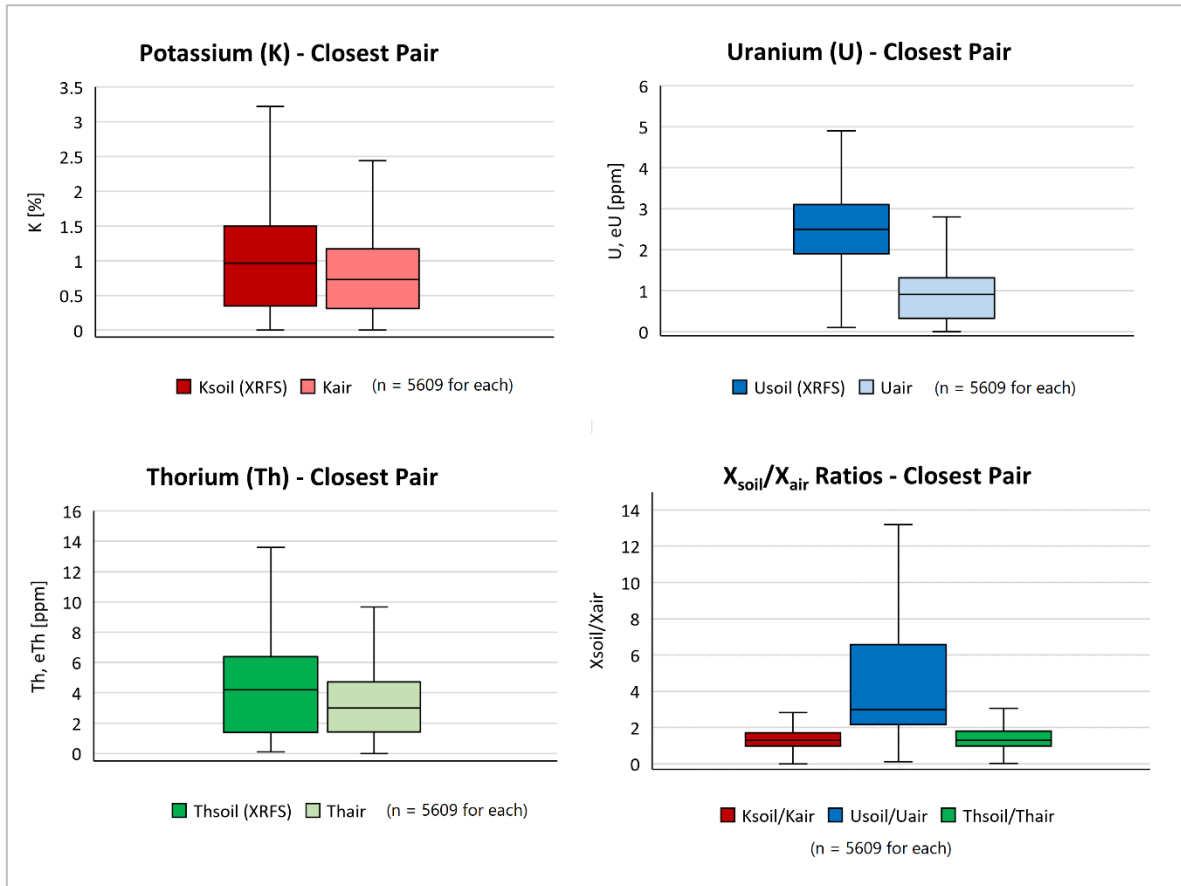


Figure 33: Boxplots summaries of soil (XRFS) and radiometric K, U and Th concentrations and ratios for new study area.

Comparing radiometric and XRFS soil data instead of ICP_{ar}, the measured soil concentrations are generally higher than the corresponding radiometric measurements. Typical *soil:air* ratios vary from around 1:1 to 2:1 in the case of K and Th but are much more variable for U, with median $U_{soil} > 2.5$ times that of U_{air} , which could be due to radon diffusion to the atmosphere resulting in lower ^{214}Bi counts that don't accurately reflect the concentration of uranium in the soil (Cinelli *et al.* 2017).

Interpolated maps (figures 34-39) show very similar distributions of soil and airborne highs and lows, this time without the effect of poor *Aqua Regia* extraction which is particularly evident in figure 34 where the high K_{soil} concentrations over granites in northern Louth mirror those in the radiometric map. Again, in all six maps low radioelement concentrations coincide with mapped peat deposits while notable highs are found over Dalradian metasediments and felsic intrusives. Moderate-to-high



K, U and Th can also be seen over Longford-Down inlier and both soil and radiometric maps of K and Th clearly show its NE-SW orientation and the lower radioelement concentrations of neighbouring clastic sediments. Both U_{soil} and U_{air} appear enriched relative to K and Th in the western border region which could be related to outcropping Neoproterozoic schist and gneiss and Namurian sedimentary units which are typically found to contain high U concentrations (Zanin *et al.* 2016).

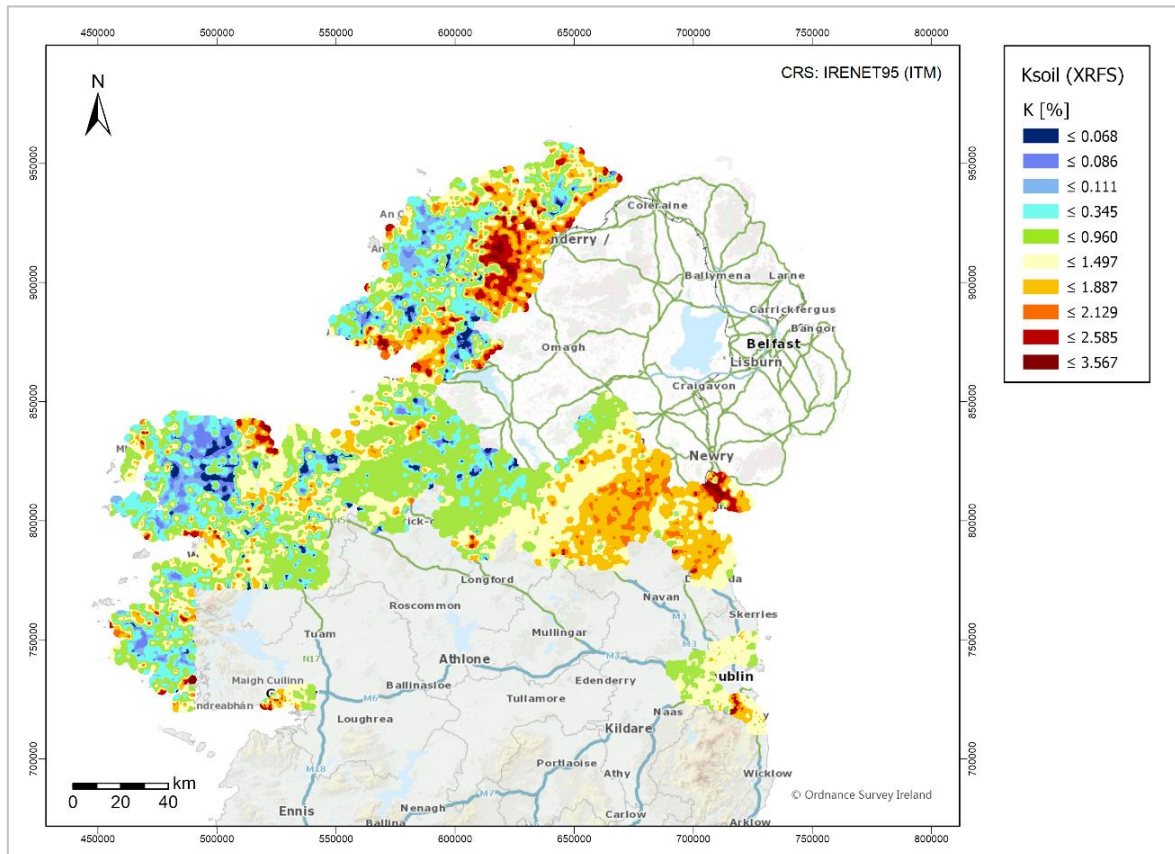


Figure 34: Map of K_{soil} based on concentrations determined by XRFs at original sample locations; new study area (G1, G3, G6).



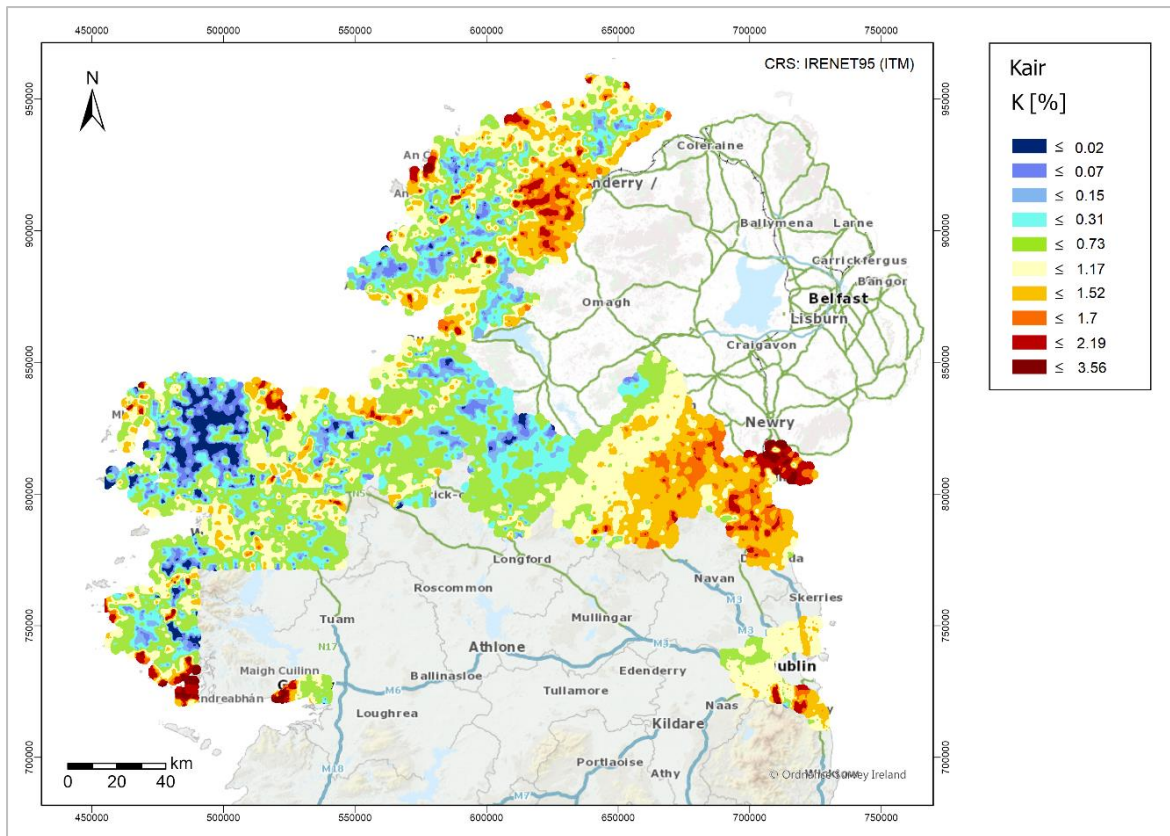


Figure 35: Map of K_{air} based on re-sampled (to match soil sample density) set of points closest to each soil location.

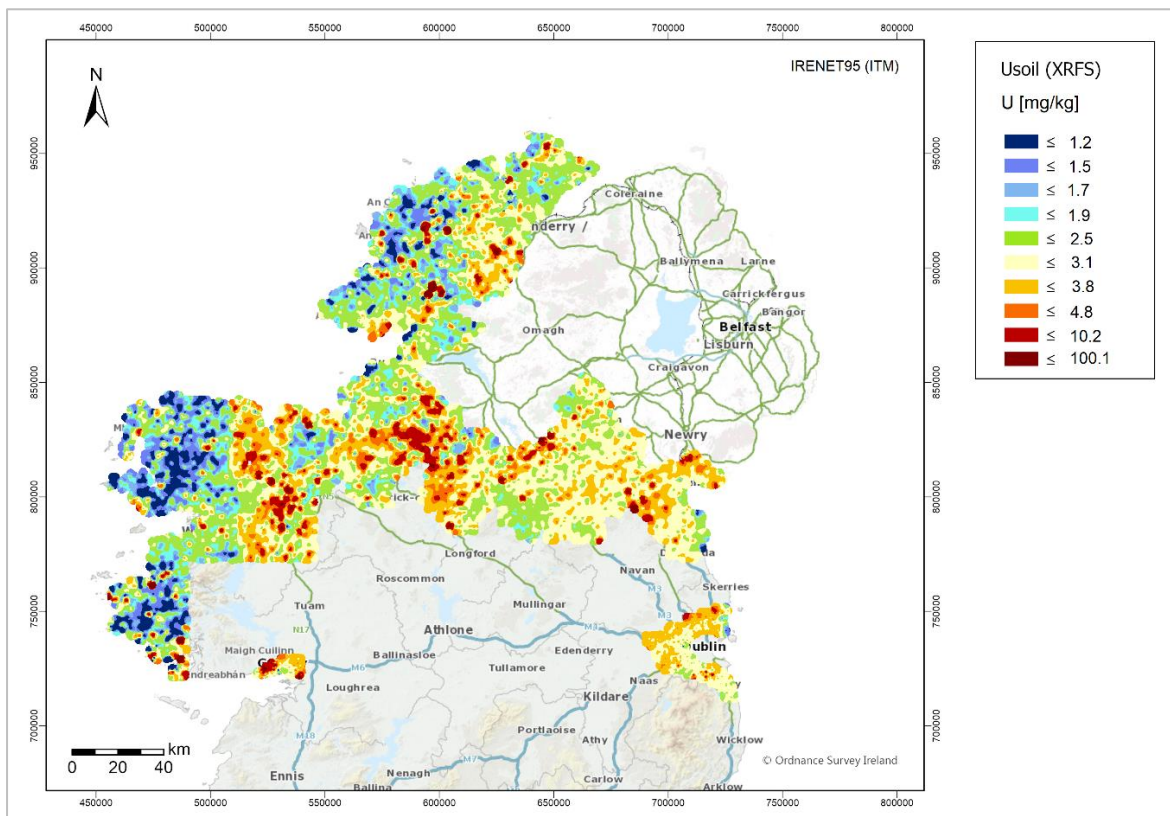


Figure 36: Map of U_{soil} based on concentrations determined by XRFs at original sample locations.



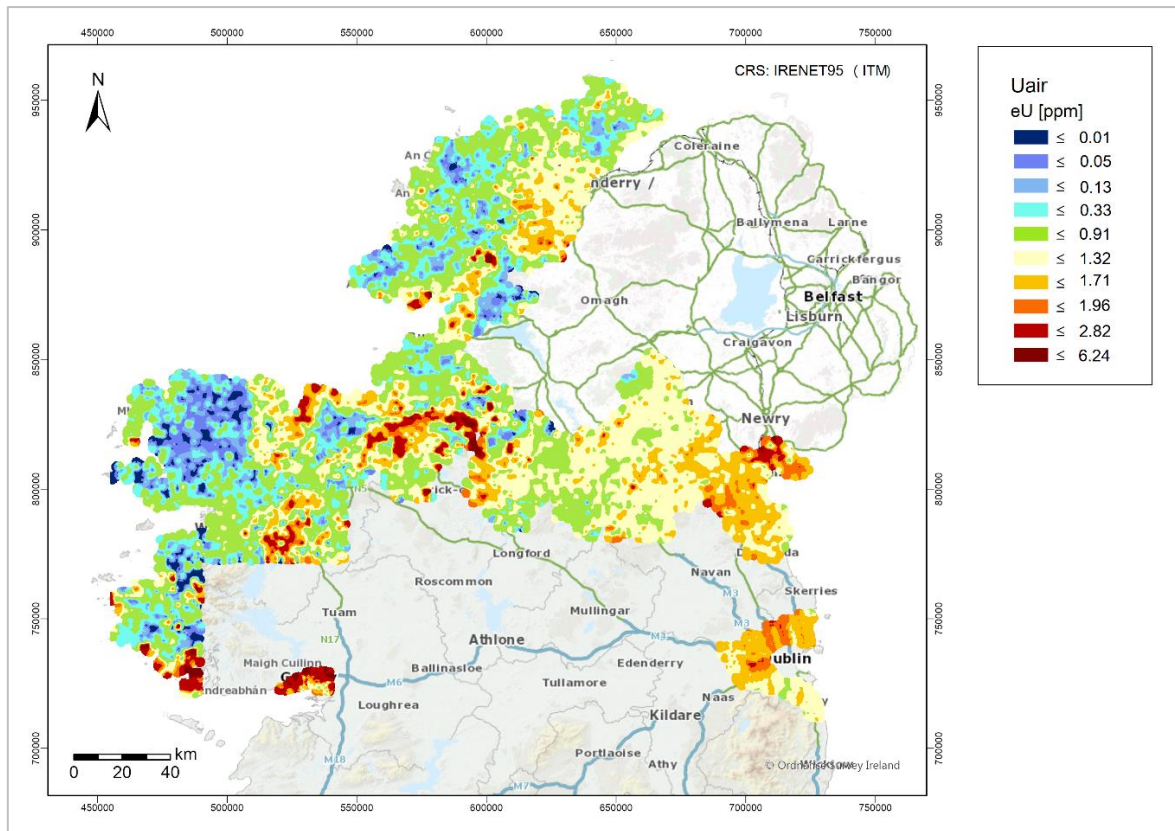


Figure 37: Map of U_{air} based on re-sampled set of points closest to each soil location.

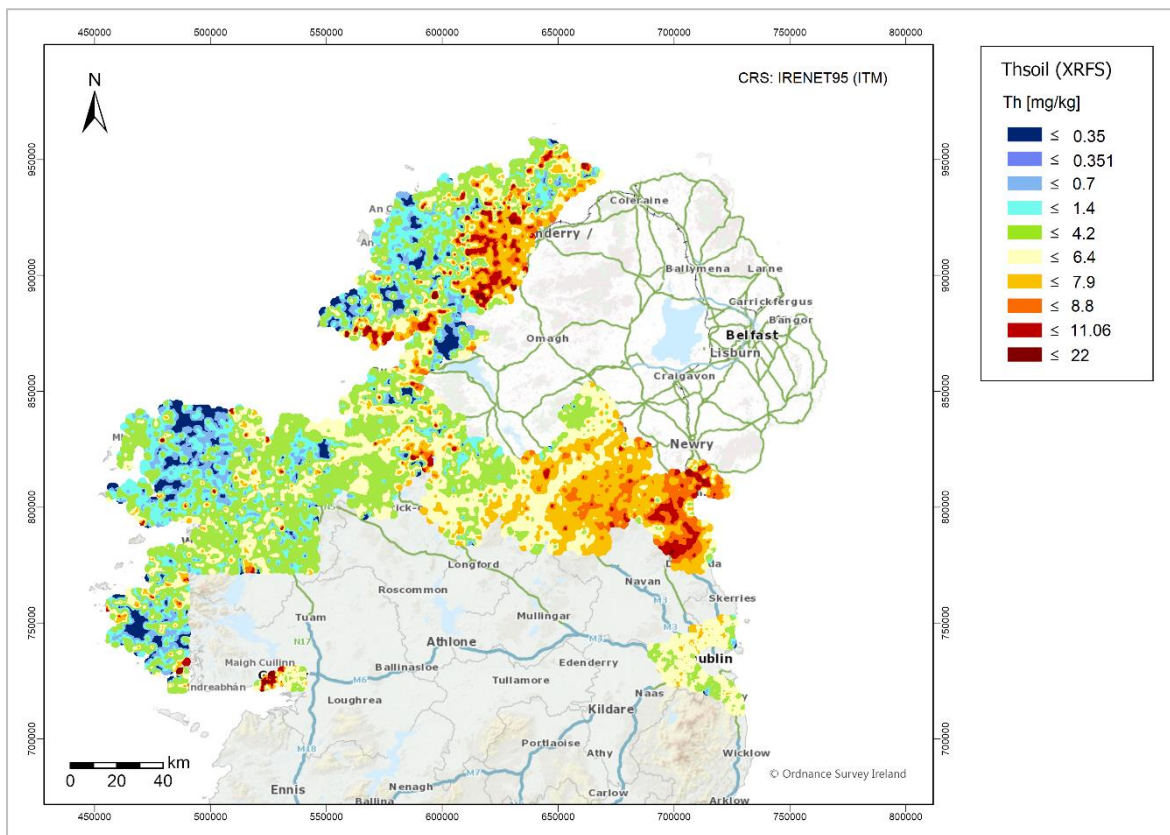


Figure 38: Map of Th_{soil} based on concentrations determined by XRFs at original sample locations.



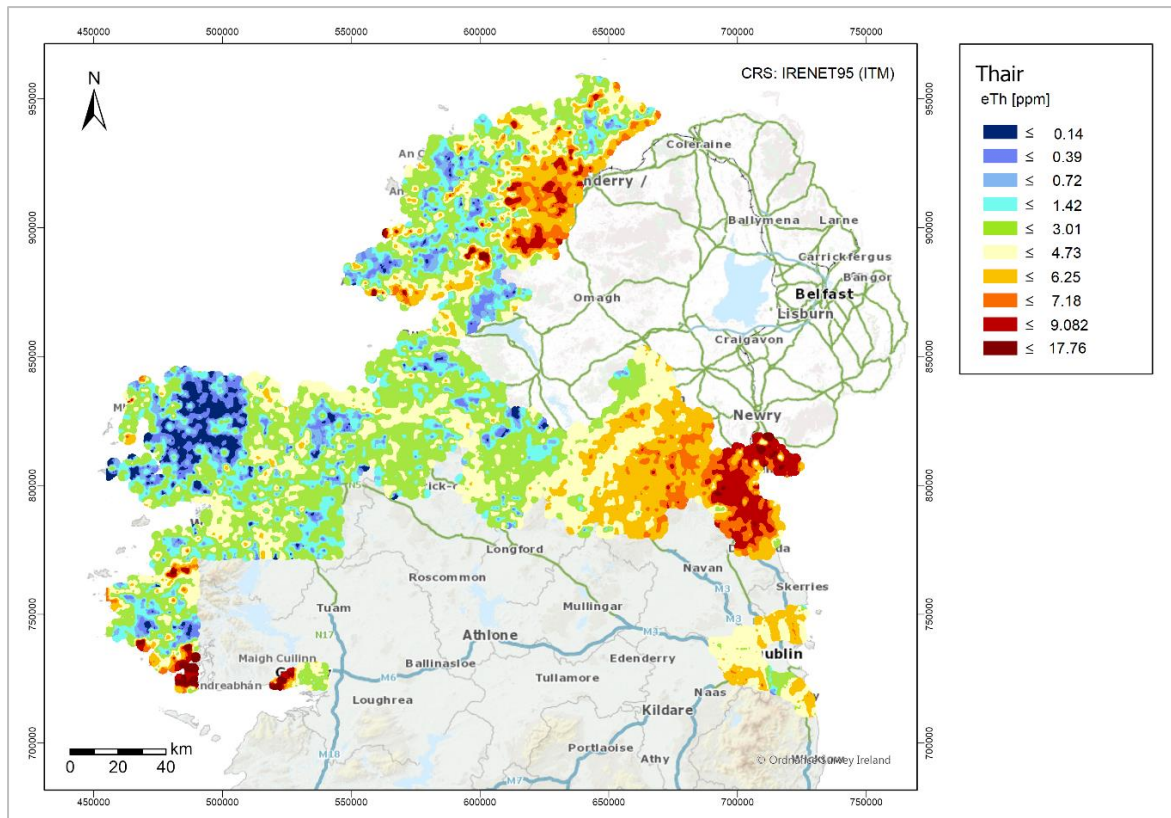


Figure 39: Map of Th_{air} based on re-sampled set of points closest to each soil location.

6.2.3. Ratio maps

Ratio maps of X_{soil}/X_{air} are shown in figures 40-42 and illustrate how the relationship between soil and radiometric K, U and Th varies across the study area despite similarities in their overall distribution patterns (figures 34-39).

The highest ratios observed in all three maps tend to coincide with blanket peat deposits (see figure 43), suggesting that the airborne measurements are affected by the presence of peat to a greater extent than soil measurements, likely due to increased gamma-ray attenuation (Beamish 2014), despite both methods recording their lowest concentrations in these areas (see figures 34-39). There are, however, greater errors associated with these low concentrations and in the case of U and Th, the soil (XRFs) LLDs are 70 and 50 times the lowest reported radiometric concentrations (0.01 ppm) (table 3), respectively. Contrastingly, a number of lows appear to coincide with shallow or outcropping bedrock, particularly in the K and Th maps, most notably in northwest Donegal and southwest Galway. In the case of K and Th, soil concentrations here are generally lower than airborne ones whereas for U ratios in the 5th percentile are still about 1.5.



In both radioelement and ratio maps the distribution of relative highs and lows is very similar for potassium and thorium while uranium is more varied. The low natural abundance of U means that the counts of ^{214}Bi are low compared to ^{40}K and ^{208}Tl and therefore the signal to noise ratio is lower (IAEA 2003). This susceptibility to statistical error along with the effects of radon emanation and disequilibrium in its decay series make radiometric uranium concentrations significantly less reliable than potassium and thorium. The low count rates make eU measurements more sensitive to variations in survey height since the count rate drops off with increasing height above ground level. Additionally, compared to Th, U is much more mobile (recall its hexavalent ion which forms soluble carbonate complexes) (Harmsen and de Haan 1980). Although potassium is also highly mobile its greater average abundance and high concentrations in many felsic igneous rocks and common clay minerals make its overall distribution less sensitive to small variations and point anomalies.

The *soil:air* ratio appears stable in the east of the border region, east Donegal and to a lesser extent around Dublin City and northeast Mayo. These areas are generally free from extensive rock outcrops and peat deposits (figure 43), have well-drained soils (figure 7), flatter terrain, experience less rainfall (figure 11) and have moderate to high radioelement concentrations.

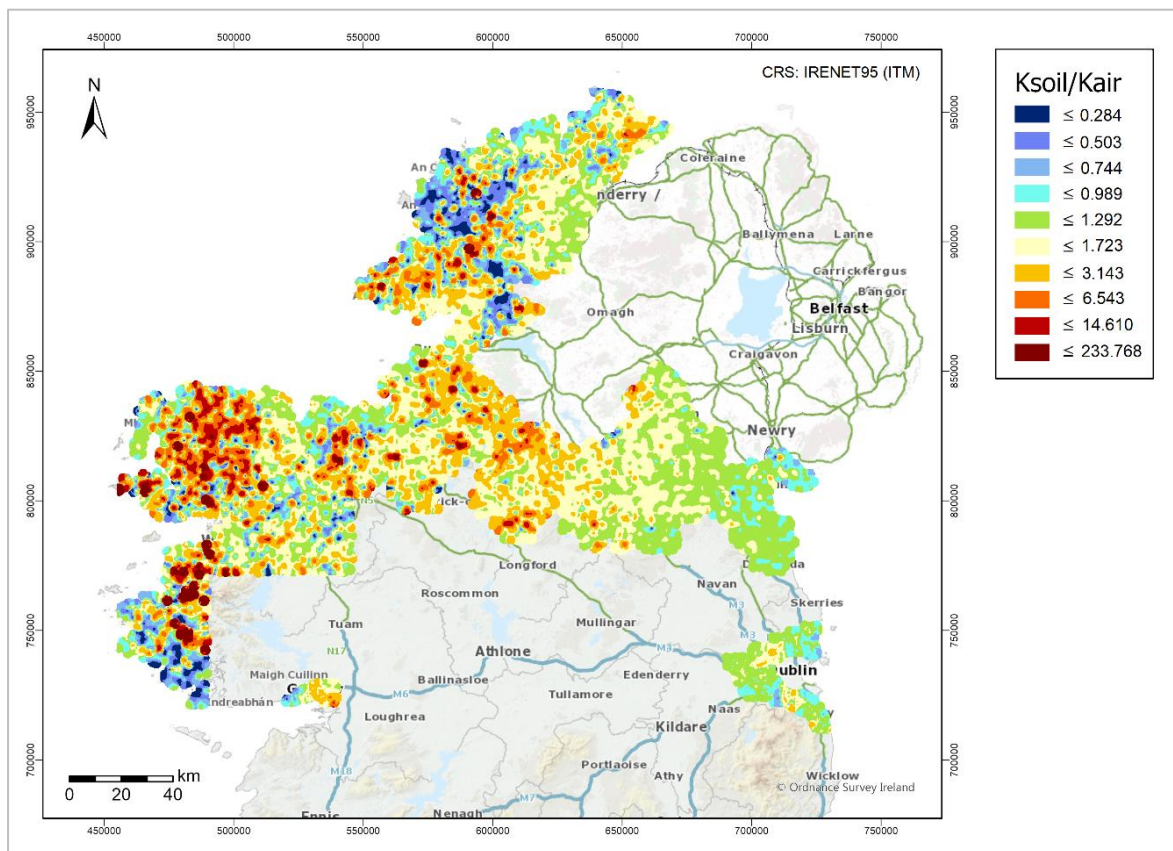


Figure 40: Ratio map of $K_{\text{soil}}/K_{\text{air}}$.



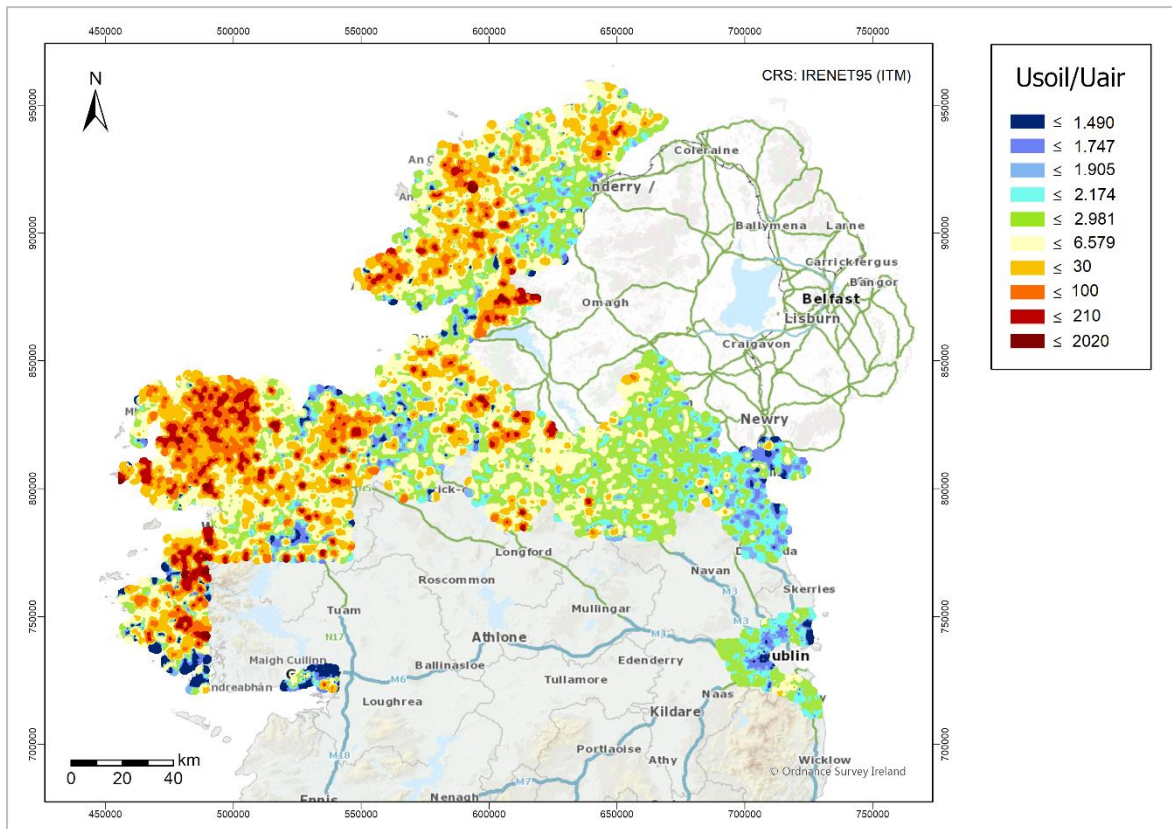


Figure 41: Ratio map of U_{soil}/U_{air} .

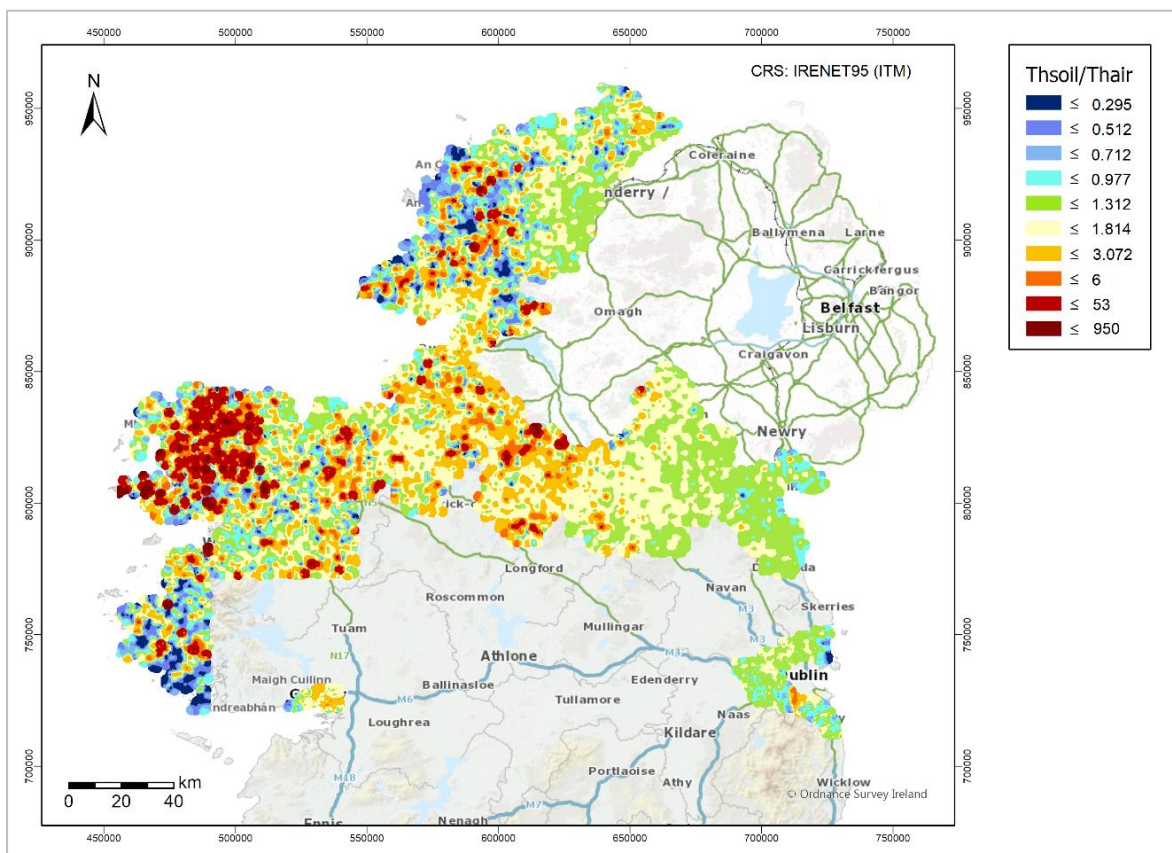


Figure 42: Ratio map of Th_{soil}/Th_{air} .



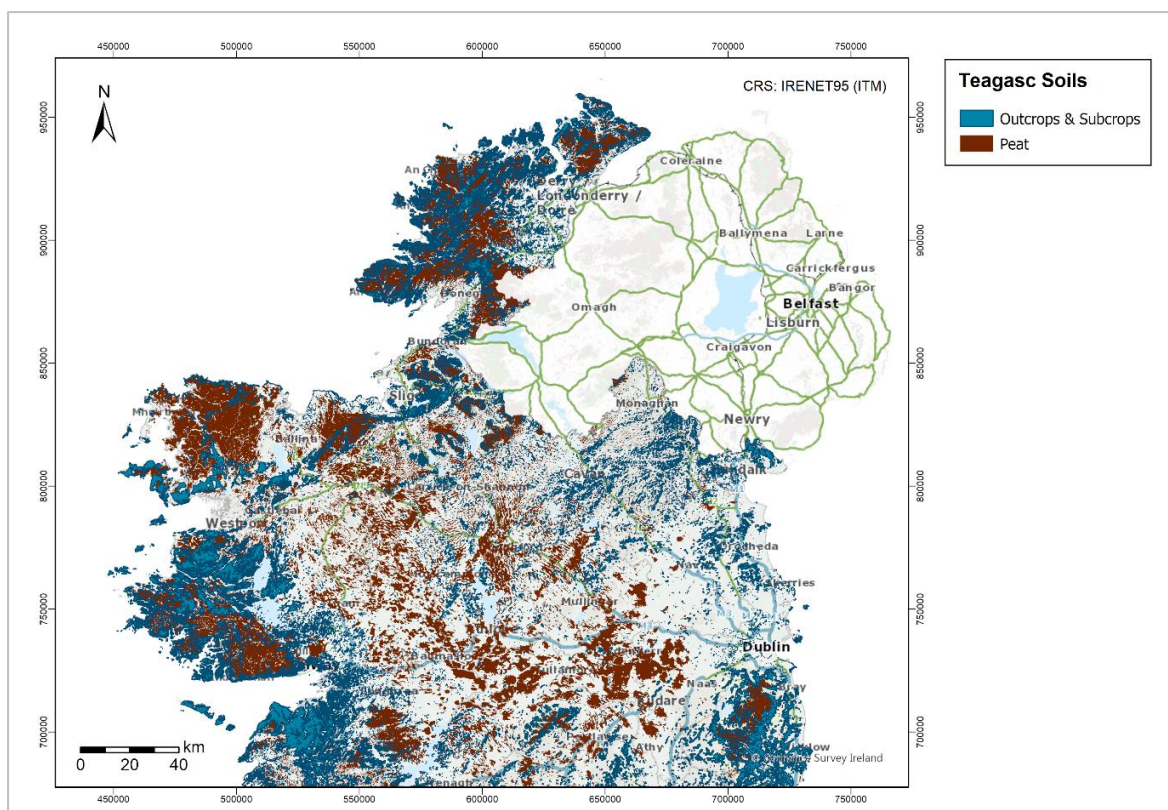


Figure 43: Distribution of peat deposits and outcropping or sub-cropping (<1 mBGL) bedrock (adapted from Teagasc soils).

6.2.4. Geochemical Domains

To investigate geochemical influences on the observed soil–radiometric relationship the data were classified by Geochemical Domain (see figure 16). The results are summarised in table 16, and $X_{\text{soil}}/X_{\text{air}}$ ratio boxplots are presented in figures 44-46. Figure A.11 illustrates the different samples sizes across domains and the spatial distribution of the points in each.



Table 16: Median K, U and Th soil (XRFs) and radiometric concentrations and ratios by Geochemical Domain.

<i>Domain</i>	1	2	3	4	5	6	7
Sample Size	462	1313	396	137	1124	469	1708
K_{soil} [%]	0.570	0.934	0.735	0.934	1.436	0.648	0.744
U_{soil} [mg/kg]	3.0	3.0	2.5	2.2	2.6	2.4	2.1
Th_{soil} [mg/kg]	4.4	4.1	3.7	3.5	6.6	2.0	2.55
K_{air} [%]	0.35	0.68	0.55	0.58	1.18	0.99	0.57
U_{air} [ppm]	0.97	1.28	0.78	0.69	1.09	0.79	0.45
Th_{air} [ppm]	2.39	2.96	2.51	2.53	5.22	2.97	2.16
$K_{\text{soil}}/K_{\text{air}}$	1.63	1.37	1.34	1.61	1.22	0.65	1.31
$U_{\text{soil}}/U_{\text{air}}$	3.09	2.34	3.21	3.18	2.39	3.04	4.67
$Th_{\text{soil}}/Th_{\text{air}}$	1.84	1.39	1.47	1.38	1.26	0.67	1.18

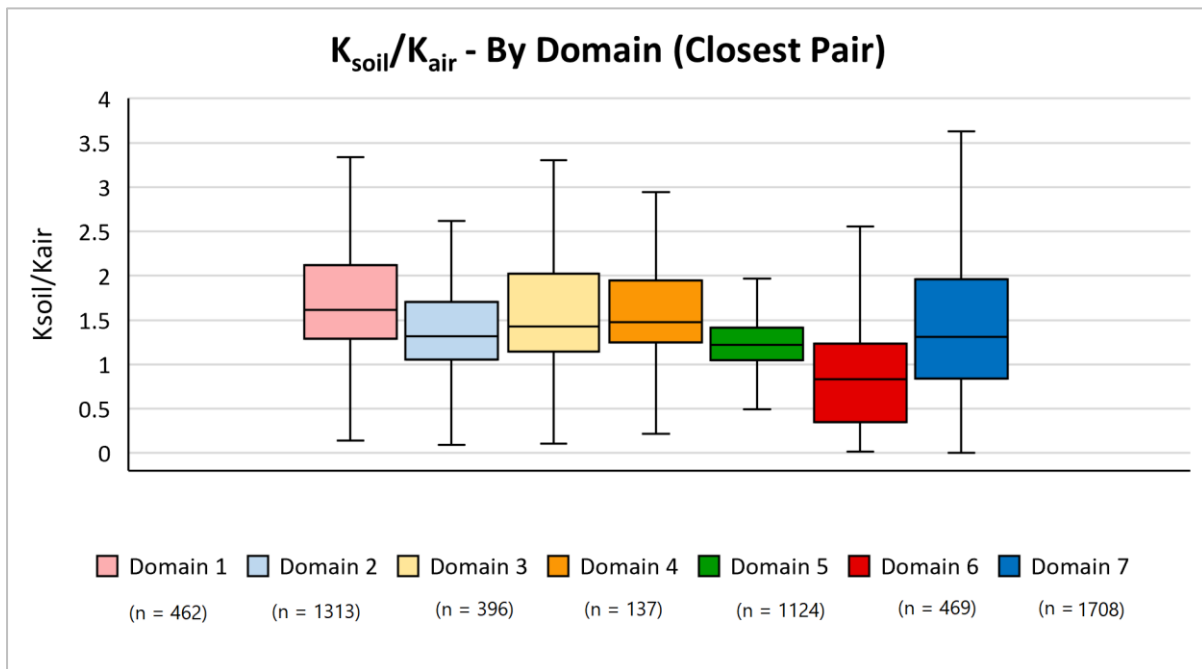


Figure 44: Boxplots of $K_{\text{soil}}/K_{\text{air}}$ by Geochemical Domain (new study area; closest pair), with outliers hidden for clarity.



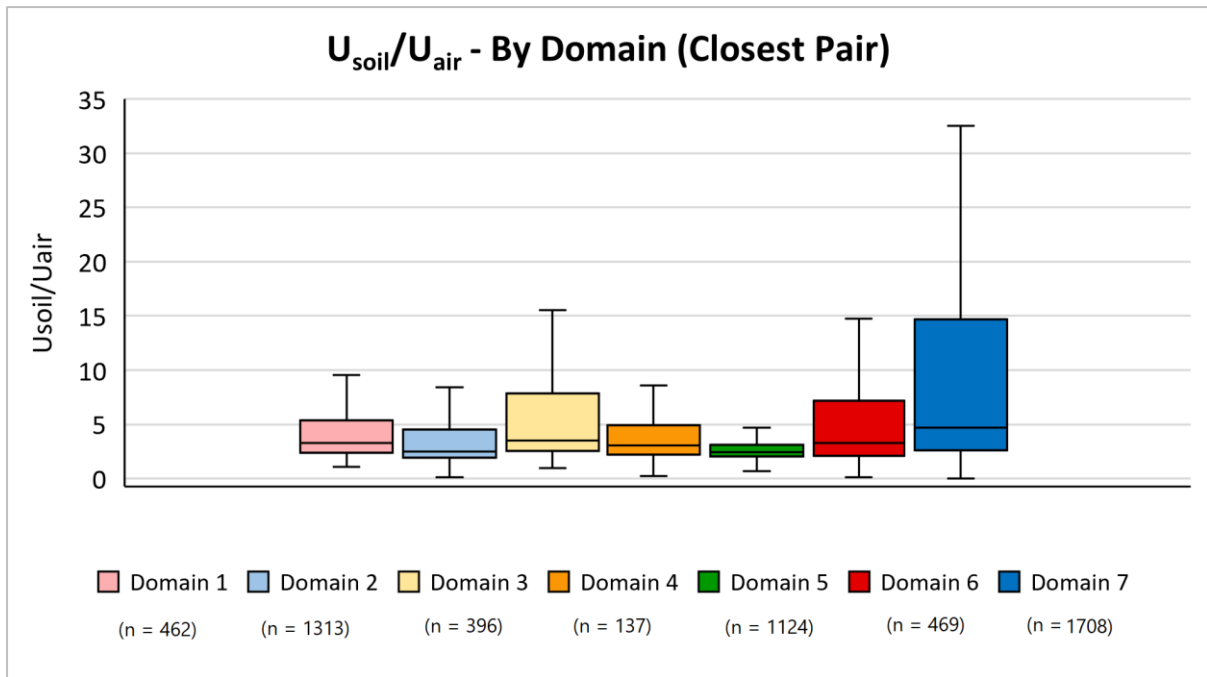


Figure 45: Boxplots of U_{soil}/U_{air} by Geochemical Domain, with outliers hidden for clarity.

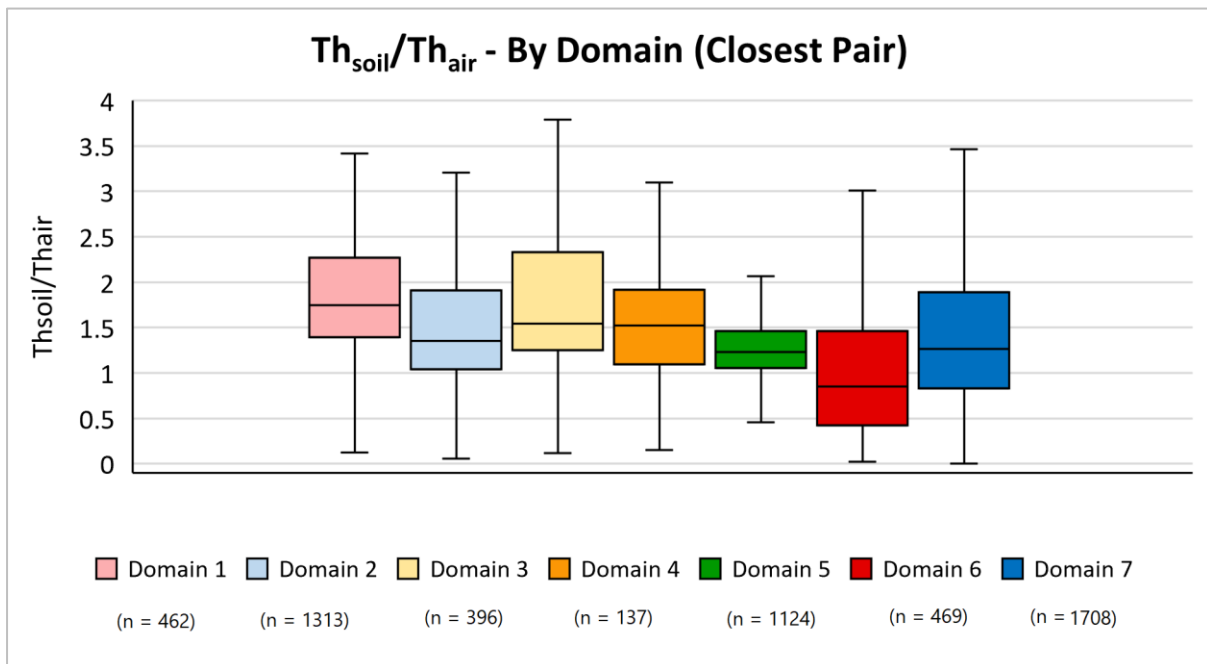


Figure 46: Boxplots of Th_{soil}/Th_{air} by Geochemical Domain, with outliers hidden for clarity.

Soil:air ratios vary somewhat with geochemical signature, with the median in domain 6 (granitic rocks) markedly lower for K and Th, median values closer to one and a smaller range in domain 5 (Lower Palaeozoic rocks) and a wider range of values in domain 7 (metamorphic rocks). Domains 1, 2 and 4, which are predominantly sandstone and shale units, have distinct geochemical signatures and different radioelement concentrations however the soil-radiometric relationship appears consistent.



While the parent geochemical signature may explain some of the variability between soil and airborne measurements, interrelationships exist between domains and other potential influences such as soil texture, peat (domains 6 and 7), uplands and outcropping rock (6 and 7) pastures and cut peat (2) and intensive agriculture (5) which are expected to impact both soil concentrations and the extent of gamma-ray attenuation.

6.2.5. Regression analysis

XY scatterplots of soil and radiometric data generated for K, U and Th in each domain may be found in figures A.12-A.18. Table 17 summarises the observed correlations. Despite the impact of some extreme outliers on the R^2 values, particularly in the case of U, the p-values and the scatterplots themselves clearly show a strong positive correlation between the datasets. In general the relationship is approximately linear although a significant spread of points about the line of best fit is observed in some domains, most notably domain 6. To try and understand the cause of such variability $X_{\text{soil}}/X_{\text{air}}$ histograms (figures A.19-A.25) were also generated. Potassium in domains 5 and 6 is presented here as an example.

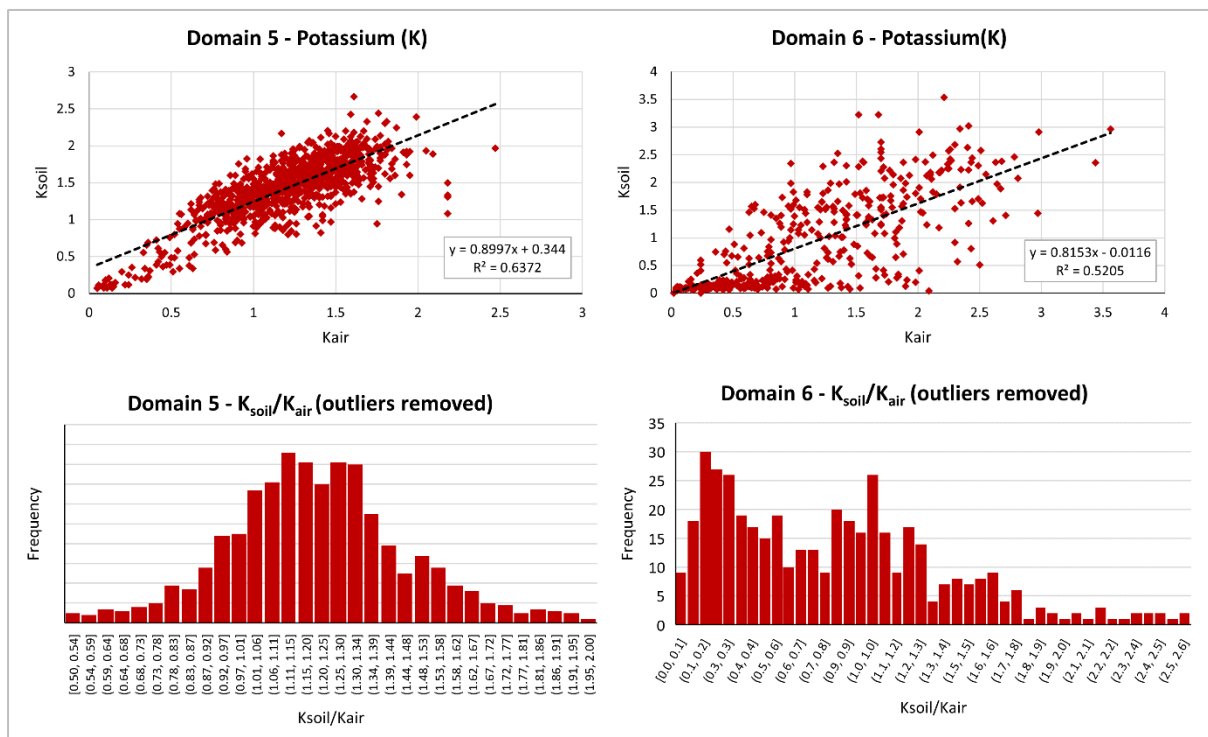


Figure 47: XY scatterplots of K_{soil} vs K_{air} for Geochemical Domains 5 and 6, and histograms of $K_{\text{soil}}/K_{\text{air}}$ corresponding to each.



Although there is still a spread of points about the line of best fit, the relationship between K_{soil} and K_{air} is noticeably more consistent in domain 5. Figure 47 shows how the *soil:air* ratios are essentially unimodally distributed and the continuous spread of values in either direction is probably due to subtle variations in soil properties such as density and moisture content or non-radioactive overburden thickness which would affect the gamma-ray signal disproportionately. Domain 6 on the other hand exhibits a wide range of $K_{\text{soil}}/K_{\text{air}}$ values because of its underlying multimodal distribution. The presence of three discrete peaks suggests that there are distinct regions within domain 6, each with a “typical” soil-radiometric relationship.

Table 17: R^2 and p-values for linear regression scatterplots (by domain; outliers removed).

<i>Domain</i>		1	2	3	4	5	6	7
K_{soil} vs K_{air}	n	418	1175	346	123	989	438	1491
	R^2	0.7484	0.5934	0.7186	0.6866	0.6372	0.5205	0.7133
	p	< 0.05	< 0.05	< 0.05	< 0.05	< 0.05	< 0.05	< 0.05
U_{soil} vs U_{air}	n	388	1114	324	118	967	402	1440
	R^2	0.5224	0.0918	0.2779	0.4406	0.2971	0.2662	0.168
	p	< 0.05	< 0.05	< 0.05	< 0.05	< 0.05	< 0.05	< 0.05
Th_{soil} vs Th_{air}	n	417	1196	351	128	1005	435	1500
	R^2	0.6421	0.4912	0.6713	0.4895	0.6391	0.4408	0.7352
	p	< 0.05	< 0.05	< 0.05	< 0.05	< 0.05	< 0.05	< 0.05

6.2.6. Peat

To investigate the effect of peat on the relationship, points intersecting mapped deposits were removed and separate regression analyses were conducted. The effect on the median ratios is illustrated in figures 48-50, and the R^2 and p-values for the new regressions are summarised in tables B.2 and B.3. The p-values indicate the correlation is statistically significant at the 95% confidence interval with the exception of a poor correlation in areas of peat in domain 4 ($p = 0.158$; $R^2 = 0.128$). This subset of data has the lowest sample size ($n = 20$) which is likely to affect the significance of any observed trend.



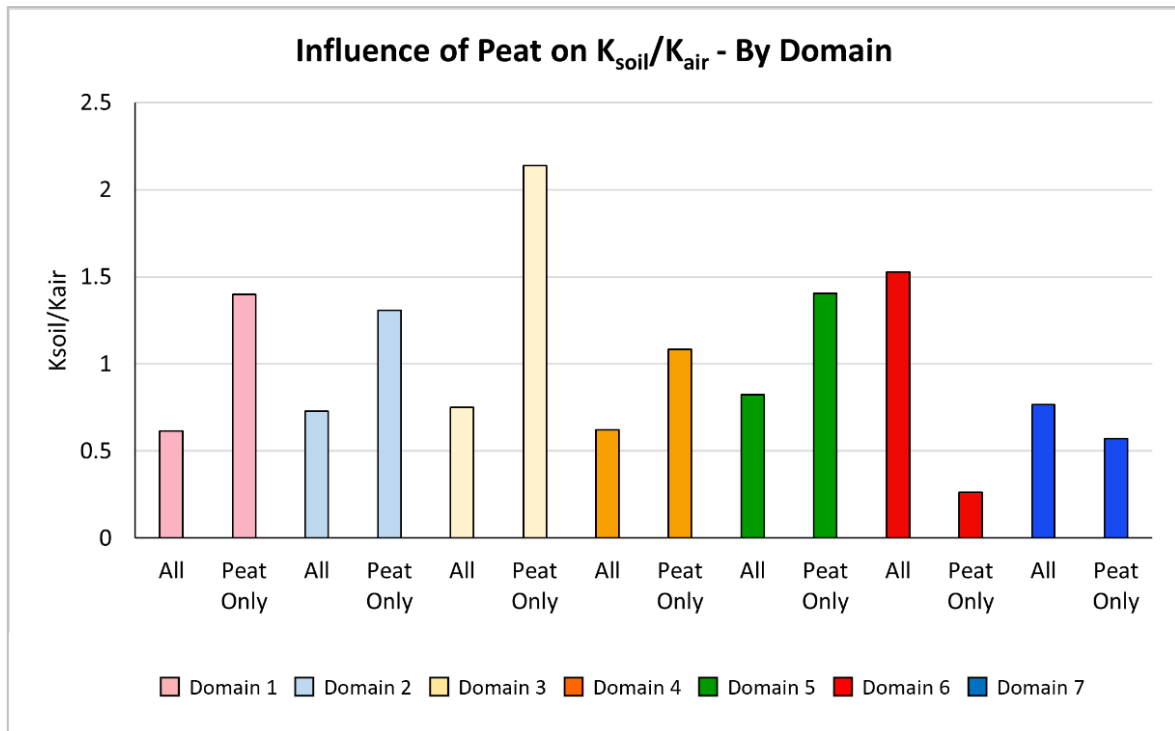


Figure 48: Median K_{soil}/K_{air} ratios for all data (G1,G3,G6) and areas of peat only; by domain.

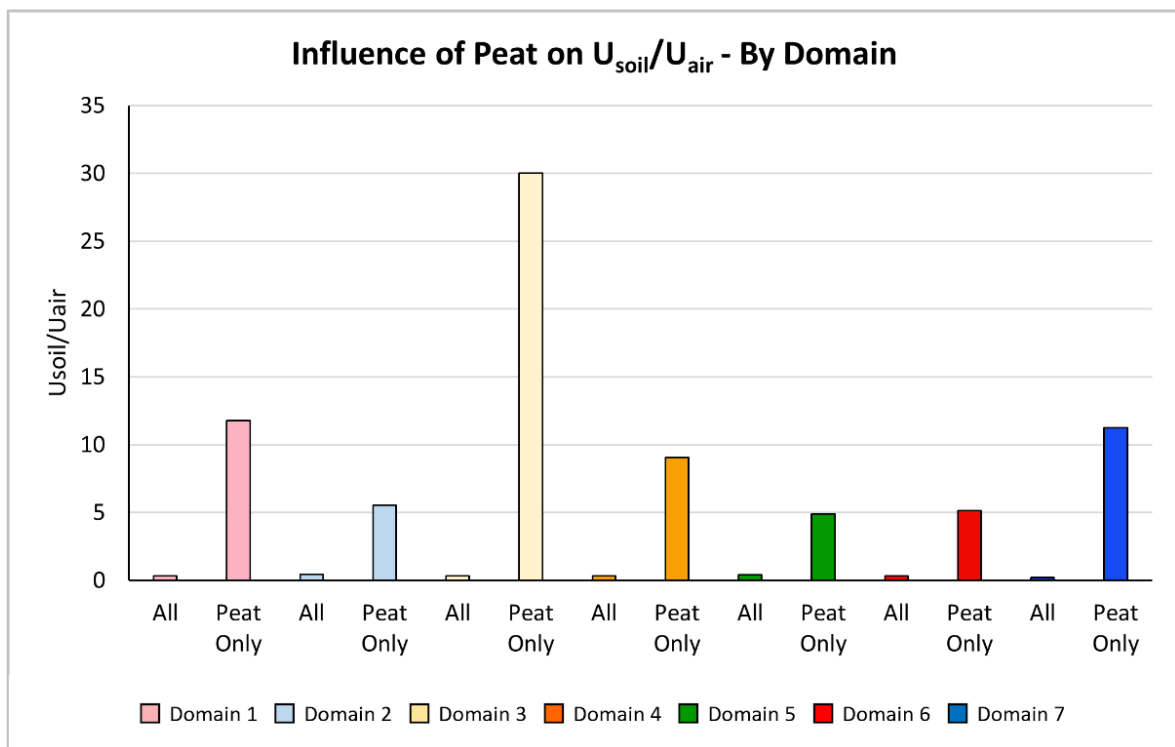


Figure 49: Median U_{soil}/U_{air} ratios for all data (G1,G3,G6) and areas of peat only; by domain.



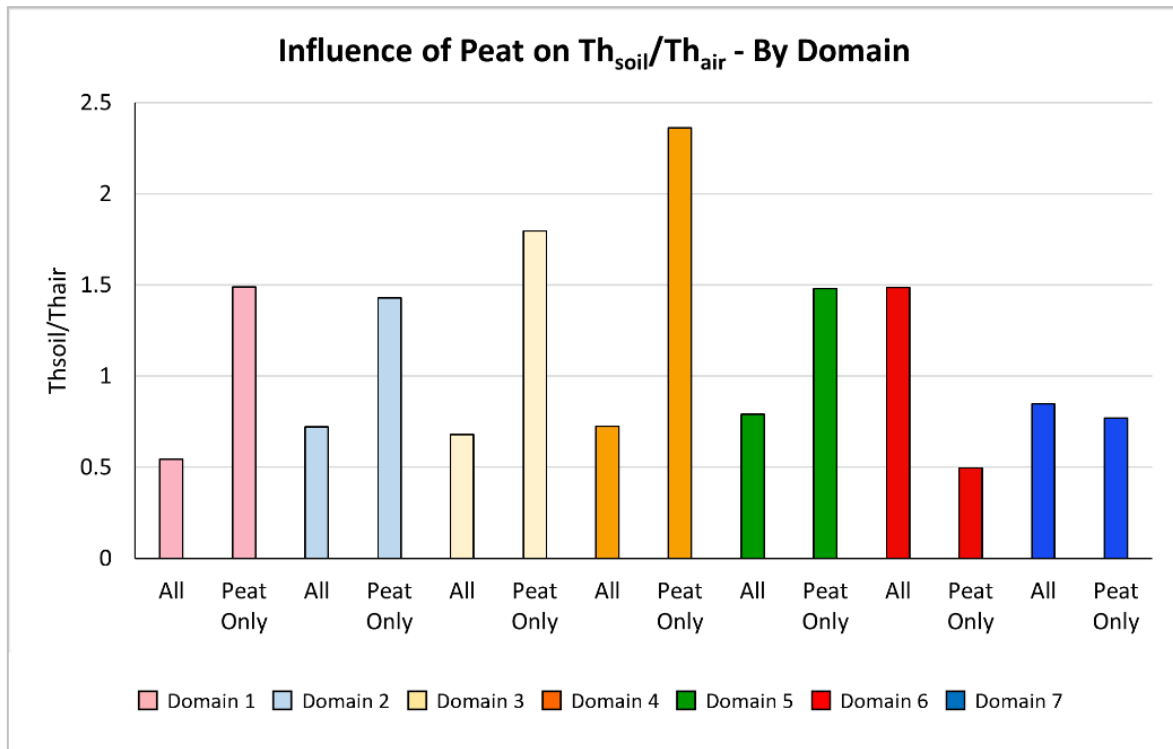


Figure 50: Median Th_{soil}/Th_{air} ratios for all data (G1,G3,G6) and areas of peat only; by domain.

The ratio of *soil:air* concentrations increases significantly over peat in the case of uranium despite the lower-than-average concentrations measured by both methods. This effect could be a combination of significant attenuation of an already weak gamma-ray signal and the higher soil LLD.

For potassium and thorium, the opposite trend is observed for domains 6 and 7 and the effect is most pronounced in the former. This implies that on average the soil concentrations decrease to a greater extent over peat relative to the radiometric signals. A possible explanation for this is the co-occurrence of blanket bog and outcropping felsic igneous and metamorphic rocks on the hilly terrain present in both domains, particularly domain 6. While wet peat is known to attenuate gamma-rays, Beamish (2014) also noted that where cover is thin and/or dry a localised increase in the gamma flux can result. The presence of outcrops and peat deposits side-by-side in these domains may also affect the observed radiometric signal relative to soil measurements because of the footprint of the airborne survey. As the aircraft traverses rock-peat boundaries the precise measurement location (directly below aircraft) may be over peat but a significant contribution to the gamma-ray count could come from outcropping rock in the spectrometer's field of view.

Relief must also be considered when interpreting changes in the radiometric signal relative to measured soil concentrations. Domains 6 and 7 cover steeper, more mountainous terrain than



domains 1-5 which has been found to significantly alter count rates both positively and negatively. Schwarz *et al.* (1992) modelled count rates over a mountainous region of Switzerland using a digital terrain model and altitude data and found a 20% reduction in count rates over peaks and increases of up to 80% in narrow valleys due to changes in the solid angle subtended at the detector by the ground.

The increase in $X_{\text{soil}}/X_{\text{air}}$ for K and Th in domains 1-5 is likely due to increased gamma-ray attenuation without significant influences from topography and exposed bedrock. It is noted that trends observed relating to the effect of peat on the soil-radiometric relationship are less reliable due the smaller 'peat-only' sample sizes in these domains, particularly domain 4 (see table 18).

Table 18: Sample sizes for areas with and without peat by domain, and the % of each domain's points intersecting peat deposits.

Domain	1	2	3	4	5	6	7
$n_{\text{without peat}}$	368	952	290	117	998	285	983
$n_{\text{peat only}}$	94	361	106	20	126	184	725
% peat	20.3	27.5	26.8	14.6	11.2	39.2	42.4

6.2.7. Soil texture

The boxplots in figures 51-53 show how the relationship between geochemical and radiometric measurements is affected by soil texture. Individual concentrations are summarised in table B.4.

The median appears lowest for the "other" category which includes exposed rock, blown sand and urban/made ground. These materials are expected to be less attenuating than the remaining soil categories and the "urban" material could contain high concentrations of radioelements (IAEA 2010), however this data is considered unreliable as these sub-categories are areas avoided in the soil survey and urban areas are flown at higher altitude in the airborne survey subjecting measurements to increased statistical noise.

The slightly elevated $X_{\text{soil}}/X_{\text{air}}$ of coarse loamy soils compared to fine loams could be the effect of larger lithic fragments which are removed from soil samples but included in the 'bulk' radiometric measurement. Rawlins *et al.* (2007) and Taylor *et al.* (2002) note an increased quartz content in larger fractions which is negatively correlated with radionuclide concentrations. This could also explain why the median ratio is closer to 1:1 for sandy stoneless drift.



A higher *soil:air* ratio is observed for clayey soils. This could be related to increased gamma-ray attenuation, as Beamish (2013) notes that materials with a higher porosity such as clay exhibit more rapid attenuation with increasing saturation than lower porosity mineral soils. This increased sensitivity to saturation could explain the wider interquartile range observed for clay.

There is noticeable variation within the peat texture class compared to other classes. The SIS Soils map (figure 9) has a larger area of peat than the Teagasc soils map (Figure 7) and likely includes areas of thin organic soils at the edges of the deposits. This could imply that intra-peat variations, in saturation or thickness for example (Beamish 2013) are significant and that the relationship cannot be inferred from soil texture alone.

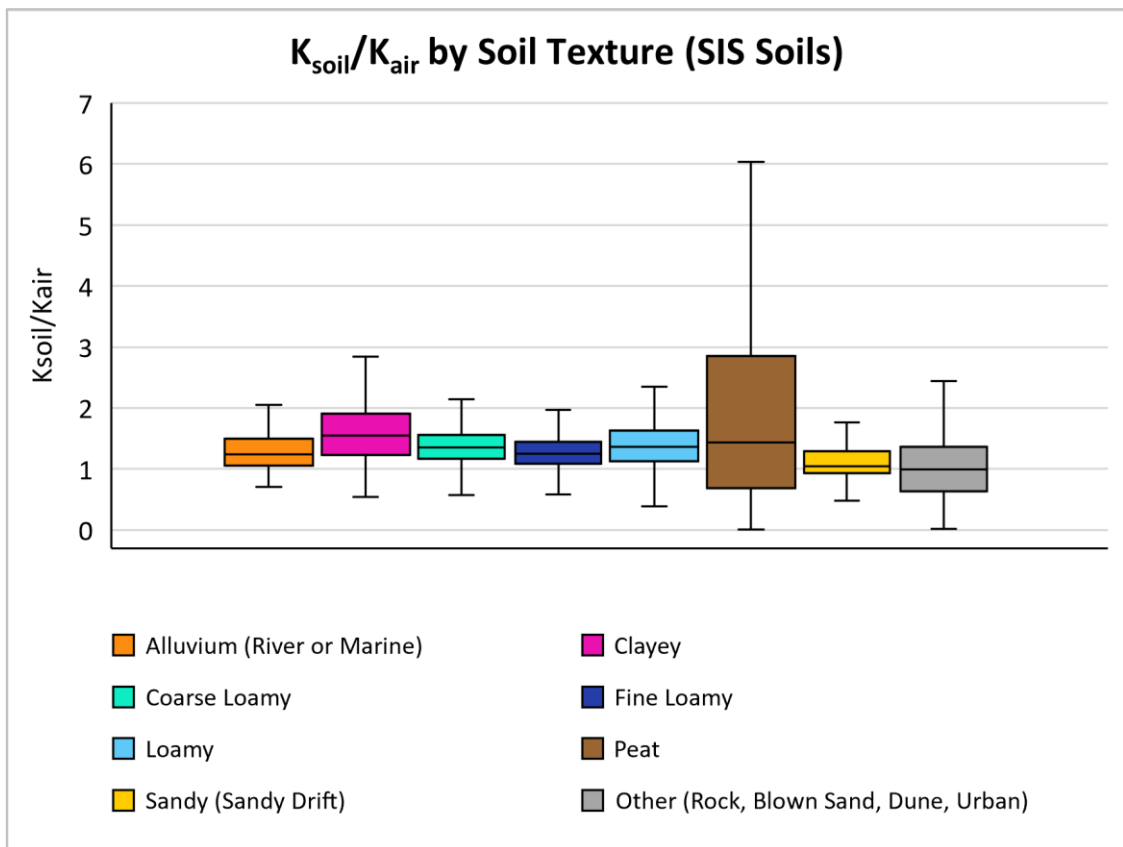


Figure 51: K_{soil}/K_{air} across different soil texture classes; outliers hidden for clarity.



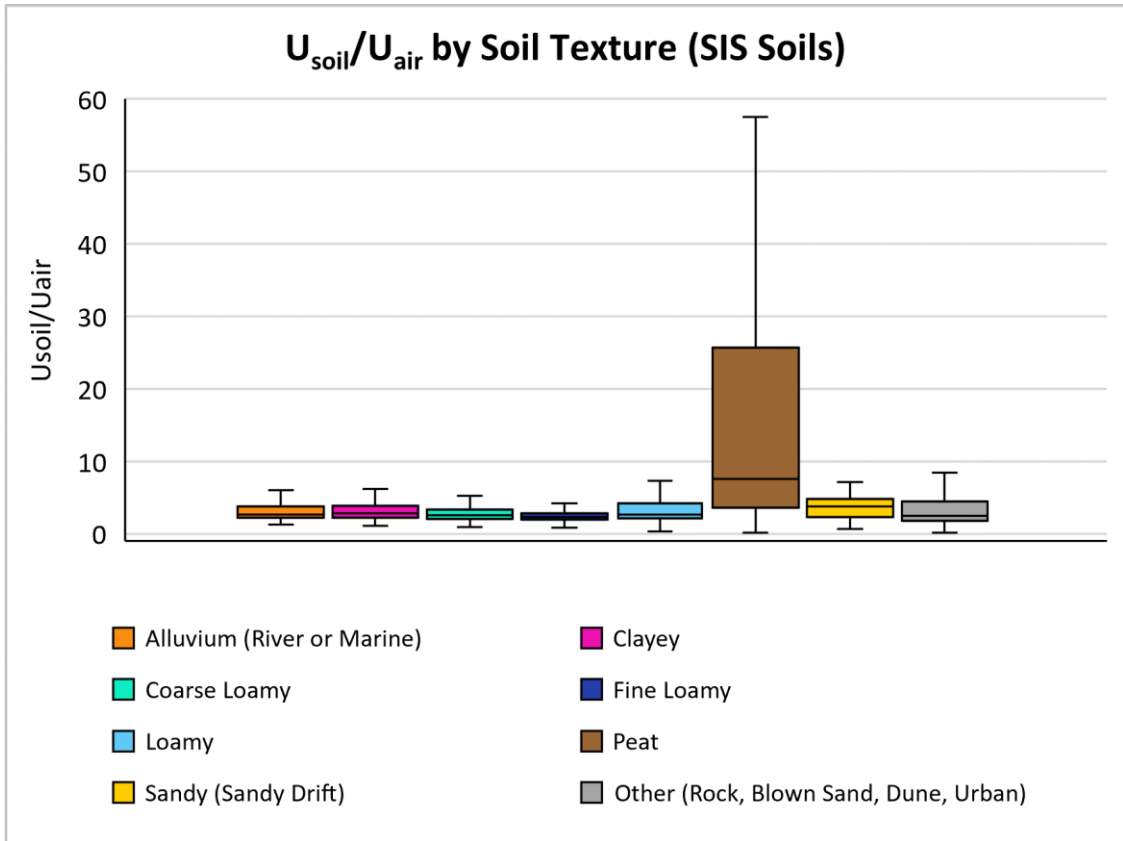


Figure 52: U_{soil}/U_{air} across different soil texture classes; outliers hidden for clarity.

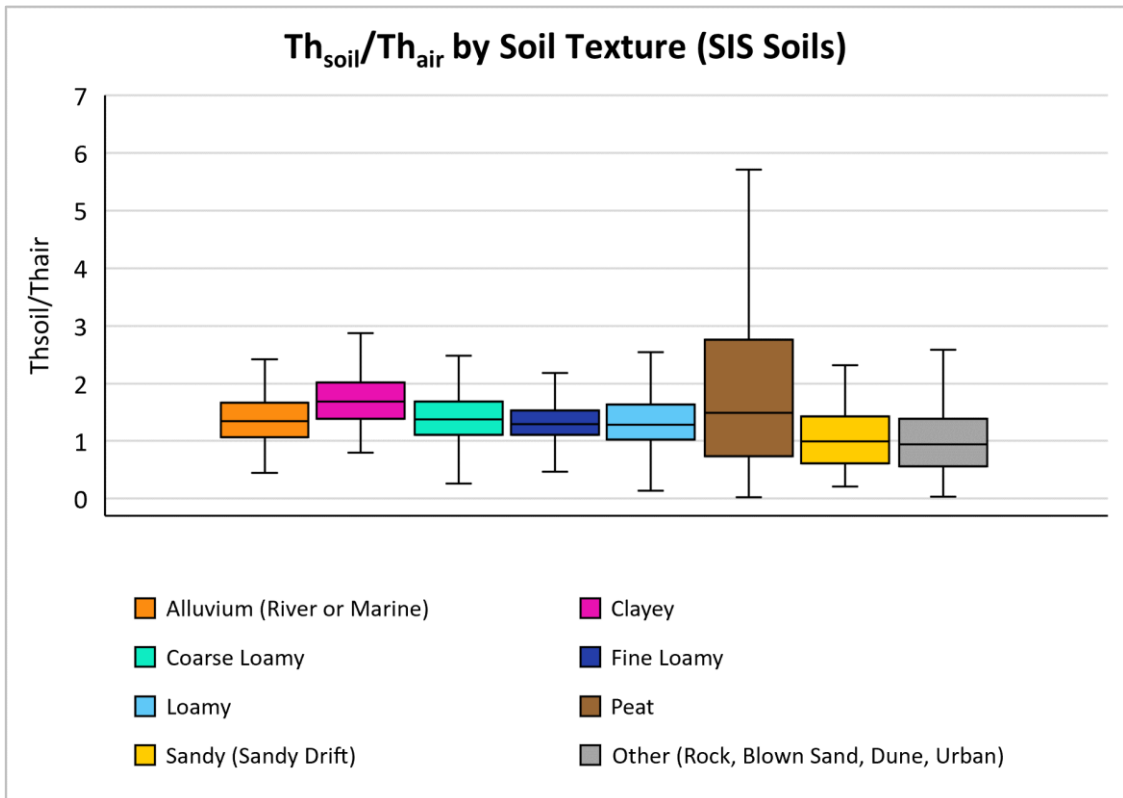


Figure 53: Th_{soil}/Th_{air} across different soil texture classes; outliers hidden for clarity.



6.2.8. Land use

Landcover classes (CORINE) were used to investigate potential effects of land use on the soil-radiometric relationship including agricultural practices, vegetation cover and anthropogenic influences.

Variations in *soil:air* ratios across the classes can be seen in figures 54-56, and the median concentrations themselves are compared in figures A.26-A.28. It is important to consider the relative sample sizes for each of the classes when interpreting the results. Table B.5 includes the sample sizes for each class within the study area. Classes with $n < 10$ were considered unreliable and have been removed from the figures below, however their median values are included in figures A.40-A.42 for comparison, as many have associated large areas of exposed concrete (e.g., airports) and have been subject to significant anthropogenic interference (e.g., mineral extraction sites) so the relationships may be informative (Cinelli *et al.* 2019; IAEA 2010).

Comparing ratios (figures 57, 58) with concentrations (figures A.40, A.41) of potassium and uranium, the influence of agricultural fertilizer application cannot be ruled out. “Land principally occupied by agriculture,” “non-irrigated arable land” and “pastures” all show relatively high concentrations (of K in particular) and the *soil:air* ratio for both elements is lowest in the arable land class which could indicate plant uptake of fertilizer is leading to decreased soil concentrations without affecting the overall gamma flux from the land. Agricultural practices such as tillage could also alter the degree of soil compaction or its drainage capacity thereby reducing gamma-ray attenuation near the surface (Wetterlind *et al.* 2012).

$K_{\text{soil}}/K_{\text{air}}$ and $\text{Th}_{\text{soil}}/\text{Th}_{\text{air}}$ suggest that the presence of forest cover could also affect the relationship, with soil concentrations substantially higher than airborne in broad leaf forest and the opposite observed for “sparsely vegetated areas.” Forests have the potential to attenuate gamma-ray signals where the tree canopy or surrounding ground retains significant moisture (Wetterlind *et al.* 2012), however Cinelli *et al.* (2018) found this effect to be negligible in their study (Belgium) and it’s possible the attenuation is significant only in areas with extremely dense canopy. The forest classes are also less reliable because the soil sampling criteria exclude forested areas except where no alternatives exist.

The impact of gamma-ray attenuation in saturated ground can be clearly seen from the high *soil:air* ratios for all radioelements in the “inland marshes” class. As previously mentioned, peat bogs display a variable soil-airborne relationship which could be related to intra-peat variations or topography.



The lower ratios observed for “green urban areas,” “discontinuous urban fabric” and “industrial or commercial units” suggest that anthropogenic features such as concrete pavements, buildings and other infrastructure within the airborne footprint could be enhancing the radiometric signal relative to the soil concentration although the airborne measurements are less reliable over urban areas with increased fly height.

While some trends in the soil-radiometric relationship are apparent these results alone are inconclusive and one must consider how land use frequently covaries with soil properties that are themselves contributing factors (Wetterlind *et al.* 2012). For example, arable farming develops where soils are deep, loamy and well-draining, pastures in the study area correlate strongly with limestone (Domain 2), and blanket peat is largely found in mountainous regions with granitic and metamorphic bedrock (domains 6 and 7).

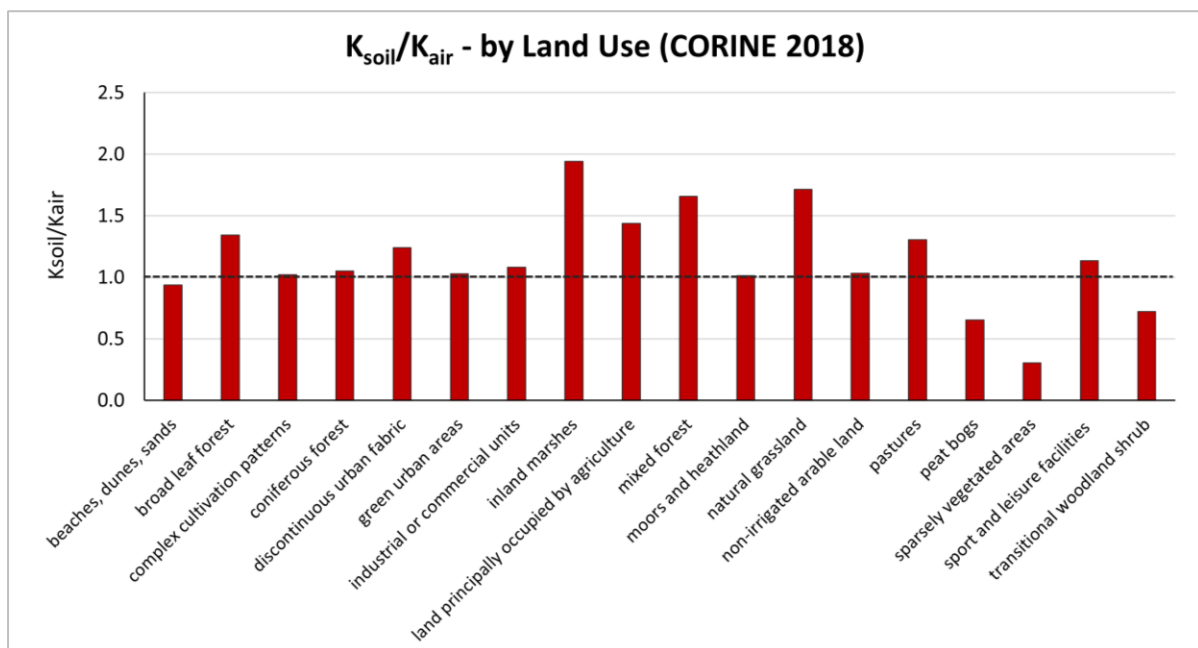


Figure 54: Median K_{soil}/K_{air} across different land use classes (CORINE). Dashed line represents a 1:1 relationship.



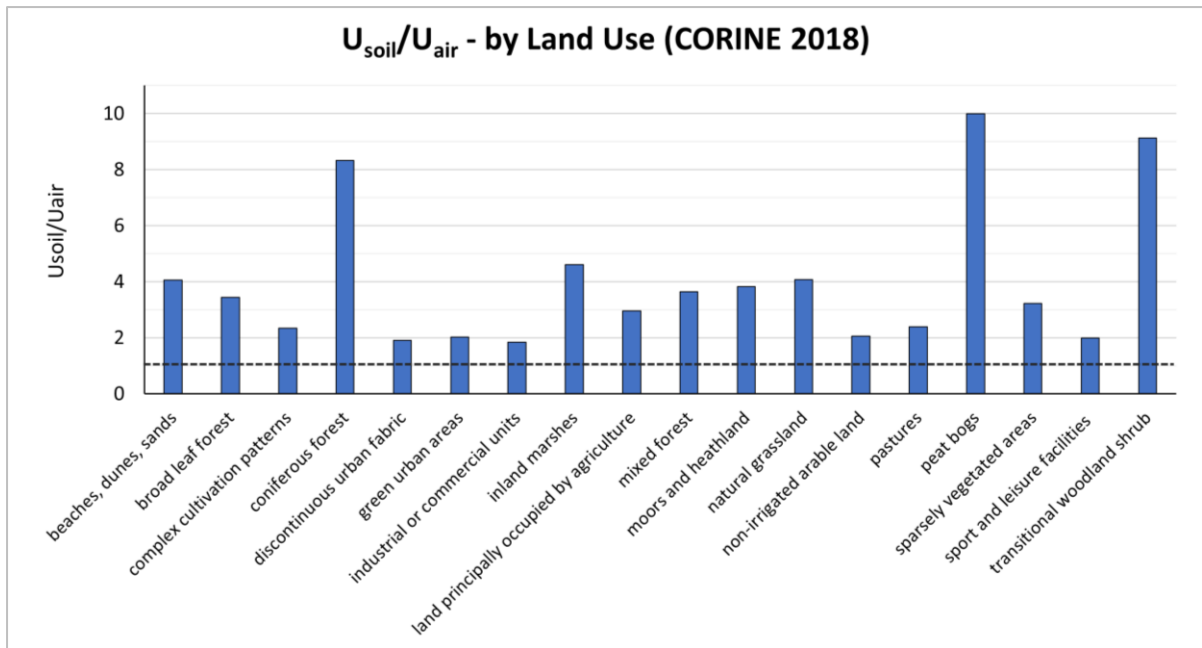


Figure 55: Median U_{soil}/U_{air} across different land use classes (CORINE). Dashed line represents a 1:1 relationship.

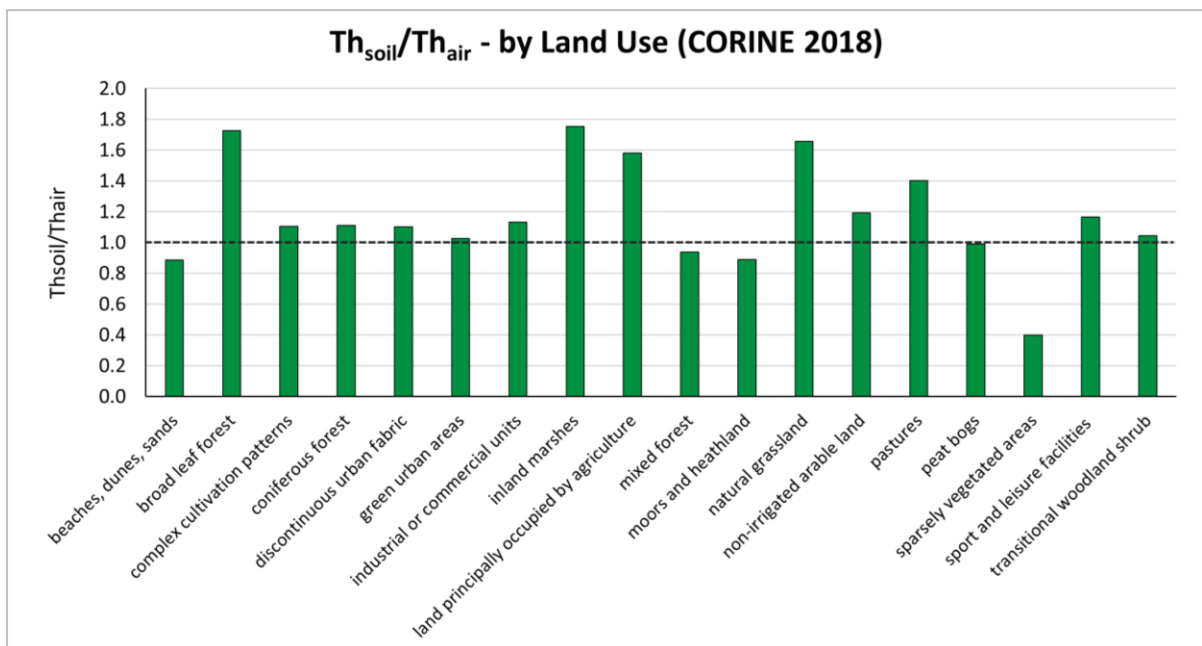


Figure 56: Median Th_{soil}/Th_{air} across different land use classes (CORINE). Dashed line represents a 1:1 relationship.



6.2.9. Outcrops, subcrops and depth to bedrock

The effect of outcropping and sub-cropping rock (< 1 mBGL) was investigated using the Teagasc Soils parent material classes *RckNCa* and *RckCa*, i.e., “bedrock at or near surface” (Teagasc 2009) (n = 724 in study area). While the GSI Bedrock Outcrops data is based on outcrops mapped in the field and is hence likely to be more accurate, soil samples taken from points intersecting mapped outcrops are justifiably scarce and somewhat suspect. The median radioelement concentrations are given in table B.6.

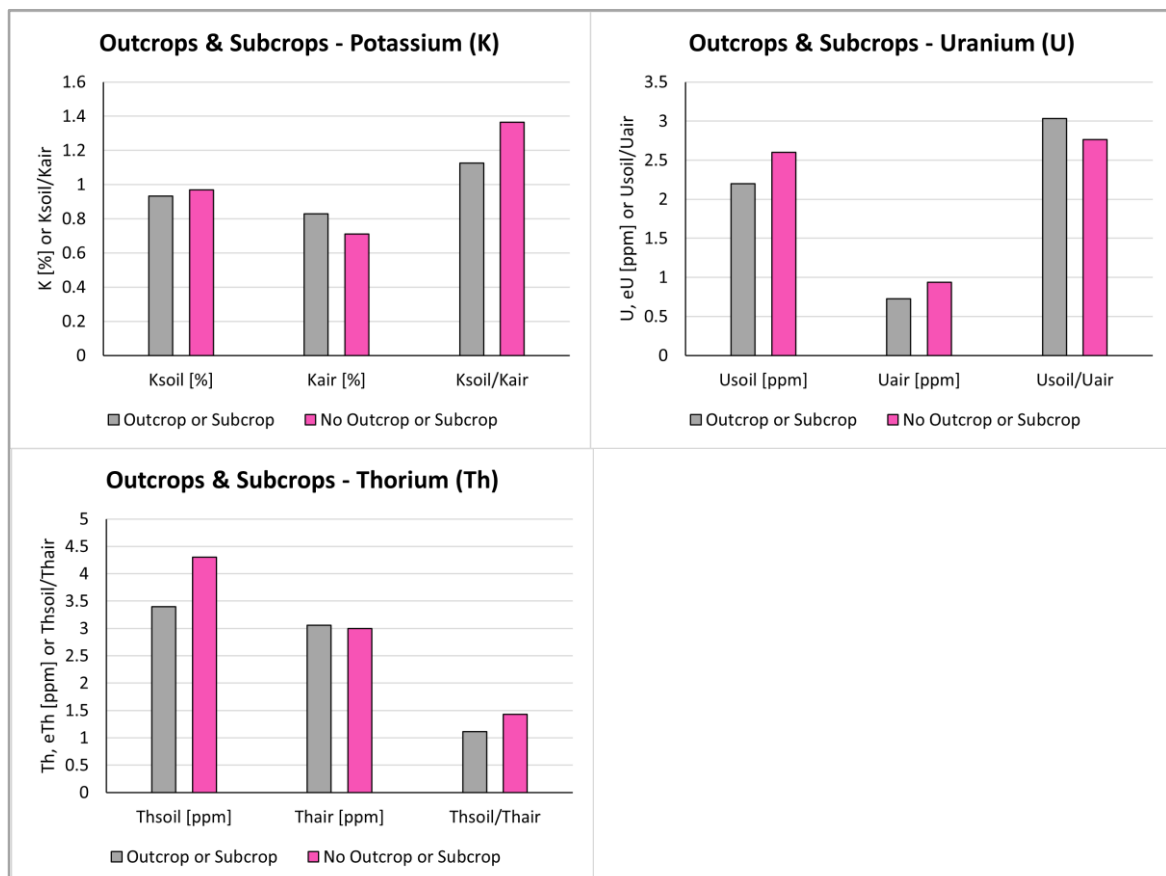


Figure 57: Effect of outcrops and subcrops on median radioelement concentrations and soil:air ratios.

Figure 57 illustrates that soil concentrations over shallow rock are typically lower than those elsewhere whereas airborne concentrations are elevated (for K and Th), most likely due to less attenuating overburden directly below the detector as well as exposed rock in the airborne footprint. U_{soil}/U_{air} , however increases on average over shallow/outcropping rock as the airborne signal is diminished. The reason for this is uncertain but could relate to the sensitivity of ^{214}Bi count detection to changes in survey height, since a significant proportion of outcrops and subcrops are found on steeper, more rugged terrain. Landscape may also explain why Th_{soil} changes to a greater



extent than K_{soil} . In mountainous environments soils are typically thin and continuously rejuvenated due to high rates of erosion “exposing less-weathered minerals” (Egli and Poulencard 2017), so the leaching of K and relative enrichment of Th that is observed in soils subject to longer periods of weathering is not seen here (Fall *et al.* 2020).

Depth to bedrock information from the GSI Groundwater Vulnerability database (Lee *et al.* 2008) was used to classify point data to investigate potential effects on the soil-radiometric relationship. The results are presented in table B.7.

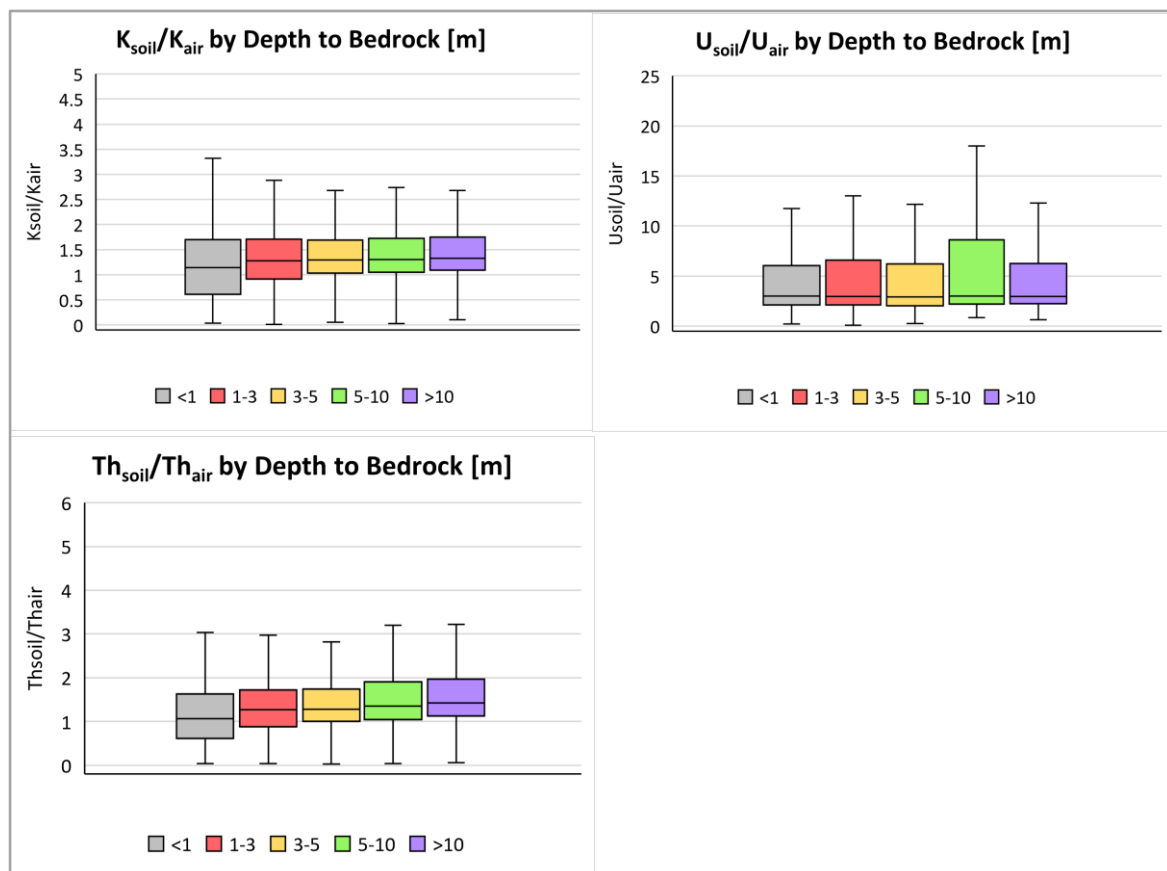


Figure 58: Effect of depth to bedrock on soil:air ratios.

Considering the median concentration ratios in figure 58, the only significant variation observed is between <1 m and the remaining classes, implying that soil and/or subsoil depth does not impact the relationship except where bedrock is sufficiently near the surface. This agrees with the general understanding that the gamma-ray signal originates in the upper 20-60 cm of soil (Rawlins *et al.* 2007).



6.2.10. Bedrock geology

Soil-radiometric relationships were investigated with respect to geology to see if there was any variation that could not be explained by the simplified Geochemical Domains. Median concentrations and ratios are presented in table B.8 and figures 59-61. The boxplots in figures A.29-A.31 show *soil:air* ratios for geological units with $n > 20$, which are considered the most reliable.

The disparity in sample size between units makes some more susceptible to anomalies or local ground conditions resulting in the large ranges of values seen for certain classes in figures A.29-A.31. Much of the already-small area occupied by units such as Neoproterozoic schist and gneiss, Lower-Palaeozoic basic-intermediate intrusives, and Lower-Middle Ordovician slate, sandstone, greywacke and conglomerate are covered by peat deposits and/or outcropping rock, both of which have been found to alter *soil:air* ratios.

Common trends are observed for all three radioelements and comparisons may be drawn between the geological unit and domain boxplots (figures 44-46), notably the lower median associated with granitic rocks (domain 6), the wide range for metamorphic rocks (domain 7), the narrow range and lower medians associated with Ordovician-Silurian rocks (domain 5), and slightly elevated but generally comparable medians for clastic sedimentary rocks despite differing geochemical signatures.

Figures 59-61 show clear geogenic influence on both soil and radiometric concentrations, however X_{soil} and X_{air} appear to follow the same trends and ratios are quite stable for K and Th with the exception of Namurian shales, granitic rocks and Old Red Sandstones. Figure 62 illustrates how similar the soil-radiometric relationship is for K and Th despite the differences in their geochemical behaviour and natural abundances. The ratio trends are greatly exaggerated for U and in some instances do not follow those of K and Th, as has been observed throughout the study. The increased sources of error associated with measuring U concentrations already discussed suggest that these trends are less reliable.



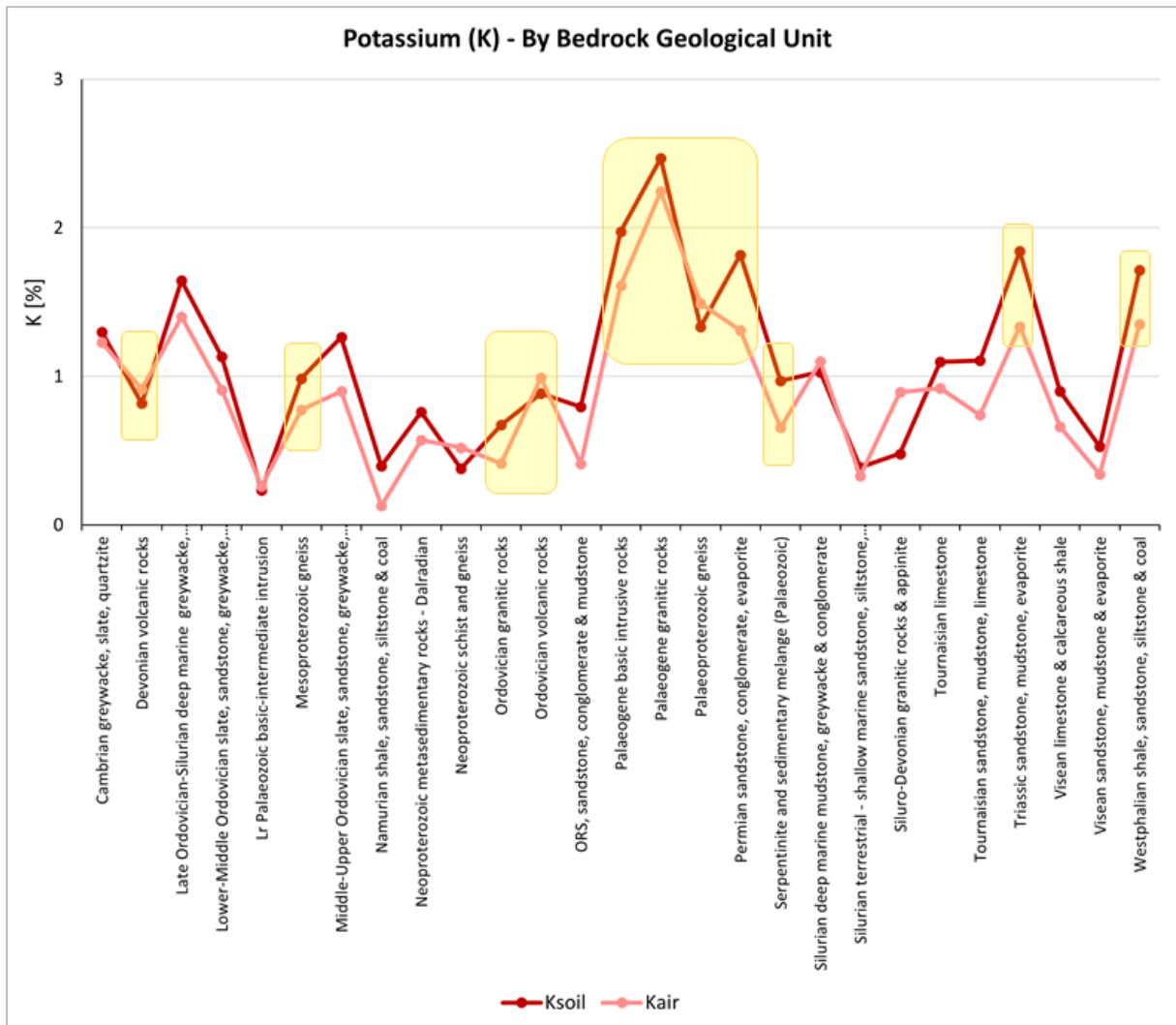


Figure 59: Variation in median K_{soil} and K_{air} with underlying bedrock geology (1:1million). Yellow boxes indicate classes with $n \leq 20$ (unreliable but included for comparison).



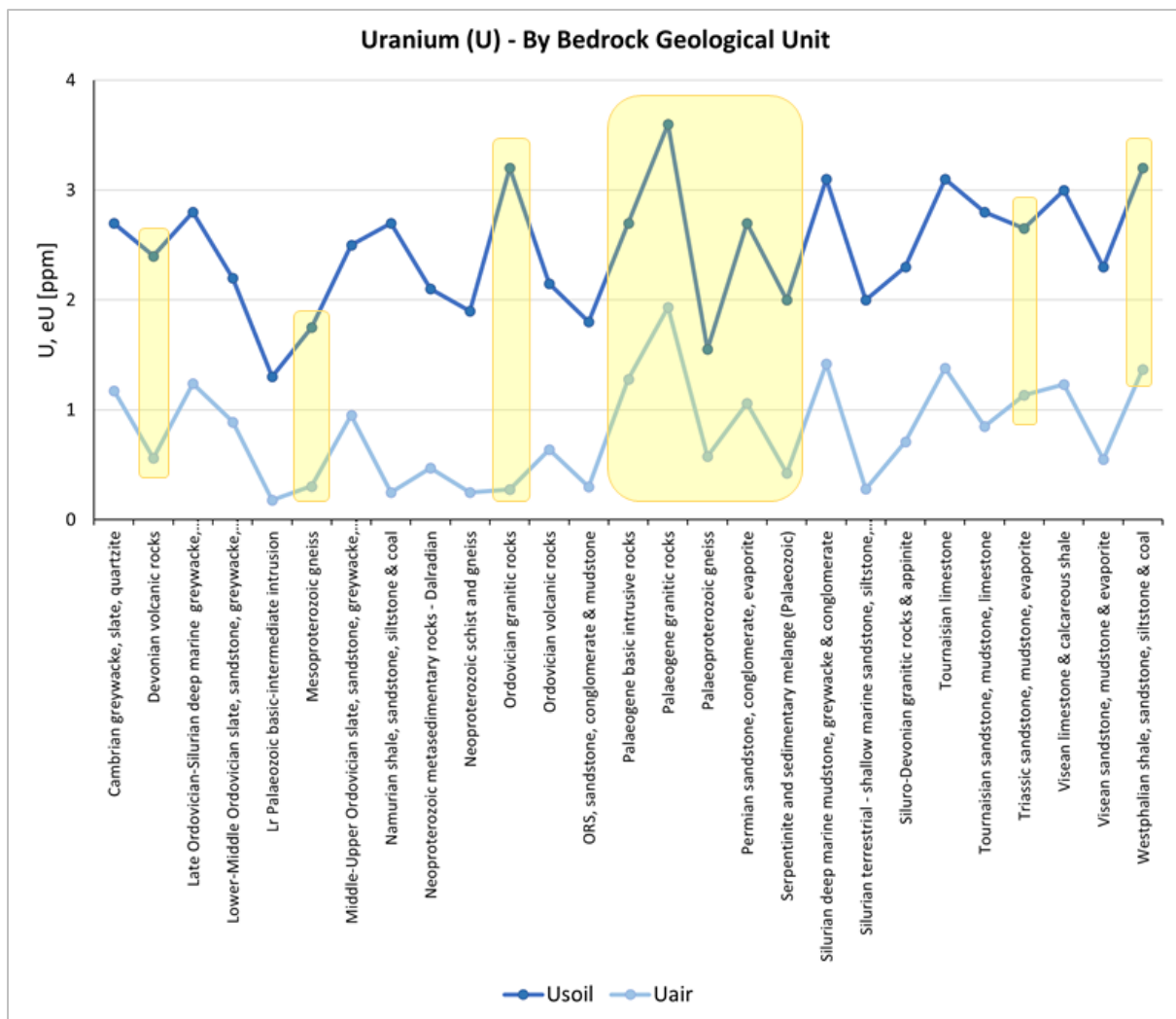


Figure 60: Variation in median U_{soil} and U_{air} with underlying bedrock geology. Yellow boxes indicate classes with $n \leq 20$.



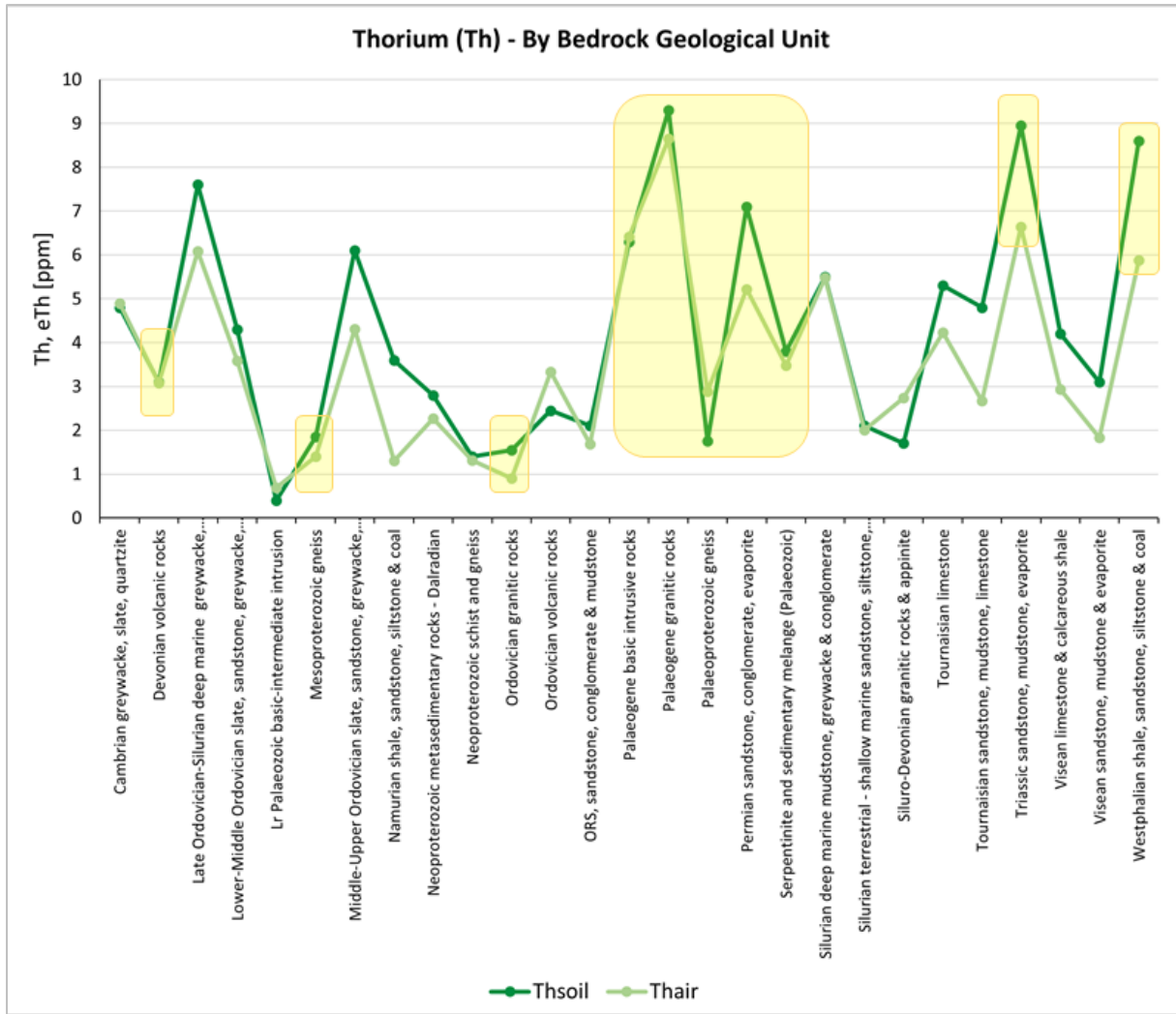


Figure 61: Variation in median Th_{soil} and Th_{air} with underlying bedrock geology. Yellow boxes indicate classes with n ≤ 20.



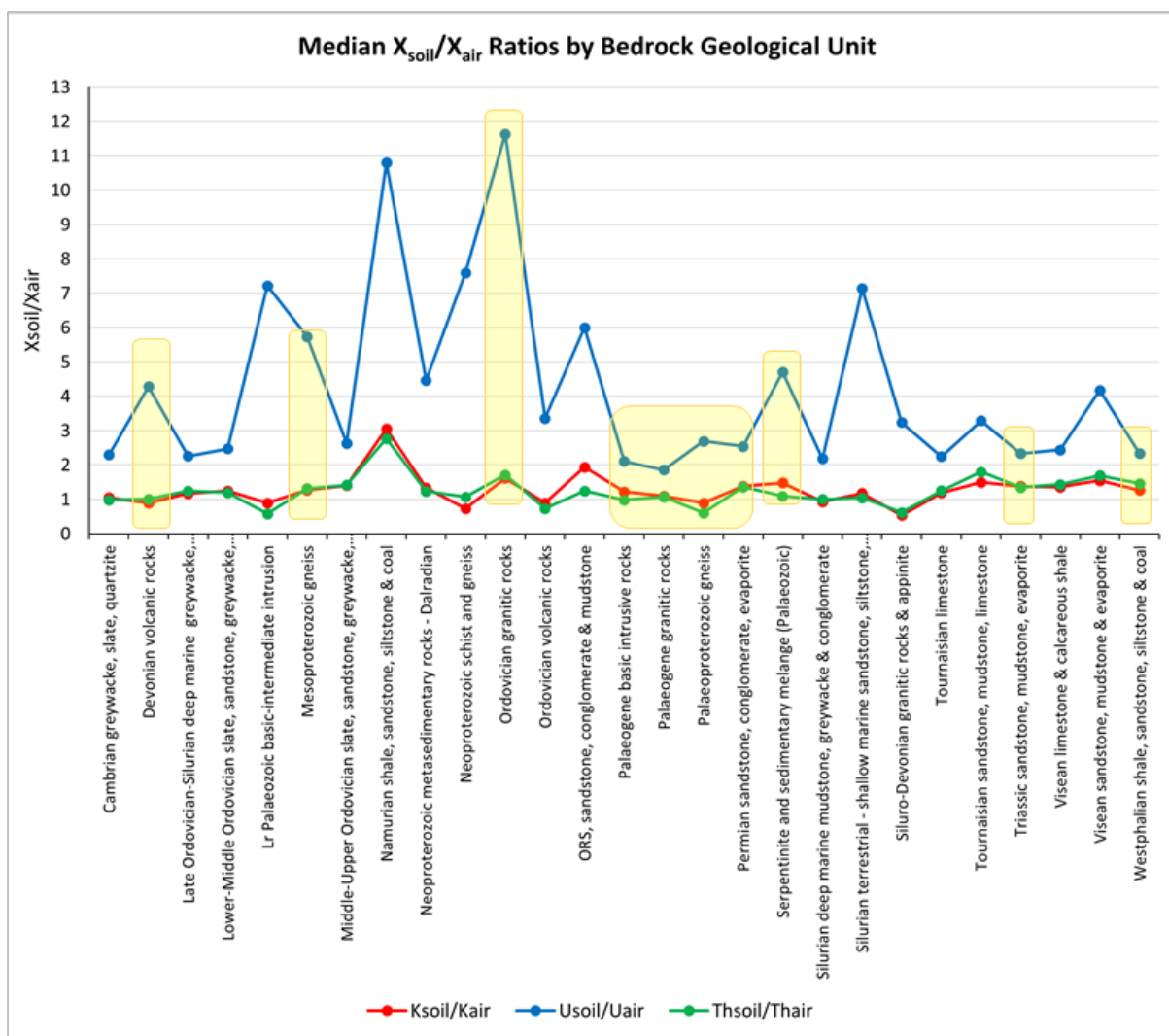


Figure 62: Median X_{soil}/X_{air} values by bedrock geological unit. Yellow boxes indicate $n \leq 20$.

6.2.11. Soil parent material

Similar trends can be observed if the data is classified according to soil parent material, as in figure 63 (unit codes and concentrations and ratios detailed in tables B.9 and B.10). Again, most K and Th ratios are between 1 and 2 for classes with $n > 20$, except blown sands for which X_{soil}/X_{air} is slightly lower. As previously noted, these classes are unreliable as soil samples are generally not taken from blown sand deposits. There are no major variations observed between soils derived from different types of till, although the granite “TGr” ratio appears slightly lower than the others, as does the “non-Calcareous rock at or near surface” (RckNCa) ratio. Sample sizes corresponding to gravels are too low to draw reasonable conclusions. The clear outliers are peat deposits which have already been discussed.



Subtle variations such as lower ratios observed for soils derived from granites compared to clastic sedimentary rocks and the elevated ratio for soils of Namurian sandstone and shale origin are also present in the bedrock graph (figure 62), supporting the idea that the bedrock, subsoil and soil are closely related, and justifying the use of simplified Geochemical Domains (Glennon *et al.* 2020). While geochemistry clearly does not explain much of the variation in the soil-radiometric relationship, these subtle differences suggest that the geochemistry (or mineralogy) likely influence factors that have a knock-on effect on soil properties such as weathering, as well as the phases in which radioelements occur and their mobility.

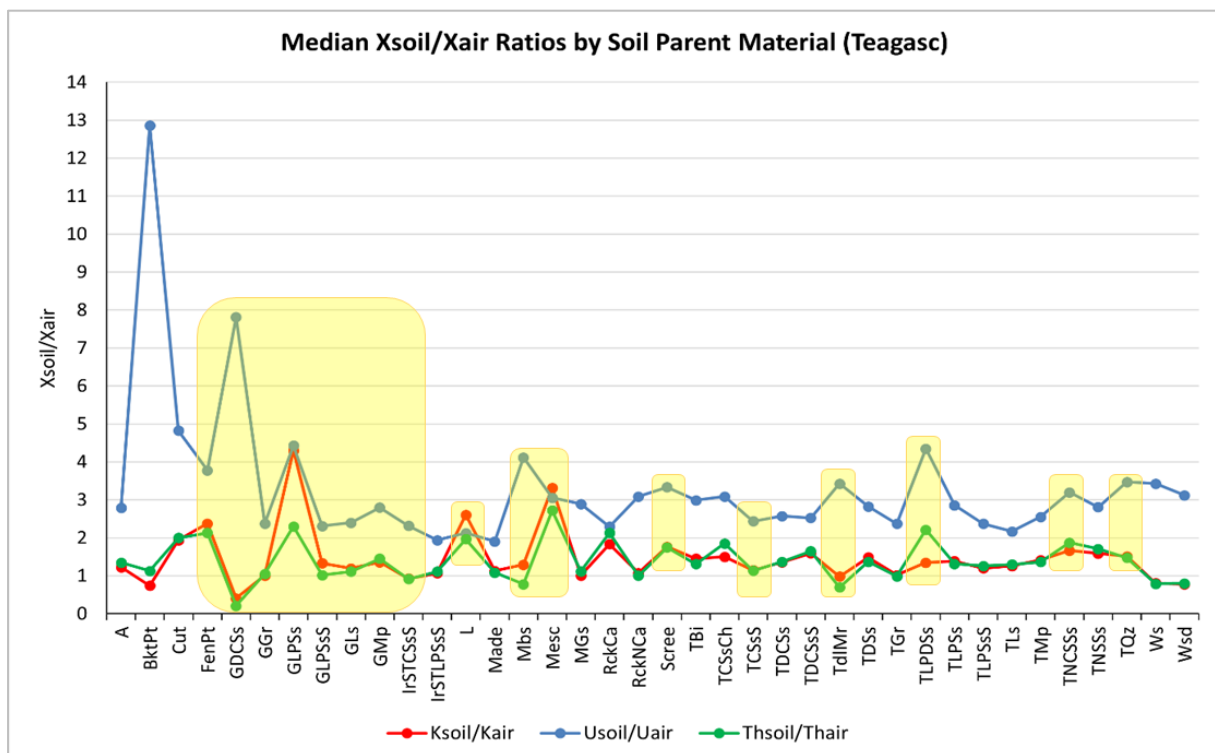


Figure 63: Variation in X_{soil}/X_{air} with soil parent material. Yellow boxes indicate classes with $n \leq 20$.

6.3. Predicting Soil Geochemistry from Radiometric Data

The linear regression equations in tables B.11-B.13 (from scatterplots in figures A.32-A.39) were used to predict soil K, U and Th concentrations at each point (soil sample location). Interpolated maps of predicted soil concentrations were classified using identical concentration ranges to the original soil maps (i.e., not percentiles based on predicted values) to assess their accuracy because as previously noted the soil and radiometric data already have similar spatial distributions.



'True' soil maps (A) and radiometric maps re-classified using these soil percentiles (B) were compared with predicted maps based on:

- Linear regression using all data (C),
- Separate regression equations for areas with and without peat (D),
- Separate regression equations for areas with and without peat for each Geochemical Domain (E).

These sets of maps are shown in figures 64-66.

Peat and Geochemical Domains were chosen as a starting point since the soil and radiometric concentrations were found to be reasonably well correlated within such classes and unnecessary complexity (e.g., using separate regressions for each rock type) is avoided. However, this study has shown that other factors such as soil texture and rock outcrops may significantly affect the soil-radiometric relationship so the predictions are likely to benefit from further refinement.

Comparing (A) and (B), the re-classified radiometric data consistently underpredicts soil values, most notably for uranium, although K and Th exhibit areas of moderate concentration (green) which fall within the correct range. Using a single equation for each element (C) succeeds in picking out more high concentrations over Louth, east Donegal and the Longford-Down inlier but over-predicts areas of peat. Adding a separate regression for peat (D) sees a notable improvement, with more subtle variation visible within these deposits. Finally, adjusting the equations by domain picks out finer detail in the midlands and areas of moderate radioelement concentrations and improves predictions of both high and low values. Comparing figures 66(A), (D) and (E) for example, the final map accurately picks out more highs over the Dalradian rocks in east Donegal without overpredicting low concentrations over granites to the west.

The uranium maps illustrate where the predictions fail to pick out point anomalies. These features could be due to localised sources of contamination, to which discrete soil samples are more vulnerable by nature and which are less likely to be detected by the airborne survey despite its higher resolution.



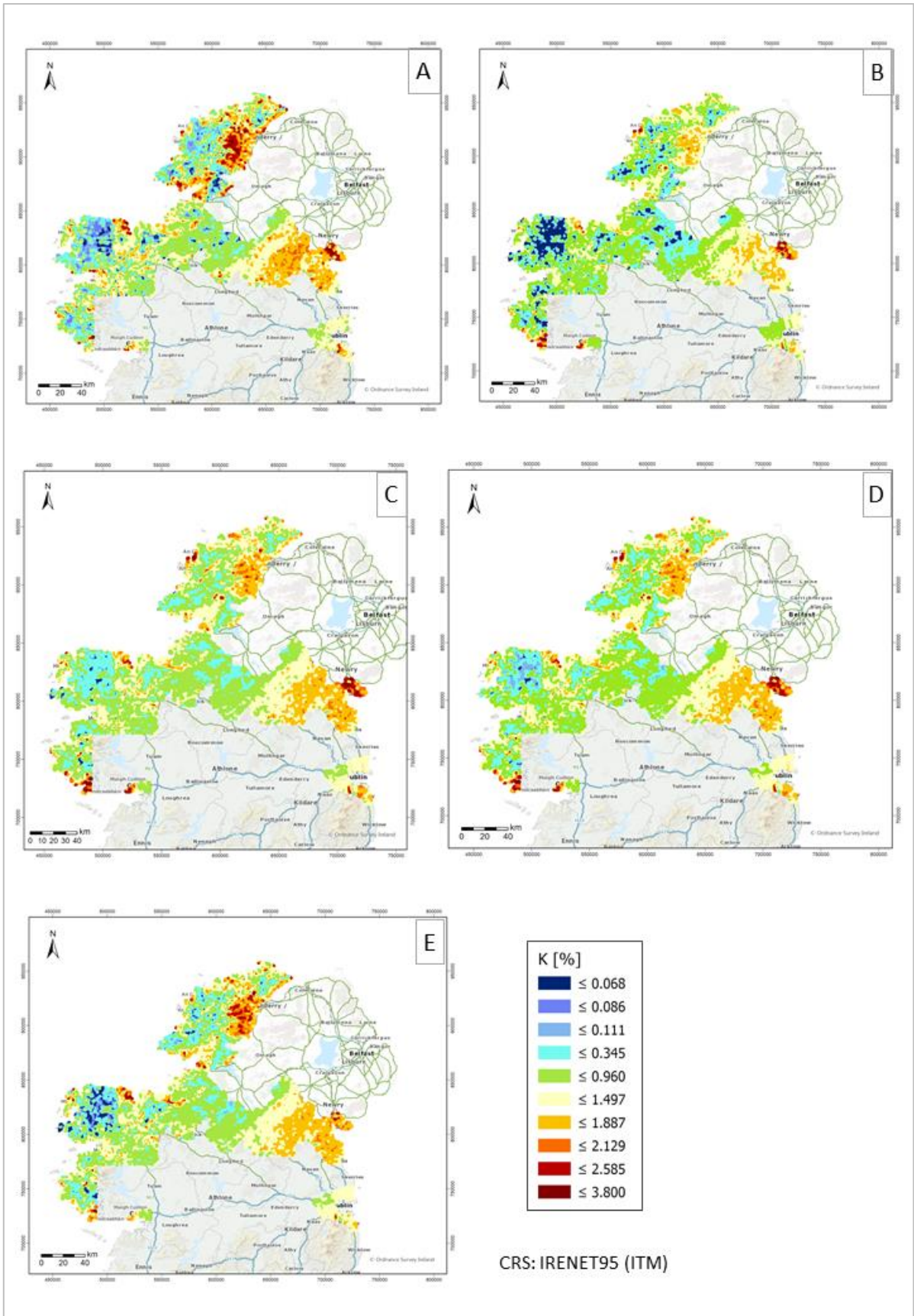


Figure 64: True K_{soil} (XRFs) map (A), reclassified K_{air} map (B) and predicted K_{soil} maps calculated from K_{air} using linear regression equations (C-E). All maps classified using original K_{soil} percentiles.



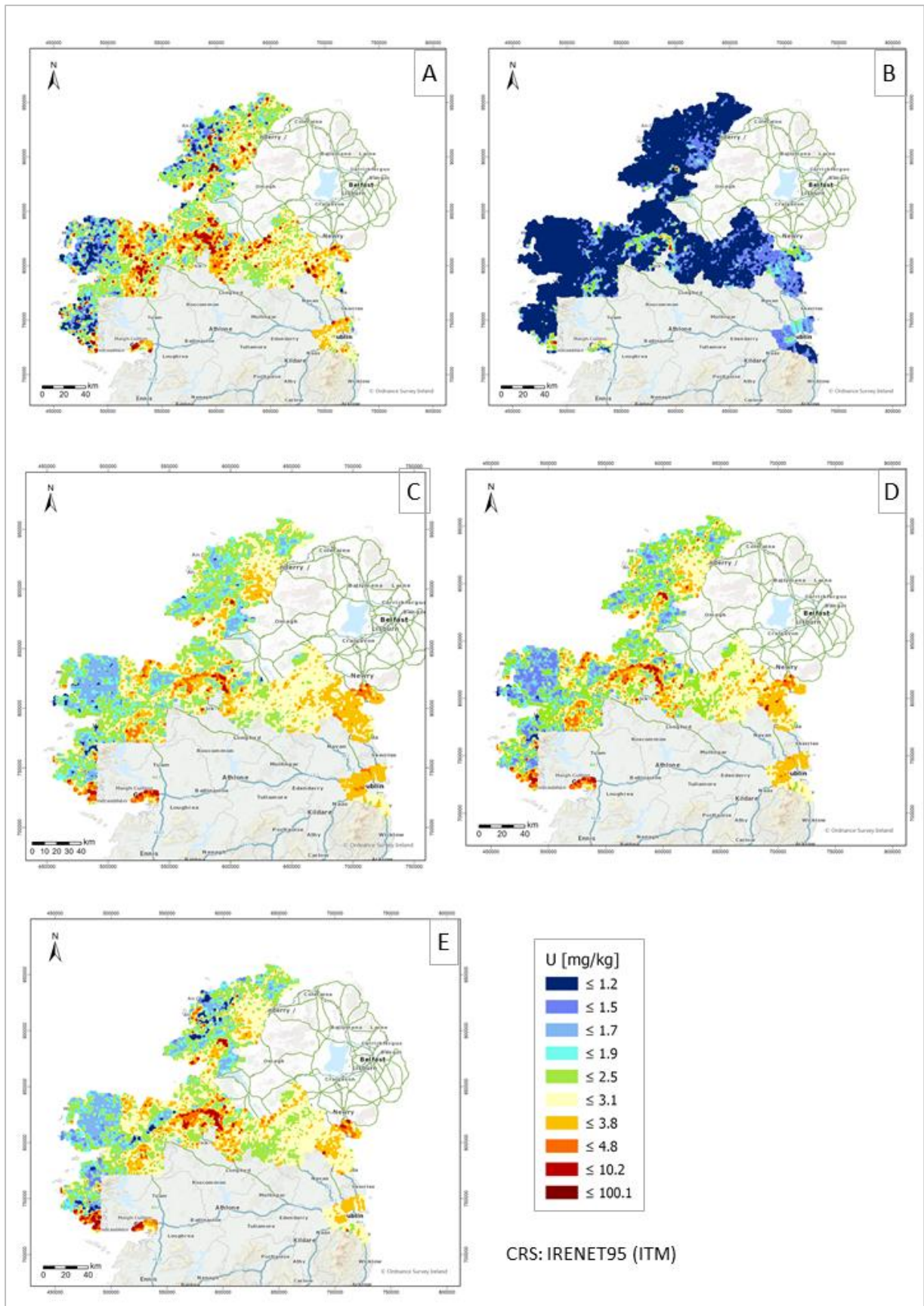


Figure 65: True U_{soil} (XRFs) map (A), reclassified U_{air} map (B) and predicted U_{soil} maps calculated from U_{air} using linear regression equations (C-E). All maps classified using original U_{soil} percentiles.



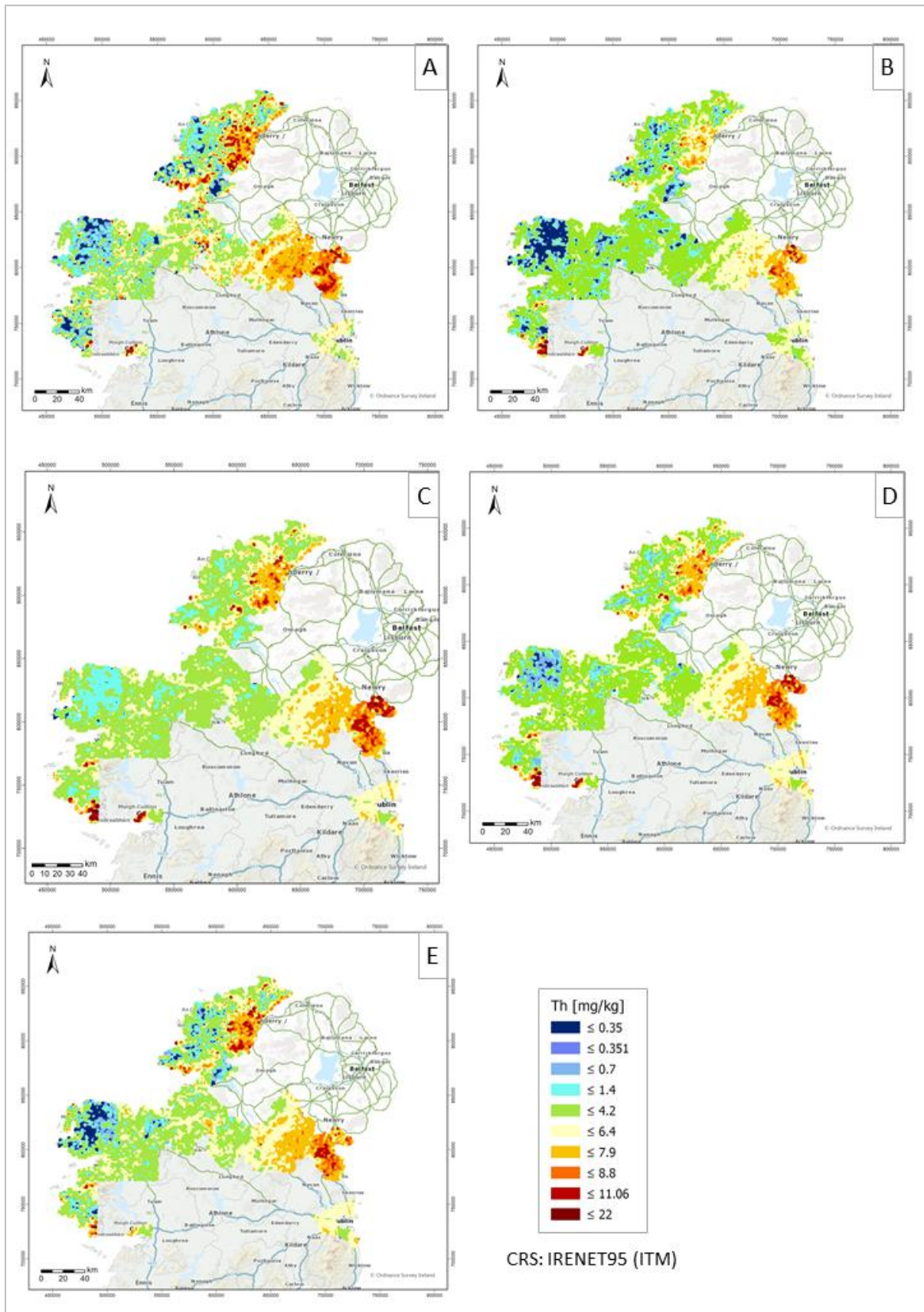


Figure 66: True Th_{soil} (XRFs) map (A), reclassified Th_{air} map (B) and predicted Th_{soil} maps calculated from Th_{air} using linear regression equations (C-E). All maps classified using original Th_{soil} percentiles.



Table 19 show the % deviation (absolute) of the predicted values from the true soil concentrations for each method (and for each domain in table B.14). The accuracy of the predictions was improved by considering factors such as the presence/absence of peat, and although the percentages suggest the improvement is minimal, figures 63-66 show how refining the predictions has the greatest effect on extreme highs and lows which are likely to be the areas of interest in many applications.

Table 19: Median % deviation (absolute) from true soil values for each set of predictions (C-E).

<i>Regression</i>	<i>K</i>	<i>U</i>	<i>Th</i>
(C) No domains, not split for peat/no peat	25.87 %	17.49 %	27.74 %
(D) No domains, split for peat/no peat	24.63 %	17.67 %	26.23 %
(E) By domain, split for peat/no peat	22.33 %	16.49 %	25.61 %

Regression analysis of the true soil concentrations and the final (E) predicted values revealed a strong positive correlation. The R^2 and p-values (table 20) suggest that changes in actual soil concentrations are generally reflected in changes in the predicted values. Despite several low R^2 -values the consistently low p-values imply the data are strongly correlated and the relationship is statistically significant at the 95% confidence level.

Table 20: R^2 and p-values for regression analysis of true soil values and final predicted values.

<i>Domain</i>		1	2	3	4	5	6	7
K	n	462	1313	396	137	1123	469	1708
	R^2	0.6594	0.5175	0.7292	0.5883	0.5720	0.5352	0.6678
	p	<0.05	<0.05	<0.05	<0.05	<0.05	<0.05	<0.05
U	n	462	1313	396	137	1123	469	1708
	R^2	0.4748	0.0758	0.3366	0.4224	0.2120	0.1214	0.1304
	p	<0.05	<0.05	<0.05	<0.05	<0.05	<0.05	<0.05
Th	n	462	1313	396	137	1123	469	1708
	R^2	0.5014	0.4584	0.7014	0.4834	0.6146	0.4465	0.6877
	p	<0.05	<0.05	<0.05	<0.05	<0.05	<0.05	<0.05



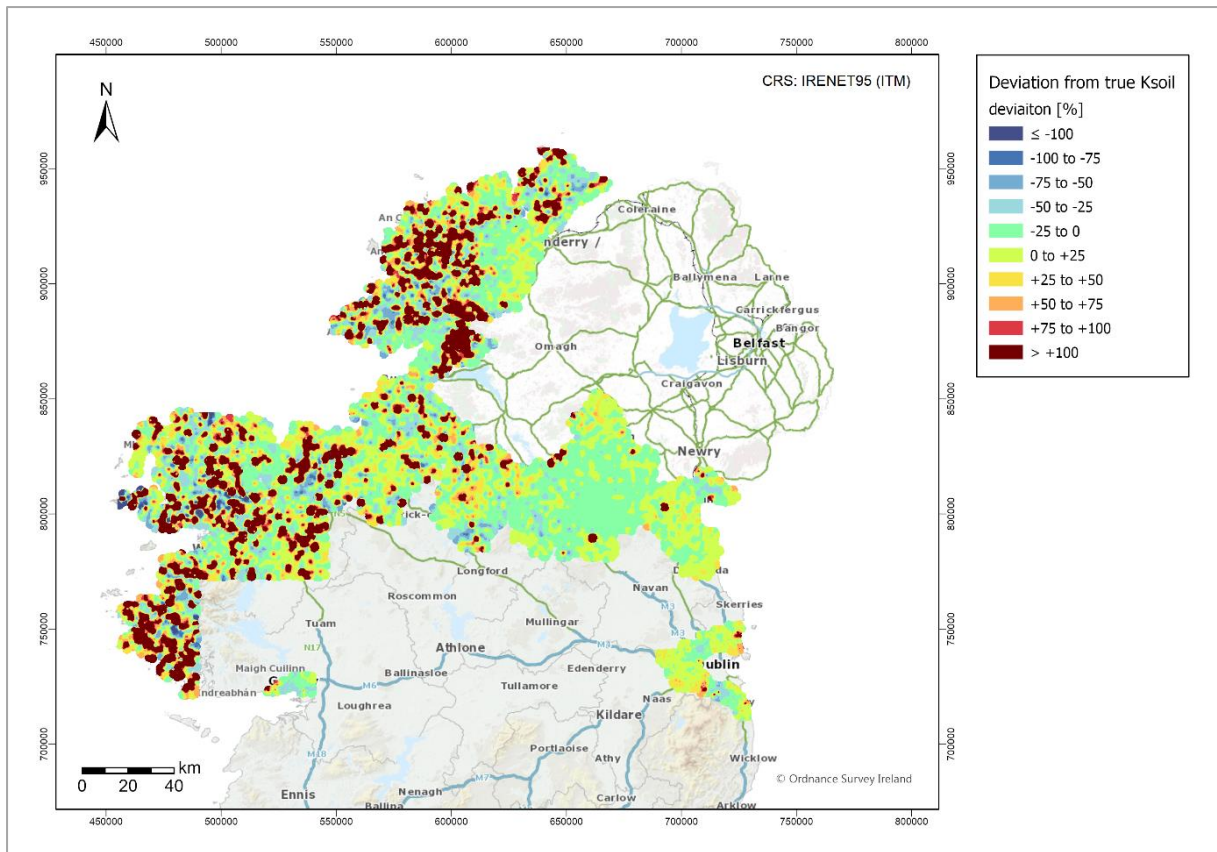


Figure 67: Map of % deviation of predicted K_{soil} concentrations from true values.

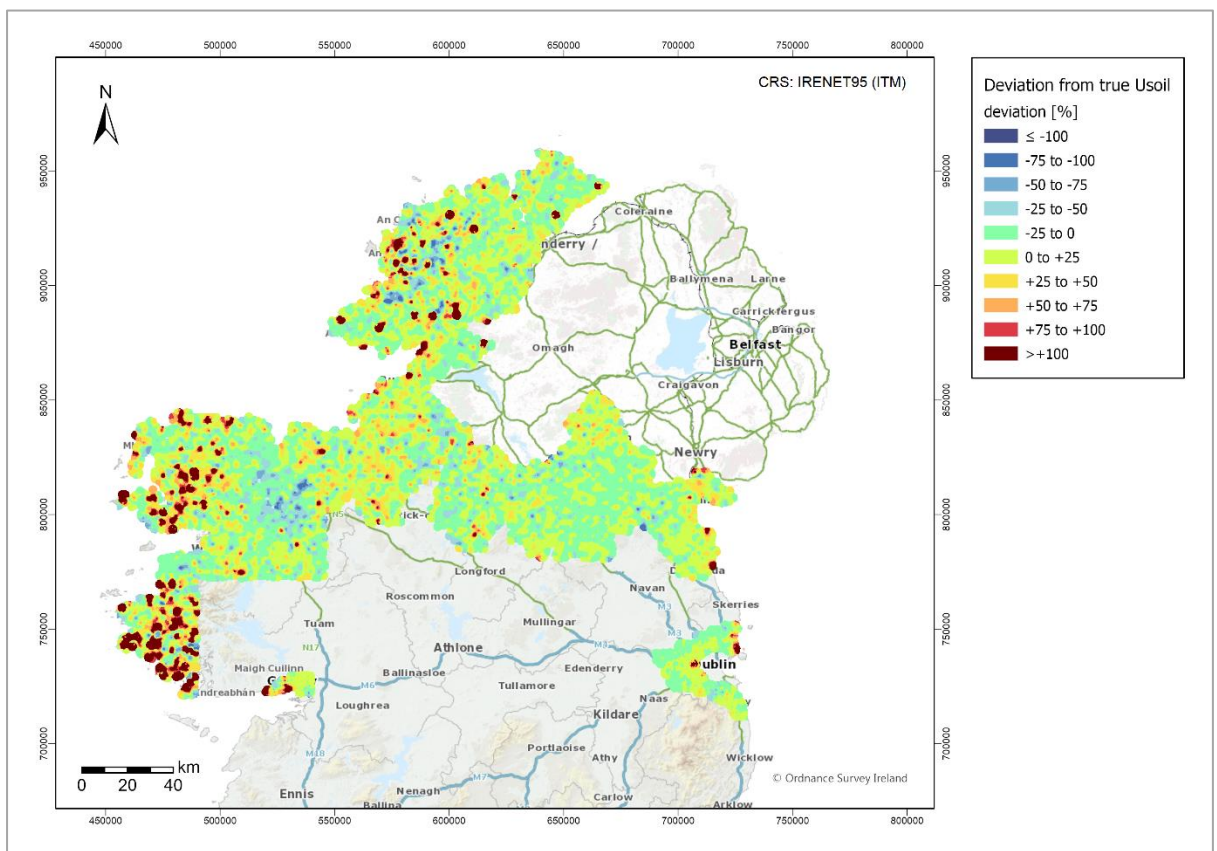


Figure 68: Map of % deviation of predicted U_{soil} concentrations from true values.



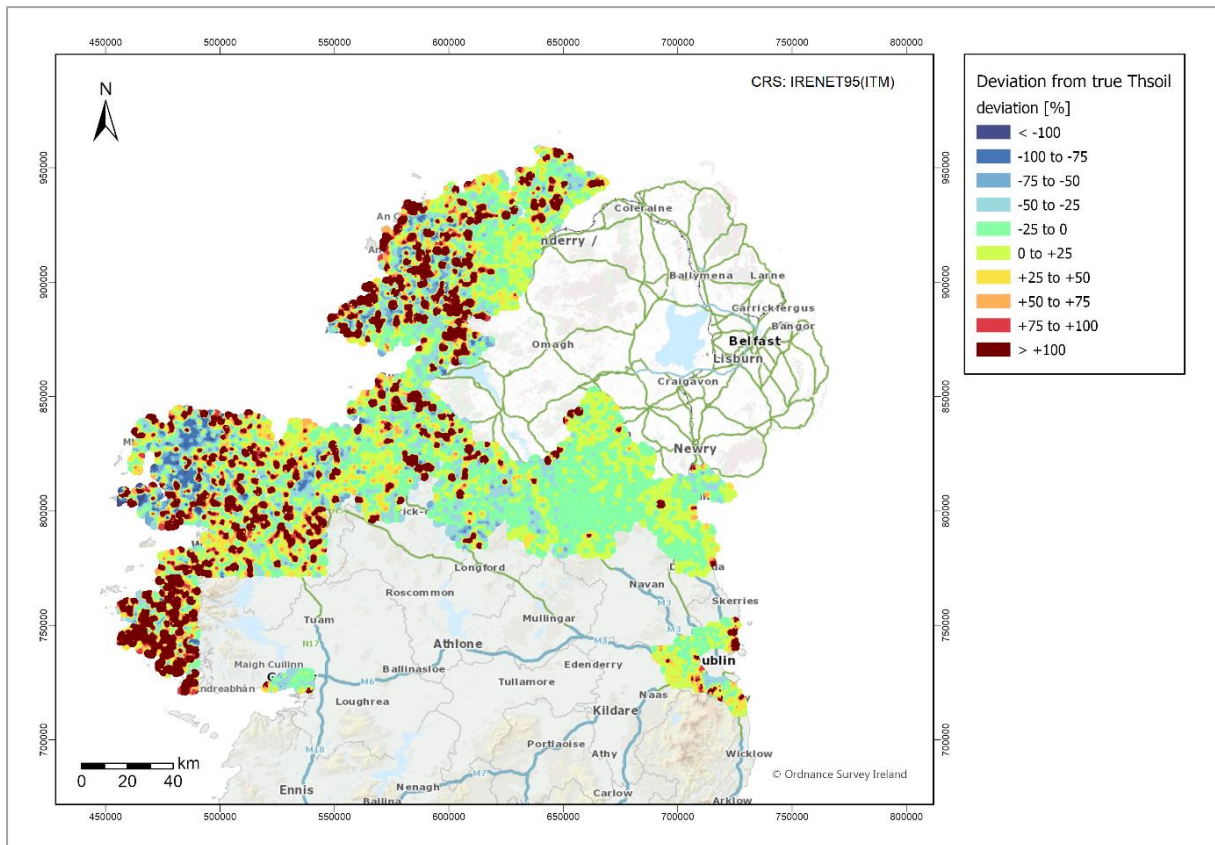


Figure 69: Map of % deviation of predicted Th_{soil} concentrations from true values.

6.3.1. Prediction errors

% Deviation (+/-) from the true soil concentration is mapped in figures 67-69. Despite poorer correlation (table 25) the uranium map (figure 71) shows fewer inaccurately predicted areas suggesting a few extreme outliers are skewing the average. Areas coinciding with peat do not appear to have been accurately predicted which is expected considering the weaker correlation in many “peat only” scatterplots (figures A.32-A.39). The maps show neighbouring overpredicted and underpredicted points, suggesting many of these errors could be related to intra-peat variations in thickness and saturation (Beamish 2013), the coincidence of peat deposits and rock outcrops, or the airborne survey footprint as previously discussed.

The geographical distribution of poorly predicted concentrations also indicates topography could be a factor. Deviations from true K_{soil} of more than 100% (+/-) are superimposed on a map of survey altitude and a hillshade map in figures 70 and 71, respectively.



Several points coincide with high fly zones wherein the radiometric measurement is considerably less reliable (Minty 1997), however there are still numerous errors which cannot be explained by altitude, particularly in south Donegal and north Mayo (areas mapped as peat).

Poor predictions in several areas may be explained by relief (figure 71). When flying over areas of rapidly changing slope it is unlikely the aircraft will be able to ascend and descend quickly enough to maintain a constant height above ground level, and as mentioned earlier the changing angle subtended by the ground can lead to higher counts over steep valleys (Schwarz *et al.* 1992), hence the inaccurate predictions may not necessarily intersect the areas of greatest altitude. However, there are still errors that cannot be explained by topography so further investigation and model refinement is needed.

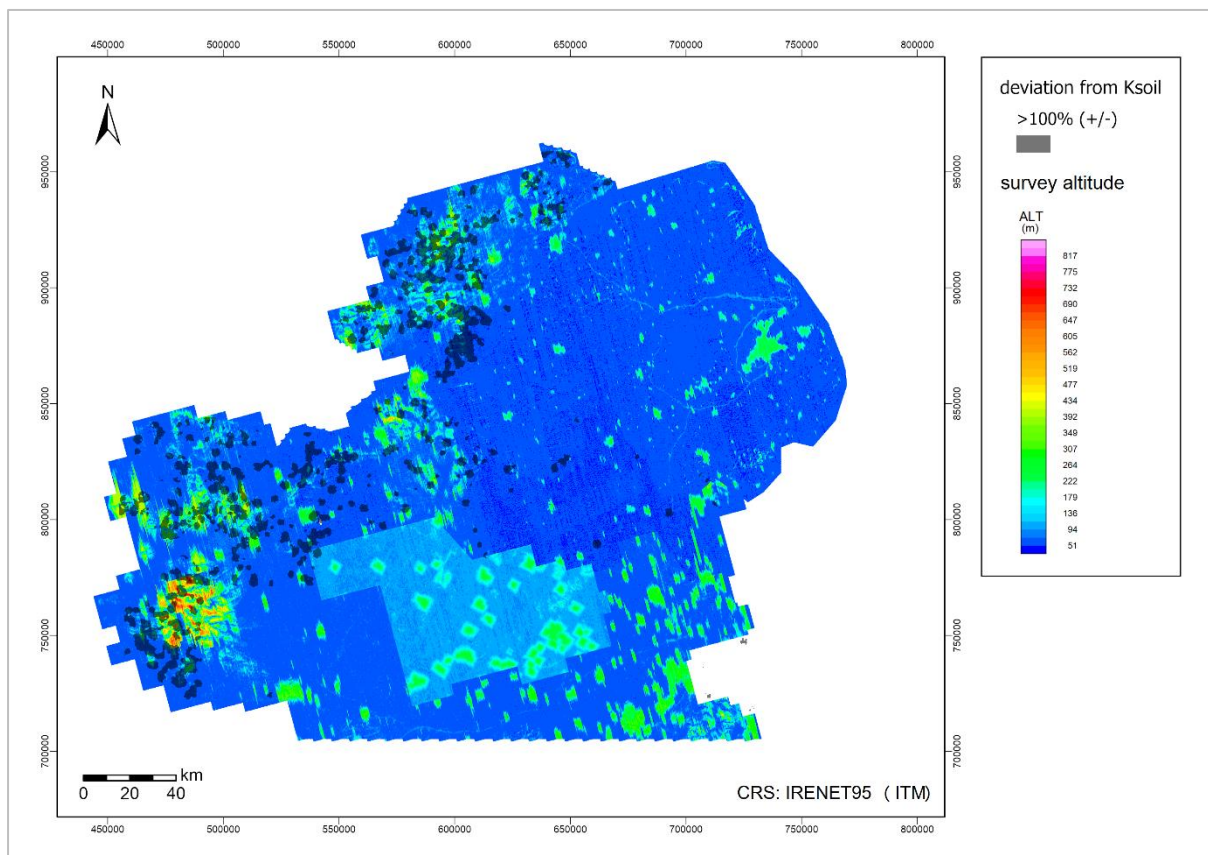


Figure 70: Poorly predicted K_{soil} values (absolute deviation >100%) superimposed on a map of survey altitude.



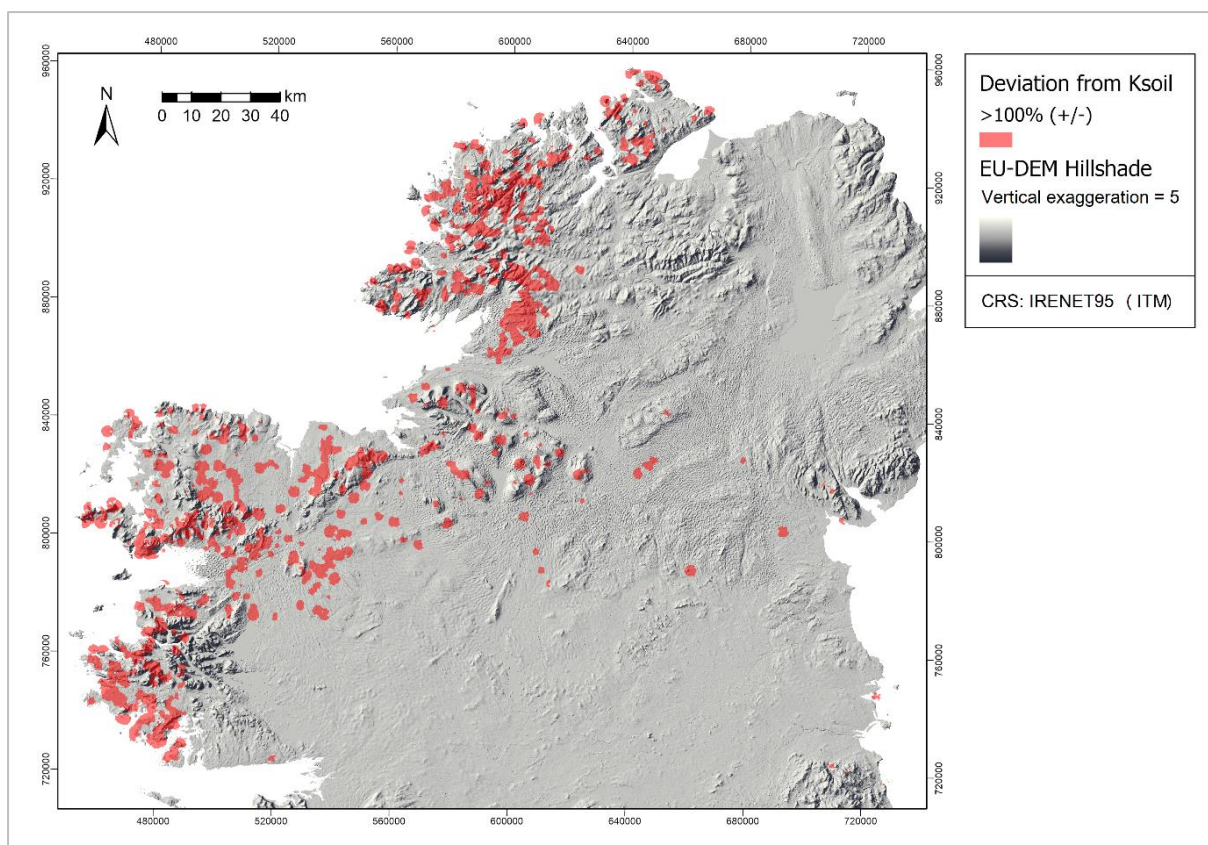


Figure 71: Poorly predicted K_{soil} values (absolute deviation >100%) superimposed on a shaded relief map.

6.3.2. High resolution predicted geochemical maps

The final set of regression equations (E) were used to generate high resolution maps of predicted soil K, U and Th concentrations using the full radiometric dataset (i.e., one point every 60 x 200 m) for the northern half of the island of Ireland (shown alongside existing XRFs soil data, figures 72-74). Note the percentile classification is based on that of the smaller study area. XRFs soil data is not available for this larger area, nor are other higher density soil data to assess the accuracy of the predicted maps, however these maps serve as an example of the resolution that can be achieved if soil concentrations of K, U and Th can be accurately and reliably modelled using airborne radiometric data.



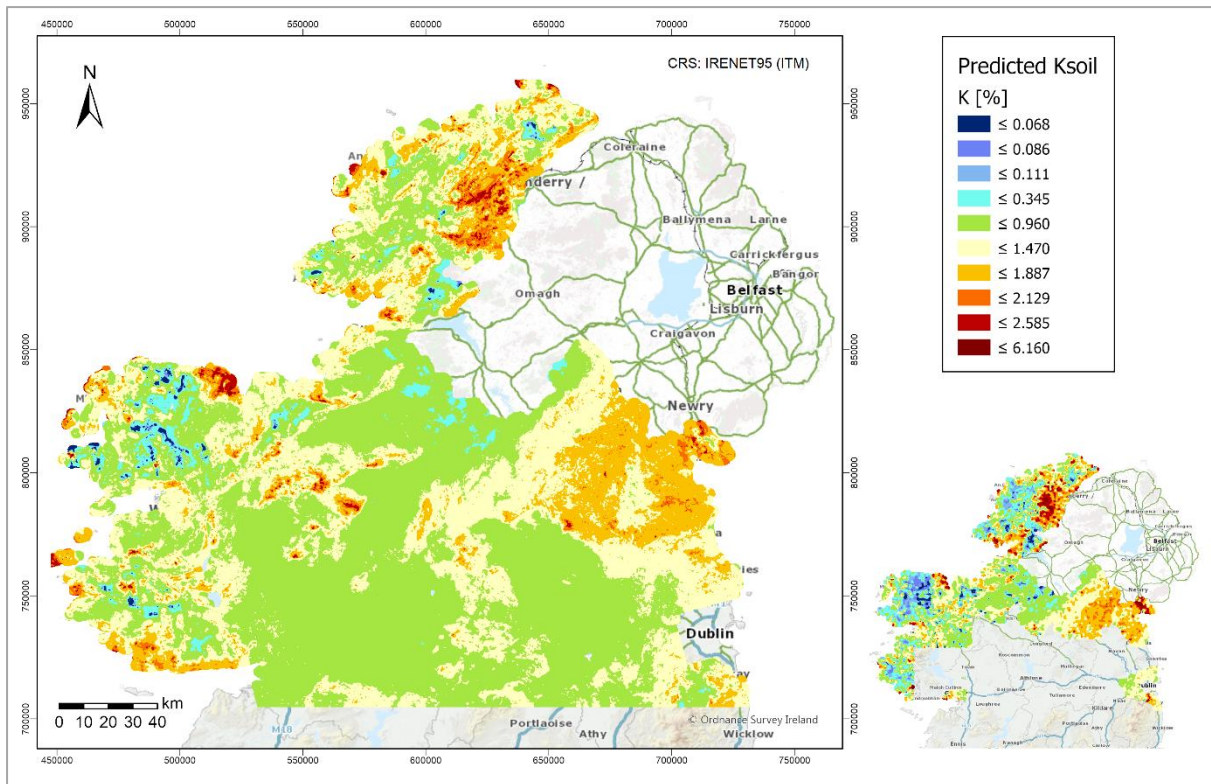


Figure 72: High resolution predicted K_{soil} map (classified according to true K_{soil} percentile values for G1, G3, G6) calculated using final set of regression equations (E) for all radiometric points.

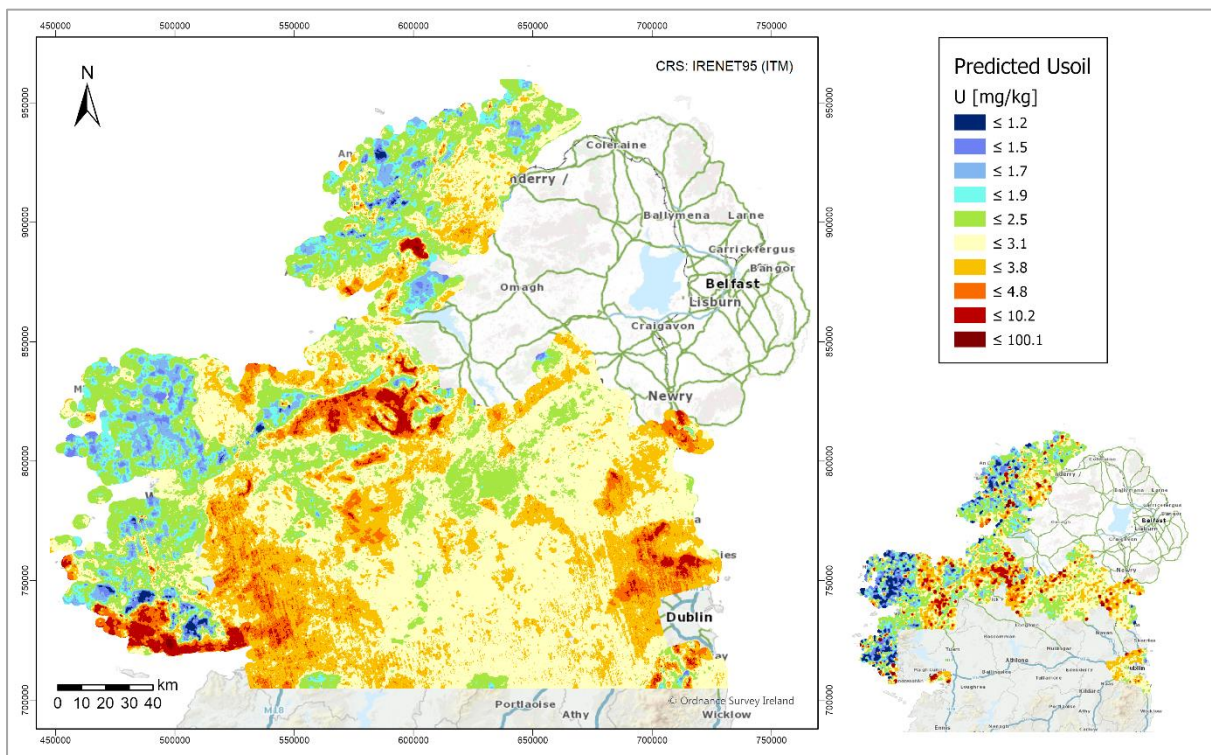


Figure 73: High resolution predicted U_{soil} map (classified according to true U_{soil} percentile values for G1, G3, G6) calculated using final set of regression equations (E) for all radiometric points.



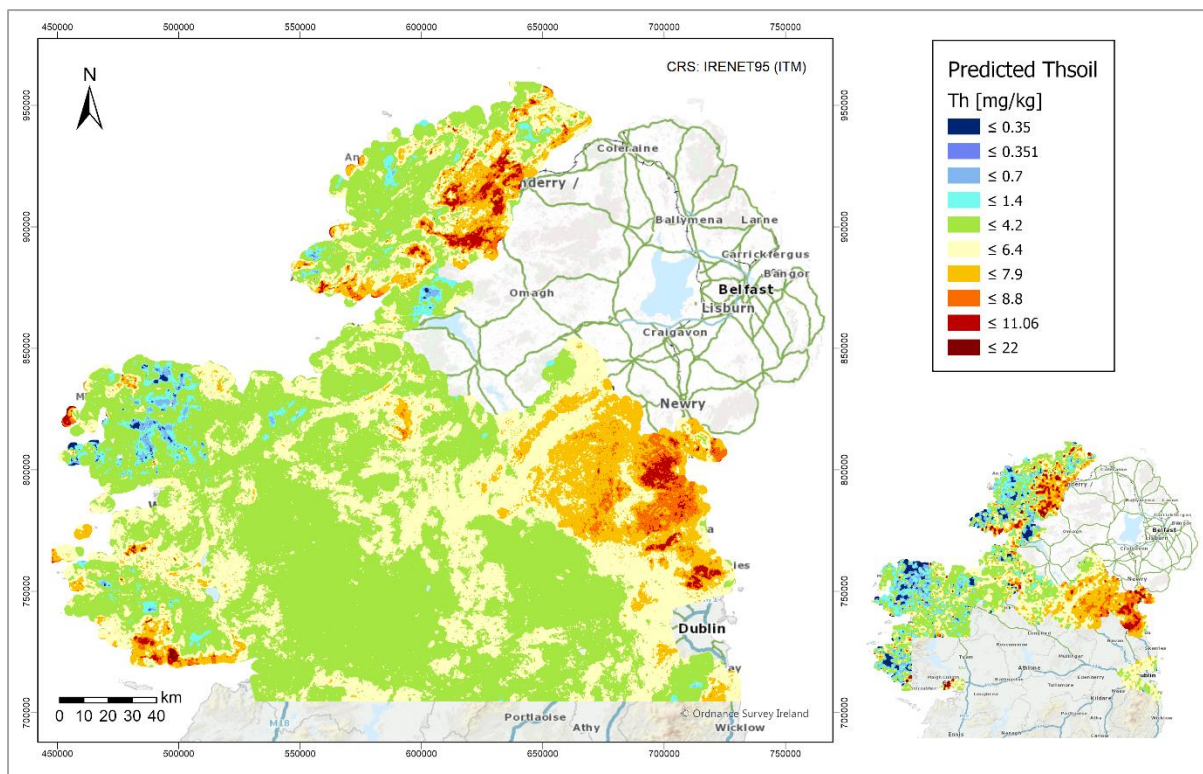


Figure 74: High resolution predicted Th_{soil} map (classified according to true Th_{soil} percentile values for G1, G3, G6) calculated using final set of regression equations (E) for all radiometric points.



7. Conclusions

This research could be considered a scoping study, aimed at investigating the relationship between geochemical and airborne radiometric measurements of K, U and Th concentrations. A positive linear correlation between the datasets was found, with interpolated maps showing similar distributions of radioelement concentrations as measured by the respective methods. Median concentrations were generally lower in soil for ICP_{ar} analyses, particularly for K. Radioelement *Aqua Regia* extraction rates varied between Geochemical Domains and soil types (mineral, organic) thus ICP_{ar} soil data were considered unsuitable for assessment of the relationship between the datasets. Substituting XRFs data found typical soil concentrations exceed those measured by gamma-ray spectrometry, with median *soil:air* ratios of 1.32 (K), 2.75 (U) and 1.4 (Th).

Radioelement distributions varied across different bedrock geological units and soil parent materials, however changes in soil concentrations were usually accompanied by comparable changes in radiometric concentrations. Ratios higher and lower than average are associated with ground conditions that exhibit “unique” gamma-ray attenuation behaviour such as saturated peat deposits and shallow or outcropping bedrock, as evidenced by multimodal distributions of $X_{\text{soil}}/X_{\text{air}}$ values in such areas. It was concluded that variations in the soil-radiometric relationship between domains and geological units are due to the different soil properties characteristic of each, rather than the underlying geochemistry.

Soil texture appeared to influence the relationship, and lower *soil:air* ratios for materials less likely to contain large lithics suggested that their presence could decrease the ‘bulk’ radiometric signal relative to measured soil concentrations. Other variations may be attributed to the sensitivity of different soils to changes in saturation. Land use was also a factor however sample size disparity and conflicting soil sampling criteria rendered this investigation inconclusive. Interrelationships between land use and soil properties were also noted as a probable cause of some variation.

Using a set of linear regression equations (for areas with and without peat, by domain) to predict soil concentrations based on radiometric data proved effective, although values were poorly predicted across areas of blanket bog. It was concluded from this result that intra-peat variations are a significant factor that must be accounted for if the accuracy is to be improved, however terrain influences should not be ruled out.



8. Recommendations For Further Work

Based on the findings of this study the following recommendations are made to further understand the relationship between geochemical and airborne radiometric datasets and improve the accuracy of predicted soil concentrations of K, U and Th:

- i. Conduct statistical tests such as ANOVA (analysis of variance) to determine how much of the variation in the soil-radiometric relationship can be attributed to changes in geology, soil texture, saturation, organic matter content, etc. (Cinelli *et al.* 2018) and incorporate these parameters in the linear regression model to improve predictions. Principal Component Analysis could also be used to reduce a large number of contributing factors to several principal components which explain most of the variance, however if categorical variables such as soil texture are to be used “numeric quantifiers” must be applied to data classes to transform these parameters into continuous variables (de Sousa Mendes and Miller Devós Ganga 2013).
- ii. Employ hand-held gamma-ray spectrometers to measure radioelement concentrations at soil sample sites to determine which variations can be attributed to gamma-ray attenuation in the subsurface and which relate to the footprint of the airborne survey and/or terrain effects.
- iii. Collect in-situ soil moisture data at the time of the airborne survey or use Tellus electromagnetic survey data to estimate soil moisture. This information would facilitate a better understanding of gamma-ray attenuation across the study area, improve X_{soil} predictions over areas of peat with substantial internal heterogeneity, and allow radon emanation to be modelled (Sasaki *et al.* 2004) to improve estimates of eU.
- iv. Carry out high resolution geochemical and radiometric surveys across a smaller study area with homogeneous geological conditions or land use to reduce the number of variables and assess the effects of local ground conditions on the relationship.



References

- Ahmed, H., Young, S. and Shaw, G. (2012). Solubility and mobility of thorium and uranium in soils: the effect of soil properties on Th and U concentrations in soil solution. In: *Geophysical Research Abstracts - EGU General Assembly 2012*.
- Appleton, J.D., Miles, J.C.H., Green, B.M.R. and Larmour, R. (2008). Pilot study of the application of Tellus airborne radiometric and soil geochemical data for radon mapping. *Journal of Environmental Radioactivity*, 99(10), pp.1687–1697.
- Banks, D., Sather, O.M., Ryghaug, P. and Reimann, C. (2001). Hydrochemical distribution patterns in stream waters, Trøndelag, central Norway. *Science of The Total Environment*, 267(1-3), pp.1–21.
- Beamish, D. and Farr, G. (2013). Airborne geophysics: a novel approach to assist hydrogeological investigations at groundwater-dependent wetlands. *Quarterly Journal of Engineering Geology and Hydrogeology*, 46(1), pp.53 – 62.
- Beamish, D. (2013). Gamma ray attenuation in the soils of Northern Ireland, with special reference to peat. *Journal of Environmental Radioactivity*, 115, pp.13–27.
- Beamish, D. (2014). Peat mapping associations of airborne radiometric survey data. *Remote Sensing*, 6, pp.521 – 539.
- Beamish, D. (2015). Relationships between gamma-ray attenuation and soils in SW England. *Geoderma*, 259-260, pp.174–186.
- Bednar, A.J., Gent, D.B., Gilmore, J.R., Sturgis, T.C. and Larson, S.L. (2004). Mechanisms of thorium migration in a semiarid soil. *Journal of Environmental Quality*, 33(6), pp.2070–2077.
- Billings, S. and Hovgaard, J. (1999). Modelling detector response in airborne gamma-ray spectrometry. *Geophysics*, 64(5), pp.1378 – 1392.
- Browne, M.A. and Gallagher, V. (2020). *Tellus geochemical survey: shallow topsoil multi-element maps for the northern half of Ireland*. Dublin.
- Chen, F.-W. and Liu, C.-W. (2012). Estimation of the spatial rainfall distribution using inverse distance weighting (IDW) in the middle of Taiwan. *Paddy and Water Environment*, 10(3), pp.209–222.
- Childs, C. (2004). Interpolating surfaces in ArcGIS Spatial Analyst. *ArcUser (ESRI)*, Summer, pp.32 – 35.
- Cinelli, G., Brattich, E., Coletti, C., De Ingeniis, V., Mazzoli, C., Mostacci, D., Sassi, R. and Tositti, L. (2020). Terrestrial gamma dose rate mapping (Euganean Hills, Italy): comparison between field measurements and HPGe gamma spectrometric data. *Radiation Effects and Defects in Solids*, 175(1-2), pp.54–67.
- Cinelli, G., De Cort, M. and Tollefsen, T. (2019). *Chapter 3: Terrestrial Radionuclides. European Atlas of Natural Radiation (EC)*. Luxembourg.



Cinelli, G., Tondeur, F., Dehandschutter, B., Bossew, P., Tollefsen, T. and De Cort, M. (2017). Mapping uranium concentration in soil: Belgian experience towards a European map. *Journal of Environmental Radioactivity*, 166, pp.220 – 234.

Cinelli, G., Tondeur, F. and Dehandschutter, B. (2018). Mapping potassium and thorium concentrations in Belgian soils. *Journal of Environmental Radioactivity*, 184-185, pp.127–139.

Dierke, C. and Werban, U. (2013). Relationships between gamma-ray data and soil properties at an agricultural test site. *Geoderma*, 199, pp.90–98.

Duffy, P., Black, K., Fahey, D., Hyde, B., Kehoe, A., Murphy, J., Quirke, B., Ryan, A.M. and Ponzi, J. (2020). *Ireland's National Inventory Report 2020: Greenhouse gas emissions 1990-2018 reported to the united nations framework convention on climate change*. [online] Wexford. Available at: <www.epa.ie> [Accessed 12 Sep. 2021].

Duval, J.S., Cook, B. and Adams, J.A.S. (1971). Circle of investigation of an air-borne gamma-ray spectrometer. *Journal of Geophysical Research*, 76(35), pp.8466–8470.

Egli, M. and Poulencard, J. (2017). Soils of Mountainous Landscapes. In: D. Richardson, N. Castree, M.F. Goodchild, A. Kobayashi, W. Liu and R.A. Marston, eds. *International Encyclopedia of Geography: People, the Earth, Environment and Technology*. [online] Hoboken: Wiley-Blackwell Publishing, Inc. pp.1–10. Available at: <<https://onlinelibrary.wiley.com/doi/full/10.1002/9781118786352.wbieg0197>> [Accessed 21 Sep. 2021].

Elío, J., Crowley, Q., Scanlon, R., Hodgson, J., Long, S., Cooper, M. and Gallagher, V. (2020). Application of airborne radiometric surveys for large-scale geogenic radon potential classification. *Journal of the European Radon Association*, 1, pp.4358 – 4370.

Fall, M., Baratoux, D., Jessell, M., Ndiaye, P.M., Vanderhaeghe, O., Moyen, J.F., Baratoux, L. and Bonzi, W.M.E. (2020). The redistribution of thorium, uranium, potassium by magmatic and hydrothermal processes versus surface processes in the Saraya Batholith (Eastern Senegal): Insights from airborne radiometrics data and topographic roughness. *Journal of Geochemical Exploration*, 219.

Gallagher, V., Knights, K., Carey, S., Glennon, M. and Scanlon, R. (2016). *Atlas of Topsoil Geochemistry of the Northern Counties of Ireland: Data from the Tellus and Tellus Border Projects*. [online] Available at: <https://secure.dccae.gov.ie/GSI_DOWNLOAD/Tellus/PDFs/EBook_Topsoils_Final_03Feb2016.pdf>.

Gaudino, S., Galas, C., Belli, M., Barbizzi, S., de Zorzi, P., Jaćimović, R., Jeran, Z., Pati, A. and Sansone, U. (2007). The role of different soil sample digestion methods on trace elements analysis: a comparison of ICP-MS and INAA measurement results. *Accreditation and Quality Assurance*, [online] 12(2), pp.84–93. Available at: <<https://link.springer.com/article/10.1007/s00769-006-0238-1>> [Accessed 9 Sep. 2021].

Glennon, M., Gallagher, V., Meehan, R. and Hodgson, J. (2020). *Geochemical Characterization and Geochemically Appropriate Levels for Soil Recovery Facilities*. [online] Available at:



<<https://www.gsi.ie/en-ie/publications/Pages/Geochemical-Characterization-and-Geochemically-Appropriate-Levels-for-Soil-Recovery-Facilities.aspx>>.

Government of Ireland (2019). *Climate Action Plan 2019 To Tackle Climate Breakdown*.

Grasty, R.L. and Minty, B.R.S. (1995). *A guide to the technical specifications for airborne gamma-ray surveys*. *Record* 1995/060. [online] Canberra. Available at: <<http://pid.geoscience.gov.au/dataset/ga/14861>>.

Grasty, R.L. (1997). Radon emanation and soil moisture effects on airborne gamma-ray measurements. *Geophysics*, 62(5), pp.1379 – 1385.

GSI (n.d.-a). *Tellus*. [online] Geological Survey Ireland - Programmes and Projects. Available at: <www.gsi.ie/tellus>. [Accessed 12 Sep. 2021].

GSI (n.d.-b). *Karst databases*. [online] Programmes and Projects - Groundwater and Geothermal Unit - Activities - Understanding Irish Karst. Available at: <<https://www.gsi.ie/en-ie/programmes-and-projects/groundwater-and-geothermal-unit/activities/understanding-irish-karst/Pages/Karst-databases.aspx>> [Accessed 19 Sep. 2021].

Guagliardi, I., Buttafuoco, G., Apollaro, C., Bloise, A., De Rosa, R. and Cicchella, D. (2013). Using gamma-ray spectrometry and geostatistics for assessing geochemical behaviour of radioactive elements in the Lese Catchment (southern Italy). *International Journal of Environmental Research*, 7(3), pp.645–658.

Guimaraes, S.N.P., Hamza, V.M. and da Silva, J.J. (2013). Airborne geophysical surveys in the north-central region of Goias (Brazil): implications for radiometric characterization of tropical soils. *Journal of Environmental Radioactivity*, 116, pp.10 – 18.

Von Gunten, H.R., Surbeck, H. and Rössler, E. (1996). Uranium Series Disequilibrium and High Thorium and Radium Enrichments in Karst Formations. *Environmental Science and Technology*, 30(4), pp.1268–1274.

Harmsen, K. and de Haan, F.A.M. (1980). Occurrence and behaviour of uranium and thorium in soil and water. *Netherlands Journal of Agricultural Science*, 28, pp.40–62.

Helling, C.S., Chesters, G. and Corey, R.B. (1964). Contribution of Organic Matter and Clay to Soil Cation-Exchange Capacity as Affected by the pH of the Saturating Solution. *Soil Science Society of America Journal*, 28(4), pp.517–520.

Hodgson, J.A., Knights, K. V., Glennon, M., Carey, S. and Ture, M.D. (2013). Airborne Radiometric Data Assessment and Comparison with Topsoil Geochemical U, Th and K. In: *Near Surface Geoscience 2013*. [online] Bochum, Germany. Available at: <<https://sci-hub.se/10.3997/2214-4609.20131436>> [Accessed 12 Sep. 2021].

IAEA (2003). *Guidelines for radioelement mapping using gamma ray spectrometry data*. Vienna.

IAEA (2010). *Radioelement Mapping - IAEA Nuclear Energy Series No. NF-T-1.3*. Vienna.

IPCC (2013). *2013 Supplement to the 2006 IPCC Guidelines for National Greenhouse Gas Inventories*:



Wetlands . [online] Switzerland. Available at: <<https://www.ipcc.ch/publication/2013-supplement-to-the-2006-ipcc-guidelines-for-national-greenhouse-gas-inventories-wetlands/>> [Accessed 12 Sep. 2021].

Jones, D.G., Scheib, C., Cuss, R.J. and Rawline, B.G. (2007). *A preliminary interpretation of Tellus airborne radiometric data*. Keyworth.

Kirkwood, C., Cave, M., Beamish, D., Grebby, S. and Ferreira, A. (2016). A machine learning approach to geochemical mapping. *Journal of Geochemical Exploration*, 167, pp.49–61.

Kisser, M.I. (2005). *Digestion of solid matrices Part 1: Digestion with Aqua Regia - Report of evaluation study*. [online] Austria. Available at: <<http://citeseerx.ist.psu.edu/viewdoc/download?doi=10.1.1.487.3715&rep=rep1&type=pdf>> [Accessed 23 Sep. 2021].

Knights, K. V., Szpak, M., Mather, J. and Collins, L. (2020). *Tellus geochemical survey: shallow topsoil data from the border and west of Ireland*.

Kock, P. and Samuelsson, C. (2011). Comparison of airborne and terrestrial gamma spectrometry measurements - evaluation of three areas in southern Sweden. *Journal of environmental radioactivity*, 102(6), pp.605–613.

Lee, M., Hunter-Williams, N., Meehan, R., Kelly, C., Kabza, M., Murphy, O. and Spillane, M. (2008). Groundwater Vulnerability Mapping. In: *Irish National Hydrology Conference 2008*. [online] Available at: <<https://hydrologyireland.ie/wp-content/uploads/2018/11/04-Groundwater-vulnerability-mapping-Lee-M.pdf>> [Accessed 21 Sep. 2021].

Løvborg, L. (1984). *The calibration of portable and airborne gamma-ray spectrometers Theory, problems, and facilities*.

Manning, D.A.C. (2010). Mineral sources of potassium for plant nutrition. A review. *Agronomy for Sustainable Development*, 30(2), pp.281–294.

Met Éireann (2018). *1981-2010 Annual Average Rainfall Grid*. [online] Rainfall - Rainfall Climate of Ireland. Available at: <https://www.met.ie/cms/assets/uploads/2018/07/IE_AAR_8110_V1.txt>. [Accessed 19 Sep. 2021].

Minty, B.R.S. (1997). Fundamentals of airborne gamma-ray spectrometry. *AGSO Journal of Australian Geology & Geophysics*, 17(2), pp.39–50.

Moonjun, R., Pkha Shrestha, D., Jetten, V.G. and van Ruitenbeek, F.J.A. (2017). Application of airborne gamma-ray imagery to assist soil survey: A case study from Thailand. *Geoderma*, 289, pp.196–212.

O'Connor, P.J., Gallagher, V., Madden, J.S., van den Boom, G., McLaughlin, J.P., McAulay, I.R., Barton, K.J., Duffy, J.T., Muller, R., Grimley, S., Marsh, D., Mackin, G. and MacNiocaill, C. (1993). *Assessment of the geological factors influencing the occurrence of radon hazard areas in a karstic region*. [online] Dublin. Available at: <http://www.burrengeopark.ie/wp-content/uploads/2014/08/GSI-Assessment_of_the_geological_factors_influenc.pdf> [Accessed 19



Sep. 2021].

Paasche, H. and Eberle, D.G. (2010). Regional geochemical mapping constrained by airborne radiometric data and satellite imagery. In: *EGM 2010 International Workshop: Adding new value to Electromagnetic, Gravity and Magnetic Methods for Exploration. Capri, Italy, April 11-14, 2010.*

Pitkin, J.A. and Duval, J.S. (1980). Design parameters for aerial gamma-ray surveys. *Geophysics*, 45(9), pp.1427–1439.

Ramsey, M.H., Thompson, M. and Hale, M. (1992). Objective evaluation of precision requirements for geochemical analysis using robust analysis of variance. *Journal of Geochemical Exploration*, 44, pp.23–36.

Rawlins, B.G., Lark, R.M. and Webster, R. (2007). Understanding airborne radiometric survey signals across part of eastern England. *Earth Surface Processes and Landforms*, 32, pp.1503 – 1515.

Rawlins, B.G., Scheib, C., Tyler, A.N. and Beamish, D. (2012). Optimal mapping of terrestrial gamma dose rates using geological parent material and aerogeophysical survey data. *Journal of Environmental Monitoring*, 14(12), pp.3086–3093.

Rock, N.M.S. (1988). Summary statistics in geochemistry: A study of the performance of robust estimates. *Mathematical Geology*, 20(3), pp.243 – 275.

Sander Geophysics (2016). *Technical Report: Fixed-Wing High-Resolution Aeromagnetic, Gamma-ray Spectrometric and Frequency-Domain Electromagnetic Survey. Tellus A1 Block, Republic of Ireland, 2015 for Geological Survey of Ireland.* [online] Available at: <www.sgl.com> [Accessed 24 Aug. 2021].

Sasaki, T., Yasuyoshi, G. and Okuda, T. (2004). Mathematical modeling of radon emanation. *Journal of Nuclear Science and Technology*, 41(2), pp.142 – 151.

Schwarz, G.F., Klingelé, E. and Rybach, L. (1992). How to handle rugged topography in airborne gamma-ray spectrometry surveys. *First Break*, 10(1), pp.11–17.

de Sousa Mendes, G.H. and Miller Devós Ganga, M. (2013). Predicting Success in Product Development: The Application of Principal Component Analysis to Categorical Data and Binomial Logistic Regression. *Journal of Technology Management & Innovation*, 8(3), pp.83–97.

Szpak, M.T., Gallagher, V., Mather, J. and Knights, K. V. (2020). *Tellus geochemical survey: shallow topsoil data from the midlands of Ireland.*

Taylor, M.J., Smettem, K., Pracilio, G. and Verboom, W. (2002). Relationships between soil properties and high-resolution radiometrics, central eastern Wheatbelt, Western Australia. *Exploration Geophysics*, 33, pp.95 – 102.

Teagasc, Fealy, R. and Green, S. (Eds) (2009). *Teagasc-EPA Soils and Subsoils Mapping Project - Final Report.* [online] Wexford. Available at: <www.epa.ie> [Accessed 29 Aug. 2021].

Ture, M. and Muller, M. (2020). *Tellus Interpretation Guide to Airborne Geophysics.*

Ture, M.D. (2020). *Tellus Merge-2019B Airborne Geophysical Technical Report (Operations, Logistics and Data Merging).*



Wang, K., Li, W., Li, S., Tian, Z., Koefoed, P. and Zheng, X. (in press). Geochemistry and cosmochemistry of potassium stable isotopes. *Geochemistry*. [online] Available at: <<https://www.sciencedirect.com/science/article/pii/S0009281921000489>>.

Wetterlind, J., Tourliere, B., Martelet, G., Deparis, J., Saby, N.P.A., Richer de Forges, A.C. and Arrouays, D. (2012). Are there any effects of the agricultural use of chemical fertiliser on elements detected by airborne gamma-spectrometric surveys? *Geoderma*, 173-174, pp.34–41.

Young, M.E. (2016). The Tellus geoscience surveys of the north of Ireland: context, delivery and impacts. In: M.E. Young, ed. *Unearthed: impacts of the Tellus surveys of the north of Ireland*. [online] Dublin: Royal Irish Academy. pp.3–10. Available at: <https://www.ria.ie/sites/default/files/chapter_1_0.pdf> [Accessed 28 Aug. 2021].

Zanin, Y.N., Zamirailova, A.G. and Eder, V. (2016). Uranium, Thorium, and Potassium in Black Shales of the Bazhenov Formation of the West Siberian Marine Basin. *Lithology and Mineral Resources*, 51(1), pp.74–85.



Appendix A: Supplementary Figures

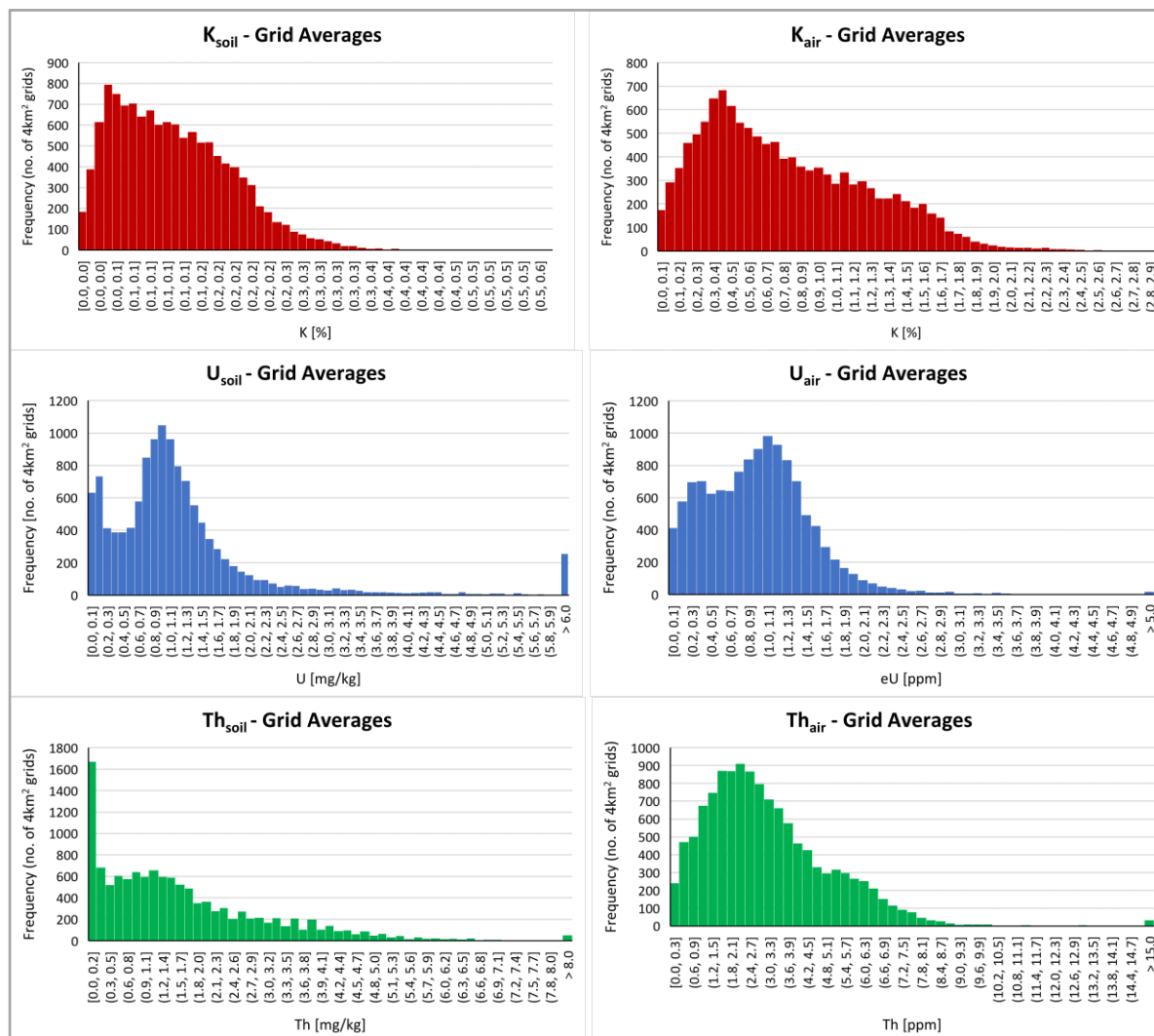


Figure A.1: Distribution of soil (ICP_{ar}) and airborne concentrations for the top half of the island of Ireland (including N.I.), based on 4km² grid square averages.



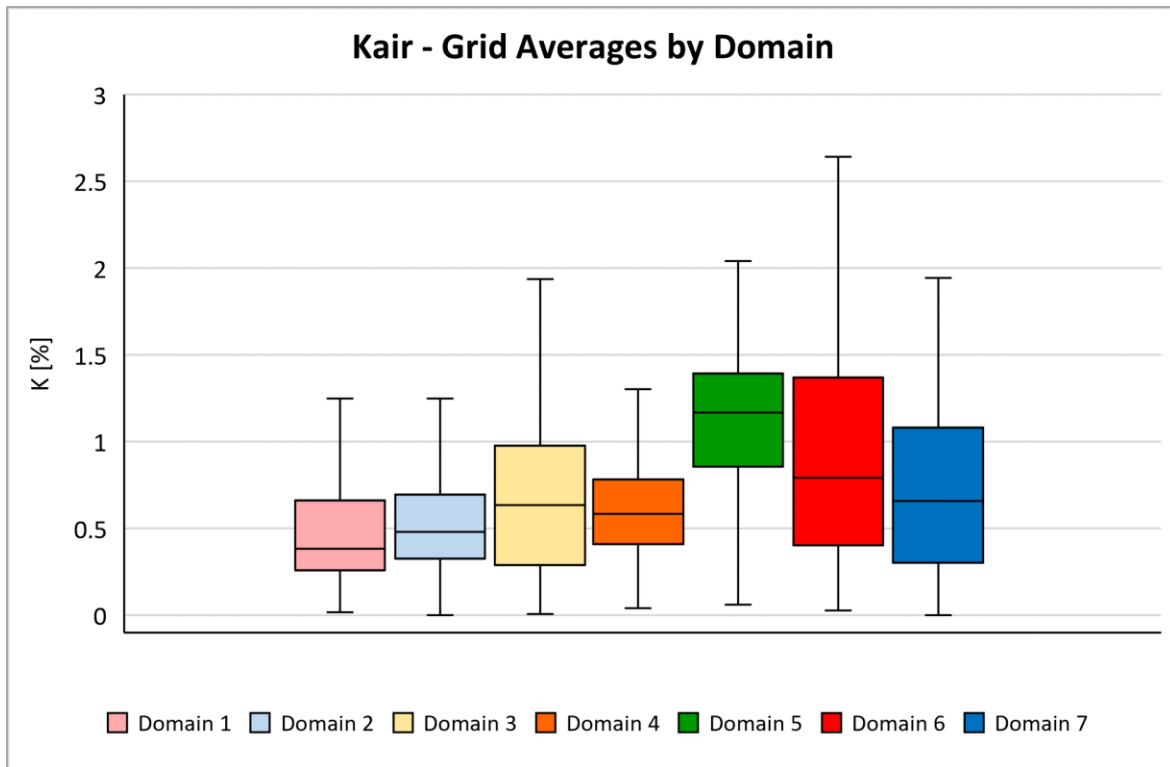


Figure A.2: Boxplot summaries of K_{air} concentrations (average in each 4km^2 grid square) by domain.

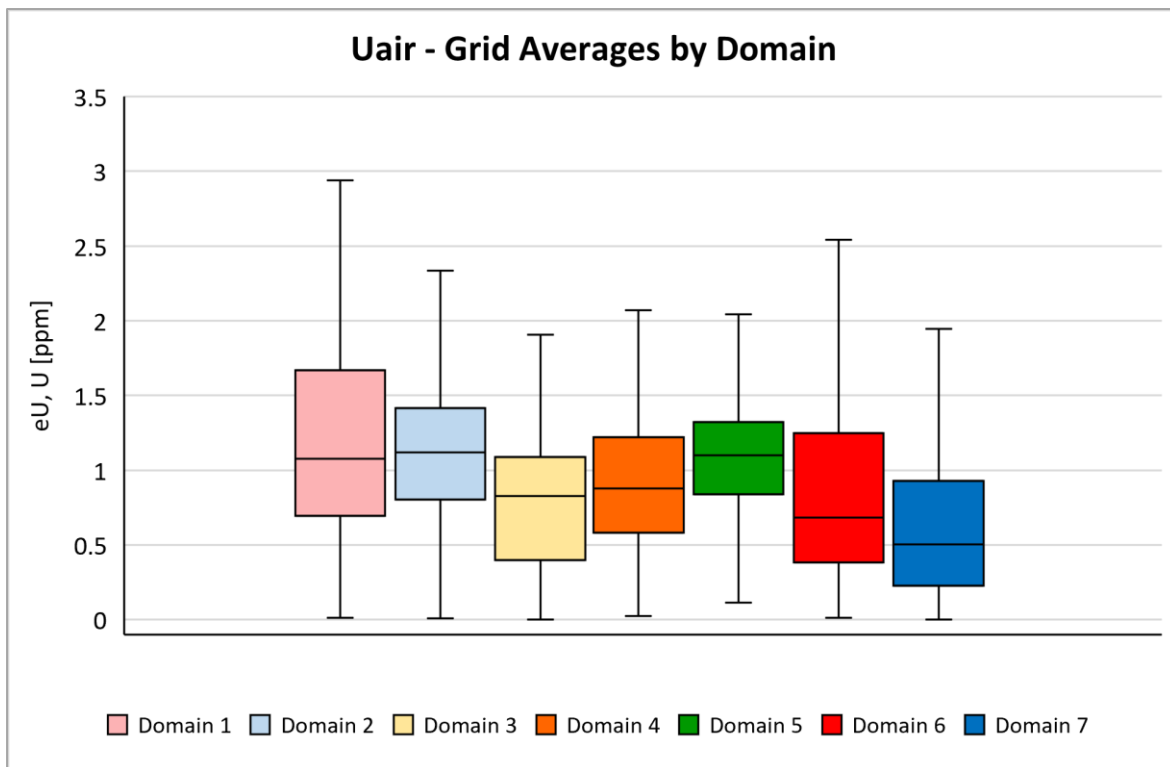


Figure A.3: Boxplot summaries of U_{air} concentrations (average in each 4km^2 grid square) by domain.



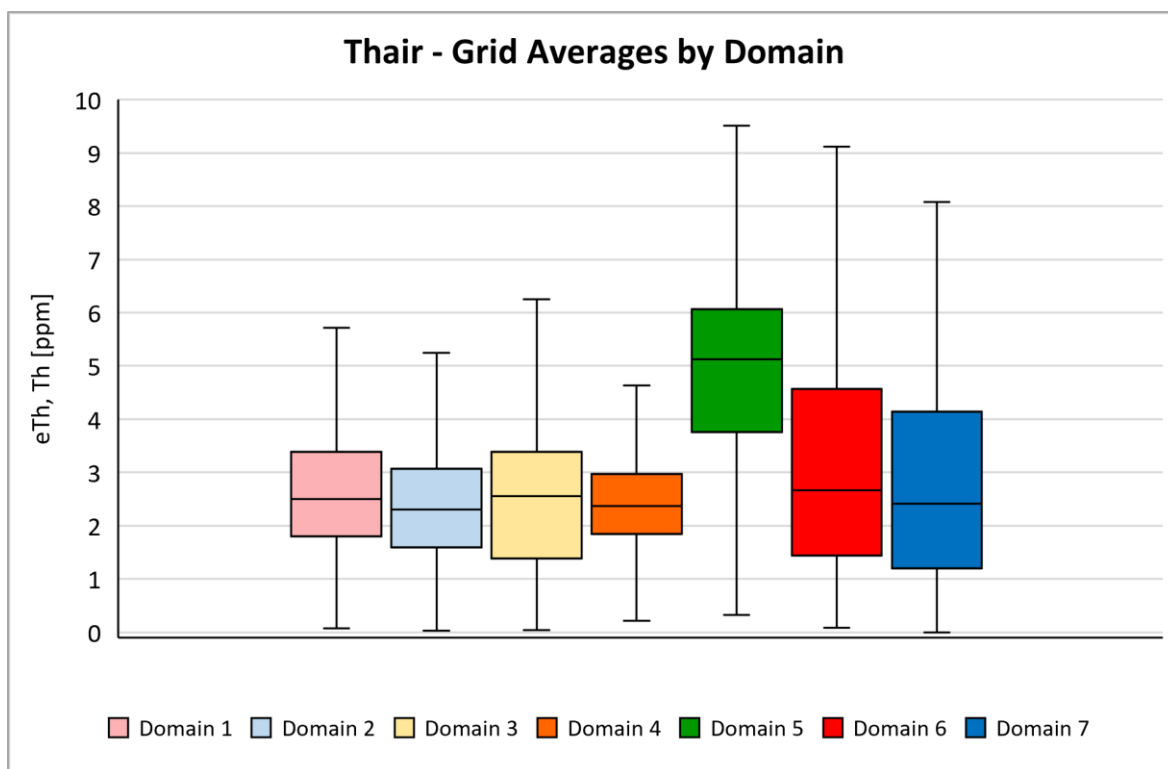


Figure A.4: Boxplot summaries of Th_{air} concentrations (average in each 4km² grid square) by domain.

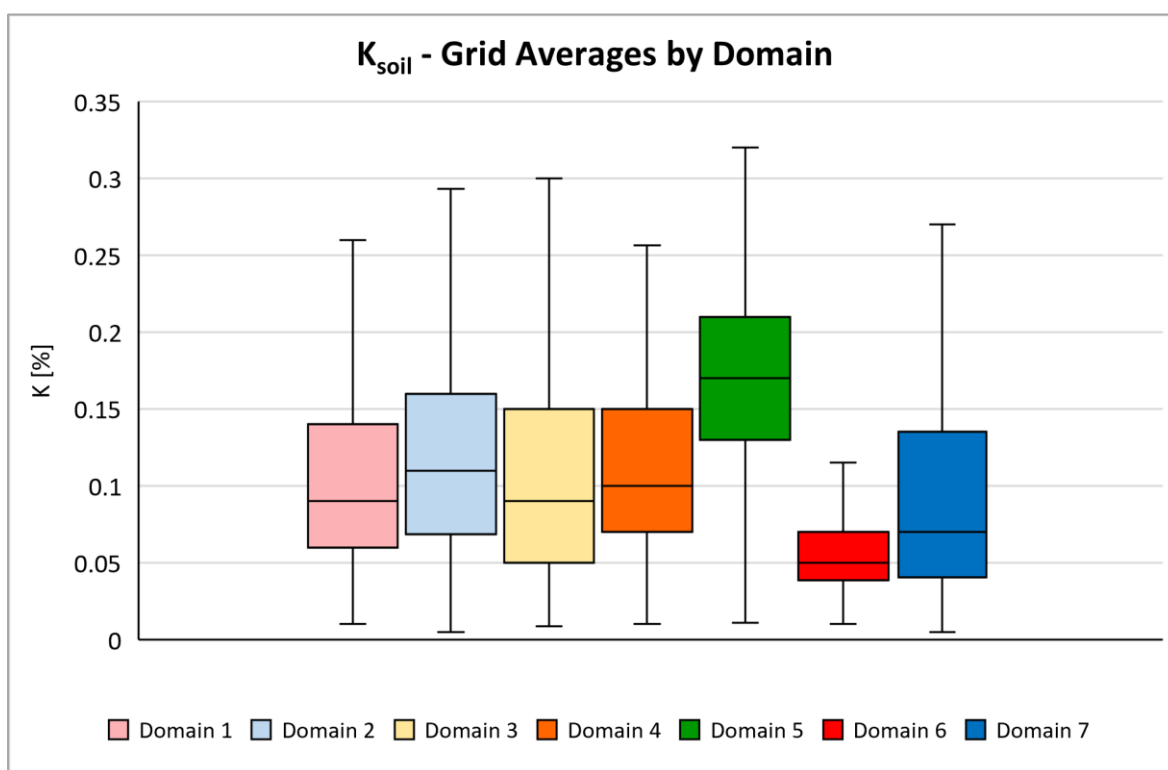


Figure A.5: Boxplot summaries of K_{soil} concentrations (average in each 4km² grid square) (analysed by ICP_{ar}) by domain.



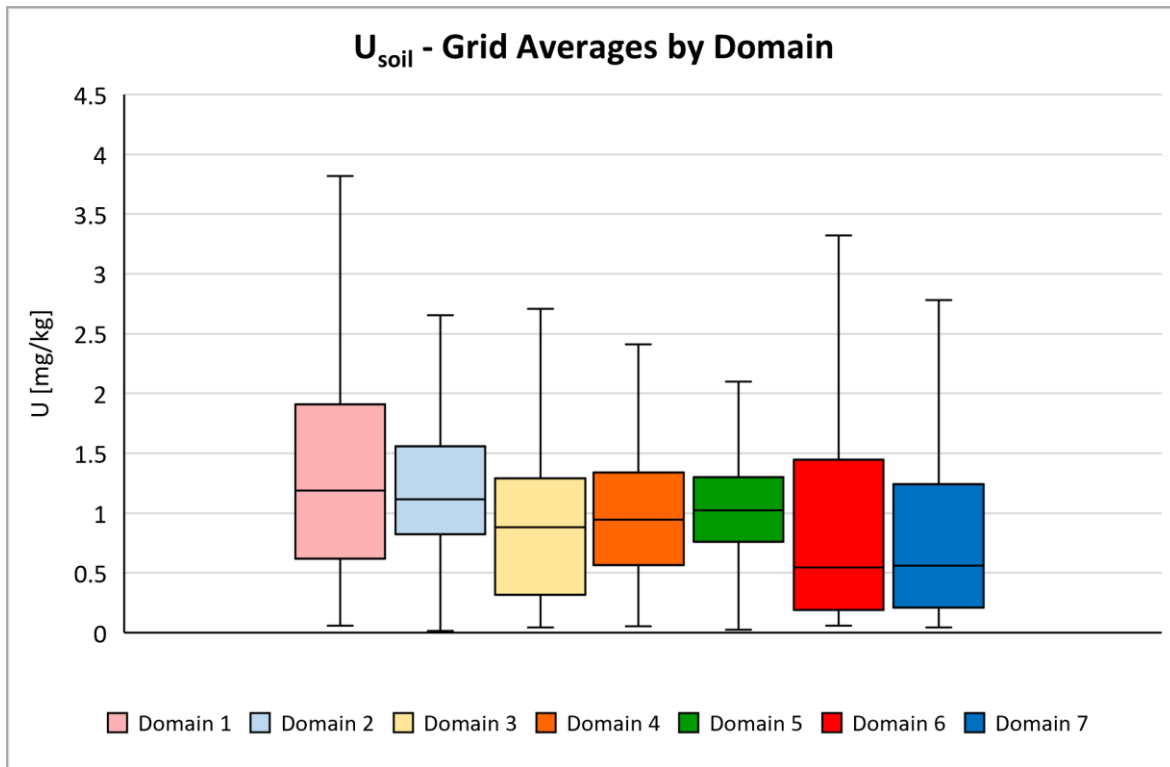


Figure A.6: Boxplot summaries of U_{soil} concentrations (average in each 4km² grid square) (analysed by ICP_{ar}) by domain.

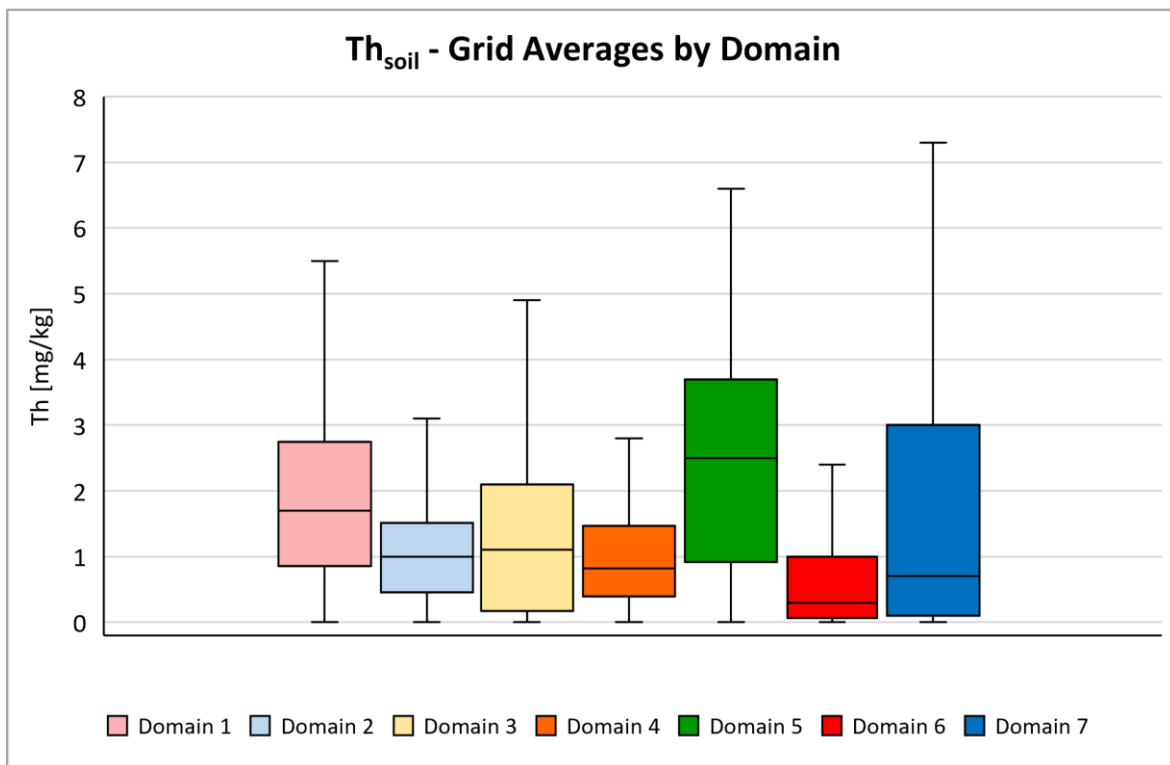


Figure A.7: Boxplot summaries of Th_{soil} concentrations (average in each 4km² grid square) (analysed by ICP_{ar}) by domain.



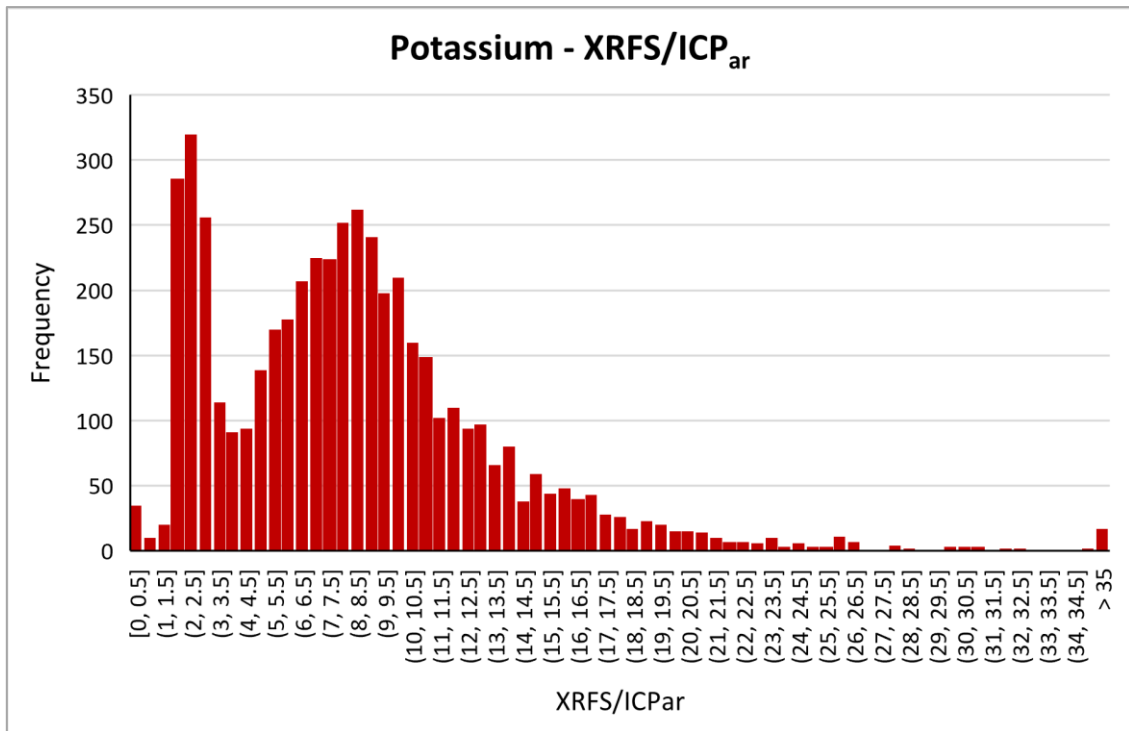


Figure A.8: Distribution of XRF/ICP_{ar} values for potassium, with overflow bin >35.

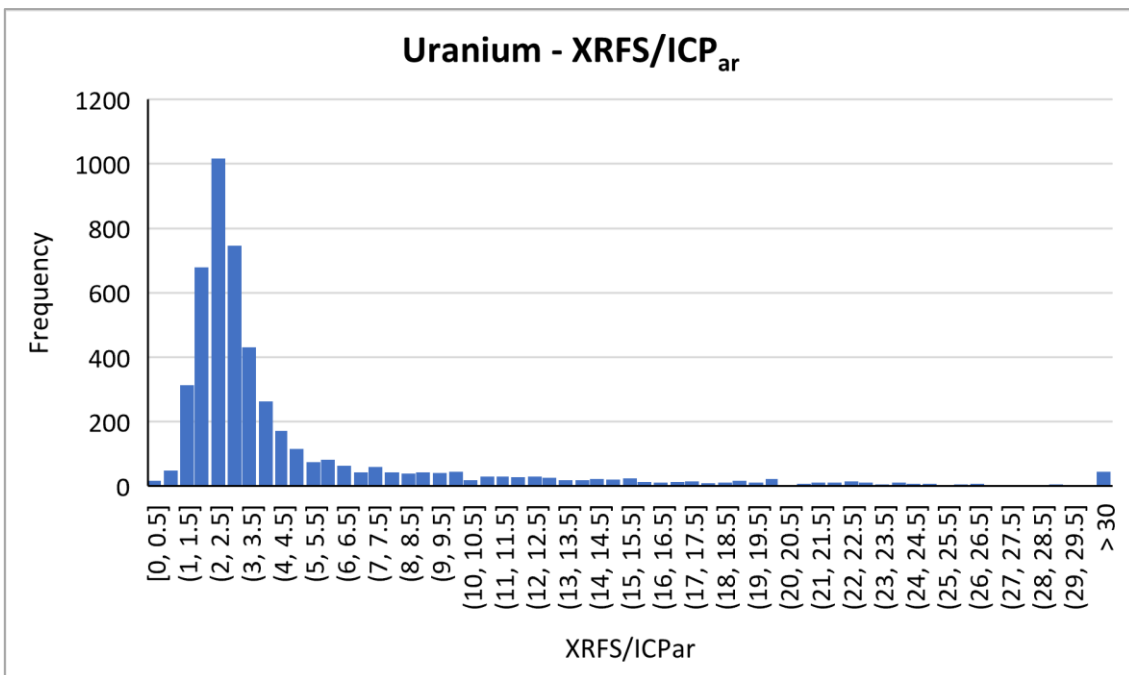


Figure A.9: Distribution of XRF/ICP_{ar} values for uranium, with overflow bin >30.



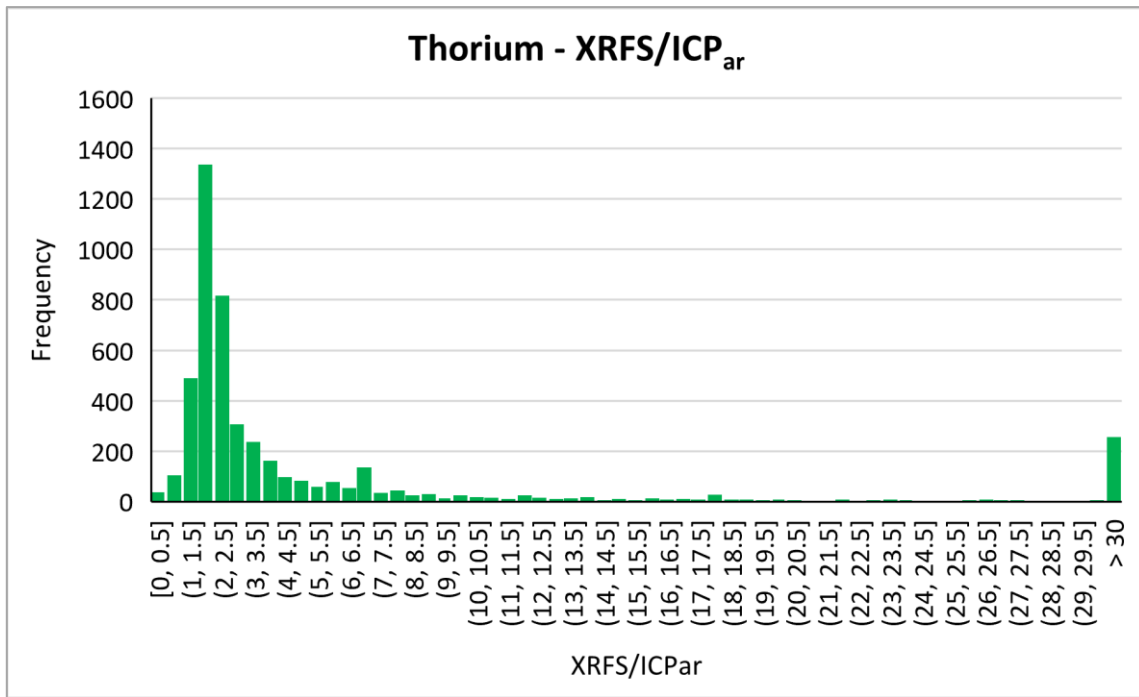


Figure A.10: Distribution of XRFS/ICP_{ar} values for thorium, with overflow bin >30.

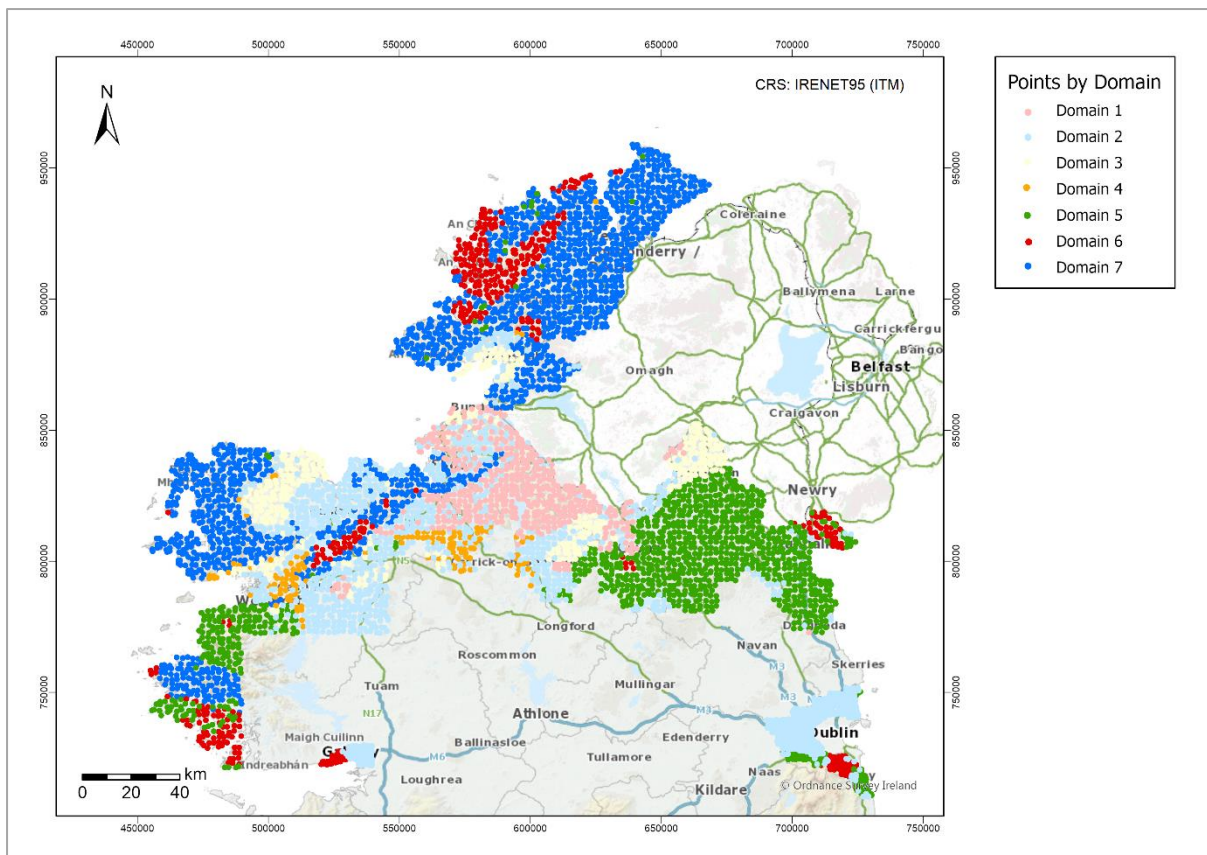


Figure A.11: Distribution of points (soil & radiometric pairs) across the Geochemical Domains.



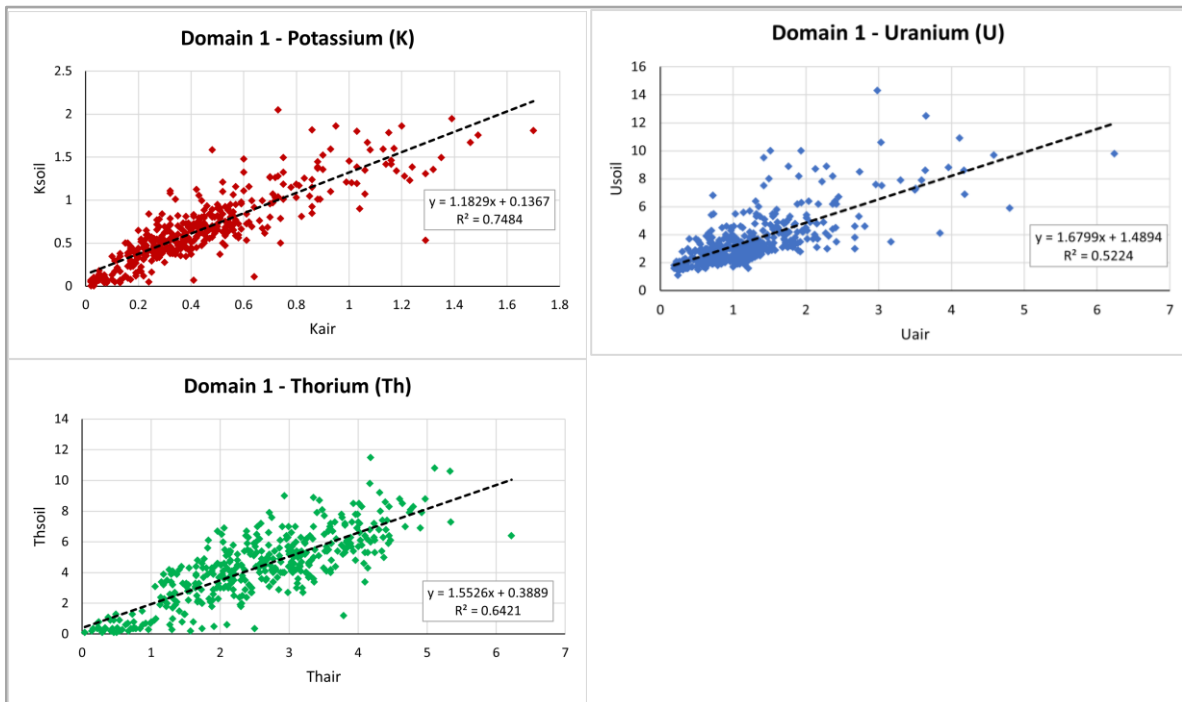


Figure A.12: XY scatterplots of X_{soil} vs X_{air} – domain 1 (outliers removed).

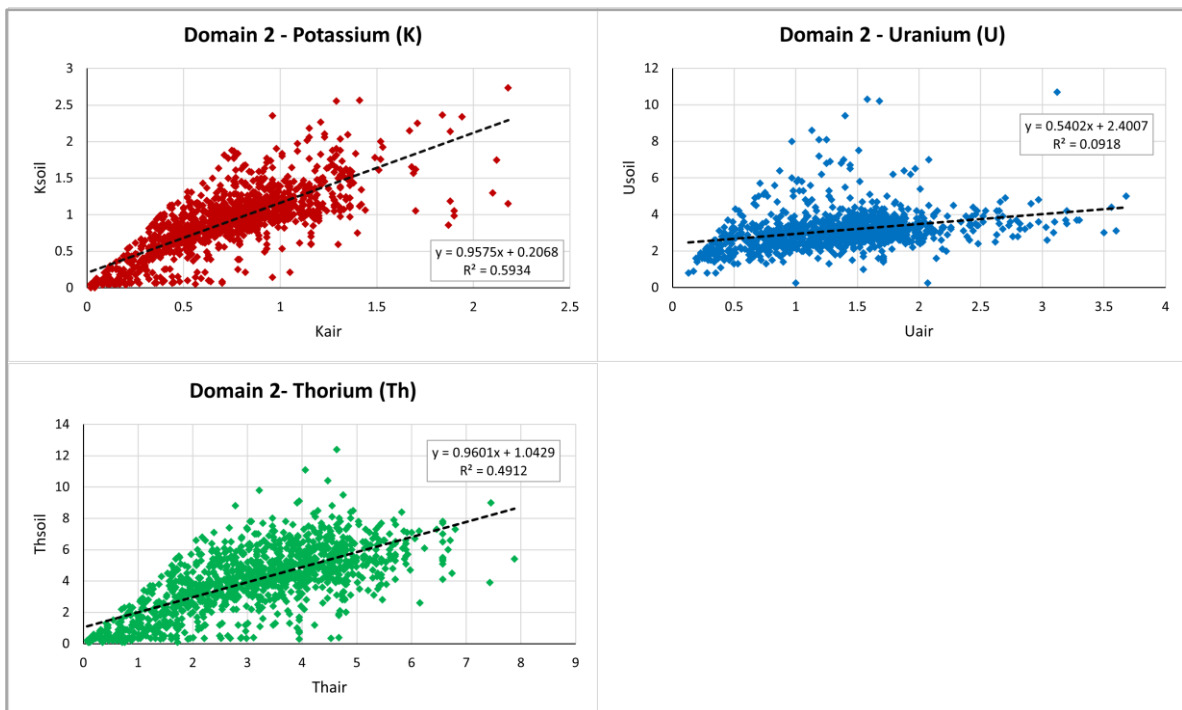


Figure A.13: XY scatterplot of X_{soil} vs X_{air} – domain 2 (outliers removed).



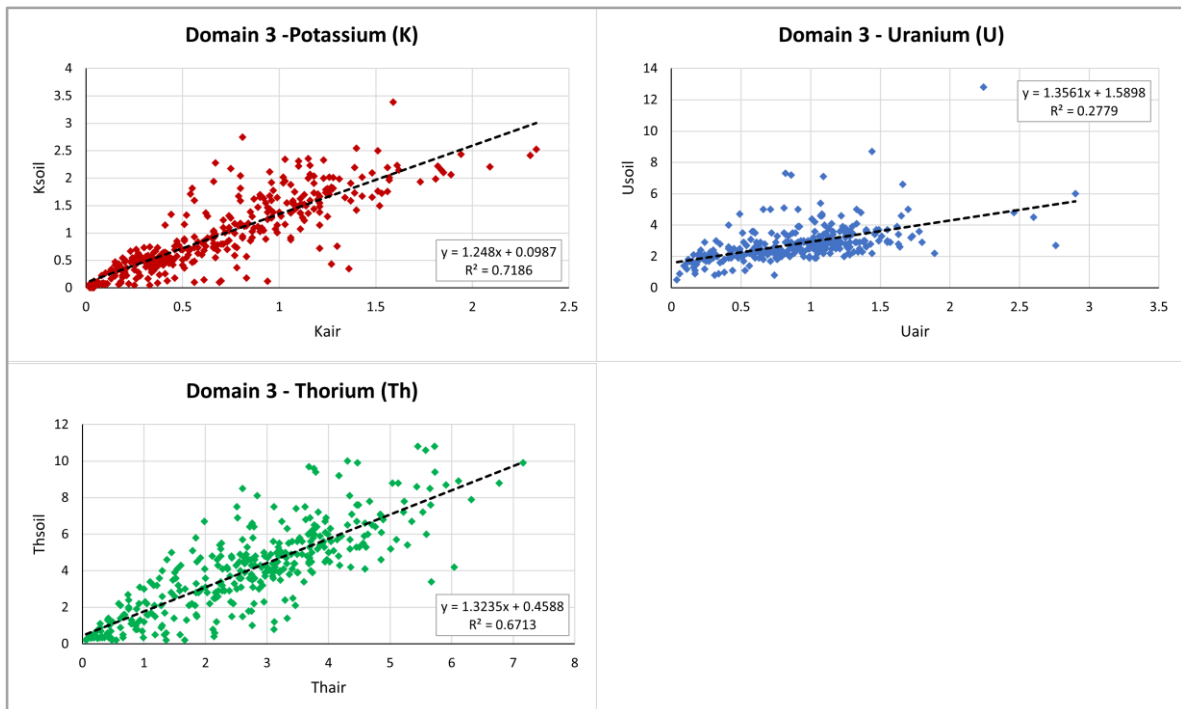


Figure A.14: XY scatterplot of X_{soil} vs X_{air} – domain 3 (outliers removed).

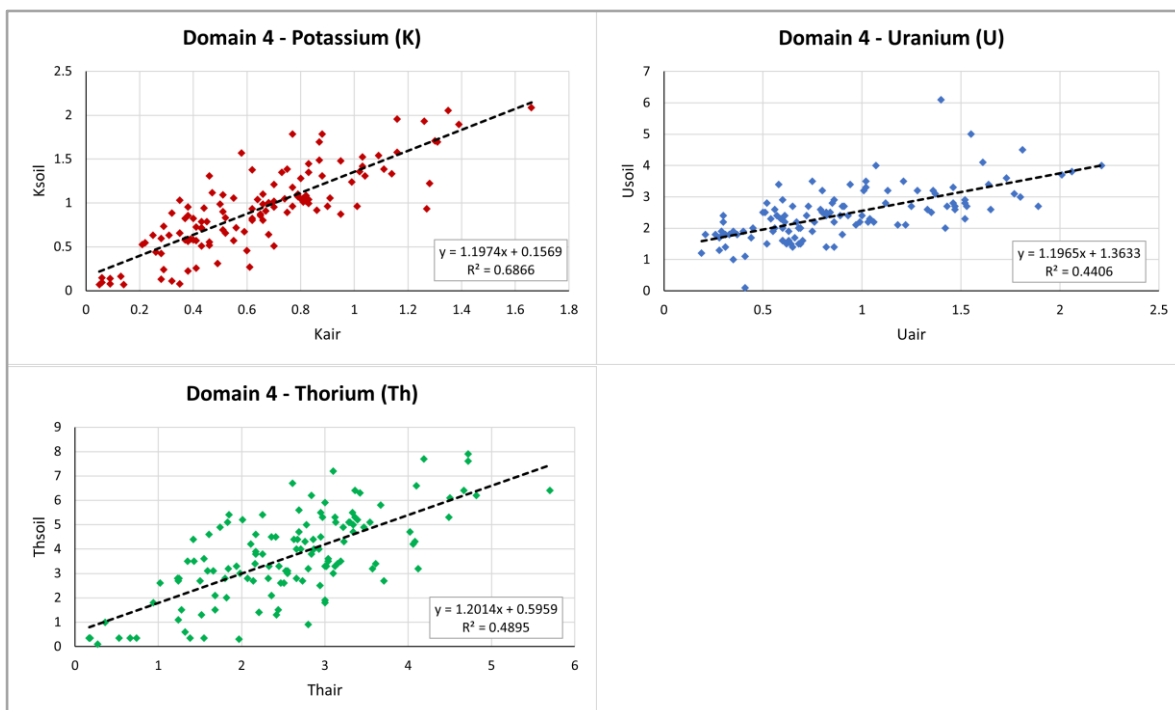


Figure A.15: XY scatterplot of X_{soil} vs X_{air} – domain 4 (outliers removed).



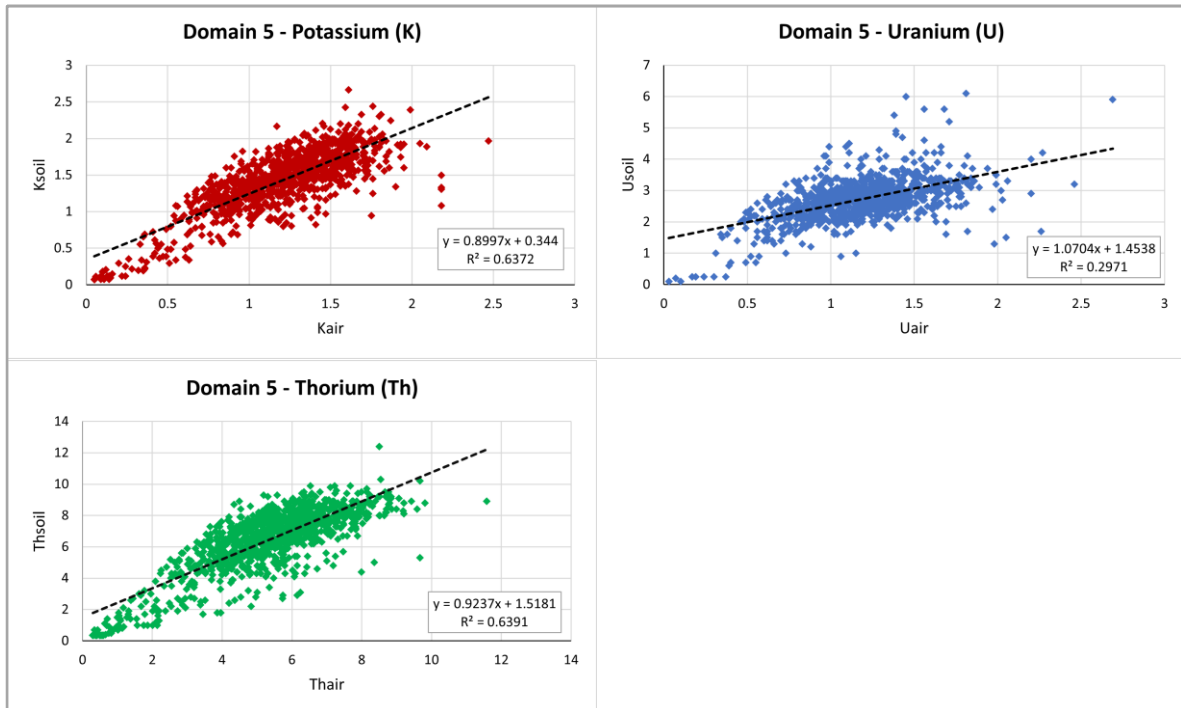


Figure A.16: XY scatterplot of X_{soil} vs X_{air} – domain 5 (outliers removed).

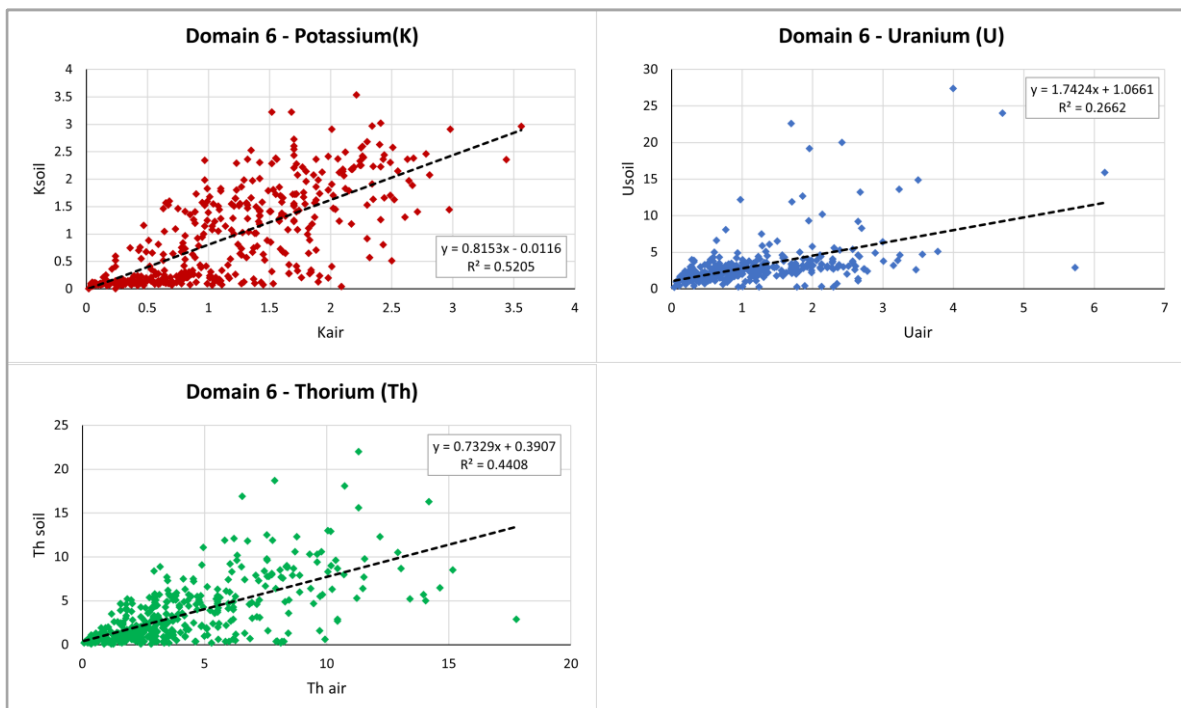


Figure A.17: XY scatterplot of X_{soil} vs X_{air} – domain 6 (outliers removed).



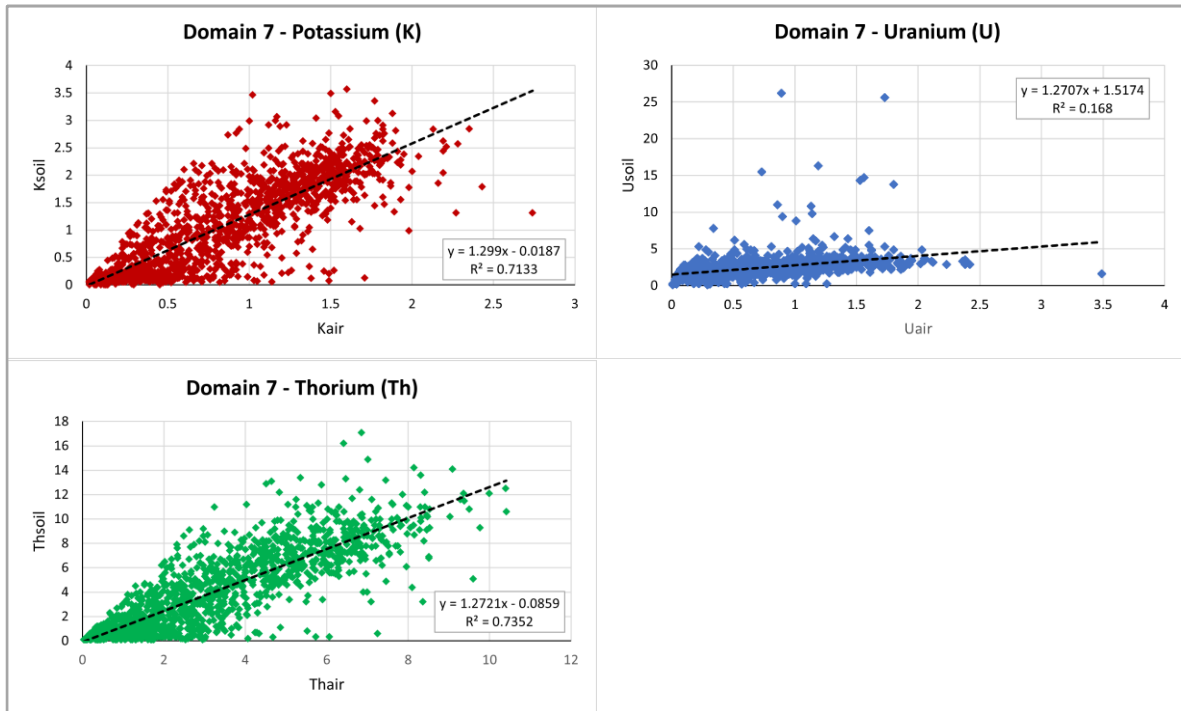


Figure A.18: XY scatterplot of X_{soil} vs X_{air} – domain 7 (outliers removed).

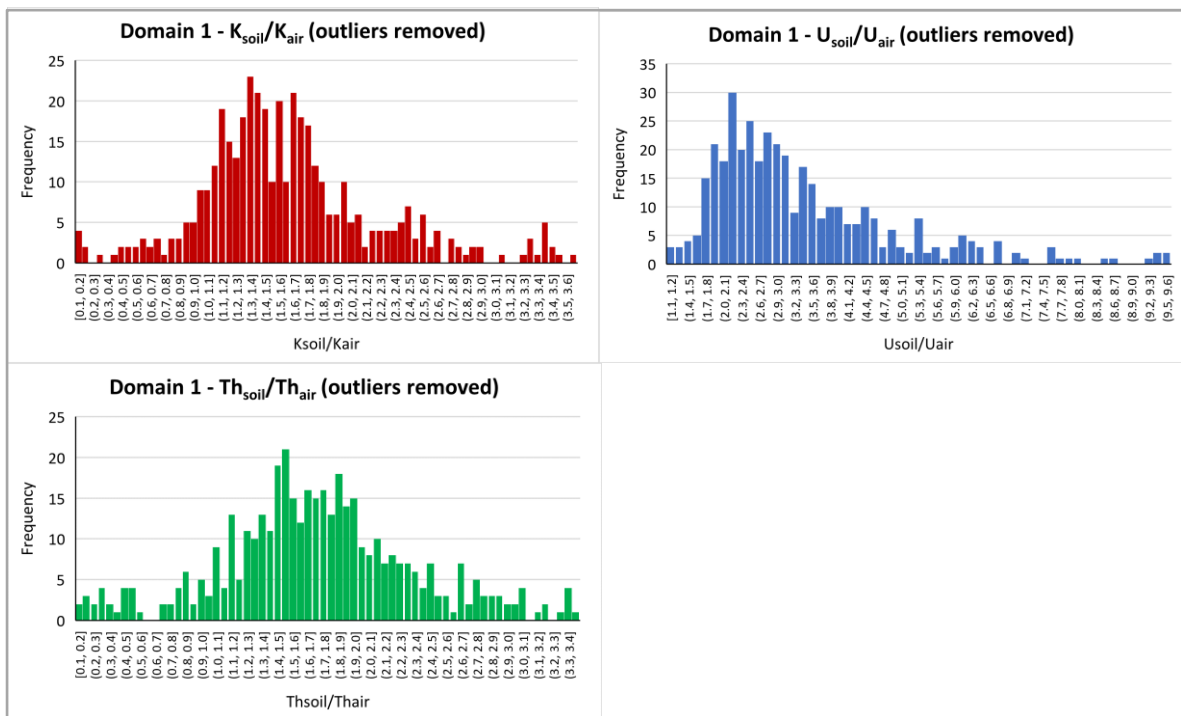


Figure A.19: Ratio (X_{soil}/X_{air}) histograms – domain 1.



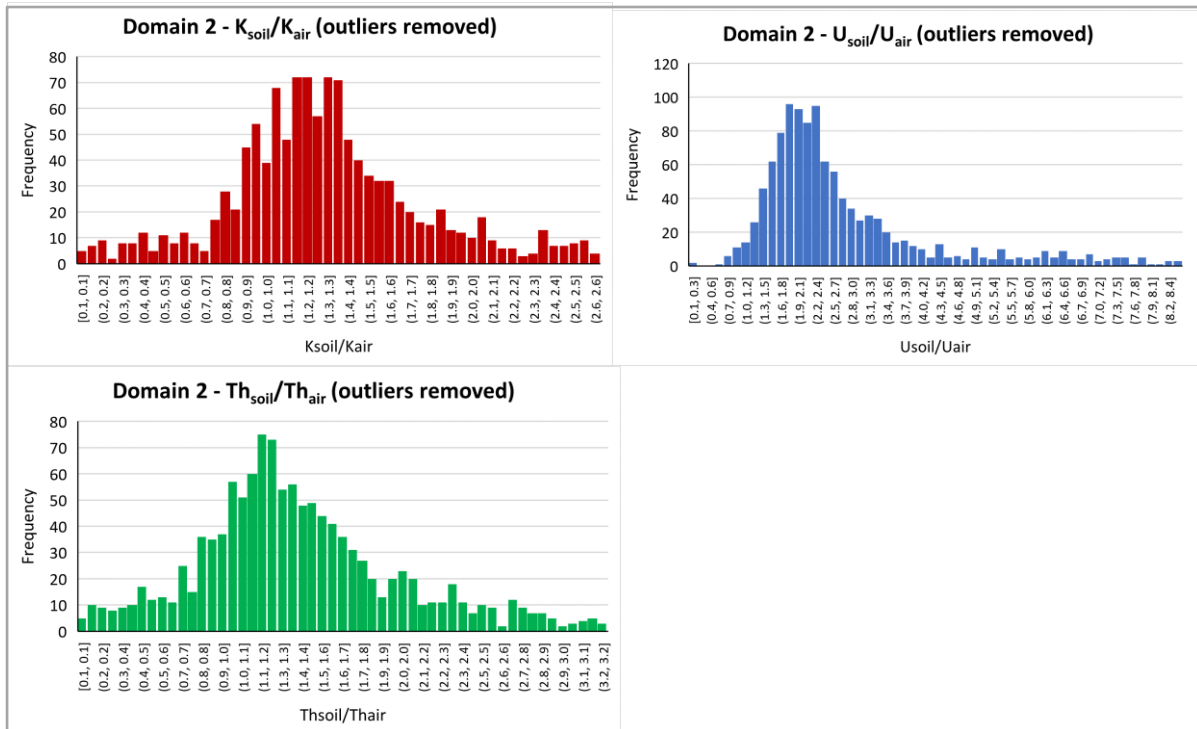


Figure A.20: Ratio (X_{soil}/X_{air}) histograms – domain 2.

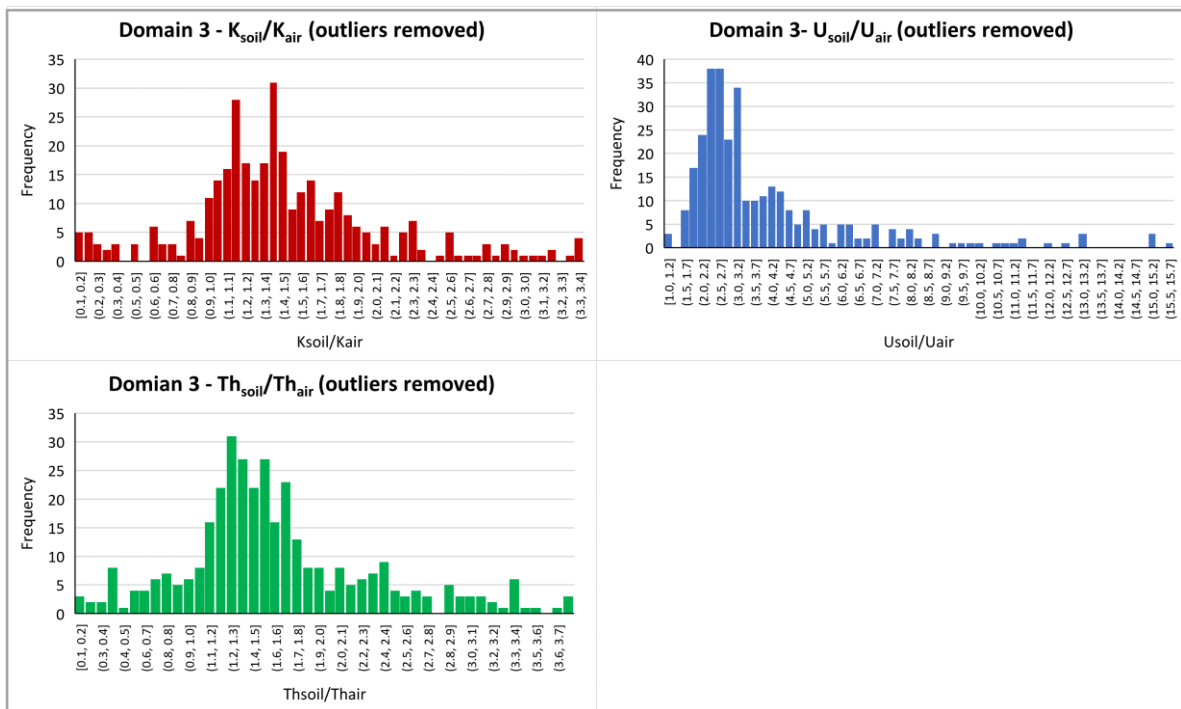


Figure A.21: Ratio (X_{soil}/X_{air}) histograms – domain 3.



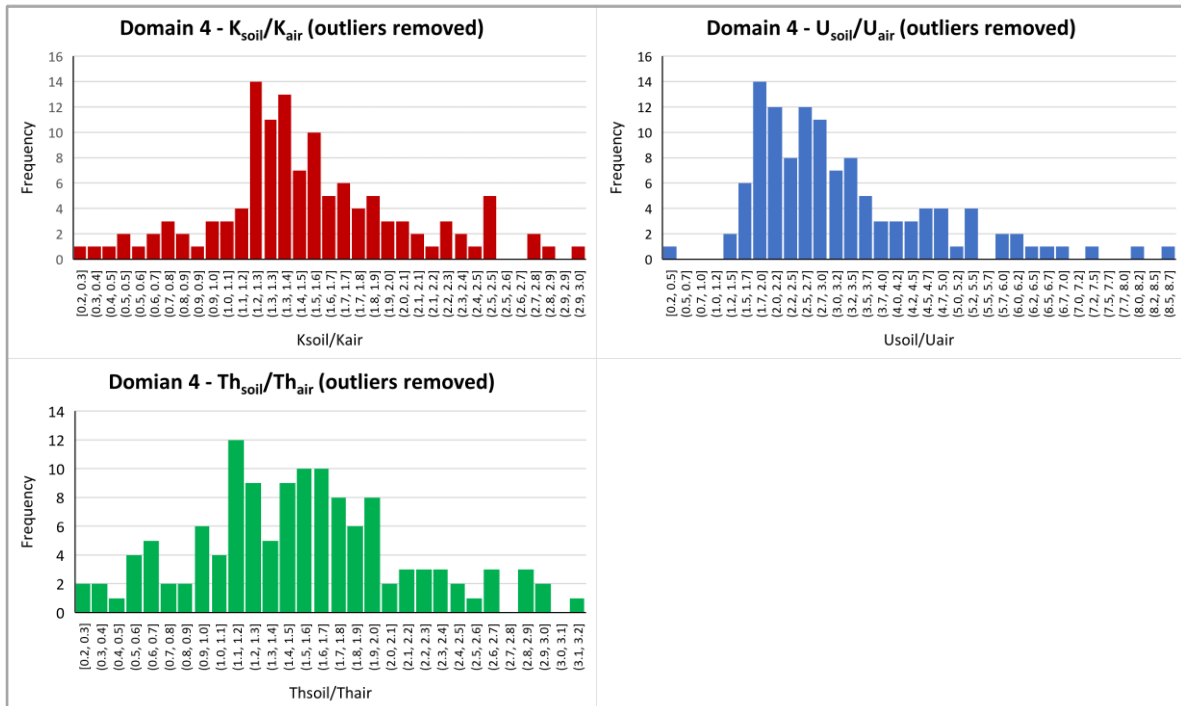


Figure A.22: Ratio (X_{soil}/X_{air}) histograms – domain 4.

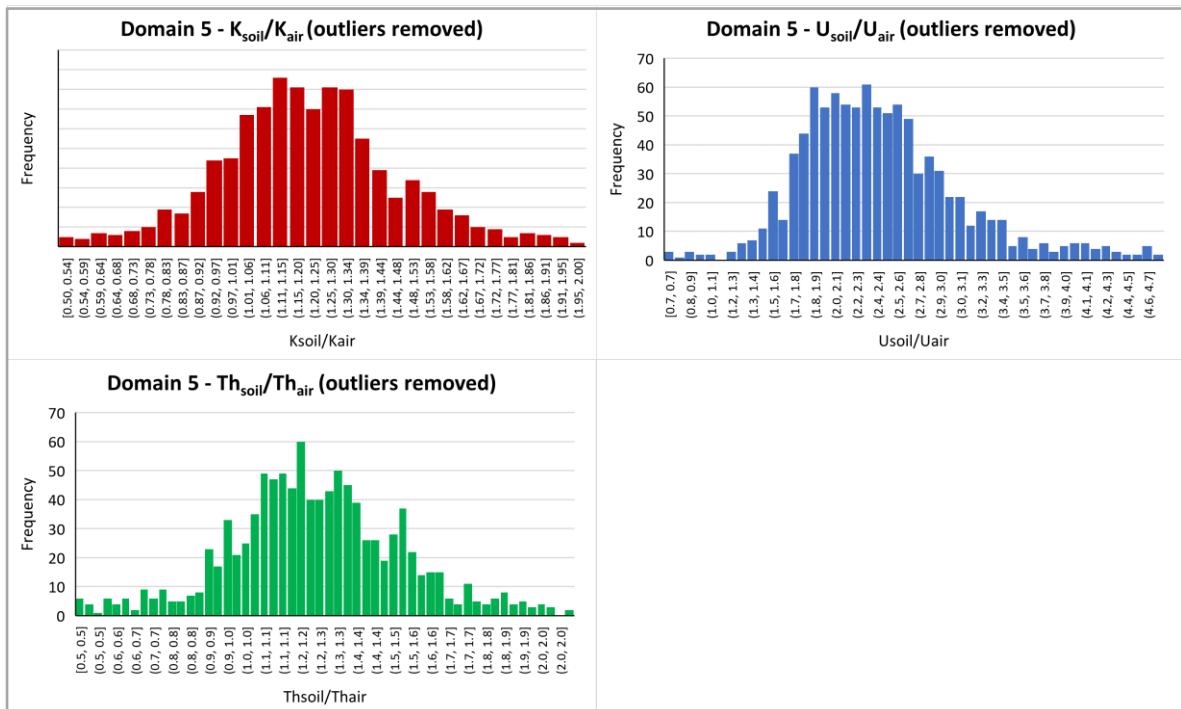


Figure A.23: Ratio (X_{soil}/X_{air}) histograms – domain 5.



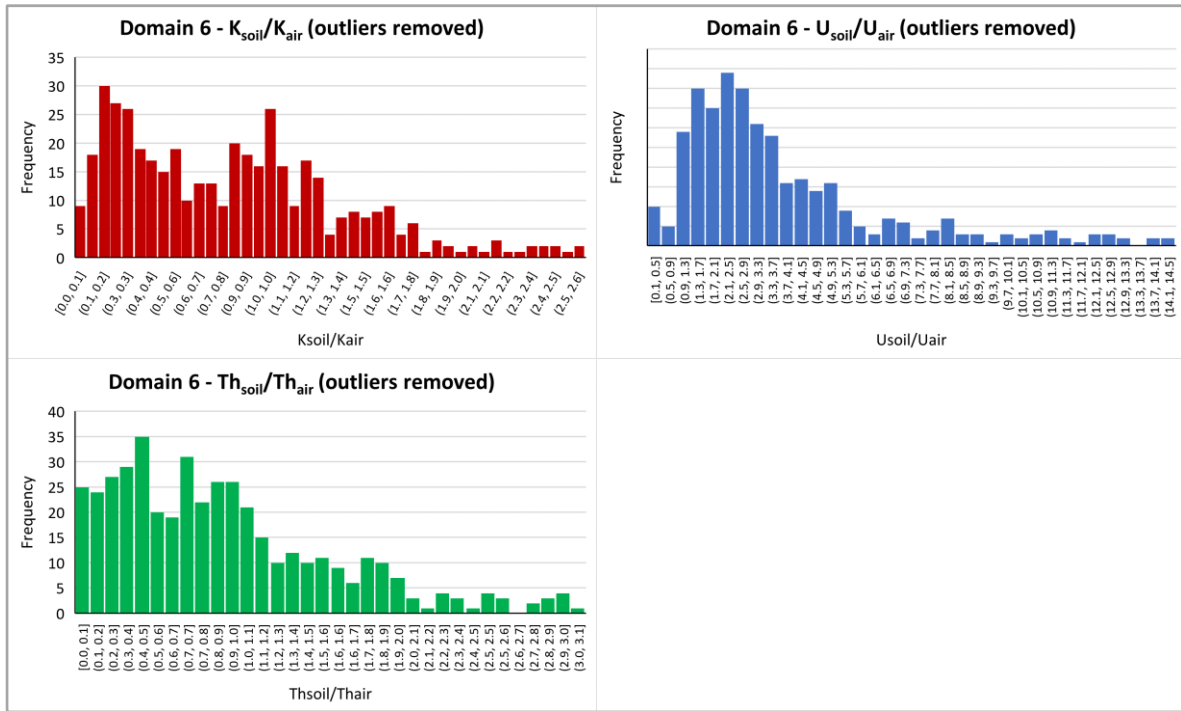


Figure A.24: Ratio (X_{soil}/X_{air}) histograms – domain 6.

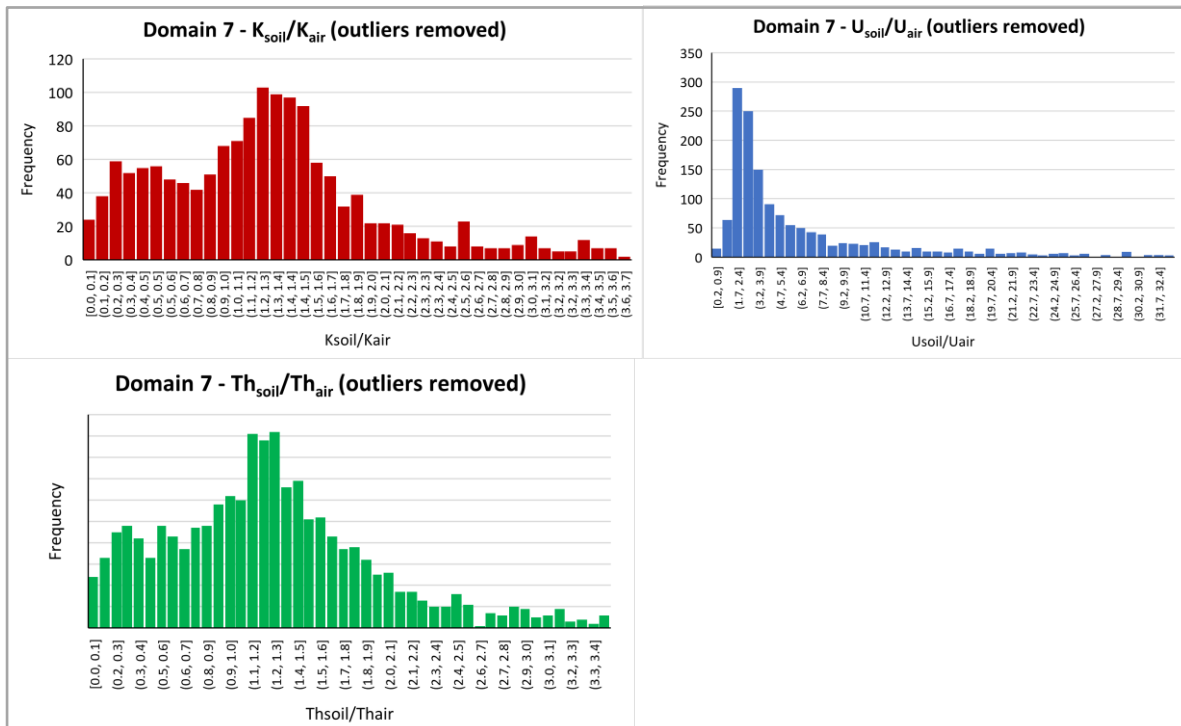


Figure A.25: Ratio (X_{soil}/X_{air}) histograms – domain 7.



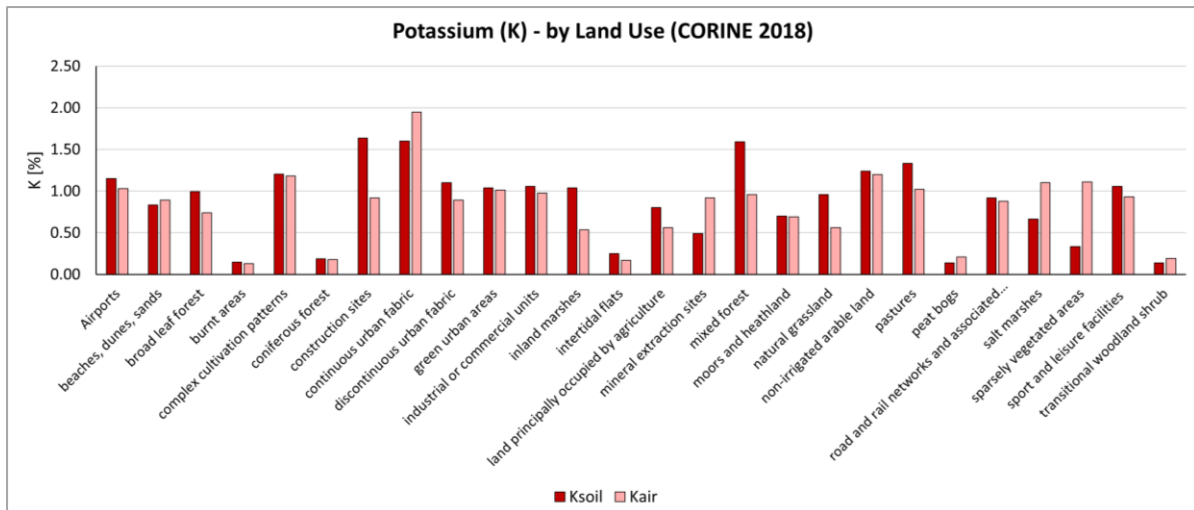


Figure A.26: Median soil and radiometric potassium concentrations by land use class (CORINE 2018).

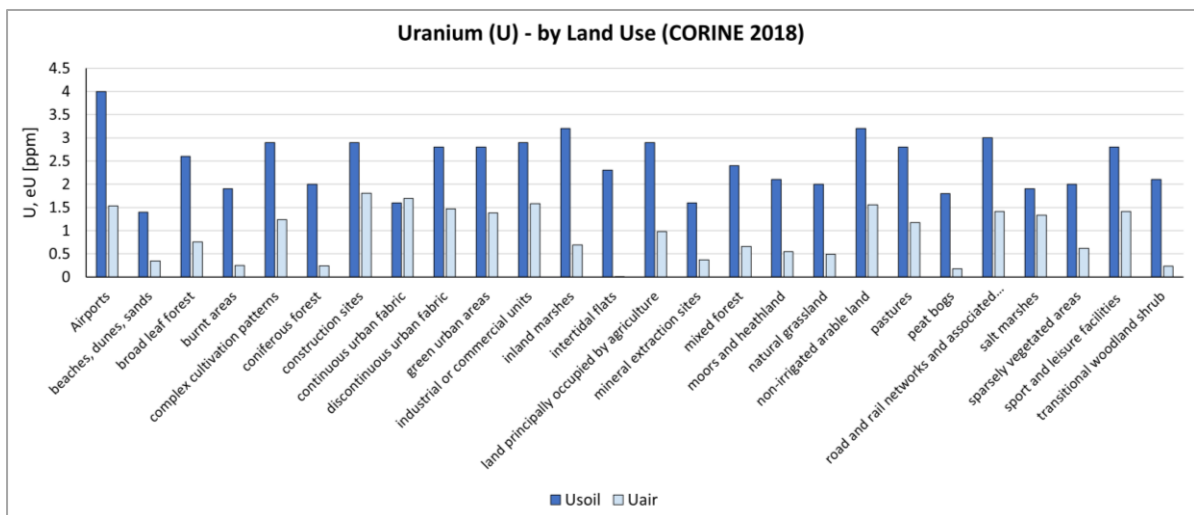


Figure A.27: Median soil and radiometric uranium concentrations by land use class (CORINE 2018).

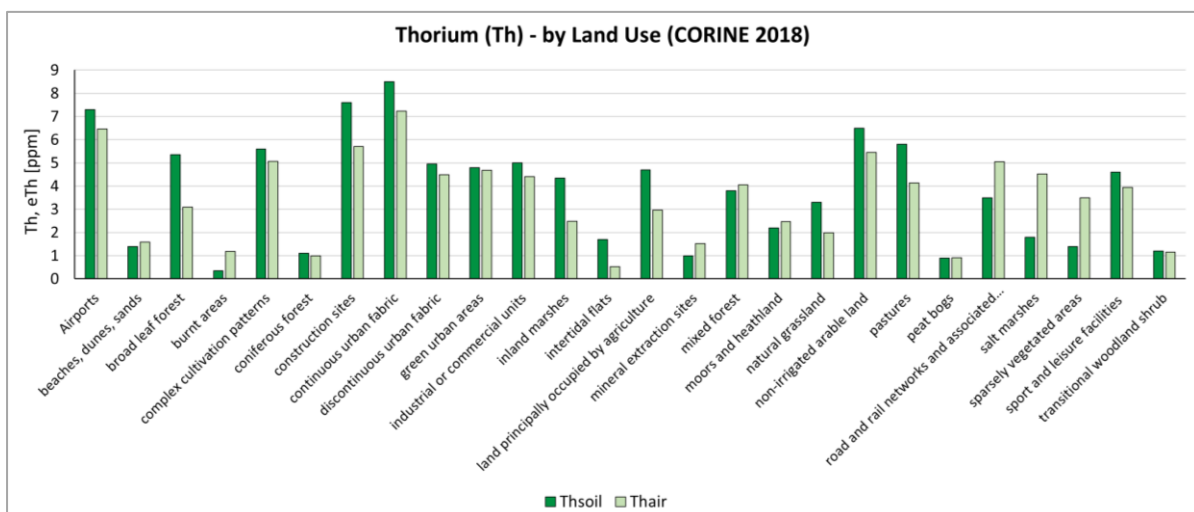


Figure A.28: Median soil and radiometric thorium concentrations by land use class (CORINE 2018).



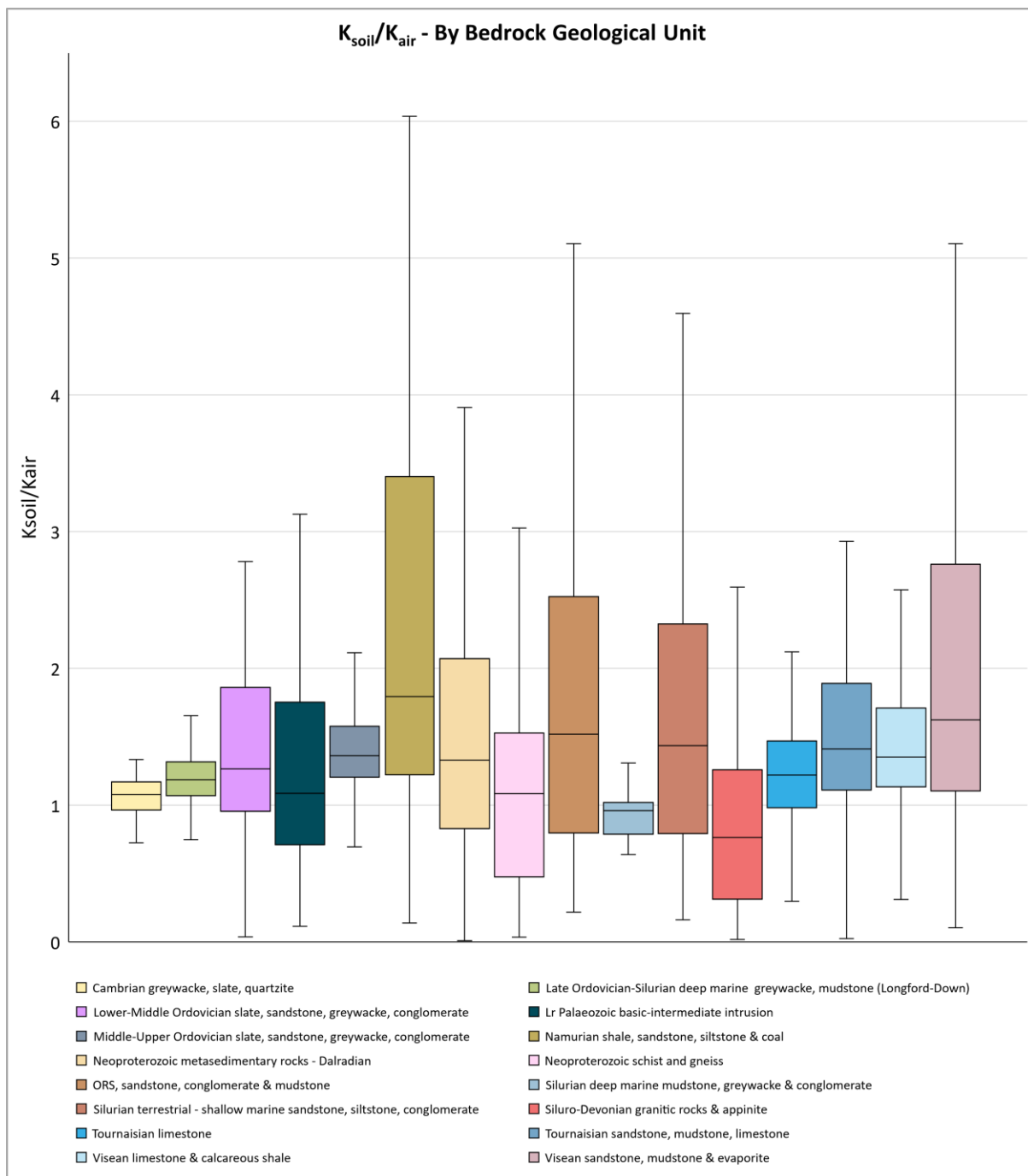


Figure A.29: Boxplots of K_{soil} vs K_{air} by geological unit (GSI Bedrock 1:1 million), classes with $n \leq 20$ removed. Outliers hidden for clarity.



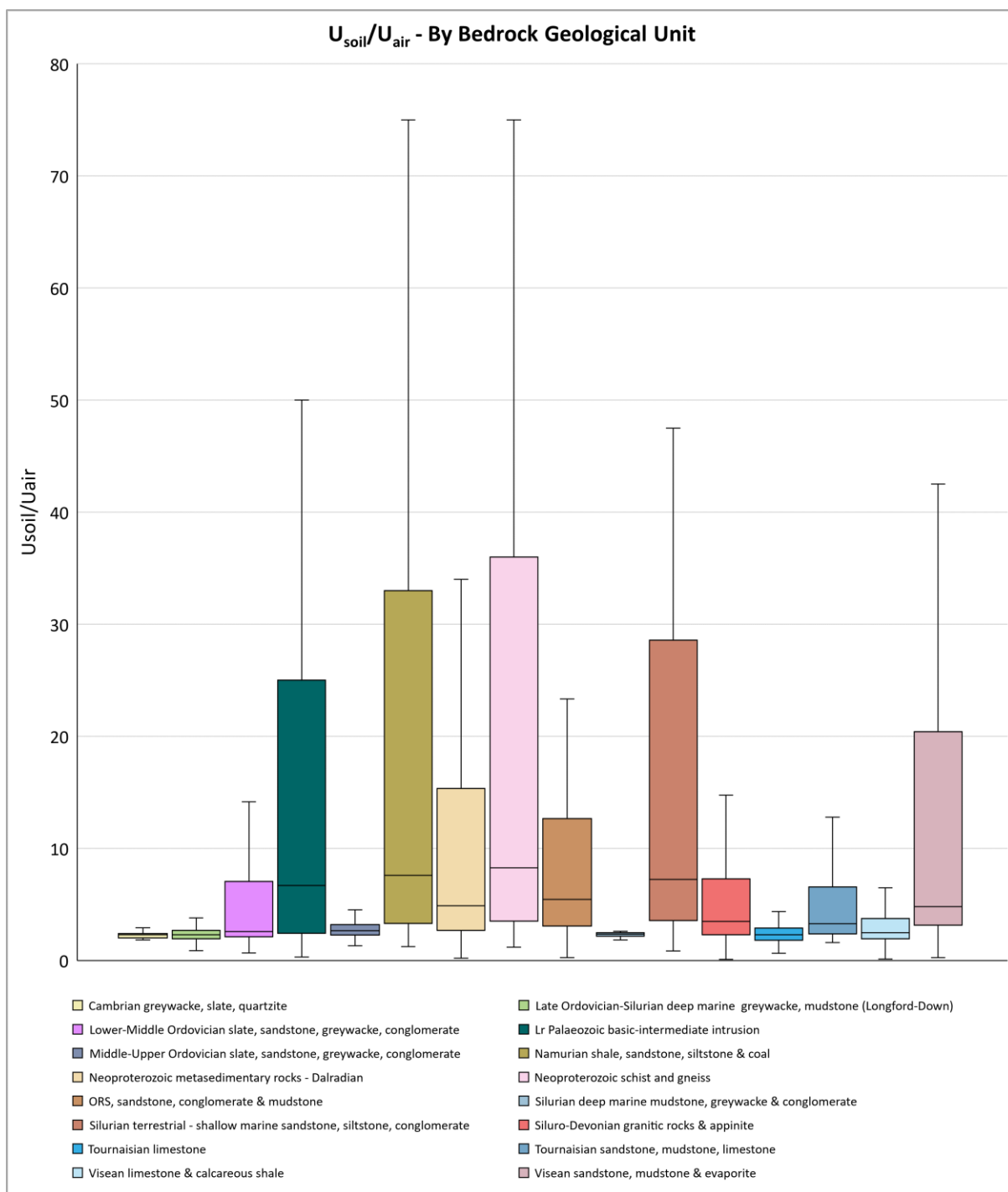


Figure A.30: Boxplots of U_{soil} vs U_{air} by geological unit (GSI Bedrock 1:1 million), classes with $n \leq 20$ removed. Outliers hidden for clarity.



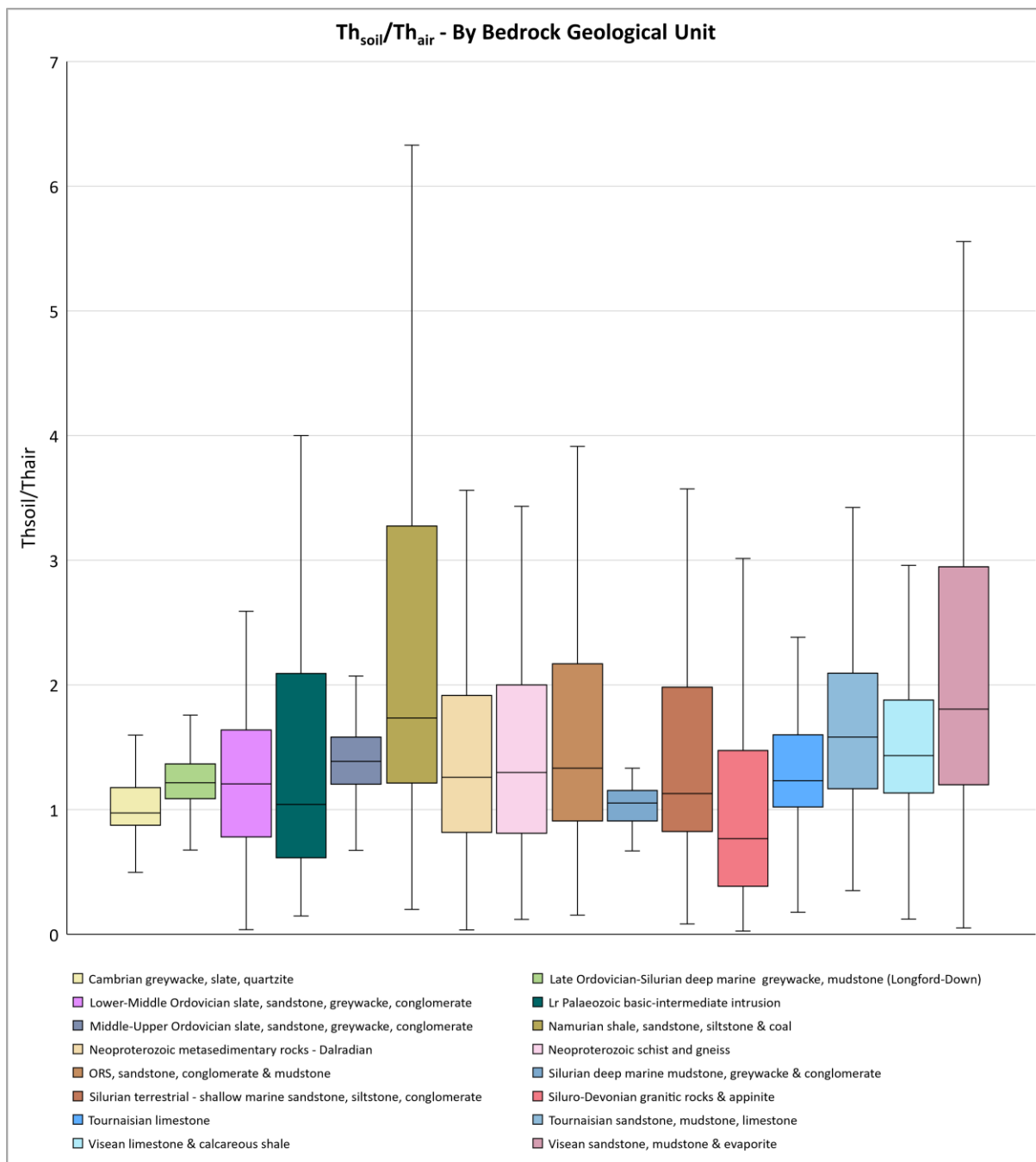


Figure A.31: Boxplots of Th_{soil} vs Th_{air} by geological unit (GSI Bedrock 1:1 million), classes with n ≤20 removed. Outliers hidden for clarity.



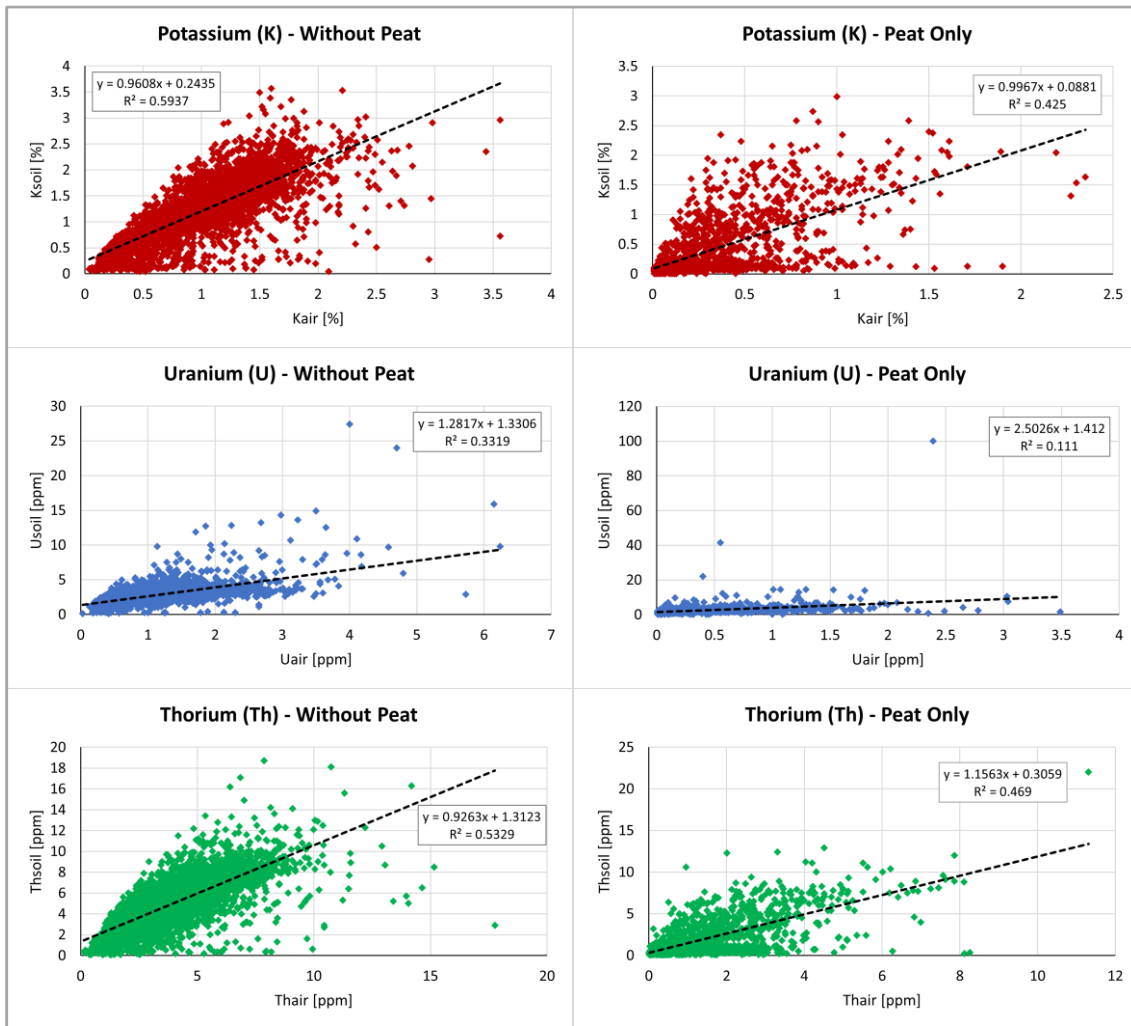


Figure A.32: XY scatterplots of soil vs radiometric concentrations of K, U and Th for areas with and without peat – (outliers removed).



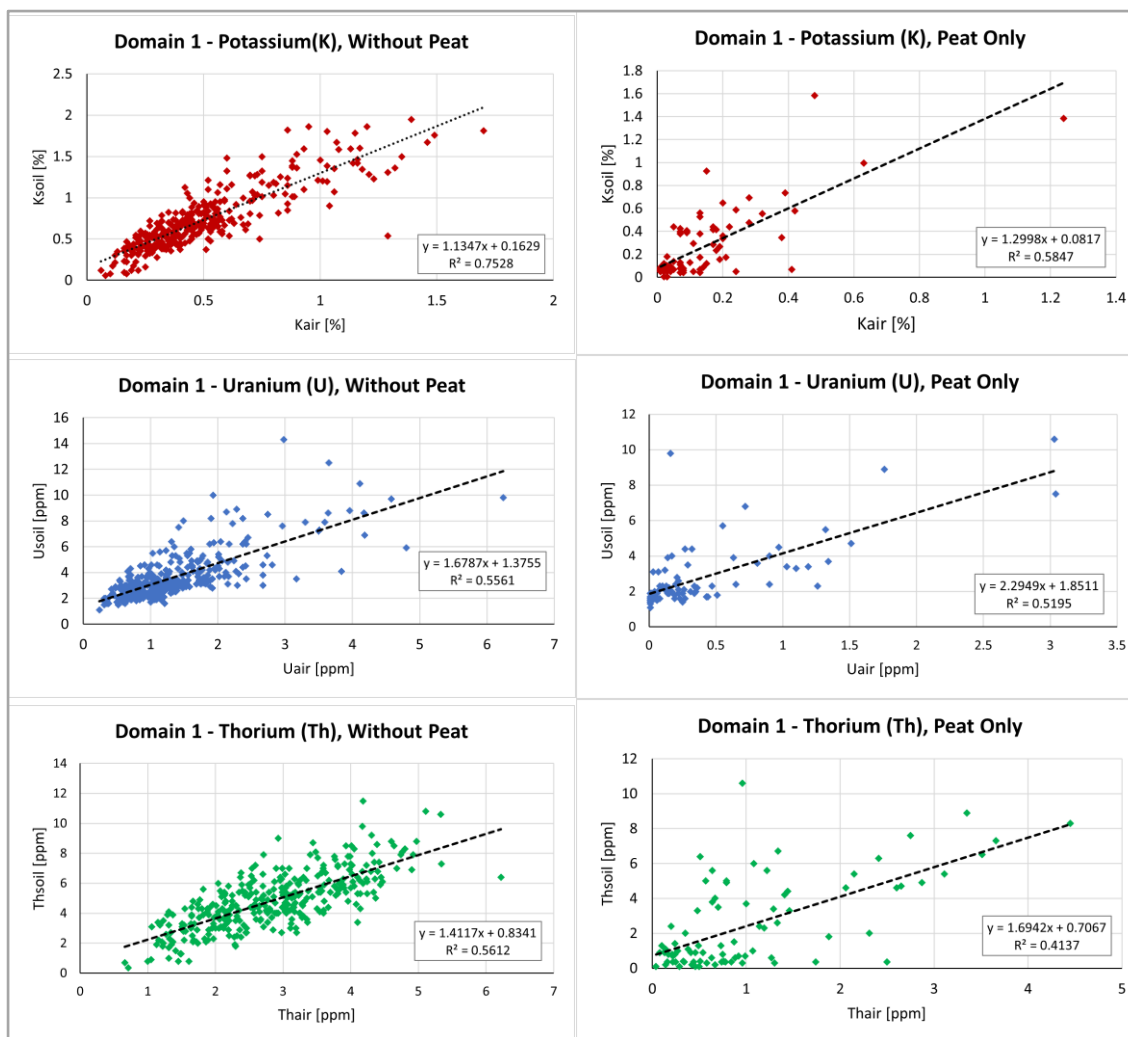


Figure A.33: XY scatterplots of soil vs radiometric concentrations of K, U and Th for areas with and without peat – Domain 1 (outliers removed).



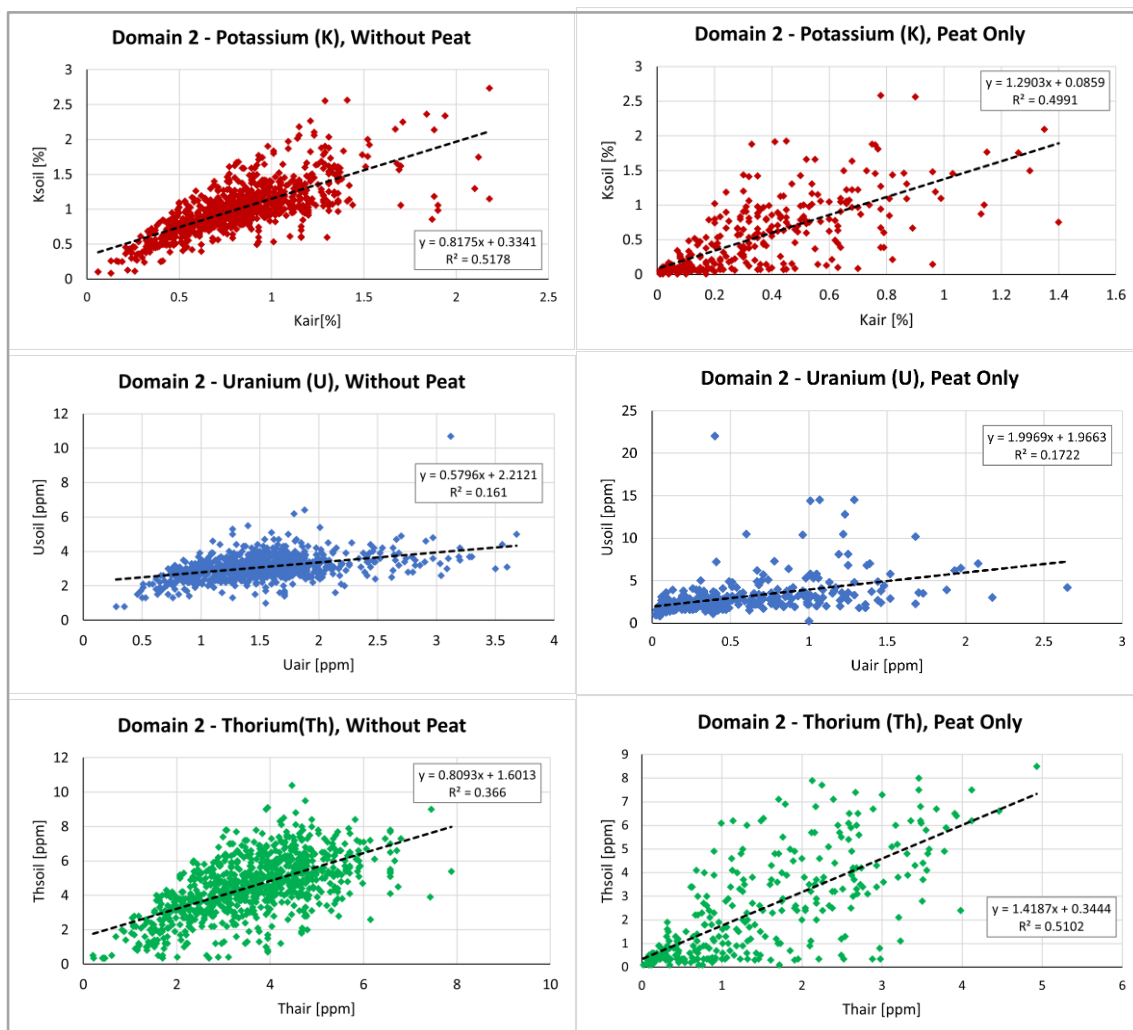


Figure A.34: XY scatterplots of soil vs radiometric concentrations of K, U and Th for areas with and without peat – Domain 2 (outliers removed).



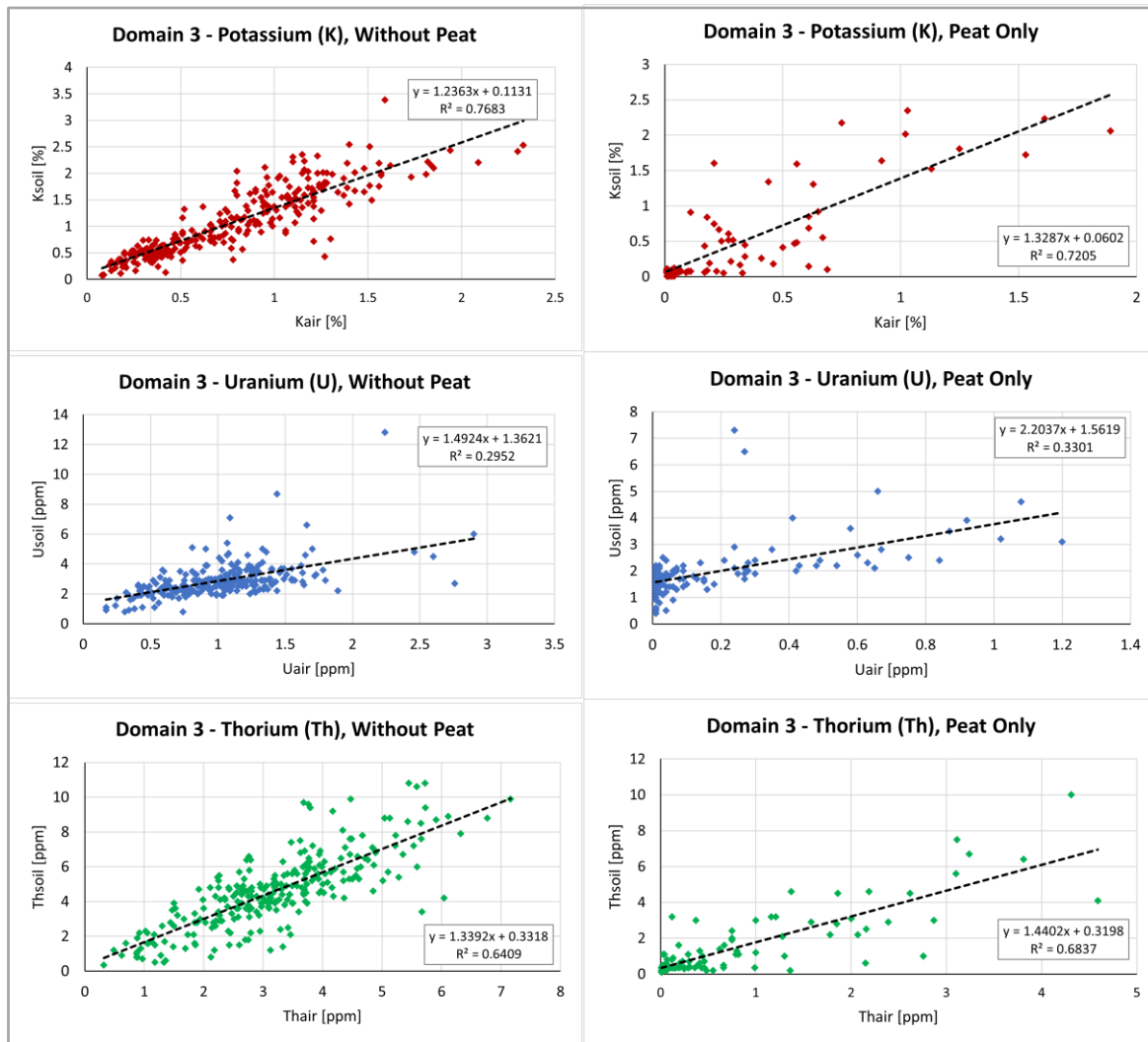


Figure A.35: XY scatterplots of soil vs radiometric concentrations of K, U and Th for areas with and without peat – Domain 3 (outliers removed).



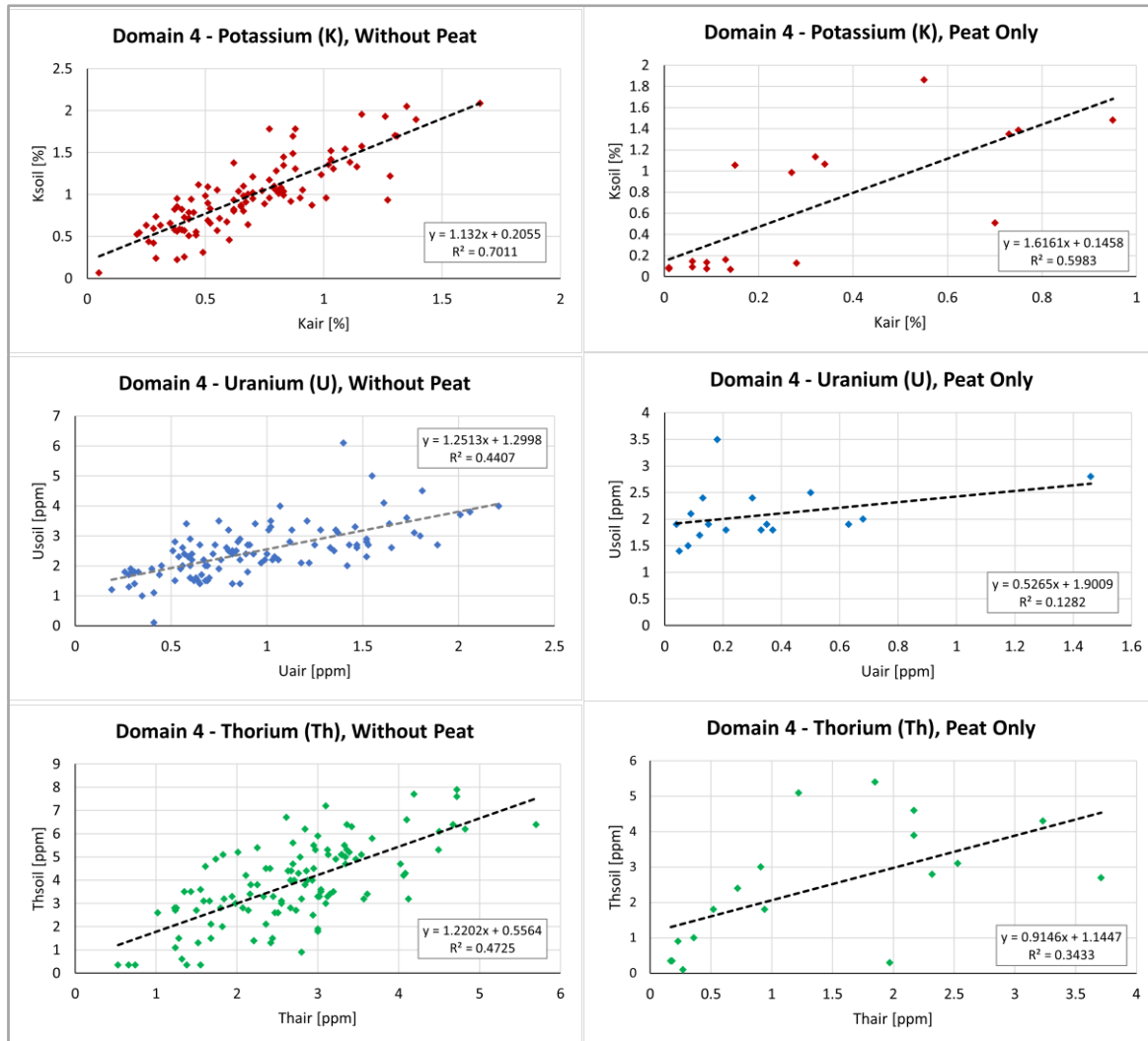


Figure A.36: XY scatterplots of soil vs radiometric concentrations of K, U and Th for areas with and without peat – Domain 4 (outliers removed).



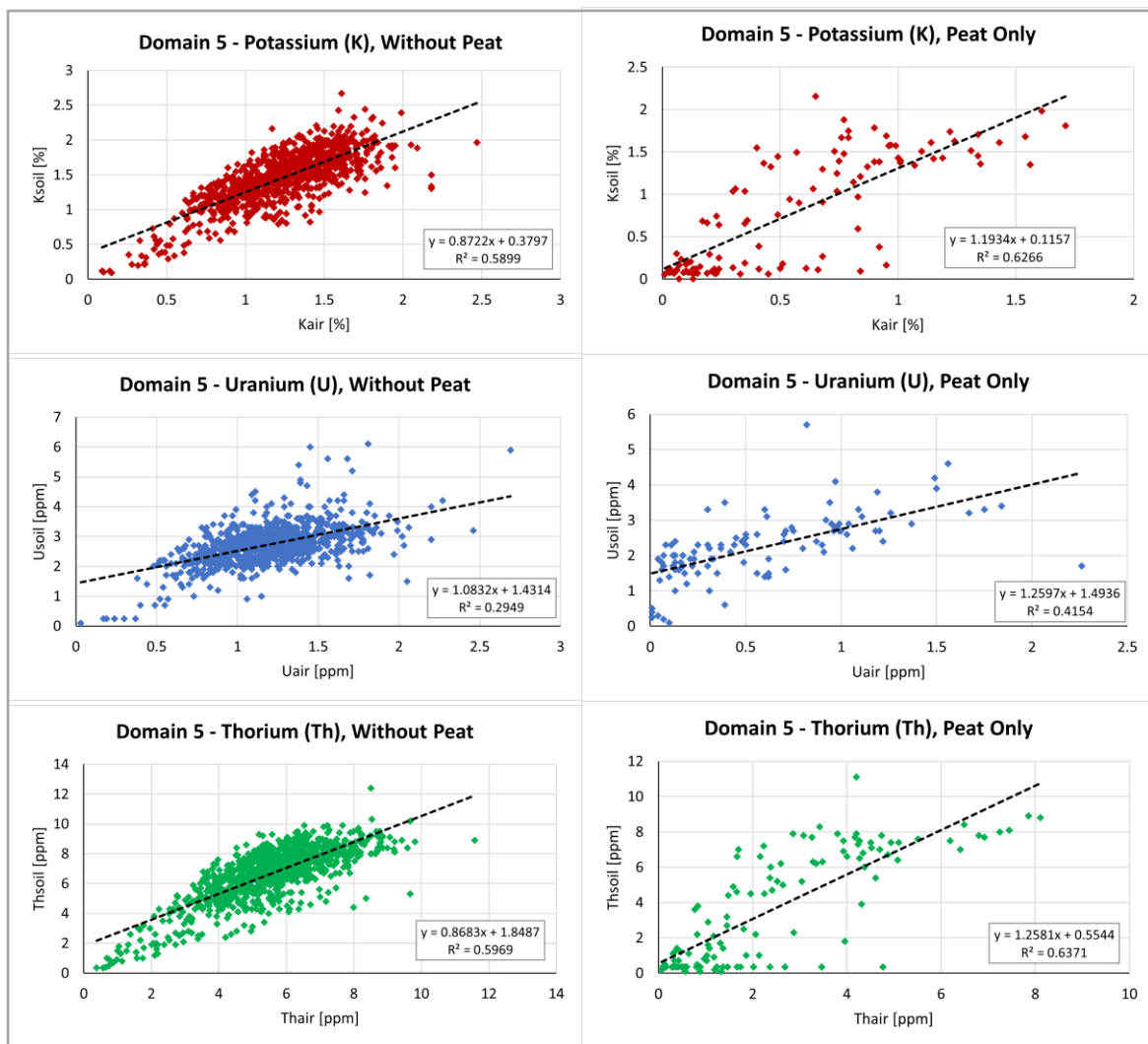


Figure A.37: XY scatterplots of soil vs radiometric concentrations of K, U and Th for areas with and without peat – Domain 5 (outliers removed).



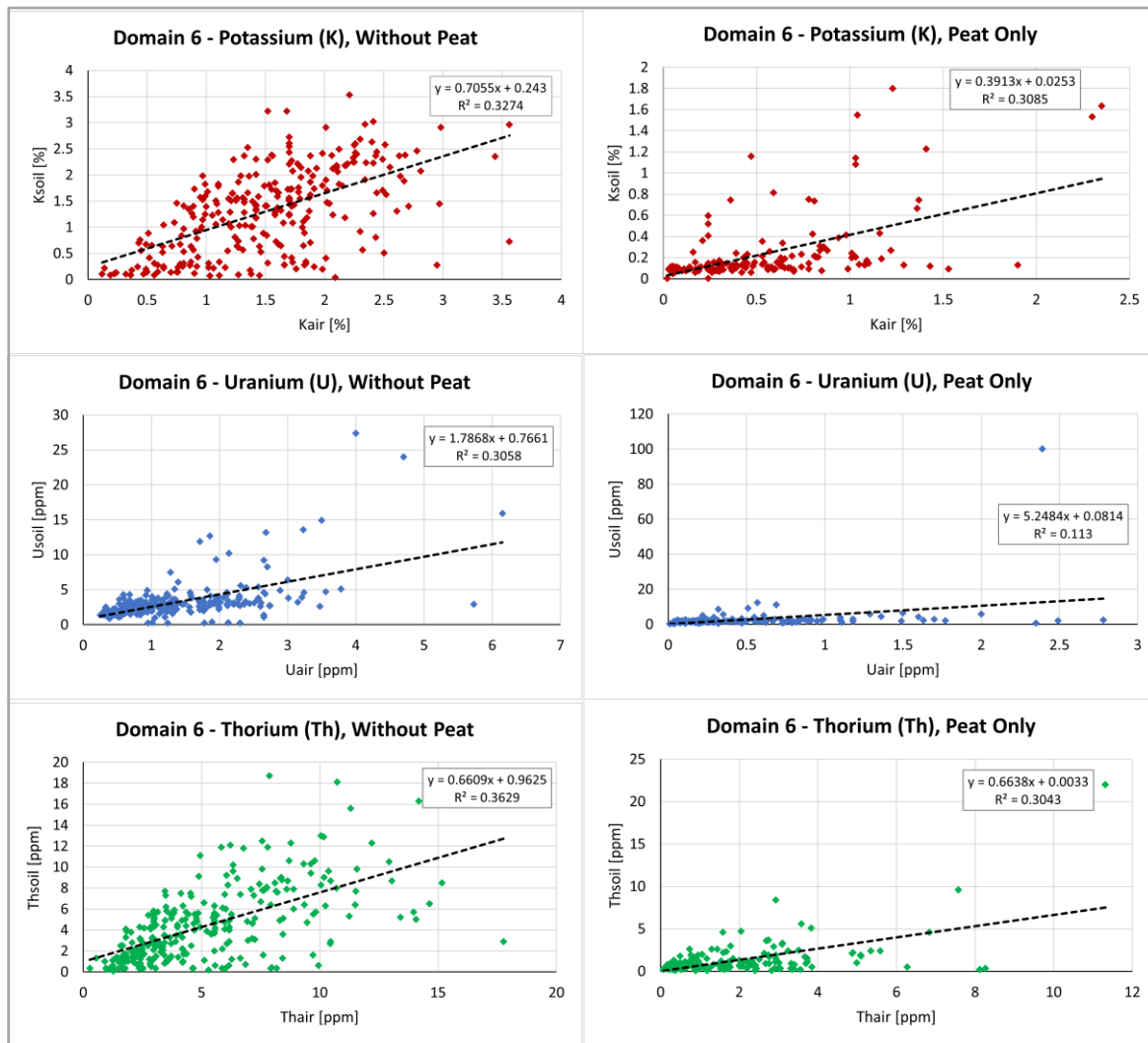


Figure A.38: XY scatterplots of soil vs radiometric concentrations of K, U and Th for areas with and without peat – Domain 6 (outliers removed).



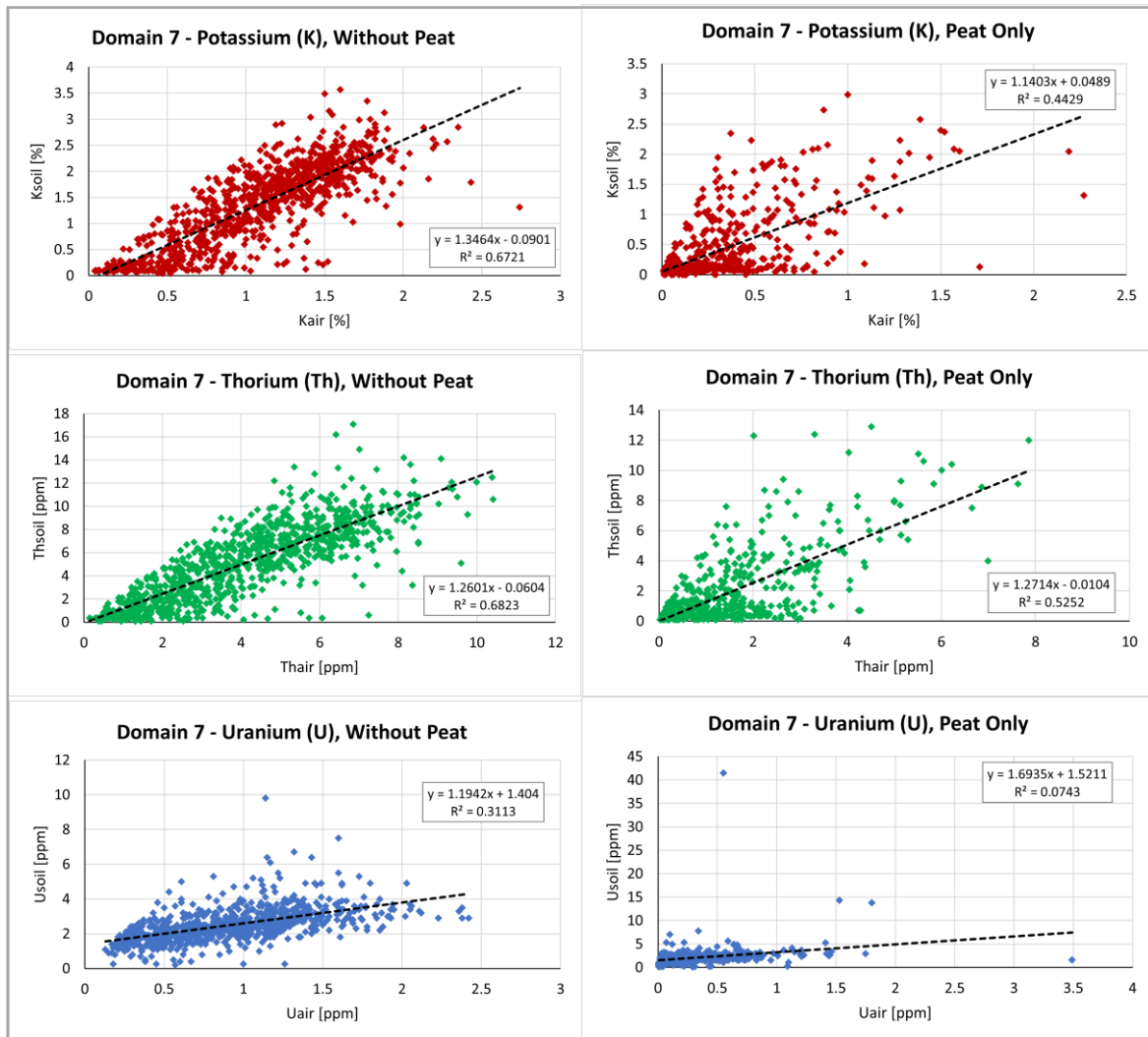


Figure A.39: XY scatterplots of soil vs radiometric concentrations of K, U and Th for areas with and without peat – Domain 7 (outliers removed).



Appendix B: Supplementary Tables

Table B.1: Radiometric survey equipment specifications (Ture 2020; Sander Geophysics 2016; Jones *et al.* 2007).

<i>Survey</i>	<i>Contractor</i>	<i>Aircraft</i>	<i>Gamma-ray spectrometer</i>
NI	Joint Airborne-geoscience Capacity (JAC) of the Geological Survey of Finland and the British Geological Survey	De Havilland DHC-6 twin Otter	Exploranium GR-820; 256 channels; crystal volume: 32 L down, 8 L up
CAV	JAC	De Havilland DHC-6 twin Otter	Exploranium GR-820; 256 channels; crystal volume: 32 L down, 8 L up
TB	Sander Geophysics Ltd. (SGL)	De Havilland DHC-6 twin Otter	Exploranium GR-820; 256 channels; crystal volume: 50.4 L down, 12.6 L up
TNM	CGG Airborne Survey (Pty) Ltd.	Cessna 208B	Exploranium GR-820; 256 channels; crystal volume: 50.4 L down, 12.6 L up
A1	SGL	De Havilland DHC-6 twin Otter	Exploranium GR-820; 256 channels; crystal volume: 50.4 L down, 12.6 L up
A2	SGL	De Havilland DHC-6 twin Otter	Exploranium GR-820; 256 channels; crystal volume: 50.4 L down, 12.6 L up
A3	SGL	De Havilland DHC-6 twin Otter	Radiation Solution RS-501; 1024 channels; volume: 67.2 L down, 12.6 L up
A4	SGL	De Havilland DHC-6 twin Otter	Radiation Solution RS-501; 1024 channels; volume: 67.2 L down, 12.6 L up

Table B.2: Regression analysis by domain for areas without peat.

<i>Domain</i>		1	2	3	4	5	6	7
K _{soil} vs K _{air}	R ²	0.753	0.518	0.768	0.701	0.590	0.327	0.672
	p	<0.05	<0.05	<0.05	<0.05	<0.05	<0.05	<0.05
U _{soil} vs U _{air}	R ²	0.556	0.161	0.295	0.441	0.295	0.306	0.311
	p	<0.05	<0.05	<0.05	<0.05	<0.05	<0.05	<0.05
Th _{soil} vs Th _{air}	R ²	0.561	0.366	0.641	0.473	0.597	0.363	0.682
	p	<0.05	<0.05	<0.05	<0.05	<0.05	<0.05	<0.05



Table B.3: Regression analysis by domain for areas of peat only.

Domain		1	2	3	4	5	6	7
K _{soil} vs K _{air}	R ²	0.585	0.499	0.721	0.598	0.627	0.309	0.443
	p	<0.05	<0.05	<0.05	<0.05	<0.05	<0.05	<0.05
U _{soil} vs U _{air}	R ²	0.520	0.172	0.330	0.128	0.415	0.113	0.074
	p	<0.05	<0.05	<0.05	0.158132	<0.05	<0.05	<0.05
Th _{soil} vs Th _{air}	R ²	0.414	0.510	0.684	0.343	0.637	0.304	0.525
	p	<0.05	<0.05	<0.05	<0.05	<0.05	<0.05	<0.05

Table B.4: Median radioelement concentrations and ratios by soil texture class.

K_{soil} [%]	U_{soil} [mg/kg]	Th_{soil} [mg/kg]	K_{air} [%]	U_{air} [ppm]	Th_{air} [ppm]	Ksoil/ Kair	Usoil/ Uair	Thsoil/ Thair	Texture	Sample size
1.26	3.1	6	0.96	1.18	4.55	1.32	2.63	1.32	Alluvium	71
0.61	3.7	5.4	0.38	1.33	3.11	1.59	2.78	1.74	Clayey	113
1.25	2.9	4.7	0.93	1.15	3.34	1.34	2.52	1.41	Coarse Loamy	615
1.23	2.9	5.9	1.01	1.25	4.515	1.22	2.32	1.31	Fine Loamy	1664
1.51	2.55	6	1.14	1.02	4.495	1.32	2.50	1.33	Loamy	447
0.24	2	1.3	0.28	0.28	1.24	0.86	7.14	1.05	Peaty	2195
1.08	1.8	2.6	0.925	0.45	2.465	1.17	4.00	1.05	Sandy drift	38
0.92	2.2	3.1	0.9	0.92	3.3	1.02	2.39	0.94	Other	445

Table B.5: Median soil and radiometric concentrations and ratios by CORINE Land Cover class.

CLC class	sample size	K_{soil} [%]	U_{soil} [mg/kg]	Th_{soil} [mg/kg]	K_{air} [%]	U_{air} [ppm]	Th_{air} [ppm]	Ksoil/ Kair	Usoil/ Uair	Thsoil/ Thair
Airports	1	1.15	4	7.3	1.03	1.53	6.46	1.12	2.61	1.13
beaches, dunes, sands	48	0.83	1.4	1.4	0.89	0.345	1.58	0.94	4.06	0.89
broad leaf forest	14	0.99	2.6	5.35	0.74	0.755	3.1	1.34	3.44	1.73
burnt areas	3	0.15	1.9	0.35	0.13	0.25	1.19	1.12	7.60	0.29
complex cultivation patterns	45	1.20	2.9	5.6	1.18	1.24	5.07	1.02	2.34	1.10
coniferous forest	91	0.19	2	1.1	0.18	0.24	0.99	1.05	8.33	1.11
construction sites	1	1.64	2.9	7.6	0.92	1.81	5.71	1.78	1.60	1.33
continuous urban fabric	1	1.60	1.6	8.5	1.95	1.69	7.23	0.82	0.95	1.18
discontinuous urban fabric	138	1.10	2.8	4.95	0.89	1.47	4.485	1.24	1.90	1.10



green urban areas	17	1.04	2.8	4.8	1.01	1.38	4.68	1.03	2.03	1.03
industrial or commercial units	28	1.06	2.9	5	0.975	1.58	4.41	1.08	1.84	1.13
inland marshes	12	1.04	3.2	4.35	0.535	0.695	2.48	1.94	4.60	1.75
intertidal flats	1	0.25	2.3	1.7	0.17	0.01	0.53	1.47	230.00	3.21
land principally occupied by agriculture	702	0.80	2.9	4.7	0.56	0.98	2.97	1.44	2.96	1.58
mineral extraction sites	1	0.49	1.6	1	0.92	0.37	1.52	0.54	4.32	0.66
mixed forest	11	1.59	2.4	3.8	0.96	0.66	4.05	1.66	3.64	0.94
moors and heathland	167	0.70	2.1	2.2	0.69	0.55	2.47	1.01	3.82	0.89
natural grassland	51	0.96	2	3.3	0.56	0.49	1.99	1.71	4.08	1.66
non-irrigated arable land	225	1.24	3.2	6.5	1.2	1.56	5.45	1.03	2.05	1.19
pastures	2270	1.33	2.8	5.8	1.02	1.17	4.135	1.31	2.39	1.40
peat bogs	1600	0.14	1.8	0.9	0.21	0.18	0.91	0.65	10.00	0.99
road and rail networks and associated land	1	0.92	3	3.5	0.88	1.41	5.05	1.04	2.13	0.69
salt marshes	5	0.67	1.9	1.8	1.1	1.33	4.53	0.61	1.43	0.40
sparsely vegetated areas	41	0.34	2	1.4	1.11	0.62	3.5	0.30	3.23	0.40
sport and leisure facilities	53	1.06	2.8	4.6	0.93	1.41	3.95	1.13	1.99	1.16
transitional woodland shrub	81	0.14	2.1	1.2	0.19	0.23	1.15	0.72	9.13	1.04

Table B.6: Effect of outcrops and subcrops on median radioelement concentrations and soil:air ratios.

	<i>K</i> _{soil} [%]	<i>U</i> _{soil} [ppm]	<i>Th</i> _{soil} [ppm]	<i>K</i> _{air} [%]	<i>U</i> _{air} [ppm]	<i>Th</i> _{air} [ppm]	<i>K</i> _{soil} / <i>K</i> _{air}	<i>U</i> _{soil} / <i>U</i> _{air}	<i>Th</i> _{soil} / <i>Th</i> _{air}
Outcrops/ subcrops	0.934	2.2	3.4	0.83	0.73	3.06	1.125	3.034	1.113
Without outcrops/ subcrops	0.969	2.6	4.3	0.71	0.94	3.00	1.364	2.766	1.433



Table B.7: Effect of depth to bedrock on median radioelement concentrations and soil:air ratios.

<i>depth to rock</i>	<i>sample size</i>	<i>K_{soil} [%]</i>	<i>U_{soil} [mg/kg]</i>	<i>Th_{soil} [mg/kg]</i>	<i>K_{air} [%]</i>	<i>U_{air} [ppm]</i>	<i>Th_{air} [ppm]</i>	<i>K_{soil}/K_{air}</i>	<i>U_{soil}/U_{air}</i>	<i>Th_{soil}/Th_{air}</i>
ALL	5609	0.96	2.5	4.2	0.73	0.91	3.01	1.31458	2.747253	1.395349
<1 m	730	0.93	2.2	3.4	0.82	0.725	3.045	1.138914	3.034483	1.116585
1 - 3 m	1339	1.01	2.4	4.3	0.79	0.83	3.11	1.28094	2.891566	1.382637
3 - 5 m	855	1.01	2.6	4.6	0.77	0.97	3.04	1.314211	2.680412	1.513158
5 - 10 m	1117	0.93	2.6	4.3	0.68	0.95	2.93	1.361188	2.736842	1.467577
>10 m	1568	0.92	2.7	4.3	0.66	0.98	2.95	1.3886	2.755102	1.457627

Table B.8: Median radioelement concentrations and ratios by bedrock geological unit (1:1million).

<i>Bedrock Geological Unit</i>	<i>sample size</i>	<i>K_{soil} [%]</i>	<i>U_{soil} [ppm]</i>	<i>Th_{soil} [ppm]</i>	<i>K_{air} [%]</i>	<i>U_{air} [ppm]</i>	<i>Th_{air} [ppm]</i>	<i>K_{soil}/K_{air}</i>	<i>U_{soil}/U_{air}</i>	<i>Th_{soil}/Th_{air}</i>
Cambrian greywacke, slate, quartzite	44	1.298	2.7	4.8	1.23	1.175	4.895	1.08	2.29	0.97
Devonian volcanic rocks	2	0.817	2.4	3.1	0.915	0.56	3.08	0.81	4.36	0.95
Late Ordovician-Silurian deep marine greywacke, mudstone (Longford-Down)	535	1.645	2.8	7.6	1.4	1.24	6.08	1.19	2.30	1.22
Lower-Middle Ordovician slate, sandstone, greywacke, conglomerate	103	1.133	2.2	4.3	0.91	0.89	3.59	1.27	2.59	1.21
Lr Palaeozoic basic-intermediate intrusion	60	0.232	1.3	0.4	0.26	0.18	0.685	1.09	6.69	1.04
Mesoproterozoic gneiss	14	0.986	1.75	1.85	0.775	0.305	1.405	1.08	6.91	1.57
Middle-Upper Ordovician slate, sandstone, greywacke, conglomerate	233	1.263	2.5	6.1	0.9	0.95	4.31	1.36	2.65	1.39
Namurian shale, sandstone, siltstone & coal	91	0.397	2.7	3.6	0.13	0.25	1.3	1.79	7.60	1.74
Neoproterozoic metasedimentary rocks - Dalradian	1463	0.760	2.1	2.8	0.57	0.47	2.27	1.33	4.87	1.26
Neoproterozoic schist and gneiss	113	0.379	1.9	1.4	0.52	0.25	1.31	1.08	8.26	1.30
Ordovician granitic rocks	2	0.673	3.2	1.55	0.415	0.275	0.905	0.93	54.15	2.15
Ordovician volcanic rocks	20	0.887	2.15	2.45	0.99	0.64	3.33	0.84	2.45	0.76
ORS, sandstone, conglomerate & mudstone	75	0.795	1.8	2.1	0.41	0.3	1.68	1.52	5.44	1.33



Palaeogene basic intrusive rocks	7	1.973	2.7	6.3	1.61	1.28	6.41	1.19	2.11	1.02
Palaeogene granitic rocks	16	2.467	3.6	9.3	2.245	1.935	8.65	1.09	1.99	1.06
Palaeoproterozoic gneiss	6	1.332	1.55	1.75	1.49	0.575	2.885	1.02	2.82	0.68
Permian sandstone, conglomerate, evaporite	3	1.818	2.7	7.1	1.31	1.06	5.22	1.49	2.41	1.32
Serpentinite and sedimentary melange (Palaeozoic)	20	0.969	2	3.8	0.655	0.425	3.475	1.53	5.52	1.22
Silurian deep marine mudstone, greywacke & conglomerate	29	1.029	3.1	5.5	1.1	1.42	5.48	0.96	2.35	1.05
Silurian terrestrial - shallow marine sandstone, siltstone, conglomerate	45	0.389	2	2.1	0.33	0.28	2.01	1.43	7.24	1.13
Siluro-Devonian granitic rocks & appinite	430	0.479	2.3	1.7	0.895	0.71	2.74	0.76	3.48	0.77
Tournaisian limestone	173	1.098	3.1	5.3	0.92	1.38	4.23	1.22	2.31	1.23
Tournaisian sandstone, mudstone, limestone	97	1.107	2.8	4.8	0.74	0.85	2.67	1.41	3.27	1.58
Triassic sandstone, mudstone, evaporite	2	1.843	2.65	8.95	1.335	1.135	6.635	1.39	2.37	1.35
Visean limestone & calcareous shale	1591	0.899	3	4.2	0.66	1.23	2.93	1.35	2.47	1.43
Visean sandstone, mudstone & evaporite	403	0.527	2.3	3.1	0.34	0.55	1.83	1.66	4.80	1.81
Westphalian shale, sandstone, siltstone & coal	1	1.713	3.2	8.6	1.35	1.37	5.88	1.27	2.34	1.46

Table B.9: Description of Teagasc Soils “parent material” codes.

<i>Parent Material</i>	<i>Description</i>
A	Alluvium (undifferentiated)
BktPt	Blanket Peat
Cut	Cutover Peat
FenPt	Fen Peat
GDCSs	Sandstone Sands and Gravels (Devonian/Carboniferous)
GGr	Granite Sands and Gravels
GLPSs	Sandstone Sands and Gravels (Lower Palaeozoic)
GLPSSs	Sandstone and Shale Sands and Gravels (Lower Palaeozoic)
GLs	Limestone Sands and Gravels (Carboniferous)
GMp	Metamorphic Sands and Gravels



IrSTCSs	Sandstone and Shale Till (Cambrian/Precambrian) with matrix of Irish Sea Basin origin
IrSTLPSs	Sandstone and Shale Till (Lower Palaeozoic) with matrix of Irish Sea Basin origin
L	Lake Sediments (undifferentiated)
Made	Made Ground
Mbs	Beach Sand
Mesc	Estuarine Sediments (silts & clays)
MGs	Raised Beach Sands and Gravels
RckCa	Bedrock at or near surface - calcareous
RckNca	Bedrock at or near surface - non-calcareous
Scree	Scree
TBi	Basic Igneous Till
TCSsCh	Carboniferous Sandstone and Chert Till
TCSs	Sandstone and Shale Till (Cambrian/Precambrian)
TDCSs	Sandstone Till (Devonian/Carboniferous)
TDCSsS	Sandstone and Shale Till (Devonian/Carboniferous)
TdlMr	Tidal Marsh
TDSs	Sandstone Till (Devonian)
TGr	Granite Till
TLPDSs	Sandstone Till (Lower Palaeozoic/Devonian) TLPDSs
TLPSs	Sandstone Till (Lower Palaeozoic)
TLPSsS	Sandstone and Shale Till (Lower Palaeozoic)
TLs	Limestone Till (Carboniferous)
TMp	Metamorphic Till
TNCSSs	Shale and Sandstone Till (Namurian and Carboniferous)
TNSSs	Shale and Sandstone Till (Namurian)
TQz	Quartzite Till
Ws	Blown Sand
Wsd	Blown Sand in Dunes



Table B.10: Median radioelement concentrations and ratios by soil parent material (Teagasc).

<i>Parent Material</i>	<i>sample size</i>	<i>Ksoil [%]</i>	<i>Usoil [mg/kg]</i>	<i>Thsoil [mg/kg]</i>	<i>Kair [%]</i>	<i>Uair [ppm]</i>	<i>Thair [ppm]</i>	<i>Ksoil/Kair</i>	<i>Usoil/Uair</i>	<i>Thsoil/Thair</i>
A	50	1.30	3.3	6.35	1.06	1.185	4.705	1.23	2.78	1.35
BktPt	1285	0.11	1.8	0.8	0.15	0.14	0.71	0.74	12.86	1.13
Cut	328	0.68	2.7	3.35	0.35	0.56	1.675	1.94	4.82	2.00
FenPt	3	0.86	3.4	3.6	0.36	0.9	1.69	2.38	3.78	2.13
GDCSs	3	0.35	2.5	0.35	0.85	0.32	1.66	0.41	7.81	0.21
GGr	9	1.72	2.9	4.8	1.71	1.22	4.56	1.01	2.38	1.05
GLPSs	1	1.42	2.7	5.2	0.33	0.61	2.26	4.30	4.43	2.30
GLPSsS	9	1.44	2.4	5.1	1.08	1.04	5.01	1.33	2.31	1.02
GLs	56	1.09	2.9	3.9	0.915	1.21	3.505	1.19	2.40	1.11
GMp	3	1.52	2.1	6.6	1.12	0.75	4.55	1.36	2.80	1.45
IrSTCSsS	5	1.30	2.8	4.9	1.4	1.21	5.36	0.93	2.31	0.91
IrSTLPSsS	31	1.50	2.6	7.2	1.4	1.34	6.47	1.07	1.94	1.11
L	6	1.60	2.55	5.8	0.615	1.2	2.95	2.60	2.13	1.97
Made	134	1.10	2.8	4.8	0.975	1.47	4.43	1.13	1.90	1.08
Mbs	12	1.06	1.4	1.25	0.82	0.34	1.61	1.29	4.12	0.78
Mesc	5	1.39	2.9	6.1	0.42	0.95	2.24	3.32	3.05	2.72
MGs	26	1.02	1.85	2.8	1.015	0.64	2.5	1.01	2.89	1.12
RckCa	65	0.92	3.1	4.9	0.5	1.35	2.3	1.83	2.30	2.13
RckNCa	659	0.93	2.1	3.2	0.87	0.68	3.19	1.07	3.09	1.00
Scree	17	0.88	2.3	5	0.5	0.69	2.86	1.76	3.33	1.75
TBi	1	1.18	2.6	4.3	0.81	0.87	3.29	1.45	2.99	1.31
TCSsCh	56	0.48	2.9	4.15	0.32	0.94	2.24	1.50	3.09	1.85
TCSsS	9	1.24	2.8	5.3	1.08	1.15	4.68	1.15	2.43	1.13
TDCSs	151	1.10	2.6	4.4	0.81	1.01	3.21	1.36	2.57	1.37
TDCSsS	68	1.58	2.6	5.8	0.995	1.03	3.52	1.59	2.52	1.65
TdlMr	2	0.83	1.25	1.5	0.845	0.365	2.15	0.98	3.42	0.70
TDSs	99	0.95	2.4	3.8	0.64	0.85	2.78	1.49	2.82	1.37
TGr	102	1.58	3	5.1	1.55	1.265	5.17	1.02	2.37	0.99
TLPDSs	2	1.03	3	4.1	0.76	0.69	1.855	1.35	4.35	2.21
TLPSSs	25	1.18	2	4.5	0.85	0.7	3.43	1.38	2.86	1.31
TLPSSsS	660	1.55	2.8	7.1	1.29	1.18	5.625	1.20	2.37	1.26
TLs	680	0.99	3.2	4.7	0.79	1.475	3.62	1.26	2.17	1.30



TMp	615	1.70	2.6	6.3	1.2	1.02	4.62	1.41	2.55	1.36
TNCSSs	16	0.57	2.4	3.9	0.34	0.75	2.085	1.67	3.20	1.87
TNSSs	333	0.67	3.2	4.7	0.42	1.14	2.75	1.59	2.81	1.71
TQz	13	1.74	2.5	6.5	1.15	0.72	4.41	1.51	3.47	1.47
Ws	26	0.70	1.2	1.4	0.87	0.35	1.77	0.80	3.43	0.79
Wsd	34	0.73	1.45	1.5	0.93	0.465	1.875	0.78	3.12	0.80

Table B.11: Linear regression equations (C) for K, U and Th pairs.

<i>Element</i>	<i>Equation</i>	<i>R²</i>
K	1.0319x + 0.1449	0.6695
U	1.2118x + 1.5556	0.1493
Th	1.025x + 0.7903	0.6256

Table B.12: Separate linear regression equations for areas with and without peat (D).

<i>Element</i>		<i>Equation</i>	<i>R²</i>
K	No peat	0.9608x + 0.2435	0.5937
	Peat only	0.9967x + 0.0881	0.425
U	No peat	1.2817x + 1.3306	0.3319
	Peat only	2.5026x + 1.412	0.111
Th	No peat	0.9263x + 1.3123	0.5329
	Peat only	1.1563x + 0.3059	0.469



Table B.13: Separate linear regression equations for areas with and without peat, by domain (E).

<i>Domain</i>		<i>K</i>	<i>U</i>	<i>Th</i>
1	no peat	1.1347x + 0.1629	1.6787x + 1.3755	1.4117x + 0.8341
	peat only	1.2998x + 0.0817	2.2949x + 1.8511	1.6942x + 0.7067
2	no peat	0.8175x + 0.3341	0.5796x + 2.2121	0.8093x + 1.6013
	peat only	1.2903x + 0.0859	1.9969x + 1.9663	1.4187x + 0.3444
3	no peat	1.2363x + 0.1131	1.4924x + 1.3621	1.3392x + 0.3318
	peat only	1.3287x + 0.0602	2.2037x + 1.5619	1.4402x + 0.3198
4	no peat	1.132x + 0.2055	1.2513x + 1.2993	1.2202x + 0.5564
	peat only	1.6161x + 0.1458	0.5265x + 1.9009	0.9146x + 1.1447
5	no peat	0.8722x + 0.3797	1.0832x + 1.4314	0.8683x + 1.8487
	peat only	1.1934x + 0.1157	1.2597x + 1.4936	1.2581x + 0.5544
6	no peat	0.7055x + 0.243	1.7868x + 0.7661	0.6609x + 0.9625
	peat only	0.3913x + 0.0253	5.2484x + 0.0814	0.6638x + 0.0033
7	no peat	1.3464x - 0.0901	1.1942x + 1.404	1.2601x - 0.0604
	peat only	1.1403x + 0.0489	1.6935x + 1.5211	1.2714x - 0.0104

Table B.14: Median % deviation (absolute) from true soil values, for areas with and without peat, by domain (prediction method E).

<i>Domain</i>	<i>K</i>	<i>U</i>	<i>Th</i>
1	21.75 %	21.34 %	22.21 %
2	19.91 %	14.24 %	25.02 %
3	21.18 %	16.35 %	23.86 %
4	18.38 %	16.43 %	25.66 %
5	12.71 %	12.16 %	13.26 %
6	42.44 %	42.90 %	53.91 %
7	35.72 %	18.13 %	38.70 %

